A contribution to the development of sensitive and isotope-selective analytical methods based on sector-field ICP-MS

For supporting the development of Generation IV nuclear reactors

Thesis submitted in fulfillment of the requirements for the degree of Doctor of Science: Chemistry

by

Tom Tindemans

Supervisor: Prof Dr Frank Vanhaecke
Co-supervisor: Dr Andrew Dobney
Co-supervisor: Dr Dorine Wambeke

Department of Analytical Chemistry
Faculty of Sciences
Academic year 2014-2015

Acknowledgements

Zoals vermoed ik wel vaker het geval is, ben ik het schrijven van dit dankwoord tot het allerlaatste moment blijven uitstellen. Niettegenstaande had dit manuscript nooit tot stand kunnen komen zonder de hulp van een heel aantal mensen. In dit opzicht wil ik in de eerste plaats mijn drie promotoren bedanken voor hun onaflatende steun en toewijding gedurende de afgelopen vier jaar, ook op de momenten dat het even wat minder ging. Frank en Andrew waren bereid om mij een plaats te gegeven in hun respectievelijke groepen, terwijl ik zonder Dorine misschien helemaal nooit aan een doctoraatsonderzoek was begonnen.

Op financieel vlak ben ik zowel aan het studiecentrum voor kernenergie (SCK•CEN) als aan het fonds voor wetenschappelijk onderzoek Vlaanderen (FWO) dank verschuldigd. Dit doctoraatsonderzoek werd dan ook enkel mogelijk gemaakt dankzij het aspirantenmandaat dat zij mij vier jaar geleden toekenden.

Daarnaast had ik dit werk natuurlijk nooit kunnen voltooien zonder de nodige ondersteuning vanuit het SCK•CEN. In het bijzonder wil ik hierbij Joris Van den Bosch, Kris Rosseel, Ben Caers en Serguei Gavrilov bedanken, voor het aanreiken van belangrijke achtergrondinformatie en het beschikbaar maken van de benodigde monsters. Joris was daarnaast ook bereid om de resultaten van een aantal neutronenactiveringsanalyses ter mijner beschikking te stellen, afkomstig van metingen die verricht werden door Liesel Sneyers en Peter Vermaercke, en waarvan de gegevens gedeeltelijk zijn opgenomen in dit werk.

Verder zou ik ook nog alle collega's van gebouwen SCH en S12 willen bedanken, en dan in het bijzonder diegene die mij gedurende mijn doctoraatsonderzoek op eender welke wijze dan ook hebben geholpen of bijgestaan. Hierbij wil ik zeker mijn voormalige bureaugenoten Liliane, Nele, An, Mirela, Lipika, Katrien, Sien, Eleonora, Steven, Stepan & Veerle vermelden, niet in het minst omdat ze met regelmaat zorgden voor een, af en toe broodnodige, luchtige noot!

Daarenboven wil ik de voorzitter van de examencommissie Prof Dr Karel Strijckmans bedanken om alles in goede banen te leiden en wil ik de leden van de leescommisie Dr Lieve Balcaen, Dr Stefaan Van Winckel en Prof Dr Frederic Lynen op hun beurt bedanken omdat ze bereid waren om mijn manuscript grondig door te nemen en vervolgens suggesties voor verbeteringen te formuleren.

Tot slot wil ik mij richten tot mijn naastste familieleden, meer bepaald de drie belangrijkste vrouwen in mijn leven. Mijn moeder, die mij de kans gegeven heeft om verder te gaan studeren en mij hierbij steeds is blijven steunen, ook al waren mijn allereerste stappen in het hoger onderwijs niet bepaald succesvol te noemen. Mijn vrouw Riet, mijn steun en toeverlaat, die de afgelopen maanden misschien

net iets meer geduld en begrip heeft moeten opbrengen om te kunnen omgaan met mijn stressgerelateerde grillen. En *last, but certainly not least,* ben ik mijn kersverse dochter Lore eeuwig dankbaar voor de onverhoopt stille nachten, althans tijdens haar eerste levensmaand, zodat ik goed uitgerust de laatste hand kon leggen aan dit manuscript. Ik draag deze tekst dan ook graag aan haar op!

Contents

Glossary

ADS
Accelerator Driven System

DCP
Direct Current Plasma

ETV
ElectroThermal Vaporisation

GC
Gas Chromatography

GFAAS
Graphite Furnace Atomic Absorption Spectrometry

GIF
Generation IV International Forum

HDPE
High-Density PolyEthylene

HLM
Heavy Liquid Metal

HPLC
High-Performance Liquid Chromatography

ICP
Inductively Coupled Plasma

ICP-MS
Inductively Coupled Plasma-Mass Spectrometry

ICP-OES
Inductively Coupled Plasma-Optical Emission Spectrometry

ICP-QMS
Quadrupole Inductively Coupled Plasma-Mass Spectrometry

ICP-SFMS
double-focusing Sector-Field Inductively Coupled Plasma-Mass Spectrometry

ID
Isotope Dilution

IRZ
Initial Radiation Zone

LA

Laser Ablation

LBE

Lead-Bismuth Eutectic

LFR

Lead-cooled Fast Reactor

MC

Multi-Collector

MIP

Microwave-Induced Plasma

MS

Mass Spectrometry

MYRRHA

Multi-purpose hYbrid Research Reactor for High-tech Applications

NAZ

Normal Analytical Zone

PFA

PerFluoroalkoxy Alkane

PHZ

PreHeating Zone

PP

PolyPropylene

PTFE

PolyTetraFluoroEthylene

QL

Quantification limit which is defined as $|avg(c_{blank})| + 10 \cdot sd(c_{blank})$

RF

RadioFrequency

SCK•CEN

Belgian Nuclear Research Centre

SFR

Sodium-cooled Fast Reactor

TIMS

Thermal Ionisation Mass Spectrometry

1 Introduction

The development, evaluation and application of a number of analytical methods is discussed over the course of this text. This first chapter, however, serves solely to provide the reader with the broader context and a general overview of this work. For this purpose, the efforts of the *Belgian Nuclear Research Centre* (SCK•CEN), towards the development of novel nuclear technologies, are discussed. Since this work aims to make a small contribution to these ambitious endeavours, some background information is essential in order to recognise why there is a specific need for the analytical methods that have been developed. Furthermore, it will become clear which issues had to be overcome and why the author resorted to the techniques and instrumentation that were used in this work. Portions of this introductory chapter have previously been published in Tindemans *et al.*[1,2]

1.1 Background and context

1.1.1 Anthropogenic climate change

Although still the subject of ongoing debate, anthropogenic climate change is a widely accepted global phenomenon that has received increased attention in the international media during recent years, especially in those countries which made commitments under the *Kyoto Protocol*. Mitigating the effects of global warming, by limiting the rise in average temperature to no more than $2\,°C$, demands decisive action in the coming decades.[3,4] As such, reducing the emission of greenhouse gasses, such as CO_2, produced by *e.g.* the burning of fossil fuels, will require effort on a global level. At the same time, however, an ever increasing demand for electrical power is expected, *e.g.* in the European Union.[5] Since, in that specific case, and as recently as 2012, the energy sector was already responsible for nearly $80\,\%$ of greenhouse gas emissions, the development and deployment of innovative energy technologies will be essential if our environment is to be safeguarded whilst adequate supplies of energy are maintained.[6] Although renewable and sustainable technologies such as wind and solar power will also have an increasingly important role to play, nuclear power is still an important and reliable low-carbon source of energy. Despite its controversial reputation, especially in the wake of the Fukushima Dai-ichi accident, nuclear power provided as much as $25\,\%$ of the electricity consumed throughout the European Union in 2010.[7] As a result, it will most likely continue to play a pivotal role in the foreseeable future. However, the development of novel nuclear technologies will be essential for ensuring the sustainability and the continued social acceptance of nuclear power.[8–11]
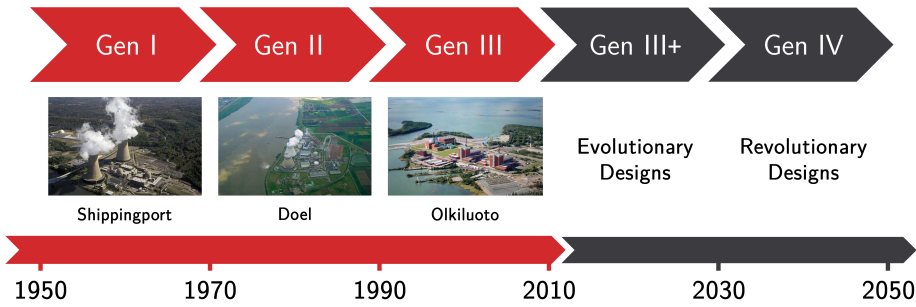
Figure 1.1: Indicative timeline for the deployment of nuclear fission reactors, from early Gen I prototypes to current Gen II & III reactors and beyond.

1.1.2   Generation IV technologies

The fourth generation (Gen IV) of nuclear fission reactors is currently being developed, although these designs will most likely not come to fruition before 2030.[12] In due time, however, these novel reactor designs will replace the second and third generation (Gen II & Gen III) nuclear power plants that are currently being constructed and operated throughout the world (see Figure 1.1). A framework for international cooperation in research and into the development of the next generation of nuclear energy systems, was established in the form of the *Generation IV International Forum* (GIF). The GIF identified four major areas of improvement for Gen IV designs in its Gen IV technology roadmap. These areas include (i) sustainability, (ii) safety and reliability, (iii) economic viability and (iv) proliferation resistance and physical protection. Whilst Gen III designs were essentially mere evolutions of existing Gen II technologies, innovative Gen IV designs are expected to offer some significant changes in these areas. The six most promising Gen IV technologies that were selected by the GIF for further development are (i) the gas-cooled fast reactor, (ii) the molten salt reactor, (iii) the sodium-cooled fast reactor, (iv) the supercritical-water-cooled reactor, (v) the very-high-temperature reactor and finally (vi) the lead-cooled fast reactor.[12–14]

The lead-cooled fast reactor (LFR), the last-mentioned of the selected Gen IV concepts, refers to Pb- or Pb/Bi-alloy-cooled fast neutron spectrum reactors operating in an advanced fuel cycle. Whilst heavy liquid metal (HLM) coolants were already considered during the 1950s, *e.g.* in the former Soviet Union, for use in nuclear propulsion systems in marine vessels, there has of late been a renewed interest in this technology. Currently, a number of applications are proposed in the conceptual designs of LFRs, including commercial electricity generation and minor actinide management in a closed fuel cycle. The minor actinides Np, Am and Cm contribute significantly to the long term radiotoxicity of high-level radioactive waste. Therefore, the management of these elements poses a critical issue in the continued and sustainable use of nuclear power. In combination with partitioning and recycling, transmutation of minor actinides could potentially reduce the re-
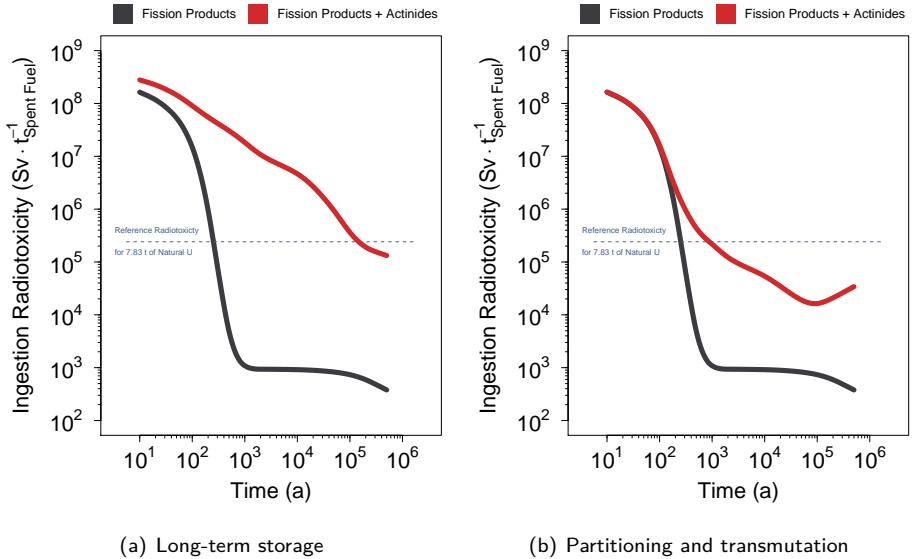
Figure 1.2: Calculated ingestion radiotoxicity for $1\,\text{ton}$ of spent fuel, based on an initial enrichment of $4.2\,\%$ ^{235}U and a burnup of $50\,\text{GWd\,ton}^{-1}$, produced from $7.83\,\text{ton}$ natural U. (a) The spent fuel is sent directly to a long-term repository, whereby the reference level is reached after more than $100\,000\,\text{a}$. (b) The reference level could be reached after as little $1000\,\text{a}$ by partitioning and transmutation of minor actinides. (Graphs reproduced from calculations published by Magill *et al.*[15])

quired storage time for high-level nuclear waste by several orders of magnitude to as little as 1000 years (see Figure 1.2). However, their efficient transmutation, into shorter-lived or stable nuclides, is only feasible with a fast neutron spectrum reactor. Aside from enabling the efficient transmutation of minor actinides, a fast neutron spectrum also allows for the conversion of fertile ^{238}U into fissile ^{239}Pu by neutron capture. The total energy potential of natural U reserves could thereby be increased by a factor of *ca.* 100. Another advantageous feature, albeit specific to LFR designs, is the fact that Pb and Pb/Bi-alloys are relatively inert towards both air and water. In addition, these HLM coolants are characterised by several favorable thermophysical and neutronic properties. However, both types of coolants have been found to be relatively corrosive towards structural steels, which poses an important design challenge. In addition, radioactive contamination of the coolant, due to the production of the volatile and radiotoxic ^{210}Po, induced by neutron capture of ^{209}Bi, will be of great concern, especially when a Pb/Bi-alloy is considered as the reactor's coolant rather than pure Pb. Furthermore, the crustal abundance of Bi may be insufficient to support a widespread use of Pb/Bi-alloy-cooled technologies. Even though Pb/Bi-alloys have lower melting points than pure Pb, which would allow for lower operating temperatures, resulting in a reduced corrosiveness towards structural steels, pure Pb has instead been selected as the coolant of choice for Gen IV systems by the GIF.[12–19]

1.1.3   The MYRRHA research reactor

The efforts of SCK•CEN towards the development of Gen IV nuclear fission reactors have been consolidated in the MYRRHA project. This *Multi-purpose hYbrid Research Reactor for High-tech Applications* (MYRRHA) has been in development at the research centre since the 1990s, under cooperation with other European research facilities. Once operational, it will serve as a source of protons and neutrons for a variety of R&D applications. Although the MYRRHA research reactor will not itself be a Gen IV reactor, it will be based on the use of HLM-cooled fast reactor technology, which will enable it to contribute significantly to the development of LFRs and other Gen IV concepts. Initially, the MYRRHA research reactor will serve as a proof of concept for nuclear waste transmutation by accelerator-driven systems (ADS). Later on, MYRRHA will also serve as a multi-purpose irradiation facility for various other R&D applications. As such, its task profile will consist of, but will not be limited to, (i) demonstrating the ADS concept, (ii) performing research on the safety of subcritical systems, (iii) conducting research on the transmutation of minor actinides and long-lived fission products, (iv) performing materials and fuel research for Gen IV concepts and other systems and also (v) producing radionuclides for medical and industrial applications.[20,21]

MYRRHA has been conceived as a flexible irradiation facility, able to operate in subcritical, but also in critical mode. Initially, MYRRHA is intended to be operated solely in subcritical mode, whereby insufficient fissile material will be present in the reactor to allow for self-sustaining criticality. Therefore, an external and continuous source of neutrons is required. A high-power proton accelerator, bombarding a *Lead-Bismuth Eutectic* (LBE) spallation target, which is coupled to an LBE-cooled fast core, fulfills this role in the MYRRHA design. The high-energy protons that impinge on the HLM target generate neutrons, which, in turn, sustain the nuclear chain reaction in the core. An ADS is inherently safe and controllable, even when the core is loaded with a substantial amount of minor actinides, whilst a fast neutron spectrum enables the efficient transmutation of those minor actinides. Therefore, such systems are considered to be especially well suited for transmuting minor actinides in high-level radioactive waste. Later on in MYRRHA's lifetime, the proton accelerator and the spallation source will be decoupled, after which the reactor will be operated as a critical LBE-cooled fast neutron irradiation facility. The main focus will then shift to fuel and materials research for Gen IV concepts and other advanced systems, such as fusion reactors.[22–26]

1.1.4   Lead-bismuth eutectic as MYRRHA's primary coolant

As discussed in the previous section, the MYRRHA research reactor will employ liquid LBE as its primary coolant and, in subcritical mode, also as its spallation target. This Pb/Bi-alloy consist of *ca.* 45 wt.% Pb and *ca.* 55 wt.% Bi (see Figure 1.3). Aside from its relative inertness to both air and water, in contrast to *e.g.* Na, LBE possesses a number of additional favorable properties. Its high boiling point ($T_b \approx 1670\,°C$) reduces the risk of core voiding due to coolant boiling whilst
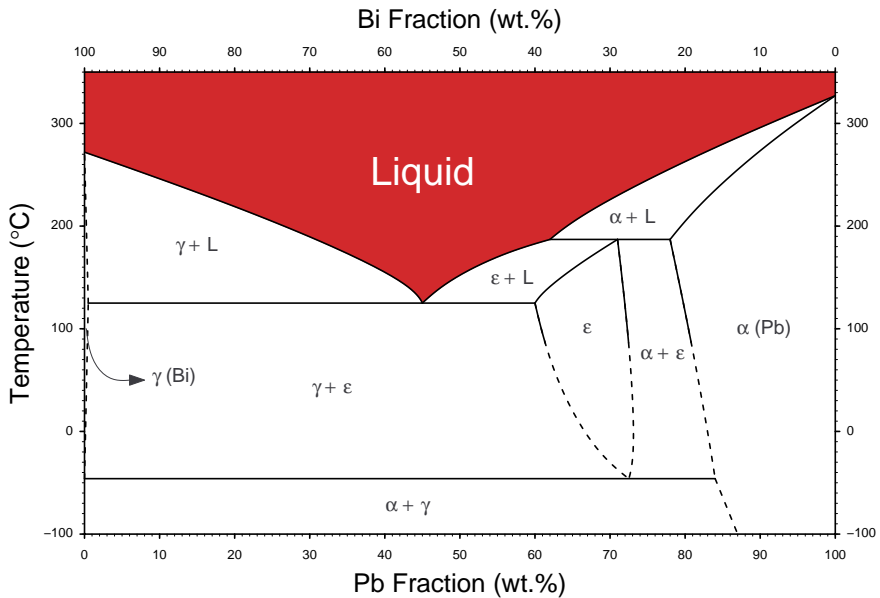
Figure 1.3: Phase diagram for the binary Pb/Bi system. This diagram shows a eutectic point at *ca.* 45 wt.% Pb with a melting temperature of *ca.* 125 °C. (What is shown is a reproduction of the binary phase diagram published in the ASM Handbook of 1992.[27])

its high heat of vaporisation and high thermal capacity provide thermal inertia in case of a loss-of-heat-sink. From a radiation protection point of view, LBE shields γ-rays whilst it is also able to retain both I and Cs, were these volatile fission products to be released from the core in case of an accident. Furthermore, its low neutron moderating power permits a fast neutron spectrum. Whilst the use of an LBE coolant ($T_m \approx 125$ °C) instead of pure Pb ($T_m \approx 327$ °C) allows for lower operating temperatures, thereby reducing the risk of corrosion, the innovative nature of HLM-cooled fast reactors such as MYRRHA still poses considerable challenges with regard to structural and fuel cladding materials performance.[14,22]

1.1.5 Selected high-alloy steels for the MYRRHA design

The austenitic stainless steels 316L and 15-15Ti have been well characterised for use as structural materials in nuclear installations such as sodium-cooled fast reactors (SFR). The ferritic-martensitic steel T91, in contrast, is a relatively newer structural material for nuclear reactors, but it has a better creep resistance, a better swelling resistance and a higher thermal strength than the aforementioned austenitic steels. However, conditions within the MYRRHA reactor will be harsher than in existing installations. The heavy liquid metal (HLM) coolant is highly corrosive under certain conditions and may also affect a steel's mechanical characteristics. Furthermore, the envisaged operating temperature range for MYRRHA is lower than for an SFR and some of its components will be exposed to

both proton and neutron irradiation. Nonetheless, currently available and already qualified industrial steels (T91, 316L and 15-15Ti) are being considered for use as structural and fuel cladding materials, rather than developing innovative materials. These three existing materials were chosen, in part, because MYRRHA is intended to be fully operational within less than a decade and because it was anticipated that these particular steels would exhibit some resistance to the corrosive nature of the LBE coolant. The austenitic stainless steel 15-15Ti has been selected as a fuel cladding material, whilst the ferritic-martensitic steel T91 has been selected for the wrapper of the fuel assembly, the core support plate and the spallation target window. For most other major components, such as the reactor vessel and the heat exchangers, the austenitic stainless steel 316L has been selected.[28–30]

1.2   Aims and objectives

1.2.1   Trace analysis of LBE and high-alloy steels

Trace and minor elements may improve or deteriorate a steel's corrosion resistance or its mechanical characteristics, such as hardness. Conversely, impurities in an LBE coolant may also affect the severity of its corrosive nature towards these high-alloy steels. Aside from the impurities inherent to Pb/Bi-alloys, corrosion and erosion products may also be taken up by liquid LBE, during normal reactor operation. Precipitation of any of the minor constituents of the LBE coolant, in colder parts of a cooling circuit, may cause flow blockages or instabilities, or otherwise hamper reactor operation. Furthermore, radiotoxic nuclides may be produced by the activation of ultra-trace, trace, minor or matrix elements in the high-alloy steels and LBE coolant. The resulting contamination, of either the steel alloys or the liquid LBE, due to exposure to neutron radiation, could then *e.g.* have implications with regard to reactor decommissioning. In addition, there is a risk of fission products ending up in the LBE coolant in case of a fuel cladding rupture. The accurate and precise multi-elemental trace analysis of high-alloy steels and LBE is therefore of great importance, both in the design phase, as well as during routine reactor operation. The results of these analyses can then *e.g.* be used in *source term* calculations or to monitor the corrosion rate of high-alloy steels. To this end, and as the first major objective of this PhD research project, analytical methods were sought for the determination of trace and ultra-trace elements in LBE and three types of corrosion-resistant steel alloys (T91, 316L, 15-15Ti).[22,31–33]

1.2.2   Isotopic analysis of nuclear fuels

In contrast to the first objective, the second objective did not stem directly from SCK•CEN's efforts towards the development of the MYRRHA research reactor. Management of spent nuclear fuel has always been an important issue in the nuclear industry, in which a nuclear criticality safety analysis play an important role. The efficient and cost-effective handling of irradiated fuels requires one to take into account a fuel's reactivity reduction, resulting from the burning of that

fuel's fissile material as well as from the buildup of neutron poisons within. The determination of this so-called *burnup credit* makes it possible to adopt responsibly a less conservative approach to the storage, reprocessing and transport of spent fuel. In essence, the result is that more, and more highly enriched, spent fuel may be kept per unit volume without compromising safety. To ensure that an adequate criticality safety margin is maintained, however, highly accurate calculation methods are essential. Development and validation of such computer models, used to calculate the fuel's isotopic composition, requires experimental assay data to be available. For such purposes, spent fuel samples are already analysed routinely at SCK•CEN. Furthermore, for research into novel fuels and into the transmutation of minor actinides, at the MYRRHA facility, similar types of analyses will be required. Currently, at SCK•CEN, such analytical assays are carried out by means of *Multi-Collector Thermal Ionisation Mass Spectrometry* (MC-TIMS) and various radioanalytical counting techniques. The second objective of this PhD research project was to evaluate the capabilities of *Inductively Coupled Plasma-Mass Spectrometry* (ICP-MS), for the isotopic analysis of nuclear fuels, to add to the set of currently available analytical methodologies.[34,35]

1.2.3   Capabilities of sector-field ICP-mass spectrometry

ICP-MS is a highly-sensitive isotope-selective analytical technique, which combines the multi-elemental capabilities of *Inductively Coupled Plasma-Optical Emission Spectrometry* (ICP-OES) with detection limits that surpass even those associated with *Graphite Furnace Atomic Absorption Spectrometry* (GFAAS). Therefore, this technique is an ideal candidate for the multi-elemental trace analysis of a wide variety of samples, including Pb/Bi-alloys and high-alloy steels. Furthermore, in addition to mere elemental concentrations, the easily interpretable atomic mass spectra also provide isotopic information. The latter allows for the isotopic analysis of various types of samples, including spent nuclear fuel, but also permits the use of *Isotope Dilution* (ID) for high-accuracy elemental analysis. Whilst samples are usually introduced into the instrument in liquid form, ICP-MS instruments can also be combined with *solid-sampling* devices (*e.g.* laser ablation). Furthermore, an ICP-MS can be coupled to a variety of separation techniques (*e.g.* liquid chromatography), whereby the ICP-MS instrument is operated as a detector in a hyphenated setup.[36,37]

Although the vast majority of ICP-MS instruments that have been sold worldwide are *Quadrupole Inductively Coupled Plasma-Mass Spectrometers* (ICP-QMS), the mass resolution of traditional quadrupole mass filters is inadequate to resolve spectral interferences. Such spectral interferences are a general term for an amalgam of different types of interfering species that are typically subdivided in three separate categories. Firstly, isobaric interferences arise when nuclides of two or more elements have the same nominal mass (*e.g.* $^{54}Fe^+ \longleftrightarrow {}^{54}Cr^+$). Luckily, at least for samples of natural isotopic composition, the vast majority of elements have at least one nuclide free from isobaric interference. Secondly, multi-

ply charged ions for which the nominal mass-to-charge ratio coincides with that of a singly charged analyte ion may also be problematic (*e.g.* $^{206}\text{Pb}^{2+} \longleftrightarrow {}^{103}\text{Rh}^{+}$). However, the formation rate of doubly or triply charged ions is usually very low, whereby only those originating from matrix constituents are of great concern. Thirdly, polyatomic species may originate from a number of different sources, including the plasma gas, the entrained air, the sample matrix or other analytes (*e.g.* $^{140}\text{Ce}^{16}\text{O}^{+} \longleftrightarrow {}^{156}\text{Gd}^{+}$). This last class of interfering species is often considered to be the most problematic, as their occurrence is less predictable, especially when analytes are accompanied by a complex matrix.[38,39]

In contrast to early quadrupole ICP-MS instruments, *double-focusing Sector-Field Inductively Coupled Plasma-Mass Spectrometers* (ICP-SFMS) allow for many of these polyatomic spectral interferences to be overcome in an elegant and straightforward manner. This is achieved simply by increasing the instrument's mass resolution, which is often defined as the ratio of an ion's mass versus its corresponding peak's width at 5 % of the peak's height (R=m/Δm). Typically, resolutions ranging from *ca.* 300 to *ca.* 10 000 are available on commercial ICP-SFMS instruments, although it should be noted that the sensitivity of such instruments decreases significantly with increasing resolution. Alternatively, an instrument's resolving power may be expressed by means of the equivalent 10 % valley definition, for two neighboring symmetrical peaks of equal height, or by the peaks' full width at half maximum (FWHM). In addition to providing access to higher resolution modes, ICP-SFMS instruments are typically characterised by a higher sensitivity and a lower background than commercially available ICP-QMS instruments. As a result, instrumental detection limits in the ng L^{-1} range and below have been reported in the literature. However, detection limits are often not limited by instrumental sensitivity or instrumental noise. Instead, detection limits are generally governed by contamination of blanks by reagents (*e.g.* high-purity mineral acids), laboratory equipment (*e.g.* digestion vessels), the instrument's very own sample introduction system (*e.g.* glass components) or through memory effects (*i.e.* carryover from previous samples). Therefore, caution must be taken during sample preparation, and reagents and materials must be selected carefully. Aside from being well suited for ultra-trace elemental analysis, ICP-SFMS may also be employed for isotopic analysis. As a result of the flat-top peaks in the mass spectra, typical for ICP-SFMS instruments operating in their lowest resolution modes, an optimum isotope-ratio precision of $\leq$0.05 % RSD is reportedly attainable.[38,40]

The *radiochemical analysis expert group* at SCK•CEN has one such ICP-SFMS instrument at its disposal, a nuclearised Element 2 (Thermo Scientific, Germany), which was used throughout this work. This particular instrument has been modified for use with a stainless-steel nuclear glovebox by the manufacturer, which will permit analysis of irradiated samples in the future (*e.g.* irradiated LBE or spent fuel). Whilst all experiments described in this work have been carried using *cold* samples, the use of an instrument coupled to a stainless-steel glovebox did prohibit the extensive use of HCl during sample preparation. Since the stainless-steel components of this glovebox are susceptible to corrosion
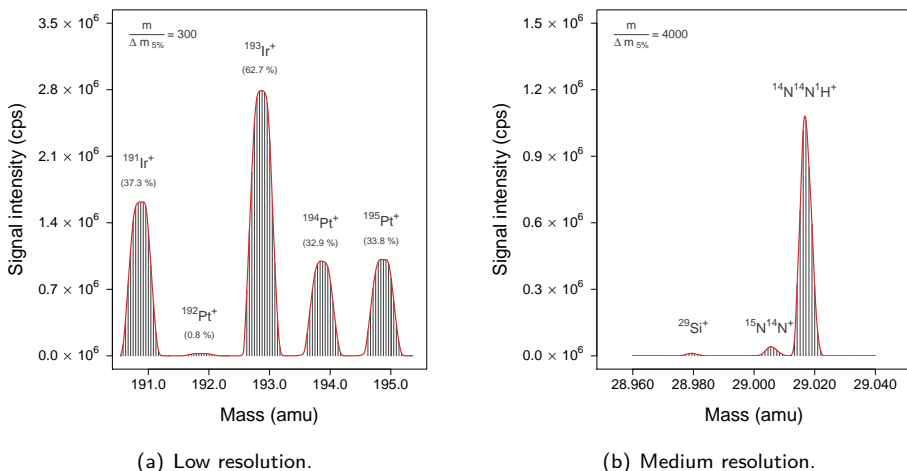
Figure 1.4: Atomic mass spectra for a $4\,\mu g\,L^{-1}$ multi-element standard solution, in the low and medium resolution modes of an Element2 ICP-SFMS. (a) A high sensitivity and a low background result in extremely low detection limits, whilst its flat-top peaks allow for an excellent precision. The spectrum does not only provide elemental information, but also yields an isotopic fingerprint. (b) Many of the frequently occurring polyatomic spectral interferences are easily resolved in the instrument's medium resolution mode, albeit with reduced sensitivity and triangular peaks.

by prolonged exposure to HCl vapours, its use may result in sporadic contaminations or a permanent increase in the chemical blank of elements such as Fe and Cr (*i.e.* the main components of stainless-steels). Two mass spectra which were obtained with this instrument are presented in Figure 1.4, demonstrating its low (R = 300) and medium (R = 4000) resolution operating modes. In addition, a high (R = 10 000) resolution mode is also available. The relevant analytical challenges for elemental and isotopic analysis by means of ICP-SFMS will be discussed in the following two sections, respectively, whilst a more extensive overview of the principles and important considerations of the technique is given in Chapter 2.

1.2.4 Elemental analysis of LBE and high-alloy steels

Although most of the frequently occurring spectral interferences can be resolved with an ICP-SFMS instrument, non-spectral interferences cannot be dealt with so easily. Non-spectral interferences have been described extensively in the literature, but, as of yet, no single approach has been proposed to systemically eliminate all of these so-called matrix effects. Furthermore, the impact of these matrix effects may be hard to predict *a priori* or even to correct for *a posteriori*. Several strategies may be considered to eliminate or to minimise the occurrence of matrix effects, approaches which are discussed more thoroughly in Section 2.9.2. One of these strategies entails selectively isolating the analytes from the matrix elements, by means of an offline chemical separation procedure. Some of the separation techniques that are often employed include precipitation, co-precipitation, liquid-liquid extraction, cloud-point extraction and column chro-

matography. In this work, ion-exchange and extraction chromatography were considered. Most often, a single target element is extracted from a complex multi-element matrix, by means of highly selective resins. In this case, however, we sought to identify resins that were capable of retaining a limited number of matrix elements, whilst exhibiting little to no affinity for a large number of target elements. The selection process of the chromatographic resins to be used for the multi-elemental trace analysis of high-alloy steel and LBE samples, is discussed in Chapters 4 and 5, respectively. A critical evaluation of the analyte/matrix separation procedures that were developed over the course of this research project is also provided in these chapters, along with results of their application to actual samples. It should be noted that the use of an analyte/matrix separation procedure has multiple benefits, as both matrix-induced polyatomic spectral interferences and memory effects are also eliminated. The latter is especially practical when a nuclearised ICP-SFMS instrument is used, where routine maintenance to alleviate such memory effects is more problematic and time-consuming.[41]

1.2.5   Isotopic analysis by means of ICP-SFMS

For commercially available ICP-SFMS instruments, like SCK•CEN's Element2, the optimum isotope ratio precision has been reported to be $\leq 0.05\,\%$ RSD. This value is relatively modest compared to the $\leq 0.01\,\%$ RSD that is routinely reported for modern MC-TIMS instrumentation. In a multi-collector design, multiple detectors are employed instead of a single one, whereby multiple isotopes can be detected and quantified simultaneously rather than sequentially. Simultaneous detection of isotopes eliminates classical sources of uncertainty, associated with sequential measurements, which results in state-of-the-art isotope-ratio precisions. Although MC-TIMS was long considered to be the analytical technique of choice for the determination of isotope-ratios, *e.g.* for $U-Pb$ dating in geochronology, the development of *Multi-Collector ICP-SFMS* instruments (MC-ICP-SFMS) has since bridged the gap between both techniques. Precisions as low as *ca.* $0.002\,\%$ RSD have been reported for MC-ICP-SFMS, values which are on par with those of MC-TIMS. Further still, as its precision and accuracy are comparable to that of MC-TIMS, the use of MC-ICP-SFMS is sometimes even preferred for specific applications. Some of its advantageous features include (i) a higher sensitivity resulting in lower detection limits, (ii) less restrictions with regard to an analyte's first ionisation potential, (iii) a higher sample-throughput and (iv) a reduced need for time-consuming sample preparation procedures.[38,42–44]

Even though the isotope ratio precision of single-collector ICP-SFMS instruments was expected to be inferior to that of MC-TIMS instruments, the aforementioned advantageous features of MC-ICP-SFMS instruments still hold true to some extent for single-collector instruments. Keeping in mind that SCK•CEN's MC-TIMS instrument is an ageing Sector 54 (VG Elemental, UK), first introduced in 1987, the Element2 ICP-SFMS may still be regarded as fit-for-purpose for the isotopic analysis of certain types of samples. An evaluation of the nuclearised

Element2 ICP-SFMS's performance, with regard to isotopic analysis, is given in Chapter 6. In addition, the instrument's performance, in terms of isotope ratio precision, is compared to that of the Sector 54 MC-TIMS instrument.

2

Inductively coupled plasma-mass spectrometry

The analytical methods that were developed in the context of this work are based on the use of *double-focusing Sector-Field Inductively Coupled Plasma-Mass Spectrometry* (ICP-SFMS). Therefore, this second chapter is devoted mainly to the operating principles and components of commercially available ICP-MS instrumentation. The basic concept of this type of instrumentation was already conceived during the late 70's and early 80's, *e.g.* by Houk at Iowa State University. To date, following the initial introduction of the ELAN 250 (Sciex, Canada) in 1983 and the PlasmaQuad (VG Instruments, UK) in 1984, over 10 000 of these systems have been installed worldwide. The vast majority of the ICP-MS instruments that have been sold have been equipped with a quadrupole mass filter, as were the aforementioned pioneering designs, with ICP-SFMS instruments constituting less than 10 % of all sales. The first of these ICP-SFMS instruments, the PlasmaTrace (VG Elemental, UK), was introduced in 1989, a few years after the first *Quadrupole Inductively Coupled Plasma-Mass Spectrometers* (ICP-QMS). The modern day Element2 (Thermo Scientific, Germany) ICP-SFMS used throughout this work was itself introduced in 1998, this instrument being an improved version of the Element (Finnigan MAT, Germany) which had first become available in 1994. Following the publication of the seminal paper by Houk *et al.* and the introduction of the first generation of ICP-MS instruments in the 80's, the technology has evolved significantly, whilst a larger number of manufacturers is currently active in the field. As each of these manufacturers approaches the challenges associated with designing an ICP-MS in a different manner, only the most basic of principles for each of the major components of an ICP-MS instrument are discussed. As such, a non-exhaustive overview of approaches is given, whilst delving too deeply into specific design choices is largely avoided. Before describing the operating principle and the components of a typical ICP-MS instrument, an overview of the advantages and disadvantages of this state-of-the-art technique is presented below.[36,37,39,45,46]

2.1 Strengths and weaknesses

Since its inception more than thirty years ago, the popularity of ICP-MS instrumentation has steadily increased. Today, it is a benchmark mass spectrometric technique for the ultra-trace and isotopic analysis of a wide variety of samples, *e.g.* in environmental and life sciences and in geo- and cosmochemistry. Its advantageous features include (i) a high sample-throughput, combined with multi-elemental capabilities, (ii) a high sensitivity and a low background resulting in $ng\,L^{-1}$ detection limits for many elements, (iii) mass spectra that

are easily interpretable and which provide both elemental and isotopic information, (iv) a wide dynamic linear range of up to $> 10^8$ and finally (v) predictable relative elemental sensitivities, which permit straightforward semi-quantitative analysis. In addition, even though the standard configuration typically only allows for the analysis of liquid solutions, solid-sampling techniques may also be readily coupled to an ICP-MS instrument, *e.g. Laser Ablation* (LA) and *ElectroThermal Vaporisation* (ETV). Furthermore, an ICP-MS instrument may be coupled, online, in a hyphenated setup, to various chromatographic separation techniques, *e.g. High-Performance Liquid Chromatography* (HPLC) and *Gas Chromatography* (GC). In this way, an ICP-MS instrument can be used as a highly sensitive and element-selective detector in elemental speciation studies.[37,47–53]

Despite the aforementioned advantages, there are still some important limitations which should be taken into consideration. Perhaps the most important issue is the frequent and sometimes unpredictable occurrence of spectral and non-spectral interferences, issues which are discussed more thoroughly in Sections 2.9.1 and 2.9.2, respectively. Furthermore, ironically as a result of two of its most important advantages, a high sensitivity and low native background, the risk of contamination is of greater concern for ICP-MS than for many other techniques. These contaminations not only limit the attainable detection limits, but may also hamper the accuracy and precision of isotope ratio measurements. Such contaminations may arise from the use of certain reagents (*e.g.* S in high-purity mineral acids), laboratory equipment (*e.g.* Si from a glass digestion vessel), the instrument itself (*e.g.* Ni from the skimmer and sampling cone), through memory effects (*i.e.* carry-over from previous samples) and even from the analyst or the surrounding laboratory environment. Therefore, extreme caution must be taken during sample preparation procedures and subsequent measurements, whilst the required reagents and materials must be selected carefully *a priori*. In addition, for multi-elemental analysis by means of ICP-MS, sample-throughput is somewhat limited by the fact that most instruments are equipped with a single detector only, whereby nuclides have to be measured sequentially. More important, however, is the fact that sequential measurements limit the isotope ratio precision attainable due to short-term fluctuations in instrumental response. Lastly, operating an ICP-MS instrument is often still viewed as being rather complex, compared to *e.g.* operating an ICP-OES instrument, although instrument manufacturers have striven to make the instruments' software and hardware more user-friendly in contemporary designs. Lastly, the acquisition and running costs of an ICP-MS instrument are typically higher compared to *e.g.* GFAAS instruments.[36,37,40]

2.2   Operating principle

Every mass spectrometric system essentially combines a number of key components including (i) a source of ions, (ii) a mass analyser able to separate the ions according to their mass-to-charge ratios and finally (iii) a detector to measure the intensity of the ion beam that is directed towards it by the mass analyser. In addition,

as the mass analyser and the detector usually operate at very low pressures, a high-vacuum pump system is also required. Moreover, an additional system is needed to register and record the detector's signal output (*i.e.* a computer for modern-day equipment). Whereas these last two components are also vital parts of any mass spectrometer, they are not discussed in the remainder this text.[54]

In the standard configuration of an ICP-mass spectrometer, a fine aerosol is first generated from a liquid sample, by means of a nebuliser. The finest droplets of this aerosol are then selected by means of a spray chamber, whereafter they are injected into an inductively coupled plasma (*i.e.* the ion source for this particular type of instrument). The aerosol droplets are dried as they travel through the plasma, after which their constituents are first evaporated and then atomised. Once these atoms reach the hottest zone of the plasma, they exist primarily as excited atoms and positively charged ions. The positively charged ions are then directed towards the mass analyser, first through an interface and then via a series of electrostatic lenses. Such an interface is essential, since the mass analyser operates under high-vacuum (10^{-7} - 10^{-8} mbar) at room temperature, whereas the plasma operates at atmospheric pressure at very high temperatures (5000 - 10 000 K). The main purpose of the ion transfer optics, which are positioned behind the interface, is to collect the analyte ions and to shape and direct the ion beam towards the mass analyser's high-vacuum region via an intermediate vacuum chamber. In addition, it ought to prevent photons and neutral species from reaching the detector. The mass filter then serves to filter out all the non-analyte ions, whilst steering the remaining ones towards one or multiple detectors. As the analyte ions impinge onto a detector, they generate an electronic signal which can be recorded. A schematic representation of an ICP-MS instrument is provided as Figure 2.1.[36,55]
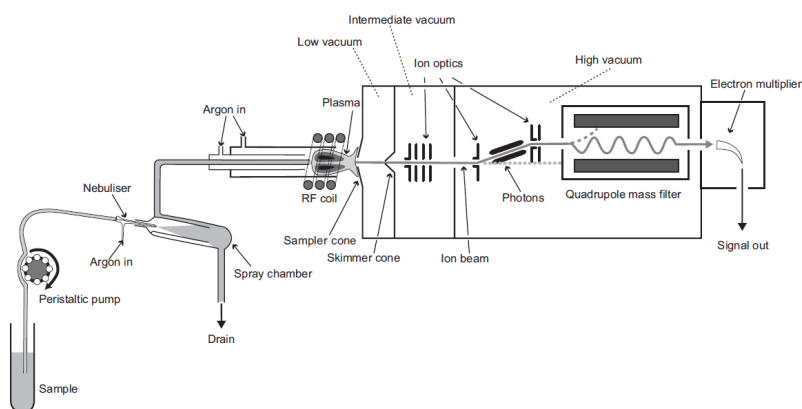
Figure 2.1: Schematic representation of a typical ICP-MS instrument. In this case, the sample introduction system consists of a peristaltic pump, a concentric nebuliser and a double-pass Scott-type spray chamber. The mass analyser shown is a quadrupole mass filter, whilst an electron multiplier serves as the instrument's detector. Photons are prevented from reaching the detector by placing the mass analyser and detector off-axis with respect to the interface.[40]

2.3   Sample introduction systems

A number of approaches have been conceived for introducing either liquid or solid samples into an ICP. Initially though, ICP-MS instrumentation was used solely for the analysis of liquid solutions, as was the case in this research project. The liquid sampling techniques, in particular those that were used throughout this work, are therefore the main subject of this section. Whereas several sample introduction systems have since been developed for handling solid samples also, they are not discussed in great detail. Although a multitude of approaches can be considered for introducing liquid solutions into the ICP, most of them essentially operate under the same principle. Firstly, the sample solution is transported towards the nebuliser, usually by means of a peristaltic pump. Then, that nebuliser is used to generate a fine aerosol from the liquid sample. Finally, the finest droplets of the aerosol are selected by means of a spray chamber and transported downstream to the ICP. The types of nebulisers and spray chambers that were used throughout this work are described below, followed by an overview of other widely used commercially available designs. Furthermore, an outline of alternative, commercially available, sample introduction techniques is also given.[36,56,57]

2.3.1   Nebulisers

As previously mentioned, the main function of the nebuliser is to generate an aerosol from a liquid sample solution. For pneumatic nebulisers, this aerosol is produced by the pneumatic action of a so-called nebuliser gas, usually Ar flowing at *ca.* $1 \, \text{L} \, \text{min}^{-1}$, onto the liquid sample. The sample solution itself is usually pumped towards the nebuliser by means of a peristaltic pump at a rate of 0.1 to $1 \, \text{mL} \, \text{min}^{-1}$. Although some nebuliser designs can operate without the use of a peristaltic pump, the use of one prevents clogging and ensures a constant flow rate, irrespective of the sample's physical characteristics (*e.g.* viscosity). The most commonly used pneumatic nebulisers are of concentric or cross-flow design.[56,58]

2.3.1.1   *Concentric nebulisers*

A schematic diagram of a concentric nebuliser is provided as Figure 2.2a, whilst an actual PFA concentric nebuliser is shown in Figure 2.2b. Such nebulisers consist of a narrow capillary centred in the middle of a wider cylindrical body; both components usually being constructed from either glass or a synthetic polymer (*e.g.* PFA). The external body converges to a narrow nozzle near the end of the capillary, leaving a thin annulus between itself and the capillary. Whilst the liquid sample solution is pumped through the inner capillary, the nebuliser gas is forced through the annulus, the latter creating an area of high velocity and low pressure at the end of the nebuliser's tip. As a result of the pneumatic action of the high-velocity nebuliser gas, the liquid solution is broken up into small droplets and thus the sample aerosol is created. This so-called primary aerosol travels at high speed, is highly turbulent and contains variably sized droplets as large as $100 \, \mu\text{m}$. Therefore, the use of a spray chamber is required, prior to introducing the aerosol into the
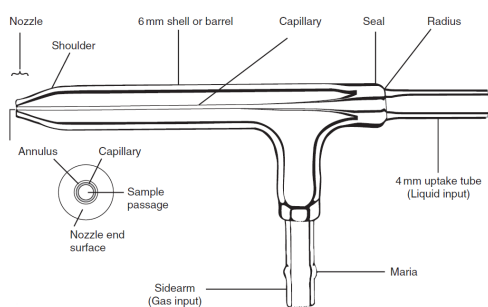
(a) Schematic diagram of a concentric nebuliser. [37]

(b) PFA concentric nebuliser.

Figure 2.2: Concentric nebulisers.

plasma. Concentric nebulisers generally provide a good sensitivity and stability, although the narrow capillary and thin annulus are prone to blockage problems. Whereas this type of nebuliser can aspirate a sample freely, as a result of the *Venturi effect* at the tip of the nebuliser, pumping the sample reduces the risk of blockages and increases long-term stability. A more recent evolution of this design, the μ-flow concentric nebuliser, operates essentially under the same principle. However, these μ-flow nebulisers are smaller and often constructed from corrosion-resistant polymer materials instead of glass. Thus, they are designed to handle smaller volumes whilst being highly suited for the analysis of corrosive samples. [56,59,60]

2.3.1.2   *Alternative nebulisers*

Other popular pneumatic designs include Babington-type nebulisers and the cross-flow nebuliser. In the case of Babington-type nebulisers, the aerosol is generated by forcing the nebuliser gas through a small orifice, over which a thin film of sample is allowed to flow. In a cross-flow nebuliser design, the nebuliser gas flows perpendicularly to the sample flow, instead of flowing in parallel. As with the concentric design, however, free aspiration of the sample solution is still an option. Lastly, in this non-exhaustive overview, ultrasonic nebulisers are also commonly used. In contrast to the previously mentioned pneumatic nebulisers, these harness the energy of acoustic waves for producing an aerosol. [56,59,60]

2.3.2   Spray chambers

The main purpose of a spray chamber is to select the finest droplets of an aerosol, produced by the nebuliser, before introducing them into the ICP. Eliminating the larger droplets is essential because the residence time of droplets in the plasma is only 1 - 2 ms, during which time only the finest droplets ($< 10 \, \mu m$) are handled efficiently by the plasma. The function of a spray chamber is two-fold, however, as it also serves to smooth out rapid fluctuations in the aerosol flow. Such fluctuations may be induced *e.g.* by the rollers of the peristaltic pump and can have a negative impact on the precision. To improve the long-term thermal

stability, a spray chamber may be cooled externally to *ca.* 2 to 5 °C. This has the added benefit of reducing the solvent load of the plasma, resulting *e.g.* in a reduction of matrix effects and oxide-based spectral interferences. The most commonly used spray chambers are of double-pass Scott-type or cyclonic design, although a design incorporating both these types is also described below.[37,56,61]

2.3.2.1   *Double-pass Scott-type spray chamber*

A schematic diagram of a double-pass Scott-type spray chamber is shown in Figure 2.3a, whilst a PFA spray chamber of this type is shown in Figure 2.3b. In addition, a water-cooled glass implementation of the design is shown in Figure 2.3c. Double-pass Scott-type spray chambers consist of two concentric cylinders, usually made of glass, quartz or a synthetic polymer. The primary aerosol is first forced through the inner cylinder, at the end of which it is forced to make a 180° turn, whereafter it is directed through the annulus between the outer and inner cylinder. As the aerosol is transported through the spray chamber it becomes heavily modified, due to a variety of complex processes taking place. The net result, however, is that the smallest droplets have a higher probability of reaching the end of the second, outer, cylinder. The modified aerosol is then, in turn, introduced into the plasma.[56,60]

2.3.2.2   *Cyclonic spray chamber*

A glass cyclonic spray chamber is shown in Figure 2.3d. In this design, the nebuliser is connected tangentially to a single circular compartment, whereby the aerosol is forced to follow a circular path in the spray chamber. The larger droplets in the aerosol have a higher probability of colliding with the wall, as a result of centrifugal forces. The smaller droplets, which are fully entrained by the vortex, however, are carried further to the plasma by the nebuliser gas flow.[56,59,60]

2.3.2.3   *Dual cyclonic/Scott-type spray chamber*

A dual cyclonic/Scott-type spray chamber is depicted in Figure 2.3e, this being a design in which a cyclonic and a vertical double-pass Scott-type spray chamber are integrated. In this arrangement, the primary aerosol is first introduced into and then modified by a cyclonic spray chamber, after which it is further homogenised in a double-pass Scott-type spray chamber. The aerosol that emerges from the second chamber produces a very stable signal, making this type of spray chamber particularly suitable for the determination of isotope amount ratios.

2.3.2.4   *Alternative spray chambers*

A single-pass spray chamber, equipped with an impact bead, onto which the largest droplets of the aerosol adhere, has also been used. However, this type of spray chamber is no longer commonly used on modern ICP-MS instrumentation.[56,60]
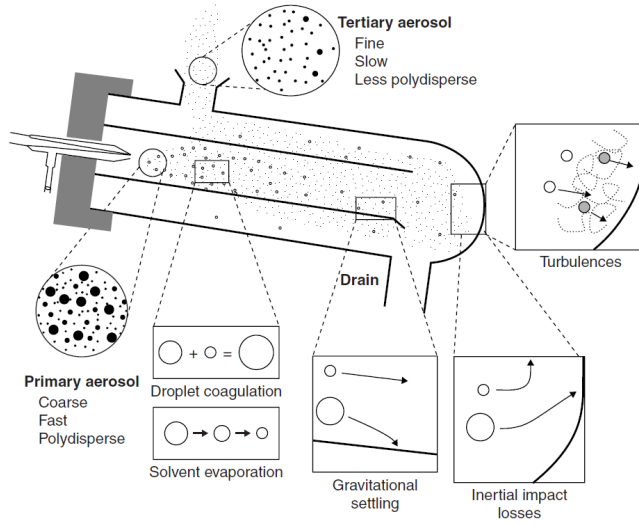
(a) Schematic diagram of a concentric nebuliser introducing an aerosol into a double-pass Scott-type spray chamber and the aerosol modification processes taking place thereafter. [60]

(b) PFA double-pass Scott-type spray chamber. [62]
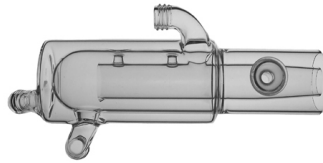
(c) Glass double-pass Scott-type spray chamber with a cooling jacket. [63]
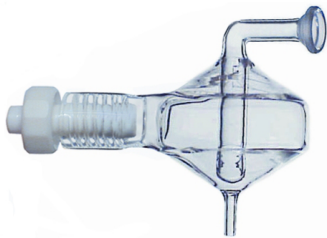
(d) Glass cyclonic spray chamber. [64]

(e) Quartz dual cyclonic/Scott-type spray chamber. [65]

Figure 2.3: Overview of spray chambers.

2.3.3   Alternative introduction systems

For specific demanding applications, additional types of sample introduction techniques are available to the analyst. These non-standard, more complex, approaches include the use of *e.g.* membrane desolvation and chemical vapour generation systems. In addition, as previously mentioned, an ICP-MS instrument can be hyphenated with various separation techniques such as *e.g.* HPLC and GC. Conversely, for the direct analysis of solid samples, *e.g.* LA and ETV are available.[37,56,66–69]

2.4   The inductively coupled plasma

An ICP-mass spectrometer's ion source is usually an Ar-based plasma, which is a macroscopically neutral high-temperature gaseous mixture of highly excited electrons and various charged, metastable and neutral Ar species. Although other types of plasmas have also been considered, *e.g. Direct Current Plasmas* (DCP) and *Microwave-Induced Plasmas* (MIP), *Inductively Coupled Plasmas* (ICP) are currently the most widely adopted ion source in analytical atomic and emission spectrometry. Using Ar to generate this type of plasma is beneficial for a number of reasons, *e.g.* as a consequence of its chemical inertness. In addition, it is available in highly-purified form, whilst being relatively inexpensive, as it is the most abundant of the noble gasses. Moreover, as a result of Ar's high first ionisation energy (15.76 eV), the plasma is capable of exciting and ionising the vast majority of the elements in the periodic table.[37,49,59,60,70]

An ICP is generated at the end of a so-called plasma torch (see Figure 2.4a), which consists essentially of three concentric tubes, each one supporting a different gas flow. These three tubes are usually made of quartz and the torch can be either one-piece or fully or partially demountable. The Ar that flows tangentially between the outer and the middle tube is often called the plasma gas, which both fuels the ICP and shields the outer tube from the plasma's heat to prevent melting. The gas that flows tangentially between the middle and the inner tube is, in turn, referred to as the auxiliary gas. The purpose of this second gas flow is to position the base of the plasma away from the middle and inner tubes, again to prevent the torch from melting. The inner injector tube is used to introduce the nebuliser gas, which, in the standard configuration, carries the sample aerosol originating from the spray chamber, into the plasma.[37,60,70]

Power is supplied to the ICP by means an oscillating magnetic field, which is induced by applying *Radio Frequency* (RF) energy to a cooled copper load coil that envelops the top end of the torch (see Figure 2.4a). Initially, the ICP is ignited by seeding the flowing plasma gas with free electrons, in the vicinity of the load coil, *e.g.* by applying a high-voltage spark. These free electrons are then accelerated by the alternating magnetic field, after which they may collide with neutral Ar atoms, producing even more free electrons. These are, in turn, also accelerated by the oscillating magnetic field, resulting in a cascade of collision-induced ionisations. This chain reaction is then maintained through

(a) Schematic representation.[71]

(b) Photo.[72]
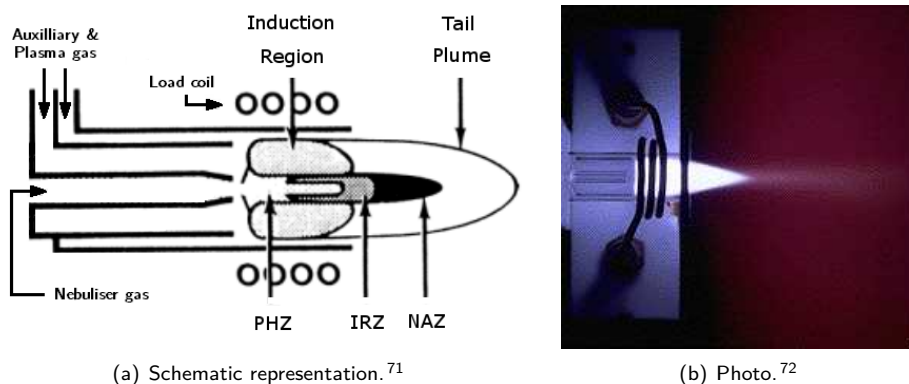
Figure 2.4: (a) Schematic representation of the ICP that is formed at the end of a plasma torch. The nebuliser gas punches a hole through the toroidal plasma's weak base, whereby the sample aerosol is transported through the preheating zone (PHZ), the initial radiation zone (IRZ) and finally the normal analytical zone (NAZ). (b) A photograph of a typical intensely-bright teardrop-shaped plasma.

inductive coupling, sustaining a bright teardrop-shaped plasma (see Figure 2.4b), for as long as RF energy is supplied to the inductive load coil.[43,49,59,70]

The nebuliser gas, flowing through the injector tube of the plasma torch, effectively punctures a hole through the centre of the ICP, thereby carrying the sample aerosol through the plasma to regions where temperatures in excess of 5000 K reign (see Figure 2.4a). Perforation of the ICP by the nebuliser gas is aided by the tangentially flowing plasma and auxiliary gasses. These tangential gas flows weaken the ICP's base and promote the formation of a toroidal plasma, with a central channel through which the sample aerosol can be transported. This central region is mainly heated by thermal conduction, convection and radiation since most of the RF energy is inductively coupled to the outer regions of the plasma discharge. As the aerosol droplets are transported towards the analytical zone of the plasma, they undergo a series of changes. Firstly, in the *PreHeating Zone* (PHZ), the aerosol droplets are desolvated and the resulting particles vaporised. Then, molecular compounds are dissociated and the sample's constituents are atomised in the *Initial Radiation Zone* (IRZ). Finally, the individual atoms are, at least partially, ionised in the *Normal Analytical Zone* of the ICP (NAZ).[37,59]

Ionisation of the sample's elemental constituents in an Ar-based plasma can occur via a number of different mechanisms, which to date have not yet been fully elucidated, the most dominant of which probably being (i) ionisation induced by collisions between ions, atoms and free electrons in the plasma (*e.g.* electron impact). Other proposed mechanisms include (ii) Penning ionisation by metastable Ar-species and (iii) charge-transfer reactions with Ar-ions. Since virtually all elements have a first ionisation energy of $< 16\,\text{eV}$, and the average ionisation energy of the plasma is determined primarily by that of Ar ($15.76\,\text{eV}$), the ICP is able to generate singly charged ions for most elements. Moreover, it can be shown that the ionisation efficiency is $> 90\,\%$ for those elements hav-

ing a first ionisation energy of $< 8\,\mathrm{eV}$, under normal operating conditions. In addition, as most elements have a second ionisation energy $> 16\,\mathrm{eV}$, a notorious exception being Ba (*ca.* $10\,\mathrm{eV}$), analyte or matrix elements will generally have a low probability of forming doubly charged ions in the ICP. However, the formation of a number of other undesirable species is commonly observed, an important limitation of the ICP which is the subject of Section 2.9.1. The analyte ions, as well as the undesirable species, that are formed in the ICP, are finally sampled from the normal analytical zone of the plasma and transported to the high-vacuum region by means of an especially designed interface.[37,49,59]

2.5   The interface region

The main purpose of the interface is to transport analyte ions efficiently, consistently, representatively and with electrical integrity from the atmospheric high-temperature ICP to the high-vacuum region, which houses the mass analyser and the detector. A schematic representation of an interface is shown in Figure 2.5a. It consists of an intermediate differentially pumped expansion chamber, located in between two metallic cones, usually made of Ni, Pt, Al or Cu (see Figure 2.5b). To prevent melting, due to exposure to the high-temperature plasma, these cones are made preferably of heat-conductive materials and placed in a water-cooled housing. In specific situations, *e.g.* when analysing corrosive liquids, corrosion-resistance may also have to be taken into account. Each of the two cones has a small orifice (*ca.* $1\,\mathrm{mm}$) at its tip, through which the ions and neutral species that are sampled from the ICP may pass.[75]

The tip of the first cone, the so-called sampler cone, is positioned within the normal analytical zone of the plasma. Some of the plasma gas, which consists
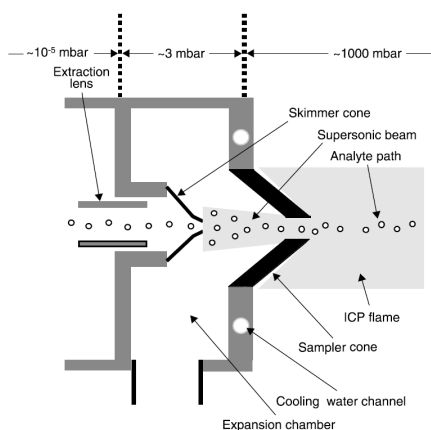
(a) Schematic diagram of the interface.[60]

(b) Pt sampler (left) and skimmer cone (right) of an Element2 ICP-SFMS instrument.[73,74]

Figure 2.5: The interface region.

mainly of neutral Ar atoms but also carries the analyte ions, flows through the sampler cone's orifice and expands supersonically inside the expansion chamber. The second cone, the so-called skimmer cone, reduces the gas load, whereby it skims ions and neutral species from the center of the expanding supersonic gas jet behind the sampler cone. Through careful design and positioning of both cones, a stable ion beam representative of the analyte population in the normal analytical zone of the ICP can be obtained. The positive ions of this ion beam are then directed towards the ion transfer optics, often by a negatively charged electrostatic extraction lens, which is located behind the skimmer cone.[37,43,49,59,60,75]

Early on in the development of ICP-MS instrumentation, it was found that the interface region, in addition to the ICP itself, contributed significantly to the formation of certain types of spectral interferences (*e.g.* multiply charged and Ar-based species). A secondary plasma discharge was observed at the orifice of the sampler cone, which was thought to be the source of this issue. In addition, this secondary discharge causes an increase in photon noise, ion kinetic energy and the spread thereof. Moreover, it was found to have a detrimental effect on sampler cone life expectancy, due to increased orifice erosion. The source of this discharge was later identified as a being capacitive coupling between the voltage on the load coil and the plasma, causing arcing between the plasma itself and grounded sampler cone. Lowering the plasma potential, to reduce this type of arcing, can be achieved in a number of ways, one such approach entails placing a grounded guard electrode between the load coil and the plasma torch.[76,77]

2.6   The ion transfer optics

The main function of the ion transfer optics is to extract and then collimate and focus the ion beam, which enters the intermediate-vacuum chamber through the skimmer cone, onwards towards the high-vacuum region of the mass analyser. These lens assemblies usually consist of one or more electrostatically controlled electrodes, flat or cylindrical, which subject the positive ions to an electric field. Applying this electric field is essential to compensate for beam defocusing, arising from two separate mechanisms. Firstly, the analyte ions are scattered by collisions with the bulk plasma gas. Secondly, as the ion beam enters the low-pressure intermediate-vacuum chamber, the small electrons diffuse readily outwards. As a result, the centre of the ion beam receives a net positive charge, whereby its positive ions start repelling each other due to so-called space-charge effects.[37,49,59,60,78]

A secondary function of the ion optics is to prevent photons and neutral species from impinging on the detector, as this would lead to an increase in the instrumental background. Several strategies have been considered by the different ICP-MS manufacturers. A grounded metal plate may be placed in the path of the ion beam, which blocks photons and neutral species, whereas the positive ions are guided around the so-called photon stop by the ion optics. Alternatively, the mass analyser and the detector may be placed off-axis, with respect to the interface, whereby the positive ions can be selectively steered towards them by

the lens assembly. In part due to the its mass analyser's geometry, an ICP-SFMS instrument suffers little from photons and neutral species (see Section 2.7.2).[60,78]

2.7 Mass analysers

At the heart of any mass spectrometric system lies a mass analyser, which separates the ions produced in the ion source according to their mass-to-charge ratio, after which it directs the analyte ions of interest to the detector (either simultaneously or sequentially, temporally-resolved or spatially-resolved). The ion beam, which is extracted from the plasma through the interface and focused by the ion optics, can be resolved into its components by any of a number of different mass analysers. Currently, however, the two most commonly used mass analysers are quadrupole mass filters and double-focusing sector-field mass analysers. These mass analysers are necessarily housed in a high-vacuum region ($ca.$ 10^{-8} mbar), as collisions of both analyte and interferent ions, with residual gasses, can have a negative impact on the sensitivity as well as on the so-called abundance sensitivity.[37,43,59,79]

This abundance sensitivity is defined as the ratio of the signal intensity observed at mass m+1, as a result of peak-tailing, versus the signal intensity at mass m.

$$abundance\ sensitivity = \frac{I_{m+1}}{I_m} \tag{2.1}$$

The resolution, also an important characteristic of mass analysers, is specified by the 5 % peak width definition, for the purposes of this text. This is defined as the ratio of an ion's mass versus its corresponding peak width at 5 % of the signal height. This definition of the resolution is equivalent to the alternative 10 % valley definition, for two neighboring symmetrical peaks of equal height.

$$R = \frac{m}{\Delta m} \tag{2.2}$$

A schematic illustration of the abundance sensitivity and the mass resolution is given in Figures 2.6a and 2.6b, respectively, to clarify their definitions.[43]

(a) Abundance sensitivity.
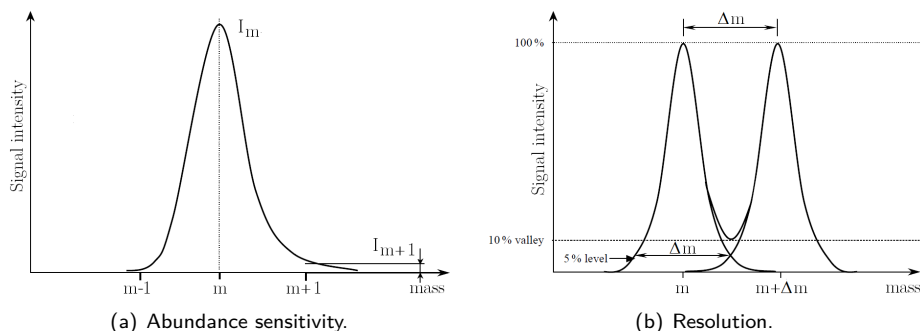
(b) Resolution.

Figure 2.6: Schematic illustrations of the abundance sensitivity and the resolution.[43]

2.7.1 Quadrupole mass analysers

The first of the commercially available ICP-MS instruments were all equipped with quadrupole mass filters and, to date, this design is still by far the most popular one. These types of instruments are considered to be technologically mature and are characterised by fast scan times and a relative ease of use, whilst at the same time they are reasonably priced. The major drawback of commercially available ICP-QMS instruments, however, is that the attainable mass resolution has always been modest. Nearby ions with the same nominal mass-to-charge ratio as the analyte ions of interest can typically not be resolved. However, to a large extent, this limitation has been overcome as a result of the advent of collision/reaction cell technology (see Section 2.9.1.2).[60,79]

A quadrupole mass filter consists of four parallel equidistant metallic rods. Even though hyperbolically shaped rods exhibit a superior separation behavior, the use of cylindrical rods has most often been found to suffice, if properly spaced. By applying a specific combination of dc and RF ac voltages to each opposed pair of cylindrical rods, thereby creating an alternating quadrupolar electric field, ions with a particular mass-to-charge ratio are allowed to reach the end of the quadrupole, whereas all other ions are ejected (see Figure 2.7a). The mathematical equations that describe the trajectory of an ion in the quadrupole's electric field are rather complex and therefore beyond the scope of this text, instead, a qualitative description of the operating principle is given below.[43,79–81]

Four parallel equidistant quadrupole rods, accompanied by the voltages that are applied to them, which induce a quadrupolar electric field, are shown in Figure 2.7b. In this figure, the rods are depicted as being positioned perpendicularly to the page. A voltage of $U + V \cdot \cos \omega t$ is applied to the first pair of opposing rods (rod pair A, defining the x-direction), whereas the second pair of rods, in contrast, is subjected to a voltage of $-(U + V \cdot \cos \omega t)$ (rod pair B, defining the y-direction). In these formulas, U represents the dc component of the voltage, whilst $V \cdot \cos \omega t$ represents its time-dependent RF ac component with amplitude V and angular frequency ω. The stability of an ion's trajectory is then determined by its mass, the dc voltage
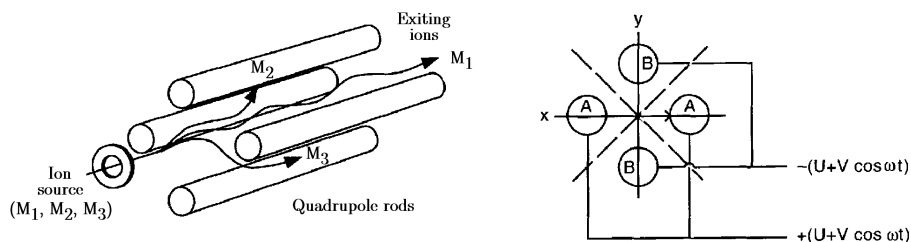
(a) Trajectory of different ions in the quadrupole.

(b) Application of dc and RF ac voltages to opposed rods.

Figure 2.7: Quadrupole mass analyser.[80]

U and the amplitude and angular frequency of the RF ac voltage $V \cdot \cos \omega t$. In practice however, ω is kept constant and only U and V are varied such that ions of all but a single mass-to-charge ratio are filtered out. As an ion passes through the quadrupole, the quadrupolar electric field exerts a force on it, the x and y components of which are independent of one another. For this reason, the motions in the perpendicular x and y directions may be considered separately.[43,49,80]

Let us first consider the pair of opposing rods in the x direction, onto which a voltage with a positive dc component is applied. By applying a positive potential to this pair rods, positively charged ions are repelled by both and focused in between them. However, as a result of the RF ac component, the voltage on these rods is not always positive. During the time that the rods are subjected to a negative potential, they instead exert an attractive force on positively charged ions. The distance traveled by an ion, whilst the rods are at a negative voltage, is determined in part by that ion's mass-to-charge ratio. The trajectory of a heavy ion, $i.e.$ with a high mass-to-charge ratio, is affected only to a minor extent by a rapidly oscillating RF ac voltage as a result of its inertia. The trajectories of lighter ions, however, are more readily affected by that same RF ac component. Hence, heavy ions are repelled by the rods and focused
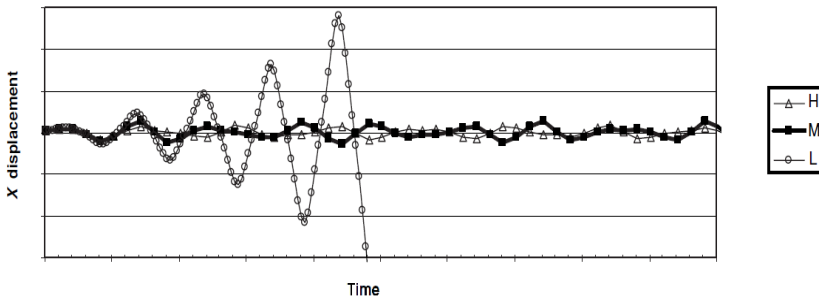
(a) Displacement of light, medium and heavy ions in the x direction (dc component of voltage > 0).
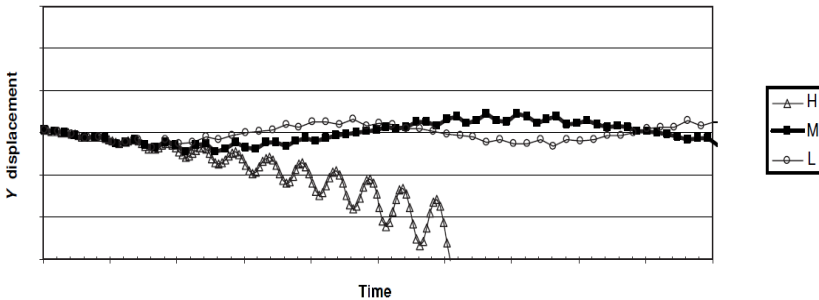
(b) Displacement of light, medium and heavy ions in the y direction (dc component of voltage < 0).

Figure 2.8: Trajectories of light, medium and heavy ions as they move through the quadrupole. Ions that are too light are forced on a highly unstable trajectory in the x direction (positive dc component) whilst ions that are too heavy are deflected in the y direction (negative dc component).[60]

in between them, by the *dc* component of the rods' potential. In contrast, light ions will move along a trajectory that is very unstable, due to the RF *ac* component of the voltage. The trajectory of the lightest ions, with a mass-to-charge ratio below a certain threshold, is so unstable that they eventually collide with the quadrupole rods, after which they are removed (see Figure 2.8a). Thus, the rods in the x direction can be thought of as acting as a high-mass filter.[49]

Let us then consider the other pair of opposing rods, in the y direction, to which a voltage with a negative *dc* component is applied. Although the average potential is negative for this pair, the voltage on the rods also oscillates between positive and negative due to the RF *ac* component. Positively charged ions with a high mass-to-charge ratio are affected mainly by the constant negative *dc* component, causing them to move steadily towards one of the rods (see Figure 2.8b). Ions with a mass-to-charge ratio above a certain threshold eventually collide with the quadrupole rods, whereafter they are neutralised. The trajectory of the lightest ions, in contrast, is not only affected by the *dc* component but also by the rapidly oscillating RF *ac* potential. Hence, during periods when the voltage is positive, these lighter ions are refocused in between the rods. Therefore, the rods in the y direction can be thought of as acting as a low-mass filter.[49]

For an ion to be able to reach the end of the quadrupole mass filter, its needs to move along stable trajectories in both the x and y direction. Since the quadrupole rods in the x direction serve as a high-mass filter and those in the y direction serve as a the low-mass filter, only ions of a narrow range of mass-to-charge ratios move along a stable trajectory. Moreover, by careful selection of U and V, ions of only a single specific nominal mass-to-charge ratio can be allowed to pass. The entire mass spectrum can then be scanned, by varying U and V whilst maintaining a constant ratio between both. However, for a number of reasons, undesirable species may still not be fully ejected from the quadrupole, leading to peak tailing (a phenomenon that is quantified by means of the abundance sensitivity). For example, if an undesirable ion is injected into the quadrupole too close to the central axis, where the magnitude of the electric field is zero, it may still be transmitted. Due to the nature of the alternating quadrupolar electric field, this peak tailing is more pronounced at the low-mass side of an interfering peak. An optimum abundance sensitivity is obtained when (i) the quadrupole rods are long enough, (ii) the angular frequency ω of the RF *ac* voltage is large enough and when (iii) the ions pass through the mass filter slowly.[49,60]

2.7.2 Double-focusing sector-field mass analyser

Limitations with respect to the resolving power of traditional ICP-QMS instruments led to the development of higher-resolution ICP-SFMS instruments. For the first time, many of the most frequently occurring spectral interferences could be eliminated in an elegant and straightforward manner (see Section 2.9.1.1). Aside from an improved resolving power over commercially available ICP-QMS instruments, ICP-SFMS instruments are also characterised by a higher sensitivity

and an improved precision. However, they are more expensive and day-to-day operation is considered to be more complicated. In addition, when compared to ICP-QMS instruments, scanning is slower, especially at higher resolutions.[82]

A double-focusing sector-field mass analyser consists of an electromagnet and an electrostatic analyser (ESA), working in tandem with one another. In commercially available ICP-SFMS instruments, the so-called Nier-Johnson and Mattauch-Herzog geometries are most commonly employed. In a Mattauch-Herzog geometry, a magnetic sector is used in combination with a electrostatic sector of opposite curvature. Conversely, in a Nier-Johnson geometry, a magnetic sector and an electrostatic sector with the same direction of curvature are employed. Whereas the ESA is positioned before the electromagnet in a so-called forward design, it is positioned behind the electromagnet in a so-called reverse design. An important difference, when compared to the design of ICP-QMS instruments, aside from the actual mass analyser itself, lies in the design of the ion optics. In contrast to a quadrupole mass filter which performs optimally when the incoming ions travel at low speed, the ions' kinetic energy is instead increased by an accelerator voltage of several kV before introducing them into a double-focusing sector-field mass analyser. The operating principle of this type of mass analyser is given below, starting by first describing the operating principle and the relevant limitations of single-focusing magnetic sector mass analysers.[39,82–85]

Consider a positively charged ion, the speed of which is increased from 0 to a given value v, by an accelerating voltage V. That ion's kinetic energy E_{kin} is then governed solely by the magnitude of the accelerating voltage and by the ionic charge q. This kinetic energy, along with the ion's mass m, determines its speed.

$$q{\cdot}V = E_{kin} = \frac{1}{2}{\cdot}m{\cdot}v^2 \tag{2.3}$$

As this ion travels through the magnetic sector's uniform magnetic field, which is characterised by a magnetic flux density B, its trajectory is affected by the *Lorentz force* F_m. This magnetic force is exerted in the direction perpendicular to that of the ion's motion and that of the magnetic field lines.

$$F_m = q{\cdot}v{\cdot}B \tag{2.4}$$

As a result of the Lorentz force, the ion is deflected and its motion describes a circular path. The radius r_m of this circular trajectory is determined by the equilibrium between the Lorentz force F_m and the centrifugal force F_c.

$$q{\cdot}v{\cdot}B = F_m = F_c = \frac{m{\cdot}v^2}{r_m} \tag{2.5}$$

Eliminating the ion's speed from equations 2.3 and 2.5 yields

$$\sqrt{\frac{2{\cdot}q{\cdot}V}{m}} = v = \frac{q{\cdot}r_m{\cdot}B}{m} \tag{2.6}$$

which, when solved for r_m, finally yields the radius of the ion's circular path.

$$r_m = \frac{\sqrt{2 \cdot V}}{B} \cdot \sqrt{\frac{m}{q}} \qquad (2.7)$$

Thus, when the accelerating voltage V and the magnetic flux density B are kept constant, ion trajectories are solely determined by their respective mass-to-charge ratios, whereby they can be spatially resolved. Nonetheless, when a single static detector is employed, it is often more convenient to vary the accelerating voltage V or the magnetic flux density B, for sequential monitoring of ions with specific mass-to-charge ratios. It must be remembered, however, that the above assumes that the ion beam is perfectly collimated and that all ions have a uniform kinetic energy. Fortunately, magnetic sectors possess angular focusing capabilities, whereby diverging ions beams are focused after emerging from the mass analyser (*i.e.* single focusing). In contrast, if their kinetic energies were to vary, the trajectories of ions of a given mass-to-charge ratio would not intersect in the same focal point, which limits the resolution attainable. Therefore, a magnetic sector mass analyser is dispersive not only with respect to mass but also with respect to ion kinetic energy. A schematic representation of a magnetic sector is shown in Figure 2.9, demonstrating the mass analyser's angular focusing capabilities. [39,43,60,80]

An ESA can be employed to compensate for the magnetic sector's dispersive nature with respect to ion kinetic energies, in order to improve the attainable resolution. As a positively charged ion with mass m, charge q and speed v passes through the electrostatic sector, it is deflected and forced on a
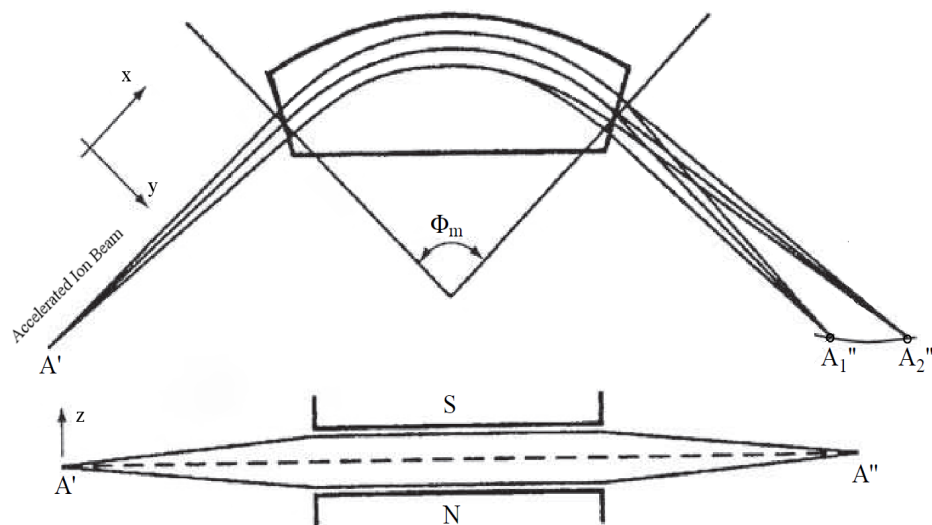
Figure 2.9: Schematic top and side view of a 90° magnetic sector mass analyser, resolving an accelerated ion beam. Ions of two different mass-to-charge ratios are focused in different points (A1 & A2). Moreover, angularly diverging ions of the same mass-to-charge ratio are focused in a single point. [43]

circular trajectory, as in a magnetic sector. An ESA consists of two sections of cylindrical or toroidal condenser plates, held at opposite potentials, which generate a radially symmetrical electrostatic field with electric field strength E. The radius r_e of an ion's circular trajectory is then determined by the equilibrium between the electrostatic force F_e and the centrifugal force F_c.

$$q{\cdot}E = F_e = F_c = \frac{m{\cdot}v^2}{r_e} \tag{2.8}$$

The kinetic energy of a positive ion, accelerated by an accelerating potential V, was already given in the previous paragraph. For an electrostatic sector, the ion's speed can then be eliminated from equations 2.3 and 2.8, yielding

$$\frac{2{\cdot}q{\cdot}V}{m} = v^2 = \frac{q{\cdot}E{\cdot}r_e}{m} \tag{2.9}$$

which, when solved for r_e, yields the radius of the ion's circular path in an ESA.

$$r_e = 2{\cdot}\frac{V}{E} \tag{2.10}$$

This relation is similar to equation 2.7, for mono-energetic ions beams, resolved by a magnetic sector, except that the radius r_e of the ion's circular path in the electrostatic analyser is independent of that ion's mass-to-change ratio. However, if the ion beam is not uniformly mono-energetic, an ESA is still dispersive with respect to ion kinetic energies, like a magnetic sector. Fortunately, an electrostatic analyser also possesses angular focusing capabilities for imperfectly collimated diverging ion beams, again just like a magnetic sector.[39,43,80]
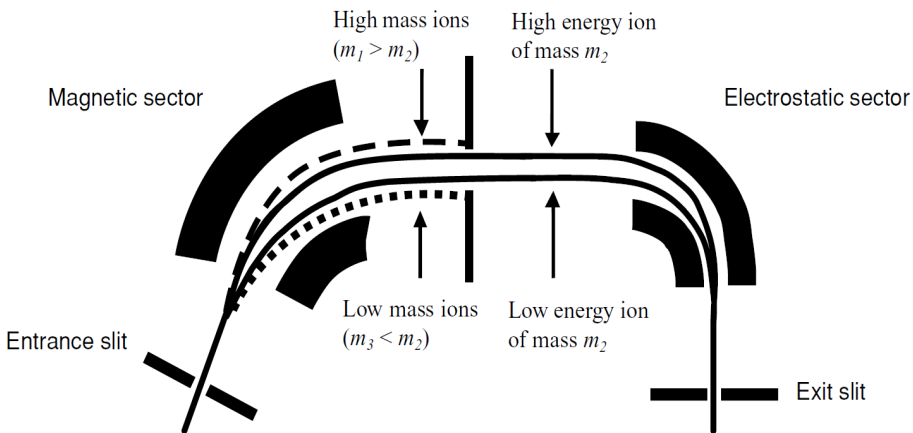
Figure 2.10: Schematic representation of a double-focusing sector-field mass analyser of reverse Nier-Johnson geometry, resolving an accelerated ion beam. The magnetic sector disperses ions according to their mass-to-charge ratios and ion kinetic energies. The ESA is subsequently used to deflect ions of equal mass-to-charge ratios such that their trajectories intersect in a single focal point.[60]

Thus, magnetic and electrostatic sector mass analysers, on their own, are incapable of resolving ion beams with a high ion kinetic energy spread, such as those generated from an ICP. In a tandem setup, however, both components are combined in such a way that the ion kinetic energy dispersion of the magnetic sector is compensated by the equal but opposite ion kinetic energy dispersion of the electrostatic sector. Thus, the combination of magnetic and electrostatic sectors possesses both angular and ion kinetic energy focusing capabilities (*i.e.* double-focusing), whilst the magnetic sector's dispersive nature with respect to mass is retained (see Figure 2.10). As a result of its double-focusing capabilities, sector-field mass analysers possess a superior resolution, which is its main advantage over traditional quadrupole mass filters. In addition to a superior resolving power, an improved sensitivity is often observed, when compared to those same quadrupole mass filters. This has been attributed to the use of an accelerating voltage, which greatly increases the average ion kinetic energy, whereby the ion beam is thought to be less susceptible to space-charge-induced scattering. Moreover, due to the curved trajectories of the ions, photons and neutral species have a very low probability of reaching the detector, which greatly reduces background levels. [37,43,60]

In order to further improve the resolution, up to values of *ca.* 10 000 for commercially available instruments, the widths of the mass analyser's entrance and exit slit can be reduced. These slits are positioned just before and after the mass analyser, respectively, in the trajectory of the ion beam. However, reducing the slits' width is accompanied by a loss of sensitivity, since ion transmission is reduced. Moreover, whereas characteristic flat-top peaks are observed in the lowest resolution mode, triangular peaks are obtained when the slits widths' are reduced. Trapezoidal flat-top peaks are advantageous because a small shift in the instrument's mass calibration would not necessarily be problematic, as long as the observed mass window still corresponds to a part of the peak's flat plateau. [86]

With single-collector ICP-SFMS instruments, having a fixed detector, mass spectra can be acquired in two ways. Firstly, the magnetic flux density of the magnetic sector can be kept constant, whilst varying the accelerating voltage (*i.e.* E-scan). This enables fast scanning, but typically only over a limited mass range upwards from a fixed magnetic sector mass, because a decrease in the accelerating voltage causes a loss in sensitivity and of focusing properties. Secondly, the entire mass spectrum can be scanned by varying the magnetic flux density, whilst keeping the accelerating voltage constant (*i.e.* B-scan). However, scanning is slower in this case, due to the self-inductance of the magnet, which counteracts magnet current changes. In practice, E-scans are used to cover a narrow range of masses above a fixed magnetic sector mass (*ca.* +30 %). When the E-scan's upper limit is reached, the magnetic sector performs a relatively slow jump to a higher mass, from where a new fast E-scan commences, after allowing for an appropriate settling time. In a multi-collector design, in contrast, both the magnetic flux density and the accelerating voltage can be kept constant. Several detectors are then placed at each of the static focal points of interest. It should be noted that only forward geometries can be used in such multi-collector designs, because, in a reverse geometry, too

small a part of the mass range is transmitted by the magnetic sector to the ESA. As a result, a reverse geometry prohibits the simultaneous monitoring of multiple isotopes across a sufficiently wide mass range. For a single-collector design, however, a reverse geometry is often preferred. The fact that the high ion current is first reduced by the magnetic sector, whereby only a limited range of masses is transmitted and subjected to the subsequent energy refocusing, has been found to lead to an improved abundance sensitivity and a reduced noise level. [39,60,86]

2.7.3   Alternative mass analysers

Currently, only one other type of mass analyser is used in commercially available ICP-MS instrumentation, *i.e.* in the less commonly employed *Time-Of-Flight Inductively Coupled Plasma-Mass Spectrometers* (ICP-TOFMS). [87,88]

2.8   Detectors

After the ions of a particular mass-to-charge ratio have been isolated from all other species, by the mass analyser, they are directed towards a detector. This detector, the third and final major component of any mass spectrometric system, is then used to measure the magnitude of the resolved ion beam's current. Often, it is assumed that this ion current is proportional to the analyte concentration in the original sample. The most commonly used detectors in ICP-MS instrumentation are secondary electron multipliers, especially for trace and ultra-trace analysis of samples, where low ion currents are encountered. [59,89]

2.8.1   Discrete-dynode electron multipliers

Early ICP-MS instruments mainly employed continuous dynode electron multipliers, but so-called discrete-dynode electrons multipliers have since become more popular, in part due to advances in the underlying technology. Although continuous and discrete-dynode electron multipliers differ somewhat in design, the operating principle of these types of detectors is quite similar. In what follows, however, only discrete-dynode electron multipliers are considered. [60]

A discrete-dynode electron multiplier is made up of a series of individual plates each coated with a metal-oxide, which possesses high secondary electron emission properties. A schematic representation and a photograph of this type of detector are shown in Figure 2.11, for illustrative purposes. The first plate of the detector, called the conversion dynode, is held at negative potential, whilst each of the consecutive dynodes is held at successively higher potentials. When a positive ion strikes the conversion dynode, a number of secondary electrons are generated. These are accelerated towards the second dynode, because it is at a higher potential than the first. When the secondary electrons impinge on the second dynode, they generate more electrons. These are then, in turn, accelerated towards the third dynode where even more electrons are generated. As a result of the potential gradient across the detector, this process is repeated

at each of the following dynodes. The number of secondary electrons generated increases exponentially, until a cascade of electrons eventually impinges on the detector's collector. In this way, a single positively charged ion, striking the conversion dynode, gives rise to a measurable pulse at the collector.[37,43,49,59,60,89]

In the so-called pulse counting mode of the detector those individual pulses are recorded, which gives rise to a certain count rate. This count rate is considered to be proportional to the analyte concentration, but only if the concentration is sufficiently low. If the analyte concentration is too high and there are too many incident ions, then the detector's response will no longer be linear. Moreover, wear of the detector is typically related to the total numbers of pulses that have been registered at the collector, whereby higher count rates result in a shorter detector life span. One solution to this problem is to continuously measure the electron current at one of the central dynodes, as an analog signal. If the current at that dynode is above a certain threshold value, then its further amplification is interrupted and the analog signal is used for quantitative purposes. The detector is then said to operate in the so-called analog mode, for which the measured current is considered to be proportional to the analyte concentration. In a dual detector mode, on modern ICP-MS instruments, the switching between pulse counting and analog modes is fully automated. By cross-calibrating the pulse counting and analog modes of the detector, in the range where both modes are valid, at count rates between *ca.* $25\,000\,\mathrm{counts\,s^{-1}}$ and $2\,500\,000\,\mathrm{counts\,s^{-1}}$, a dynamic linear range of up to nine orders of magnitude can be obtained. Depending on the design of the detector, the resulting analog-to-counting cross-calibration factor may be either mass-dependent or mass-independent.[43,60,89]

An important consideration for many pulse counting systems is the occurrence of a so-called detector dead time τ, whereby fewer pulses are recorded than actually occur at the detector. When an ion strikes the detector and generates a pulse, a short but finite time is required to detect and handle the resulting signal, typically in the order of magnitude of some ns. During this short time, the detector is "blind" to all other incident ions, such that pulses are "lost". This phenomenon is of greatest importance when high count rates are considered ($> 1\,000\,000\,\mathrm{counts\,s^{-1}}$),
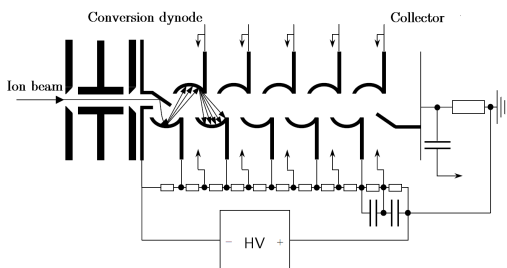
(a) Schematic representation.[43]   (b) Photograph.
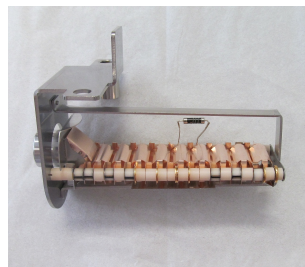
Figure 2.11: Discrete-dynode electron multipliers.

as the probability of two ions arriving within a very short period is increased. Therefore, this loss of counts must be corrected for, especially for the accurate determination of extreme isotope ratios. For a non-paralysable system, *i.e.* one where an undetected pulse does not lead to an extension of the dead time τ, the measured count rate I_{meas} can be corrected by using the following equation.

$$I_\tau = \frac{I_{meas}}{1 - I_{meas} \cdot \tau} \tag{2.11}$$

Thus, it can be shown that, for a corrected count rate I_τ of $1\,000\,000\,\mathrm{counts\,s^{-1}}$ and a dead time of $20\,\mathrm{ns}$, only *ca.* $98\,\%$ of all pulses would be registered. Both the detector itself and the detection system's electronics are believed to contribute to this phenomenon, which inhibits the linearity of the detector, if not corrected for. Several approaches for determining the dead time are discussed in Chapter 6, as its determination is a prerequisite to accurate isotopic analysis .[37,43,60,80,90]

2.8.2   Alternative detectors

As mentioned previously, continuous dynode electron multipliers have been used extensively in ICP-MS instrumentation, especially in the early designs. In addition, the use of Daly detectors has also been considered in a number of ICP-MS concepts. Whereas these types of detector can be operated in the same range as discrete-dynode electron multipliers, Faraday cups are usually employed for higher ion currents. The latter are less sensitive, but more stable.[60,89]

2.9   Interferences

The intensities of ion beams impinging on the detector cannot always be assumed to be proportional to analyte concentrations, due to the occurrence of interferences. If not taken into account, these will inevitably hinder the accurate and precise quantitative analysis of samples. In ICP-MS, interferences are most often classified as being either spectral or non-spectral in nature. Spectral interferences arise when the nominal mass-to-charge ratio of one of the analyte ions coincides with that of another atomic or molecular ionic species, whereby they both contribute to the observed signal intensity. This results in an overestimation of the analyte concentration. In contrast, non-spectral interferences tend to affect the determination of all analytes in a sample, although not necessarily to the same extent. This type of interference results in a multiplicative distortion of the expected signal intensities, which are either suppressed or enhanced, across the entire mass range. Their origins and the approaches for attenuating these spectral and non-spectral interferences are the main subject of the remainder of this section.[37,40,91]

2.9.1   Spectral interferences

The general term spectral interferences actually encompasses three distinct and separate classes of interfering ionic species, which may be formed either in the plasma or in the interface region. The first and most important class of such

interferences are polyatomic ions. The second and third are multiply charged and isobaric interferences, which are both typically less problematic.[37,39,59,91]

Polyatomic spectral interferences arise from precursors from various sources, including the analytes themselves, the sample matrix, the plasma gas and the air surrounding the ICP. Most often, however, only diatomic (*e.g.* $^{14}N^{14}N^+$) or triatomic (*e.g.* $^{40}Ar^{16}O^1H^+$) interfering species are observed, although the occurrence of more complex cluster ions has also been reported (*e.g.* $^{142}Nd^1H^{31}P^{16}O_4^+$).[92] First and foremost, the $^{40}Ar^+$ monomer and $^{40}Ar_2^+$ dimer are two of the most dominant interfering species in an Ar-based ICP, hampering the determination of $^{40}Ca^+$ and $^{80}Se^+$, respectively. However, in addition to such simple Ar monomers and dimers, other argide-based spectral interferences are commonly encountered. These comprise diverse combinations of Ar and other species predominant in the plasma (*e.g.* H, O, C, N). A number of oxide- and hydride-based cluster ions are also frequently observed at appreciable levels and are second only in importance to the abovementioned Ar-based interferents. Typical examples are the molecular oxides that readily form from the lightest lanthanides, which then hamper the determination of their heavier brethren. This is of particular importance for ICP-MS instruments being operated in the standard configuration, in which aqueous samples are aspirated, because a considerable amount of water vapor is then introduced into the plasma. In addition, impurities in the plasma gas, along with the constituents from the surrounding air, contribute to the formation of these oxide- and hydride-based interferences. Moreover, the plasma gas and the surrounding air give rise to nitride- and carbide-based polyatomic interferents also. Another important source of polyatomic interferences can be traced back to the sample pretreatment procedures employed, specifically to the reagents that are used for digestion or preservation of samples (*e.g.* HNO_3, H_2O_2, HF and HCl). Some of these reagents may give rise to cluster ions that would otherwise not be observed, a typical example being the diatomic $^{40}Ar^{35}Cl^+$, which masks the signal of the mono-isotopic $^{75}As^+$ at unit-mass resolution. Therefore, HNO_3 and H_2O_2 are generally considered to be reagents of choice, as these do not introduce any "foreign" precursors into the plasma.[37,39,59,91,93,94]

Multiply charged spectral interferences arise from precursors that are either highly abundant in the sample matrix and the plasma gas (*e.g.* $^{40}Ar^{4+}$) or from those that possess a second ionisation energy below 16 eV (*e.g.* $^{137}Ba^{2+}$). As the mass analyser resolves an ion beam with respect to the ions' mass-to-charge ratios, doubly charged ionic species interfere with the signals of lighter ions, found at half the interfering species' nominal mass in the mass spectrum. However, most elements possess a second ionisation energy that lies well above 16 eV, *i.e.* above the first ionisation energy of Ar. As a result, they have a very low probability of forming doubly charged ions in an Ar-based plasma (see Section 2.4).[39,59,95]

Isobaric overlap occurs when the nominal mass-to-charge ratios of two nuclides from different elements coincide (*e.g.* $^{54}Fe^+$, $^{54}Cr^+$). Although isobaric interferences are quite commonly encountered, they are certainly not insurmountable, at

least for samples of natural isotopic composition. Fortunately, with the exception of In, most elements possess at least one nuclide that is free from isobaric interference. In general, though, it is considered good practice to monitor two or more nuclides for each element under consideration, whenever possible.[39,59,91]

2.9.1.1   High-resolution mass spectrometers

A straightforward approach to eliminating spectral interferences is to exploit the so-called mass defect, which is the difference between the sum of the masses of a nucleus' nucleons and its exact mass. Although being somewhat counter-intuitive, this phenomenon results from a relativistic loss of mass, through the release of binding energy, at the time when the stable nucleus is first formed. Most important, however, is the fact that the magnitude of the mass defect is unique to each of the elements' isotopes. The ability to identify nuclides of the different elements, coinciding at specific nominal mass-to-charge ratios, but with unique exact masses, is therefore only limited by the mass resolution achievable.[43,96]

However, commercially available ICP-SFMS instruments have never been able to provide resolutions of much more than *ca.* 10 000. Although the resolution of these types of instruments is vastly superior to that of traditional ICP-QMS instruments, resolutions of up to 10^8 would be required for resolving the most troublesome of isobaric interferences. Fortunately, however, many of the frequently occurring polyatomic and multiply charged interferences can be easily resolved at resolutions of less than 4000. Nonetheless, even in these cases, some important limitations should be taken into consideration. Firstly, not all of the polyatomic and multiply charged interferences can be resolved so easily, *e.g.* a number of molecular oxides in the range of 100 to 140 amu are particularly troublesome. Secondly, when the resolution is increased, the instrumental sensitivity inevitably suffers and the ability to obtain flat-top peaks is sacrificed (see Section 2.7.2).
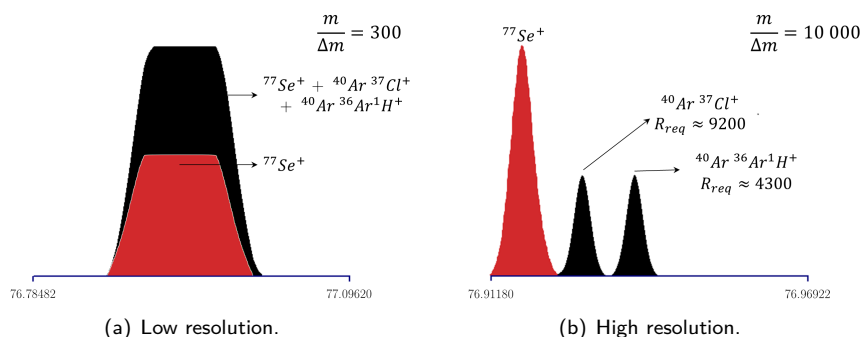
Figure 2.12: Simulation of a low and high resolution mass scan at a nominal mass-to-charge ratio of 77, created by means of the *ICP-MS Interferences Workshop* program (Thermo Finnigan, Germany). Spectral overlap occurs in the lowest resolution mode, masking the $^{77}Se^+$ signal. In the higher resolution mode, both interferences can be resolved, although trapezoidal flat-top peaks can no longer be obtained.

The use of higher resolution modes, for the determination of $^{77}Se^+$, is illustrated in Figure 2.12. If considerable amounts of Cl are anticipated in a sample in which ^{77}Se has to be determined, then the use of the very highest resolution mode is required. If not, and if the intensity of the argide-based interference is sufficiently small, then a resolution of *ca.* 4000 may be adequate. Alternatively, the signal of $^{82}Se^+$ can be monitored for the determination of Se.[39]

2.9.1.2 Collision/reaction cell technology

Whereas ICP-QMS instruments were initially not capable of dealing with polyatomic spectral interferences, at least not in a very efficient manner, most modern instruments are now equipped with so-called collision/reaction cells. A schematic representation of this type of instrument is presented in Figure 2.13. As in a traditional ICP-QMS instrument, ions are extracted from the plasma through the interface, after which the ion beam is shaped and focused by the ion optics. However, before subjecting the resulting ion beam to mass analysis, it is first directed through a collision/reaction cell. This type of cell makes use of collisions and/or selective ion-molecule reactions, which purge the ion beam of undesirable species, before it is transmitted onwards towards the quadrupole mass filter. Spectral interferences, even isobaric ones that cannot be resolved on an ICP-SFMS instrument, can thereby be eliminated.[91,97]

A collision/reaction cell essentially consists of a multipole (4, 6 or 8 rods), subjected to a voltage with a *dc* and RF *ac* component. This multipole is placed in a pressurised chamber, into which inert (*e.g.* He) or reactive (*e.g.* H_2, NH_3, CH_4) gasses are introduced, at flow rates of either up to a few $mL\,min^{-1}$ or less than one $mL\,min^{-1}$, respectively. The purpose of the multipole is to guide the ions to the quadrupole mass filter, whilst they interact with the atoms or molecules of the collision/reaction gas. The mechanisms through which the spectral interferences are dealt with in a collision/reaction cell can be classified as being either physical or chemical in nature.[98–101]

Figure 2.13: Schematic representation of a an ICP-QMS unit equipped with a collision/reaction cell.[97]

Firstly, physical processes such as collision-induced fragmentation and kinetic energy dampening can suppress interfering species. The latter, kinetic energy dampening is the result of ions colliding with an inert cell gas, whereby their mean kinetic energy is reduced. However, since polyatomic interferents are physically larger than analyte ions of equal mass-to-charge ratios, they have a higher probability of colliding with the cell gas molecules. In this wa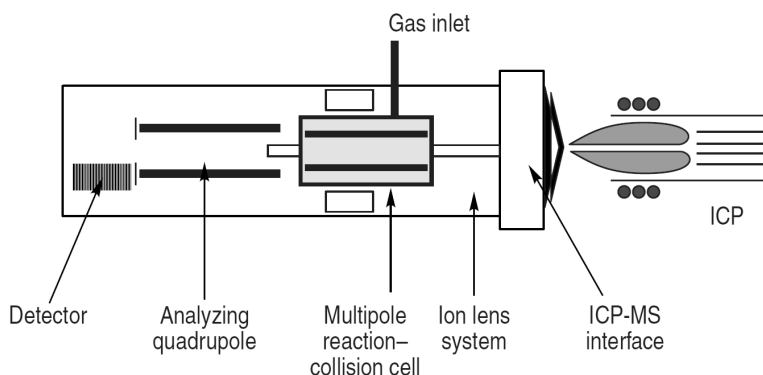y, their average kinetic energy is reduced to a larger extent than that of the analyte ions. By then applying a potential barrier, insurmountable to ions with a kinetic energy below a certain threshold, the polyatomic interferents can be preferentially eliminated. The main drawback of this approach is that the potential barrier also reduces the transmission efficiency for analyte ions, especially lighter ones, thereby decreasing the overall sensitivity. However, kinetic energy dampening may be made use of even in the absence of interfering species, when no potential barrier has to be applied. Collisions of ions with the cell gas result not only in a lower mean kinetic energy but also in a narrower energy distribution of the ion beam. As a result, the quadrupole mass filter's ion transmission efficiency is improved, whereby the instrumental sensitivity has been found to increase. Moreover, it typically results in a better (isotope ratio) precision and an improved abundance sensitivity.[101]

Secondly, next to physical processes, a variety of other ion-molecular interactions may occur when using a reactive gas instead of an inert one, including charge-transfer and chemical reactions. In this case, two approaches may be considered, either the spectral interference may be eliminated, or the analyte itself can be altered in some way (an example of both is given below).

$$^{40}\text{Ar}^+ + {}^{14}\text{N}^1\text{H}_3 \longrightarrow {}^{40}\text{Ar} + {}^{14}\text{N}^1\text{H}_3{}^+ \qquad (2.12)$$

$$^{40}\text{Ar}^1\text{H}^+ + {}^1\text{H}_2 \longrightarrow {}^{40}\text{Ar} + {}^1\text{H}_3{}^+ \qquad (2.13)$$

$$^{77}\text{Se}^+ + {}^{16}\text{O}_2 \longrightarrow {}^{77}\text{Se}^{16}\text{O}^+ + {}^{16}\text{O} \qquad (2.14)$$
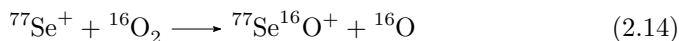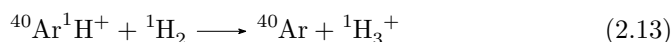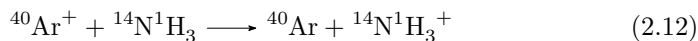
These examples already give some indication as to the versatility and applicability of this particular approach, even for resolving isobaric interferences. Nonetheless, it should be kept in mind that there is no single reactive gas capable of eliminating every type of spectral interference. On the contrary, a reactive gas, used to eliminate one particular interference, may give rise to undesired side reactions, *e.g.* resulting in the formation of a plethora of other cluster ions (*e.g.* $\text{Fe(NH}_3)_n{}^+$). However, formation of new cluster ions can be prevented or mitigated to some extent. When a quadrupole assembly is employed, the multipole may be operated as a bandpass filter, whereby the precursors to these unwanted interferences are expelled beforehand. Conversely, when a hexapole or an octapole is employed, which cannot serve as a bandpass filter, kinetic energy discrimination may be employed by applying a potential barrier, since newly formed cluster ions have a lower mean kinetic energy than the ions that were sampled from the plasma.[101]

2.9.1.3 Alternative approaches

Mathematical interference correction equations, which are implemented in most contemporary ICP-MS software suites, are routinely applied. Using this approach, the contribution of an interfering species (*e.g.* $^{40}Ar^{35}Cl^+$), to the signal observed for an analyte (*e.g.* $^{75}As^+$), is estimated by monitoring a species related to the interference at another mass (*e.g.* $^{40}Ar^{37}Cl^+$). If the relevant isotopic abundances are known, then that additional measurement can be used to determine the severity of the interference in question. However, this approach is only considered to be reliable if the contribution of the interfering species, to the analyte signal, is sufficiently small. Moreover, additional corrections may be required in complex samples (*e.g.* to correct for the presence of $^{77}Se^+$).[39,91,102]

Cool/cold plasma conditions may also be considered for attenuating certain types of spectral interferences. In this approach, a lower temperature plasma is employed, which is obtained by reducing the RF power that is supplied to the load coil and by increasing the nebuliser flow rate. By operating under such conditions, the prevalence of many argide-based interferences is greatly reduced. However, the opposite is true for many other types of interferences, *e.g.* molecular oxides. Moreover, the overall ionisation efficiency decreases, especially for elements with high first ionisation energies, whilst the susceptibility to non-spectral interferences has also been found to increase.[39,91,103]

Proper selection of the sample introduction system, in combination with optimising relevant instrumental parameters, may also result in a significant reduction of spectral interferences. Examples of these preventive measures include the use of cooled spray chambers or, in more advanced setups, membrane desolvation systems. These types of introduction systems reduce the amount of water vapour introduced into the plasma, thereby reducing the intensity of hydride- and oxide-based interferences, whilst increasing the analytical sensitivity. Furthermore, molecular oxides, in addition to multiply charged interferents, may be attenuated by simply adjusting *e.g.* the RF power, the nebuliser gas flow rate and the sampling depth. Alternatives to Ar-based plasmas have also been considered for reducing some types of spectral interferences, including mixed gas (*e.g.* Ar + N_2) and He plasmas. Finally, if all else fails, or for samples of unknown isotopic composition, the selective isolation of analytes may be required.[39,104,105]

2.9.2 Non-spectral interferences

The origins of non-spectral interferences have been described extensively in the literature, even though the mechanisms behind these so-called matrix effects are not yet fully understood. Initially, the occurrence of non-spectral interferences was attributed mainly to the manifestation of space-charge effects in the ion transfer optics, *i.e.* the defocusing of an ion beam due to the mutual repulsion of its positively charged ions. As a result of this phenomenon, non-spectral interferences ought to be more severe for lighter elements, because they are expelled more easily from the centre of the ion beam. In reality though, a

number of other phenomena also play an important role, the origins of which can be traced back to the various components of an ICP-MS instrument (*e.g.* the sample introduction system, the ICP and the interface region). To illustrate, changes in a liquid sample's physical properties (*e.g.* surface tension) may alter its aerosol's droplet size distribution, which *e.g.* has an impact on the aerosol transport efficiency. Although a number of these phenomena have been identified and described in the literature, to date, no single approach has been proposed to systematically eliminate all sources of these non-spectral interferences. [41,91,106,107]

2.9.2.1   Analyte/matrix separation

A logical approach to attenuating non-spectral interferences is to decrease the absolute concentration of the troublesome matrix. Instead of turning to simple dilutions, which would obviously have a negative impact on detection limits, this may be achieved by employing highly selective analyte/matrix separation procedures. However, selectively isolating and quantitatively recovering every single analyte, from a complex matrix, is often no trivial task. Therefore, most often only a single analyte, or a few analytes, are isolated and preconcentrated from their concomitant matrix. Techniques that have been employed previously for this purpose include *e.g.* precipitation, co-precipitation, liquid-liquid extraction, cloud-point extraction and column chromatography. [41] In this work, however, ion-exchange chromatography and extraction chromatography were used. Both techniques are widely used, *e.g.* in radioanalytical separation procedures, and are characterised by their simplicity and a relative ease of use, compared to some of the other approaches mentioned above. They rely on the use of highly selective chromatographic resins which are, most often, loaded into plastic columns. When a liquid sample is brought onto such a column, a partitioning of its components, between the liquid mobile phase and the solid stationary phase, takes place. Typically, one or a few analytes are strongly sorbed onto the stationary
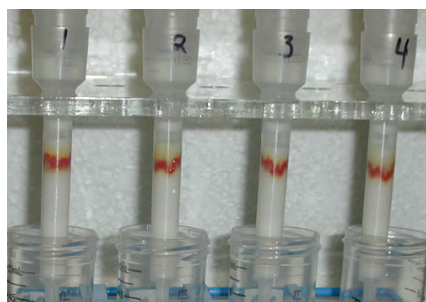
(a) Analyte/matrix separation. [108]
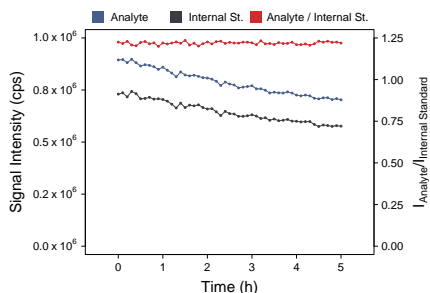
(b) Internal Standardisation.

Figure 2.14: (a) Example of an offline column chromatographic separation procedure. In this particular example, the element Ni, whose presence is indicated by the red bands, is isolated and preconcentrated on columns loaded with Ni Spec extraction chromatographic resin (Eichrom Technologies, USA). (b) Illustration of the use of internal standardisation to correct for instrumental sensitivity drift.

phase, permitting their preconcentration from a large sample volume, whilst all other elements are easily eluted with any of a number of dilute mineral acids or other complexing agents (see Figure 2.14a). The analytes can then be desorbed from the column, often sequentially, by modifying the mobile phase.[41,109,110]

2.9.2.2 Internal standardisation

The most widely used technique for dealing with non-spectral interferences, which is also used to correct for instrumental sensitivity drift, entails the use of an internal standard (see Figure 2.14b). In this approach, a known amount of an internal standard element is added to each blank, sample and calibration standard. The signal suppression or enhancement that is observed for that element can then be used to correct for the distortion of analyte signals, assuming that the internal standard is not inherently present at appreciable concentrations in any of the samples and that its behaviour is similar to that of the analyte. The most important parameter that should be considered when selecting an internal standard, for most analytes, is their respective similarity in mass, followed by similarity in first ionisation energies. In general, for multi-elemental trace analysis of samples, more than one internal standard is required. Care must be taken, however, as spectral interferents may arise from the use of such internal standards.[41,111,112]

2.9.2.3 Alternative approaches

Some of the approaches that have been described for attenuating spectral interferences, may also be employed for reducing non-spectral interferences, *e.g.* the use of alternative introduction systems and mixed-gas plasmas has been described in the literature. In general though, a plasma that is more robust towards matrix effects can be obtained by increasing the RF power and by reducing both the nebuliser gas flow rate and the sample uptake rate. Other strategies for coping with non-spectral interferences include matrix-matched external calibration, the method of standard additions and isotope dilution. In all three cases, however, the concomitant matrix is still introduced into the ICP-MS instrument, which may lead to issues with respect to memory effects. Furthermore, both the method of standard additions and isotope dilution are relatively laborious and time-consuming, making these techniques less suited for multi-elemental trace analysis.[41]

3

Instrumentation, reagents and laboratory ware

This third chapter is devoted, firstly, to describing the ICP-MS instruments that were employed during this work. To this end, the two relevant ICP-MS designs are outlined in some greater detail than in the previous chapter, which served to provide the reader with a very general overview of the operating principles and components of this type of instrumentation only. In Chapter 2, the need for high-purity reagents and labware was already emphasised, as blank levels are most often the limiting factor for ICP-MS detection limits. With this important consideration in mind, the high-purity consumables and cleaning procedures used during sample pretreatment are also described below. Portions of this chapter have been published previously in Tindemans *et al.*[1,2]

3.1 Instrumentation

Virtually all quantitative measurements reported upon in this work were carried out using an Element2 single-collector ICP-SFMS instrument (Thermo Scientific, Germany). A limited number of analyses were carried out using an XSeries2 ICP-QMS instrument (Thermo Scientific, Germany) also.

3.1.1 Element2 ICP-SFMS

The particular Element2 ICP-SFMS instrument used throughout this work had been outfitted with a stainless steel nuclear glovebox. A photograph of a different Element2 instrument, that has been modified in the same way, is shown in Figure 3.1a, whilst a schematic overview of its components is given in Figure 3.1b. It differs from regular instruments in that all components, up to and including the interface region, are housed in a glovebox that is kept at a slight under pressure. This type of setup permits the safe analysis of radioactive samples, if desired. One specific design feature of the Element2 is the use of a grounded electrode, enveloping the plasma torch, which helps to reduce the plasma potential and which improves the sensitivity. The positive ions that are sampled from the grounded plasma, along with residual plasma gas, through the interface region, are extracted by an extraction lens ($-2\,\mathrm{kV}$), which is positioned just behind the skimmer cone. The ion beam is then transmitted to the mass analyser by an electrostatic lens assembly consisting of a focusing lens, X-Y deflector lenses, a beam shaping lens and transfer lenses. The focusing lens focuses divergent ions onto the mass analyser's entrance slit, whilst the shaping lens modifies the beam's cross-sectional shape into a rectangle, similar to the contours of the entrance slit. The deflector lenses can be used to deflect and direct the ion beam through the entrance slit, whilst the transfer lenses accelerate the ion beam towards the

mass analyser, with an acceleration voltage of 8 kV. The double-focusing mass analyser consists of a 90° electrostatic sector, positioned behind a 60° magnetic sector, in a reverse Nier-Johnson geometry. Its resolving power can be adjusted by modifying the widths of the mass analyser's entrance and exit slits to one of three predetermined values. These are referred to as either *Low Resolution* (LR, 300), *Medium Resolution* (MR, 4000) or *High Resolution* (HR, 10 000). Another set of electrostatic lenses, placed in close vicinity of the magnetic and electrostatic sectors, so-called rotation and focus quadrupoles, can be used to further fine-tune the ion beam. As the beam emerges from the exit slit, it is directed to the detector's conversion dynode (-8 kV) by a deflection plate, the use of which ensures a flat detector response across the mass range. The instrument's discrete-dynode electron multiplier, operating in a dual pulse counting/analog mode, is able to provide a dynamic linear range of up to 9 orders of magnitude.

The instrument's sample introduction system consisted of a PFA-ST concentric nebuliser (Elemental Scientific, USA), a number of different spray chambers, a demountable quartz torch and injector (Thermo Scientific, Germany), and a SC-2 FAST autosampler (Elemental Scientific, USA). For elemental analysis, both the sample line and the internal standard line were pumped using a multichannel peristaltic pump (Spetec, Germany). The two resulting flows were then mixed online, in a 1:1 ratio, by means of a T-piece (Elemental Scientific, USA), which was positioned just before the nebuliser. For isotopic analysis, a low-flow PFA-ST concentric nebuliser (Elemental Scientific, USA), operated in self-aspirating mode with only a sample line, was employed. The spray chambers used for elemental analysis included a water-cooled glass double-pass Scott-type spray chamber (Thermo Scientific, Germany), an inert PFA spray chamber (Thermo Scientific, Germany) and a glass cyclonic spray chamber
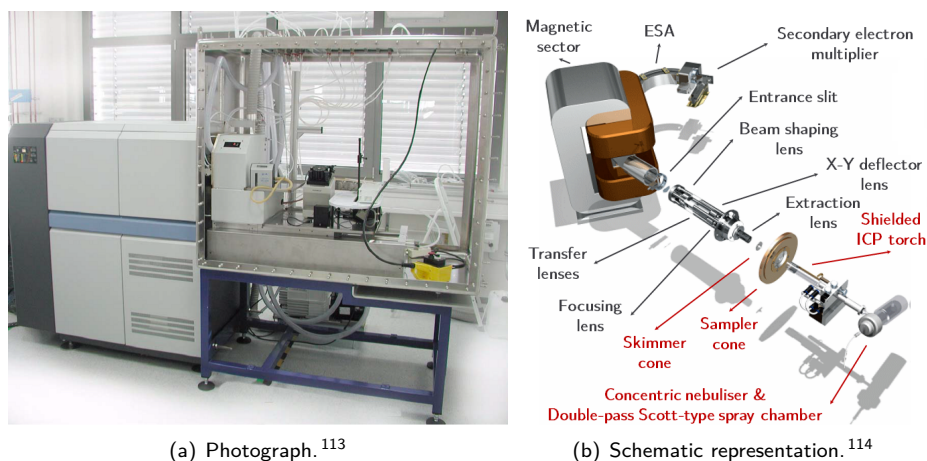
(a) Photograph. [113]

(b) Schematic representation. [114]

Figure 3.1: (a) Photo of a nuclearised Element2 ICP-SFMS, with the side panels of the glovebox not yet installed. (b) Schematic representation of the components of an Element2 ICP-SFMS. The names of the components that are housed in the nuclear glovebox are highlighted in red.

(Glass Expansion, Australia). For isotopic analysis, a specialised quartz dual cyclonic/Scott-type spray chamber was available (Elemental Scientific, USA).

The Element2 was tuned daily for maximum sensitivity and stability to count rates of $\geq 10^5$, $\geq 10^6$ and $\geq 10^6$ counts s^{-1} per µg L^{-1} for ^{7}Li$^+$, ^{115}In$^+$ and ^{238}U$^+$, respectively, in the low resolution mode. Essentially, this amounted to optimising the nebuliser gas flow rate and the torch position on a day-by-day basis. As most spectral interferences can be easily resolved by operating the Element2 at higher resolution modes, oxide formation was not taken into account when tuning the instrument. As a result, the observed oxide formation rate,

Table 3.1: Typical instrument settings for the Element2 ICP-SFMS unit.

Setting/parameter	Value/Description		
Autosampler	ESI SC-2 Fast		
Peristaltic pump speed	6 rpm		
Peristaltic pump tubing	Orange-green (i.d. 0.38 mm, sample)		
	Purple-black (i.d. 2.29 mm, waste)		
Nebuliser	PFA-ST		
Aspirating mode	Pumped (2×125 µL min^{-1})		
	Self-aspirated (60 µL min^{-1})		
Spray chamber	Water-cooled glass double-pass Scott-type		
	Glass cyclonic		
	PFA double-pass Scott-type		
	Quartz dual cyclonic/double-pass Scott-type		
Torch and injector	Demountable/Quartz		
Sampling cone	Ni or Pt (1.0 mm aperture diameter)		
Skimmer cone	Ni or Pt (H-type, 0.8 mm aperture diameter)		
Guard electrode	Enabled		
Plasma/Cool gas flow rate	16 L min^{-1}		
Auxiliary gas flow rate	0.8 L min^{-1}		
Sample/Nebuliser gas flow rate[†]	1.0 to 1.1 L min^{-1}		
Additional gas flow rate	0 L min^{-1}		
RF Power	1250 to 1300 W		
Torch x-position	0.0 mm		
Torch y-position	0.2 mm		
Torch z-position[†]	-2.4 to -1.4 mm		
Extraction lens	-2000 V		
Focus lens	-1700 V		
X-deflection lens	-2.8 V		
Y-deflection lens	-1.3 V		
Shape lens	135 V		
Scan type	E-Scan		
Detector mode	Dual		
	Pulse counting		
Resolution ($m/\Delta m$)	300	4000	10 000
Rotation quadrupole 1	0 V	-8 V	4 V
Rotation quadrupole 2	-13.5 V	-4 V	0 V
Focus quadrupole 1	14 V	-1 V	4 V
Focus quadrupole 2	-1.5 V	-1.5 V	-1.5 V

[†] *Optimised on a daily basis for optimum ^{7}Li$^+$, ^{115}In$^+$ and ^{238}U$^+$ signal intensities and stabilities*

defined as UO^+/U^+, could range anywhere from 5 to as much as 30 %. Doubly charged ion formation, defined by the Ba^{2+}/Ba^+ ratio, was typically around 5 %. Although the medium and high resolution modes can be employed to resolve many such interferences, in a straightforward manner, their use necessitated the regular reoptimisation of the voltages on the rotation and focus quadrupoles. Optimising these high resolution lenses at regular intervals, *i.e.* every couple of weeks, ensured that adequate mass resolution and symmetrical peak shapes were maintained. For medium resolution mode, these lens settings were tuned by observing the peak shape and mass separation of the adjacent $^{56}Fe^+$ and $^{40}Ar^{16}O^+$ peaks. For high resolution mode, they were optimised by monitoring the $^{39}K^+$ and $^{38}Ar^1H^+$ peaks. An overview of typical instrument settings is given in Table 3.1.

Mass calibrations in the medium and high resolution modes were carried out on those days when measurements where made in these modes. In addition, the accuracy of the higher resolution mass calibrations was verified throughout each measurement sequence, by continuously monitoring the mass spectra. If necessary, the relevant mass offsets were adjusted, iteratively, as required, in the Element2 software. For the low resolution mode, mass calibration was found to be necessary only once every couple of weeks. Low, medium and high resolution measurements were each carried out in separate measurement sequences, sometimes on different days. Even though the instrument's detector was operated in the dual pulse counting/analog mode, for elemental analysis, calibration standards and samples were prepared such that the signal intensities used for quantitative purposes could be registered in the pulse counting mode. For isotopic analysis, the detector was operated purely in the pulse counting mode.

3.1.2 XSeries2 ICP-QMS

The XSeries2 is an ICP-QMS instrument equipped with a collision/reaction cell for resolving spectral interferences. As with the Element2, the plasma potential is reduced by placing a grounded screen in between the load coil and the outside

(a) Photograph. [115]   (b) Schematic representation. [116]
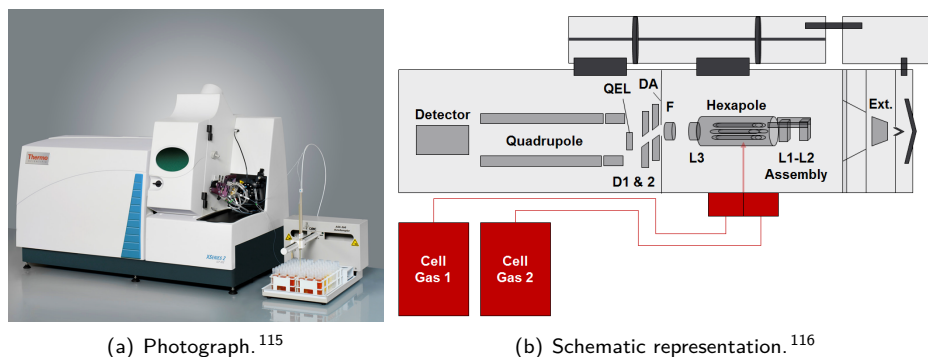
Figure 3.2: XSeries2 ICP-MS.

of the plasma torch. In this way, ion kinetic energies and the spread thereof are reduced, which improves the abundance sensitivity of the quadrupole mass filter. A photograph and a schematic representation of this type of instrument are shown in Figures 3.2a and 3.2b, respectively. Here, it can be seen that a hexapole collision/reaction cell is placed in-between the interface region and the quadrupole mass filter. Before reaching this hexapole, however, the ions are first accelerated from behind the skimmer cone into the intermediate-vacuum region by the extraction lens. The L1-L2 lens assembly then shapes and focuses the ion beam, prior to introducing it into the hexapole. In the instrument's standard operating mode, whereby the collision/reaction cell is vented, this hexapole simply guides the ions through the cell, using an RF field. When the so called *Collision Cell Technology*-mode (CCT) is employed, a reaction/collision gas is introduced into this chamber. The ion beam emerging from the reaction/collision cell is then

Table 3.2: Typical instrument setting for the XSeries2 ICP-QMS unit.

Setting/parameter	Value/Description	
Autosampler	ESI SC-2 Fast	
Peristaltic pump speed	19 rpm	
Peristaltic pump tubing	Orange-green (i.d. 0.38 mm, sample)	
	Red-red (i.d. 1.14 mm, waste)	
Nebuliser	PFA-ST	
Aspirating mode	Pumped ($2 \times 500\,\mu L\,min^{-1}$)	
Spray chamber	Peltier-cooled glass cyclonic	
Torch and injector	Demountable/Quartz	
Sampling cone	Ni or Pt (1.1 mm aperture diameter)	
Skimmer cone	Ni or Pt (Xt-type, 0.75 mm aperture diameter)	
Plasma/Cool gas flow rate	$13\,L\,min^{-1}$	
Auxiliary gas flow rate	$0.7\,L\,min^{-1}$	
Sample/Nebuliser gas flow rate†	0.95 to $1.00\,L\,min^{-1}$	
RF/Forward power	1300 W	
Torch x-position/Horizontal	0 to 50	
Torch y-position/Vertical	500 to 700	
Torch z-position/Sampling depth†	100 to 200	
Detector mode	Dual	
CCT/Standard mode delay	20 s	
Mode	Standard	CCT
Cell gas (7 % H$_2$ + 93 % He)	$0\,mL\,min^{-1}$	$4.8\,mL\,min^{-1}$
Extraction lens†	-100 to $-200\,V$	-100 to $-200\,V$
L1	$-1280\,V$	$-1280\,V$
L2	$-83\,V$	$-83\,V$
L3	$-192\,V$	$-192\,V$
Hexapole bias	$-4\,V$	$-20\,V$
Focus lens	$12\,V$	$-10\,V$
DA	$-33\,V$	$-33\,V$
D1	$-42\,V$	$-42\,V$
D2	$-140\,V$	$-100\,V$
Quadrupole bias	$-1\,V$	$-17\,V$

† *Optimised on a daily basis for optimum $^7Li^+$, $^{115}In^+$ and $^{238}U^+$ signal intensities and stabilities. As an additional constraint, CeO^+/Ce^+ and Ba^{2+}/Ba^+ levels were kept $< 2\,\%$, in standard mode*

extracted, collimated and accelerated towards the focus lens by lens L3. The focus lens, in turn, focuses the ion beam onto the differential aperture, which separates the intermediate-vacuum region from the true high-vacuum analyser chamber. The D1-D2 lens assembly selectively steers the positively charged ions off-axis, whereby photons and neutral species are removed from the beam. A quadrupole entry lens then focuses the ions into the quadrupole mass filter, where they are separated from one another according to their mass-to-charge ratio. Finally, the resolved ion beam is directed towards the discrete-dynode electron multiplier, which can operate in a dual pulse counting/analog mode also.

The sample introduction system used with the XSeries2 was very similar to that of the Element2 described above, except that a Peltier-cooled glass cyclonic spray chamber was employed (Elemental Scientific, USA). The instrument was tuned daily, in the standard mode, to maximise the sensitivities and stabilities for $^7Li^+$, $^{115}In^+$ and $^{238}U^+$, whilst ensuring that both CeO^+/Ce^+ and Ba^{2+}/Ba^+ were kept below 2%. In practice, this entailed daily optimisation of the nebuliser gas flow rate, the torch position and the extraction lens voltage. In the CCT mode, a premixed blend of H_2 (7%) and He (93%) was employed, at a flow rate of $ca.$ $4.6\,mL\,min^{-1}$. CCT-mode performance was evaluated by monitoring the transmission-loss for ^{59}Co ($< 90\%$) and by visually verifying that the Ar dimers had been efficiently eliminated. When both modes were used together, in a single measurement sequence, a settling time of $ca.$ $20\,s$ was allowed, when switching from one mode to the other. Typical instrument settings are summarised in Table 3.2.

3.2 Reagents, laboratory ware and cleaning procedures

Exploiting an ICP-SFMS instrument's superior detection power to its full potential requires the use of specialised reagents and labware during all steps of sample pre-treatment. The high-purity materials that were used during this work are therefore listed below. In addition, the extensive cleaning procedures employed, which were applied in order to further reduce blank levels and attenuate potential contamination of materials, are also briefly outlined. Furthermore, the provenance of each sample and certified reference material, considered in this work, is described.

3.2.1 Ultra-pure water and mineral acids

Trace metal grade HNO_3 (67 - 69 wt.%), HF (47 - 51 wt.%) and HCl (34 - 37 wt.%) were obtained from Fisher Scientific (Belgium). These trace metal grade acids and ultra-pure (UP) water with a resistivity of $\geq 18.2\,M\Omega\,cm$ (Arium Pro UV, Sartorius Stedim Biotech, Belgium) were used throughout to treat samples and prepare chromatographic eluents, calibration standards and dilutions.

3.2.2 Digestion vessels and other recipients

All Falcon tubes, bottles, digestion vessels and other recipients were made of either HDPE, PP, PFA or PTFE. In order to limit any potential contaminations, these

items were precleaned, by leaching with 1.5 M HNO_3 for at least 48 h, before being rinsed thoroughly with UP water, and air-dried, prior to use. Sealable PTFE digestion vessels (Savillex, USA) were cleaned of contaminants by leaching with concentrated mineral acids, at elevated temperatures of 150 to 200 °C, on a hotplate. The exact composition of the leaching solution depended upon the digestion protocol for which the vessels were destined (*i.e.* if a sample was to be dissolved in 7.5 M HNO_3, then an excess volume of 7.5 M HNO_3 was used to clean the vessels).

3.2.3   Elemental and isotopic standard solutions

Calibration and isotopic standards were prepared by serial volumetric or gravimetric dilution of commercially available single-element stock solutions (1000 mg L^{-1}). Most of these stock solutions were obtained from CPI (The Netherlands), Johnson Matthey (UK) and, in the case of Spex Certiprep (UK) solutions, from Boom BV (The Netherlands). Multi-element stock solutions (10 mg L^{-1}), originating from Spex Certiprep (UK), were used to verify calibration curves, and to prepare "synthetic" and "mock" samples used in the development and validation of chromatographic separation procedures (see Chapters 4 and 5). Lastly, on one occasion, a 1000 mg L^{-1} stock solution was prepared by dissolving an appropriate amount of Lu_2O_3 powder, obtained from Acros Organics (Belgium), in dilute HNO_3.

3.2.4   Samples and certified reference materials

High-purity Pb (> 99.9999 %) and Bi (> 99.9995 %) powders were purchased from ESPI metals (USA), whilst two Pb-matrix certified reference materials (IMN PL33 & PL66) were obtained from the *Institute of Non-ferrous Metals* (IMN, Poland). Actual LBE samples were provided to us by Joris Van den Bosch, Ben Caers and Kris Rosseel of SCK•CEN, but were originally purchased from Sidech (Belgium).

Three steel alloy certified reference materials were obtained from the *National Institute of Standards and Technology* (NIST, USA), in the form of chips (NIST SRMs 361, 362 & 363). Small samples of genuine high-alloy steels were obtained through Serguei Gavrilov of SCK•CEN. Originally though, these three different types of steel alloys had been purchased from Industeel (Belgium), in the case of T91 and 316L, or from OCAS (Belgium), in the case of 15-15Ti.

3.2.5   Chromatographic columns and resins

Propylene columns of two different sizes, 2 mL and 5 mL, were obtained from Triskem International (France). These chromatographic columns were thoroughly cleaned by first rinsing them with UP water, after which they were stored in 1.5 M HNO_3 until needed. On the actual day of use, they were rinsed first with small volumes of the initial eluent and then copiously with UP water.

Four different types of chromatographic resins were purchased from Triskem International (France), namely two ion-exchange resins and two extraction chromatographic resins, which are described in greater detail in Chapters 4 and 5. The

extraction chromatographic Pb Spec (100-150 µm) and TRU Spec (100-150 µm) resins were used as received. They were simply slurried with a small volume of the initial eluent to be used in the separation procedure, before being pipetted into a polypropylene column. The AG 1x4 anion-exchange (100-200 mesh) and AG 50Wx8 cation-exchange (100-200 mesh) resins, on the other hand, were treated before use. They were rinsed first with UP water, after which the resins were stored in 0.1 M HCl for at least one week prior to use. On the actual day of use, they were slurried first with UP water and then repeatedly with whichever eluent would be used during the separation procedure, before being pipetted into a polypropylene column. As a final step in the cleaning procedure, any column loaded with one of the four resins was conditioned with 10 to 20 mL of the initial eluent.

3.2.6   Other reagents and laboratory ware

Solid samples were collected either by means of cutting shears or by means of titanium nitride-coated steel (for high-alloy steel samples) or solid tungsten carbide (for LBE samples) drill bits. A hotplate with a ceramic top plate was used for sample digestion (VWR, Belgium). Laboratory grade ammonium citrate (> 98 wt.%) was purchased from Fisher Scientific (Belgium). Argon gas (> 99.999 %), used to operate the ICP-SFMS and ICP-QMS instruments, was obtained either from Air Products (Belgium) or Air Liquide (Belgium).

(a) Single-element stock solutions.

(b) Trace metal grade mineral acids and laboratory grade ammonium citrate.
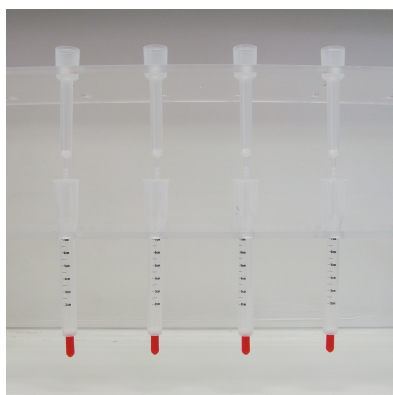
(c) Chromatographic columns.

(d) Chromatographic resins.
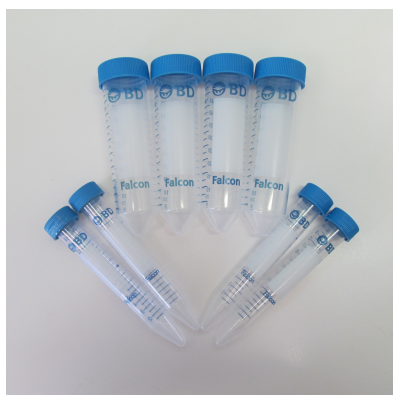
(e) Falcon tubes.

(f) Digestion vessel.

Figure 3.3: Overview of reagents and labware.

4

Multi-elemental trace analysis of high-alloy steels

In this chapter, the development of an analytical method for the multi-elemental trace analysis of steel alloys, by means of ICP-SFMS, is described. For this purpose, three particular types of high-alloy steels were investigated, *i.e.* those steel alloys that are being considered for use in the MYRRHA research reactor at SCK•CEN (see Section 1.1.5). Photographs of small samples of the T91, 316L and 15-15Ti high-alloy steels in question are given in Figure 4.1. All three of these Fe alloys have a high Cr content ($> 5\%$) whilst both 316L and 15-15Ti also have a similarly high Ni content. In addition to those three main matrix elements, a number of impurities and alloying elements are also expected to be present. Firstly, Si, V, Mn, Co, Cu and Mo were identified as being the most important minor alloying elements ($< 2\%$). In addition, on the basis of internal communications at SCK•CEN, a list of potentially interesting trace elements comprising B, Al, P, S, Ti, As, Zr, Nb, Ta and W was compiled also. These target elements were to be determined by means of ICP-SFMS, but in the presence of a vast excess of Cr, Fe and Ni and minor amounts of Si, V, Mn, Co, Cu and Mo. In order to attenuate spectral and non-spectral interferences, which often hamper ICP-MS analyses of this kind, as well as pronounced memory effects, a highly selective analyte/matrix separation procedure was developed and applied (see Section 2.9).[117,118] To this end, a column chromatographic separation protocol was devised, which was later found to be applicable not only to the ultra-trace analysis of B, Al, P, S, Ti, As, Zr, Nb, Ta and W in these alloys, but also to the determination of a wider range of trace elements including Be, Ge, Se, Rh, Pd, Sn, Sb, Hf, Re, Ir and Pt. The development of this highly selective analyte/matrix separation is discussed below, whilst the procedure's validation and eventual application are also described. Portions of this chapter have been published previously in Tindemans *et al.*[2]

(a) T91.   (b) 316L.   (c) 15-15Ti.
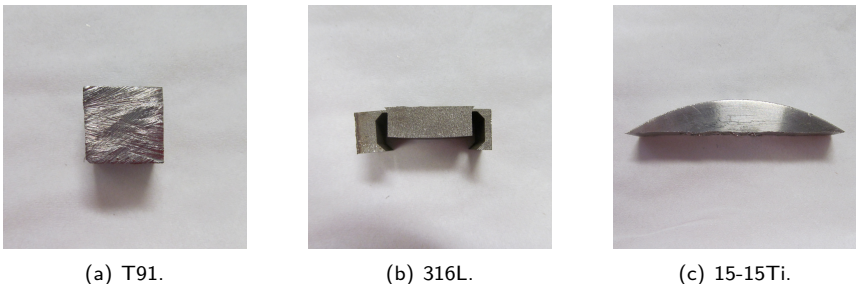
Figure 4.1: High-alloy steels under consideration.

4.1   Introduction

Ideally speaking, a suitable analyte/matrix separation procedure should allow all target elements to be selectively isolated from each and every matrix element. Most important, though, was that at least the three main matrix elements Cr, Fe and Ni were removed. An additional constraint, however, was that the extensive use of HCl should be avoided. If the proposed procedure were to be applied to irradiated samples, then it would likely be carried out inside a nuclear glovebox. Unfortunately, the stainless steel components of such gloveboxes are susceptible to corrosion by exposure to HCl, which would increase the risk of contaminating future samples with *e.g.* Fe. In the past, both trace and macro-quantities of Fe have been separated from a number of other elements *e.g.* by using liquid-liquid extraction or anion-exchange chromatography. However, whereas liquid-liquid extraction is deemed less practical, anion-exchange separation requires the use of large amounts of HCl. Furthermore, by employing anion-exchange chromatography, and using an HCl-based eluent, it is impossible to remove either Cr or Ni from the target elements. Other chromatographic separation procedures have also been considered for the isolation and preconcentration of trace Fe, including *e.g.* the use of solid-phase extraction. Conversely, the determination of trace amounts of B in an Fe matrix has been achieved by a combination of matrix precipitation and cation-exchange chromatography. In this case, however, whilst matrix removal was highly efficient, the recovery of B was $< 40\%$, as a result of its coprecipitation with the matrix elements, which necessitated the use of isotope dilution as a calibration strategy. Naturally, this approach would be impractical for the determination of a large number of trace elements in a large number of samples. In this work, we have therefore attempted to develop a procedure based solely on the use of column chromatography. Initially, it was envisioned that the matrix elements ought to be selectively retained by a highly specific chromatographic resin, whilst all other elements would elute rapidly. Two candidate chromatographic resins were identified for this purpose.[119–125]

The TRU Spec resin was first described by Horwitz *et al.*, for the separation and preconcentration of actinides from acidic media. This particular resin consists of a

(a)   (b)

Figure 4.2: (a) The active component of TRU Spec extraction chromatographic resin (octyl(phenyl)-N,N-diisobutylcarbamoylmethylphosphine oxide). (b) A styrene-divinylbenzene copolymer lattice with sulfonic acid functional groups, such as the AG 50W×8 cation-exchange resin, in the hydrogen form.[126]

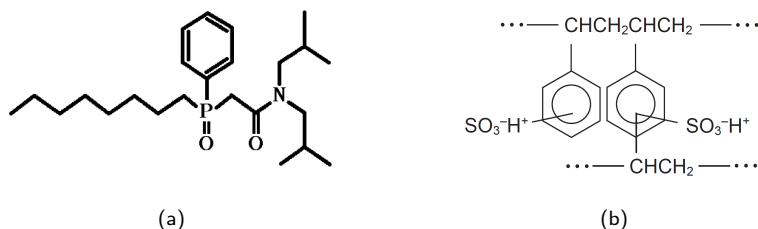solution of octyl(phenyl)-N,N-diisobutylcarbamoylmethylphosphine oxide (CMPO) in tri-n-butyl phosphate (TBP), which is sorbed on an inert polymeric support. At the time, this transuranic-specific resin was shown to have a high affinity for Fe also. Shortly after, Huff *et al.* reported distribution coefficients on TRU Spec resin in acidic media for a larger number of elements. Their combined data suggest that this resin should have a limited affinity for most elements in HNO_3 media, unfortunately, however, that includes Cr and Ni. Exploratory experiments with HNO_3- and HF-based eluents confirmed this to be the case. As a result, further investigation of this resin was abandoned. In addition, as the resin's active component is a solution of CMPO in TBP, the determination of P would have been all but impossible due to the severe contamination of the eluate by the resin.[127–129]

The AG 50Wx8 strongly acidic cation-exchange resin is composed of sulfonic acid functional groups attached to a 8 % cross-linked styrene-divinylbenzene copolymer lattice (see Figure 4.2b). Although Nelson *et al.* studied the affinity of a large number of elements towards the AG 50Wx8 cation exchange resin in HCl media extensively, data on their affinity for similar resins in HNO_3 or HF media is much sparser. Nonetheless, from the data available, it can be concluded that Cr, Fe and Ni ought to be retained on the resin in dilute HNO_3/HF media. At the same time, a large number of the minor alloying elements and impurities should exhibit little or no affinity towards the resin in these types of media. As a result, this resin was considered promising and its use was pursued further.[130–132]

4.2 Experimental

The reagents and labware employed in the preparation of blanks, standards, samples and eluents were described in Chapter 3. Chapter 3 also included a general overview of the Element2 ICP-SFMS's typical instrumental parameters. Specifically for the experiments described in Chapter 4, an inert PFA double-pass Scott-type spray chamber, and T-piece positioned just before the nebuliser, were used. This T-piece was used to mix the sample and the internal standards, both pumped, online in a 1:1 ratio. Unless otherwise stated, this instrument was employed for quantitative analysis. The relevant data acquisition parameters are discussed below, as well as the sample preparation procedures.

4.2.1 Data acquisition parameters

The elements Li, Sc, Ga, Sr, In, Eu and Th were monitored as internal standards, in at least one resolution mode, because these cover the greater part of the mass range (see Section 2.9.2.2). The nuclides of Be, B, Zr, Nb, Rh, Pd, Sn, Sb, Hf, Ta, W, Re, Ir, Pt were measured only in low resolution mode, whilst those of Al, Si, P, S, Ti, V, Cr, Mn, Fe, Co, Ni, Cu, Mo and those of Ge, As, Se were measured in medium and high resolution mode, respectively. In the case of the target elements, two of the most abundant nuclides, free from isobaric interference, were monitored whenever possible. Generally speaking, the most abundant nuclide was used most often for quantitative analy-

Table 4.1: Typical data acquisition parameters for the Element2 ICP-SFMS unit.

Setting/parameter	Value/Description		
Resolution ($m/\Delta m$)	300	4000	10 000
Runs	6	6	6
Passes	12	6	6
Dwell time	10 ms	20 ms	20 ms
Mass window	5 %	100 %	125 %
Integration window	5 %	60 %	60 %
Samples per peak	100	20	20
Element Nuclides	^{9}Be, ^{10}B, ^{11}B, ^{90}Zr, ^{91}Zr, ^{93}Nb, ^{103}Rh, ^{104}Pd, ^{105}Pd, ^{118}Sn, ^{119}Sn, ^{121}Sb, ^{123}Sb, ^{178}Hf, ^{179}Hf, ^{181}Ta, ^{182}W, ^{183}W, ^{185}Re, ^{187}Re, ^{191}Ir, ^{193}Ir, ^{194}Pt, ^{195}Pt	^{27}Al, ^{29}Si, ^{30}Si, ^{31}P, ^{32}S, ^{34}S, ^{47}Ti, ^{49}Ti, ^{51}V, ^{52}Cr, ^{53}Cr, ^{55}Mn, ^{56}Fe, ^{57}Fe, ^{59}Co, ^{60}Ni, ^{62}Ni, ^{63}Cu, ^{65}Cu, ^{95}Mo, ^{97}Mo	^{72}Ge, ^{73}Ge, ^{75}As, ^{77}Se, ^{78}Se
Internal standard nuclides	^{7}Li, ^{45}Sc, ^{69}Ga, ^{88}Sr, ^{115}In, ^{153}Eu, ^{232}Th	^{45}Sc, ^{69}Ga	^{45}Sc, ^{69}Ga, ^{88}Sr

sis. Typical data acquisition parameters are summarised in Table 4.1. Calibration standards and sample dilutions were prepared such that the instrument's detector always operated in the pulse counting mode for quantitative analysis.

4.2.2 Sample preparation procedures

Simple "synthetic" samples were prepared by serial volumetric dilution of multi-element and single-element (in the case of Fe) stock solutions in such a way that these samples contained $2 \, \mathrm{mg \, L^{-1}}$ Fe and $0.2 \, \mathrm{mg \, L^{-1}}$ of all other elements.

Real samples were prepared by digesting portions of the steel alloys under investigation. The high-alloy steel was first drilled with a metal drill bit to a depth of *ca.* 2 to 3 mm, after which the material originating from this surface layer was collected and discarded (in order to remove potential surface contaminants). The same metal drill bit was then used to drill further down into the sample, after which the drillings from the sub-surface layers were collected for quantitative analysis. For sample digestion, *ca.* 0.5 g metal was weighed accurately in a sealable PTFE digestion vessel. A 2.5 mL aliquot of HCl was pipetted into this vessel, followed by a 2.5 mL aliquot of HNO_3 and 0.25 mL of HF. The vessel was then closed and placed on a hotplate at 175 °C for 8 h, after which it was left to cool before being opened. Visual inspection revealed that the bulk of the material had usually dissolved at this stage, although the solution was most often not yet clear. Therefore, a 1.75 mL aliquot of UP water was pipetted into the vessel, after which it was closed and placed on a hotplate at 200 °C for another 8 h. After cooling, *ca.* 18 mL of UP water was pipetted into this vessel, bringing the total volume to *ca.* 25 mL. The sample solution then contained at most $20\,000 \, \mathrm{mg \, L^{-1}}$ Fe and acids at concentrations of, at most, $1.5 \, \mathrm{M}$ HNO_3, $1.2 \, \mathrm{M}$ HCl and $0.3 \, \mathrm{M}$ HF.
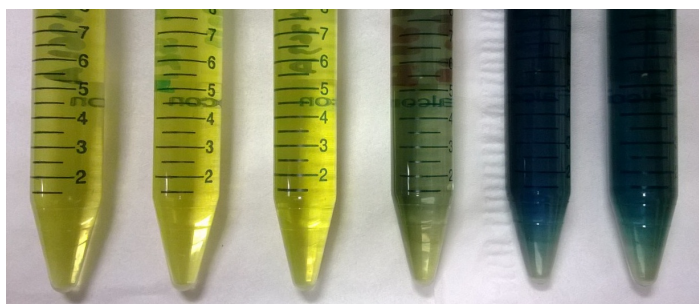
Figure 4.3: Solutions of digested high-alloy steels and certified reference materials. Shown from left to right are NIST SRM 361, NIST SRM 362, NIST SRM 363, T91, 316L and 15-15Ti. The certified reference materials are alloyed to a lesser extent than the high-alloy steels under investigation, as is apparent from the solutions' distinctly different colors. The 316L and 15-15Ti's higher Ni content, compared to T91, results in an even more vibrant emerald green color.

Certified reference materials, obtained in the form of chips, were digested in the same way as drillings from real samples. A photograph of a number of dissolved high-alloy steels and certified reference materials is shown in Figure 4.3. Procedural blank samples were also prepared in the same manner as these samples, except that no actual solid material was placed in the digestion vessel.

"Mock" samples used in the development and validation of the analytical method were also prepared by first digesting drillings, as described in the previous paragraphs (mock samples prepared for validation purposes were all prepared from T91 steel drillings). A 4.4 mL aliquot of the resulting solution was spiked with 0.2 mL of three different $10 \, \mathrm{mg \, L^{-1}}$ multi-element stock solutions, such that the amount of spike added would be equivalent to an additional $20 \, \mathrm{\mu g \, g^{-1}}$ amount of each of the target elements in the original solid material.

4.3 Results and discussion

The AG 50Wx8 cation-exchange resin had been selected for the development of a highly-selective analyte/matrix separation procedure, which would facilitate the multi-elemental trace analysis of high-alloy steels by means of ICP-SFMS. A literature review had already indicated that this resin would exhibit a high affinity for the matrix elements Cr, Fe and Ni in dilute HNO_3 media, whilst it ought to exhibit little to no affinity towards many of the target elements in those same dilute HNO_3 media. Nevertheless, the supposed behaviour of a number of elements, in dilute acidic media, was first corroborated through a series of simple experiments. These results were then used to develop a highly selective analyte/matrix separation procedure, which was subsequently validated and applied to real samples.

4.3.1 Development of an analyte/matrix separation procedure

The affinity of the following elements B, Al, P, Ti, V, Cr, Mn, Fe, Co, Ni, Cu, As, Mo, Zr, Nb, Ta and W towards the AG 50Wx8 resin, in acidic media (dilute HNO_3,

HCl, HF), was investigated. The behaviour of all these elements was studied by loading a 1 mL aliquot of a synthetic sample onto a 5 mL column containing AG 50Wx8 resin. Such samples were then eluted using a variety of eluents with various HNO_3 (0.15 M, 0.3 M, 0.75 M, 1.5 M, 3 M, 4.5 M), HCl (0 M, 0.12 M, 0.24 M, 0.6 M, 1.2 M) and HF (0.003 M, 0.012 M, 0.3 M) concentrations. Based on the experimental data obtained, the separation procedure was optimised in terms of the acid concentrations in the eluent. In essence, the HNO_3 concentration in the eluent needed to be sufficiently low to ensure retention of Cr, Fe and Ni, as was expected, whilst the HF concentration needed to be high enough to ensure rapid elution of Al, Ti, Zr, Nb and W. As an example of matrix element behaviour, Figure 4.4a depicts elution profiles of Ni for a range of HNO_3 concentrations, at a constant 0.012 M HF concentration. This shows that Ni is retained fully on the resin at molarities $\leq$ 1.5 M, whilst the adsorbability is expected to be highest at 0.15 M HNO_3. As an example of target element behaviour, Figure 4.5a depicts elution profiles of Zr for the same range of HNO_3 concentrations, showing that Zr is eluted rapidly from the resin at all molarities studied. Figure 4.5b depicts elution profiles of Zr for a range of HF concentrations, at a constant 0.3 M HNO_3 concentration. Although these elution profiles show that a concentration of 0.012 M HF in the eluent ensured rapid elution of Zr, a concentration of 0.3 M HF was found to be necessary in order to rapidly elute all target elements that readily form fluoride complexes (*e.g.* Ti). Rapid elution of the target elements ensures good separation from the matrix elements, if the latter are strongly bound to the resin under the same conditions. Figure 4.4b reveals that HF concentrations of up to 0.3 M do not impede retention of the matrix element Ni on the AG 50Wx8 resin, and a similar observation was made for the two other matrix elements, Cr and Fe. Whilst the use of HCl was found to be essential for the actual digestion of real high-alloy steel samples, it was feared that the presence of this HCl in the digested samples might still reduce the resin's affinity for a matrix element such as Fe. However, as shown in Figure 4.4c and Figure 4.5c, the presence of HCl at concentrations up to 1.2 M in the eluent did not affect elution behaviour adversely. Although the behaviour of only two elements is elaborated upon here, comparable elution profiles were generated for all elements for which the adsorbability onto the AG 50Wx8 resin was studied. These additional elution profiles can be found in the appendix to this chapter, with the exception of those obtained for Cr. For that particular element, no reliable results were obtained in these exploratory experiments, since no reliable recoveries could be determined, because Cr's background level in the column's eluate was found to increase and vary substantially at the highest acid concentrations studied. As such, the behaviour of Cr was initially assumed to be similar to that of Fe and Ni. Generally speaking, when using a 0.15 M HNO_3 / 0.3 M HF eluent, the elements V, Cr, Mn, Fe, Co, Ni and Cu have a high affinity towards the AG 50Wx8 resin; whilst B, Al, P, Ti, As, Zr, Nb, Mo, Ta and W are rapidly eluted. The elements initially retained on the column can then be stripped with a 7.5 M HNO_3 / 0.3 M HF eluent and determined separately.
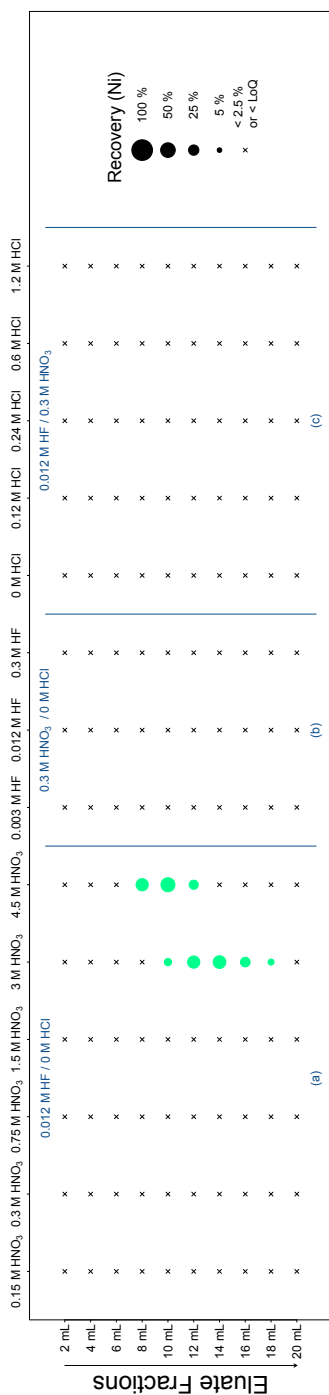
Figure 4.4: Isocratic elution profiles of Ni obtained upon loading $1\,\mathrm{mL}$ of a synthetic sample, containing $ca.$ $0.2\,\mathrm{mg\,L^{-1}}$ Ni, onto a $5\,\mathrm{mL}$ AG 50W×8 column. For each of the different eluents investigated, the elution profile is represented as a series of circles, the areas of which are proportional to the recovery of an element in each respective fraction.

Figure 4.5: Isocratic elution profiles of Zr obtained upon loading $1\,\mathrm{mL}$ of a synthetic sample, containing $ca.$ $0.2\,\mathrm{mg\,L^{-1}}$ Zr, onto a $5\,\mathrm{mL}$ AG 50W×8 column. For each of the different eluents investigated, the elution profile is represented as a series of circles, the areas of which are proportional to the recovery of an element in each respective fraction.
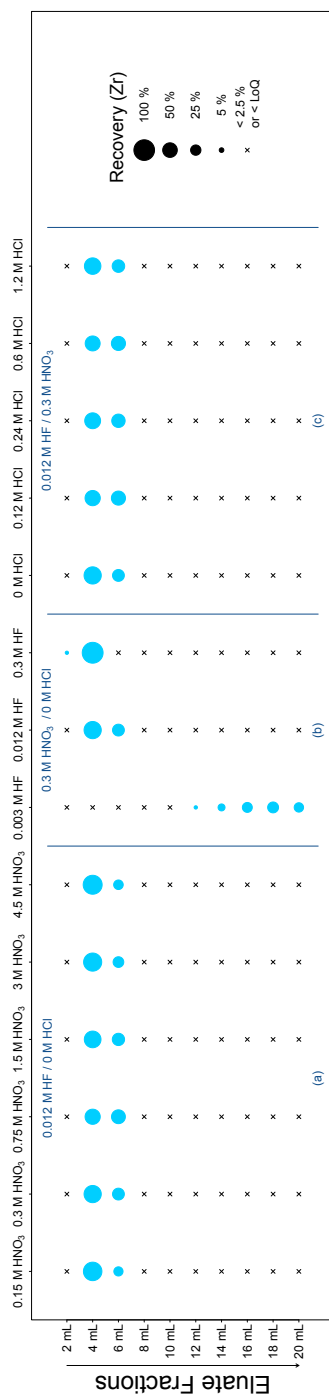
The analyte/matrix separation procedure was then applied to mock samples, which had much higher concentrations of the matrix elements compared to the synthetic samples. In addition, the elution behaviour of a larger number of elements, when using a $0.15\,M$ HNO_3 / $0.3\,M$ HF eluent, was investigated. Experiments with these mock samples revealed that the procedure could most likely also be used for the determination of Be, S, Ge, Se, Rh, Pd, Sn, Sb, Hf, Re, Ir and Pt. Conversely, it was deemed unlikely that it could be used for the determination of Li, Ga, Rb, Sr, Ru, Cd, In, Cs, Ba, Tl, Pb or U in high-alloy steels. However, it should be noted that none of the rare-earth elements were considered in these experiments. The separation protocol was then applied to mock samples prepared from the three different types of high-alloy steels T91, 316L and 15-15Ti, from which three individual elution profiles could be generated for each element, which are all provided in the appendix to this chapter (an example is shown in Figure 4.8). The consistency of these elution profiles was considered to be testament to the reproducibility of the procedure.

In the optimised procedure, a $1\,mL$ aliquot of a digested sample, containing *ca.* 10 000 to 20 000 $mg\,L^{-1}$ Fe and, at most, $1.5\,M$ HNO_3, $1.2\,M$ HCl and $0.3\,M$ HF, is loaded onto a $5\,mL$ AG 50Wx8 column (see Figure 4.6). Most of the trace elements and minor elements are easily stripped from the column by eluting with $9\,mL$ of a $0.15\,M$ HNO_3 / $0.3\,M$ HF eluent (Fraction T). The remaining elements V, Cr, Mn, Fe, Co, Ni and Cu are eluted using $30\,mL$ of a $7.5\,M$ HNO_3 / $0.3\,M$ HF eluent (Fraction M). Examples of elution profiles, for all of the elements considered in this work, obtained by applying the analyte/matrix separation procedure to a mock sample prepared from 15-15Ti steel, are presented in Figure 4.8. Two other series of elution profiles, obtained for mock samples prepared from T91 and 316L, can be found in the appendix to this chapter.

Approximately $5\,\%$ of the total Cr content of a high-alloy steel, *i.e.* $< 1\,\%$ of the initial matrix, elutes prematurely and is found in the first fraction containing target elements (Fraction T). Initially, the presence of relatively large amounts of HCl, in the digested sample solutions, was suspected of lying at the root of this
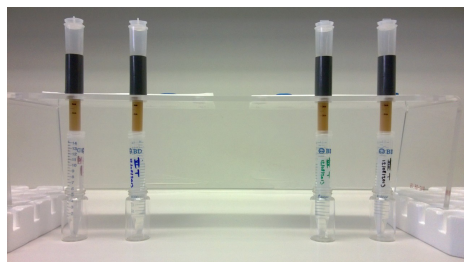
Figure 4.6: Four $5\,mL$ chromatographic columns placed in a rack, each loaded with slurried AG 50Wx8 cation-exchange resin.
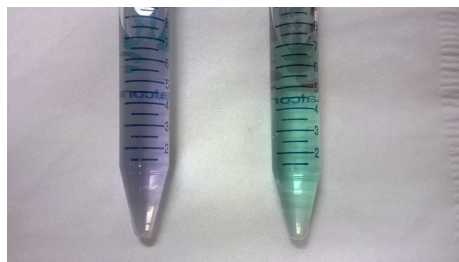
Figure 4.7: (left) A $1000\,mg\,L^{-1}$ Cr stock solution. (right) A $1000\,mg\,L^{-1}$ Cr stock solution that has been heated on a hotplate at *ca.* $200\,^{\circ}C$.
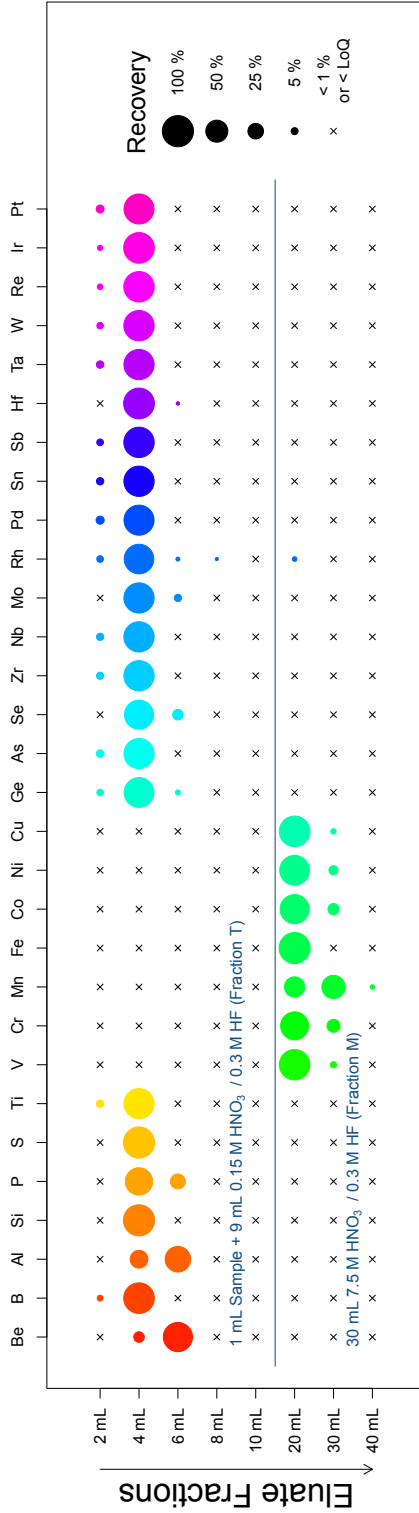
Figure 4.8: Gradient elution profiles for all elements of interest, obtained by applying the procedure developed to a mock sample prepared from 15-15Ti high-alloy steel. This mock sample was prepared such that it contained $10\,000$ - $20\,000\,\mathrm{mg\,L^{-1}}$ Fe and acid concentrations of, at most, $1.5\,\mathrm{M}$ HNO_3, $1.2\,\mathrm{M}$ HCl and $0.3\,\mathrm{M}$ HF. For each element, the elution profile is represented as a series of circles, the areas of which are proportional to the recovery in each respective fraction. The eluent used corresponds to the fractions collected as follows: [$2\,\mathrm{mL}$] $1\,\mathrm{mL}$ Sample $+ 1\,\mathrm{mL}$ Sample $+ 1\,\mathrm{mL}$ $0.15\,\mathrm{M}$ HNO_3 / $0.3\,\mathrm{M}$ HF; [$4\,\mathrm{mL}$ - $10\,\mathrm{mL}$] $4 \times 2\,\mathrm{mL}$ $0.15\,\mathrm{M}$ HNO_3 / $0.3\,\mathrm{M}$ HF; [$20\,\mathrm{mL}$ - $40\,\mathrm{mL}$] $3 \times 10\,\mathrm{mL}$ $7.5\,\mathrm{M}$ HNO_3 / $0.3\,\mathrm{M}$ HF.

problem. However, the problem could not be alleviated by evaporating a sample to incipient dryness and then taking it up again in dilute HNO_3 and HF. Further still, in that one single experiment, the opposite appeared to be true, as more of the Cr was found to elute prematurely in comparison to previous observations. It was then postulated that the speciation of Cr changes as a sample undergoes heating. In a separate experiment, it was found that prolonged heating did indeed result in an increase of the amount of Cr that broke through. Two 10 mL aliquots of a $1000\,mg\,L^{-1}$ Cr stock solution were collected, one of which was stored in a Falcon tube whilst the other was pipetted into a sealable PTFE digestion vessel. The digestion vessel was then closed and placed on a hotplate at *ca.* 200 °C for three successive 8 h periods. A change in the colour of the solution could be observed (see Figure 4.7), possibly indicative of a change in speciation. The heated and the untreated aliquot were then subjected to the separation procedure alongside each other, in duplicate. For this particular experiment, measurements were performed not using an Element2 ICP-SFMS unit but using an XSeries2 ICP-QMS unit, operated in the CCT mode. In the case of the heated sample, 6.5 % and 7.4 % of the Cr broke through prematurely, whereas this was only *ca.* 0.5 % for the untreated sample. Prolonged heating was thus shown to indeed result in an increase in the amount of Cr that eluted prematurely, for reasons not fully elucidated. However, this issue was not investigated further. The minor element Mo, constituting *ca.* 1 to 2 % of the total of each steel alloy matrix, also co-elutes with the target elements. Given that the amount of Mo eluting with the target elements exceeds that of prematurely eluting Cr, no further effort was made to reduce the amount of Cr that breaks through. In the case of Fe and Ni, in contrast to Cr, > 99.9 % could be separated from the target elements. However, in an additional experiment, it was found that as much as 10 % of Fe could elute from the AG 50Wx8 column prematurely if the HCl concentration in the digested sample was doubled to 2.4 M, instead of being limited to 1.2 M.

4.3.2   Validation and application of the procedure

Validation of the procedure was carried out by analysing three types of samples. Firstly, the procedure was applied to three steel alloy matrix certified reference materials (NIST SRMs 361, 362 and 363). Secondly, to evaluate the procedure for the determination of elements not present in the *Certified Reference Materials* (CRMs) nor in the real samples under study, the procedure was also applied to one type of mock sample (prepared from T91 steel). Thirdly, the procedure was applied to three real high-alloy steel samples (T91, 316L and 15-15Ti). Procedural *Quantification Limits* (QL, 10s) were determined by analysing five procedural blanks. The procedural QLs for all the trace and minor elements, found in fraction T, are shown in Table 4.2. These were calculated as if the procedural blank signal originated from a 0.5 g metal sample. These QLs ranged from low $ng\,g^{-1}$ levels for Re and Hf to sub-$mg\,g^{-1}$ levels for S. All analyses of samples for validation purposes were carried out in quintuplicate ($n = 5$) under reproducibility conditions. For each replicate analysis, separate aliquots of any particular solid sample were

Table 4.2: Procedural quantification limits (QL, 10s) for all the trace and minor elements that elute in fraction T.

QL (μg g^{-1})											
Be 0.2	B 1	Al 20	Si 900	P 7	S 200	Ti 0.4	Ge 0.2	As 0.1	Se 0.5	Zr 0.1	Nb 0.02
Mo 4	Rh 0.01	Pd 0.1	Sn 0.4	Sb 0.02	Te 0.06	Hf 0.007	Ta 0.02	W 0.03	Re 0.005	Ir 0.8	Pt 0.2

Table 4.3: Experimental results and certified values for all target elements that elute in fraction T, for NIST SRMs 361, 362 and 363. The uncertainties on the experimentally determined concentrations have been rounded off to two significant figures whilst the associated average values have been rounded off accordingly.

SRM 361 (μg g^{-1})	B	Al	P	S	Ti	Ge	As	Se	Zr	Nb	Sn	Sb	Hf	Ta	W
Experimental (n=5, u=2×SE)	4.85 ± 0.16	200.2 ± 4.1	120.9 ± 1.7	< 200	204.8 ± 2.8	33.81 ± 0.86	182.1 ± 3.2	32.38 ± 0.79	93.9 ± 5.1	210 ± 12	92.8 ± 4.3	41.7 ± 1.8	0.3236 ± 0.0087	196.5 ± 7.0	179.2 ± 4.9
Certified (k=2)	4.78 ± 0.15	210 ± 50	140 ± 10	143 ± 3	200 ± 10	-	170 ± 10	(40)	90 ± 10	220 ± 10	100 ± 10	42 ± 1	(2)	200 ± 10	170 ± 10

SRM 362 (μg g^{-1})	B	Al	P	S	Ti	Ge	As	Se	Zr	Nb	Sn	Sb	Hf	Ta	W
Experimental (n=5, u=2×SE)	26.26 ± 0.63	791 ± 14	339 ± 9.0	324 ± 40	1000 ± 42	9.78 ± 0.31	835 ± 33	11.47 ± 0.51	2058 ± 72	3000 ± 120	182.2 ± 8.5	111.8 ± 5.9	0.529 ± 0.023	1978 ± 67	2253 ± 71
Certified (k=2)	25 ± 1	950 ± 50	410 ± 10	360 ± 3	840 ± 10	(20)	920 ± 50	(12)	1900 ± 100	2900 ± 100	160 ± 10	130 ± 10	(3)	2000 ± 100	2000 ± 100

SRM 363 (μg g^{-1})	B	Al	P	S	Ti	Ge	As	Se	Zr	Nb	Sn	Sb	Hf	Ta	W
Experimental (n=5, u=2×SE)	12.63 ± 0.72	2436 ± 67	243.7 ± 5.4	< 200	515 ± 39	30.3 ± 2.2	92.4 ± 4.3	1.89 ± 0.29	458 ± 35	491 ± 39	991 ± 87	16.1 ± 1.4	0.959 ± 0.071	506 ± 36	481 ± 31
Certified (k=2)	13.1 ± 0.37	2400 ± 100	290 ± 50	68 ± 1	500 ± 10	(100)	100 ± 10	(2)	490 ± 10	490 ± 10	1040 ± 50	20 ± 10	(5)	(530)	460 ± 10

digested on different days. ICP-SFMS measurements for each of the replicates were also carried out on separate days using different calibration standards.

The certified values and information values (in brackets) of the three CRMs are shown in Table 4.3, along with the experimentally determined concentrations for the target elements recovered in fraction T. For those target elements of which the concentrations in the three CRMs are certified, the experimentally determined concentrations were generally found to be in good agreement with the corresponding certified values. The experimentally determined concentrations of B, Al, Ti, As, Zr, Nb, Sn, Sb, Ta and W lay within a range of -7% to $+7\%$ with respect to these certified values for NIST SRM 361, whilst laying in a range of -17% to $+19\%$ of certified values for NIST SRM 362. In the case of NIST SRM 363, they lay within a range of -8% to $+4\%$ for B, Al, Ti, As, Zr, Nb, Sn and W with respect to certified values; excluding a value of *ca.* -20% for Sb (because the relative uncertainty associated with the certified value was 50%). For P, a similar bias was observed for all three CRMs (*ca.* -15%), whilst the attainable procedural QL for S was found to be too high to draw any conclusions for that particular element. Unravelling the reason behind the observed bias for P (*e.g.* loss of volatile species during digestion) was assessed by the author to be beyond the scope of the current study. Information values available for Se were also in good agreement with experimental values for two of the three CRMs, whilst experimental values for Ge and Hf were found to be considerably lower than their respective information values. When analysing mock samples, however, adequate recoveries (see next paragraph) were obtained for both Ge and Hf.

Recoveries of target elements from mock samples, prepared by spiking dissolved T91 steel with multi-element stock solutions, were around 100%, within the reproducibility uncertainty ($k = 2$). For those target elements found to be present in T91 steel at concentrations of no more than $10\,\mu g\,g^{-1}$, the recoveries are shown in Table 4.4. These ranged from 98% for B to 106% for Zr. Most importantly, excellent recoveries were also obtained for both Ge (102%) and Hf (99%), which had not been the case for the three CRMs.

Finally, samples of the three real high-alloy steel types under consideration (T91, 316L and 15-15Ti) were subjected to the optimised procedure. Experimentally determined concentrations of all trace and minor elements recovered from fraction T are presented in Table 4.5, while values for minor and matrix elements recovered from fraction M are presented in Table 4.6 (the latter purely for information purposes). When combining the data presented in Tables 4.5 and 4.6, for the three samples under consideration, quantitative recovery was obtained in each case. None of these high-alloy steel samples (T91, 316L and 15-15Ti) were found to contain measurable levels of Be, S, Se, Hf or Ir.

4.4   Conclusions and outlook

A quick, simple and efficient analyte/matrix separation procedure, facilitating the determination of more than twenty target elements in a high-alloy steel

Table 4.4: Recoveries for target elements, obtained by applying the analyte/matrix separation procedure developed to mock samples prepared from T91 steel. The recoveries of the target elements are expressed as percentages of the amount of spike, added (from multi-element stock solutions) to the dissolved samples, that was recovered. Only those elements for which the initial concentration in T91 steel was found to be $< 10\,\mu g\,g^{-1}$ are presented (amount of spike added is equivalent to $20\,\mu g\,g^{-1}$).

Recovery (%)	Be	B	Ge	Se	Zr	Rh	Pd	Sb	Hf	Ta	Re	Ir	Pt
Spiked T91 (n=5, u=2×SE)	102.4 ± 1.5	98.1 ± 5.0	101.8 ± 6.7	100.1 ± 5.1	105.5 ± 7.0	104.8 ± 7.6	98.5 ± 6.7	100.4 ± 8.1	98.9 ± 4.6	98.6 ± 5.1	99.6 ± 5.4	104.3 ± 5.6	99.0 ± 5.4

Table 4.5: Experimentally determined concentrations of trace and minor elements found in fraction T in three types of steel alloys (T91, 316L and 15-15Ti). The concentrations of Be, S, Se, Hf and Ir were found to lie below the procedural QL in all samples and have therefore not been reported in this table.

Conc. ($\mu g\,g^{-1}$) (n=5, u=2×SE)	B	Al	Si	P	Ti	Ge	As	Zr	Nb	Mo	Rh	Pd	Sn	Sb	Ta	W	Re	Pt
T91	1.09 ± 0.11	50.9 ± 2.3	2132 ± 84	178.0 ± 3.9	14.3 ± 1.1	6.57 ± 0.20	44.57 ± 0.65	< 0.1	691 ± 26	8560 ± 170	0.0128 ± 0.0041	< 0.1	30.52 ± 0.70	7.62 ± 0.20	0.811 ± 0.060	20.14 ± 0.51	1.235 ± 0.021	< 0.2
316L	15.48 ± 0.14	< 20	6750 ± 290	230 ± 10	9.70 ± 0.35	6.67 ± 0.15	70.50 ± 0.89	0.1163 ± 0.0099	6.10 ± 0.29	20160 ± 240	0.0717 ± 0.0091	< 0.1	80.1 ± 2.2	17.51 ± 0.41	0.034 ± 0.019	175.5 ± 2.5	1.276 ± 0.023	0.207 ± 0.014
15-15Ti	45.1 ± 1.2	169.3 ± 4.3	5830 ± 200	95.3 ± 3.1	4110 ± 110	2.295 ± 0.042	11.80 ± 0.15	0.111 ± 0.022	25.2 ± 1.3	12040 ± 220	0.029 ± 0.011	0.125 ± 0.012	5.40 ± 0.18	2.026 ± 0.066	0.1502 ± 0.0074	11.1 ± 1.1	0.619 ± 0.012	< 0.2

Table 4.6: Experimentally determined concentrations of minor and matrix elements found in fraction M in three types of steel alloys (T91, 316L and 15-15Ti).

Conc. ($\mu g\,g^{-1}$) (n=5, u=2×SE)	V	Cr	Mn	Fe	Co	Ni	Cu
T91	2033 ± 21	86 580 ± 660	3736 ± 62	897 000 ± 17 000	109.9 ± 2.2	1165 ± 28	583.4 ± 2.4
316L	599 ± 15	164 100 ± 1200	18 280 ± 320	684 000 ± 13 000	602.1 ± 8.7	97 200 ± 2900	2155 ± 30
15-15Ti	359.2 ± 8.0	149 000 ± 1100	19 120 ± 240	659 000 ± 11 000	190 ± 11	145 600 ± 3700	227 ± 11

matrix, has been successfully developed. The matrix elements Cr, Fe and Ni are retained on an AG 50Wx8 cation exchange resin, whilst all of the the target elements elute rapidly. With the proposed procedure, Be, B, Al, Si, P, S, Ti, Ge, As, Se, Zr, Nb, Mo, Rh, Pd, Sn, Sb, Hf, Ta, W, Re, Ir and Pt can be isolated from the matrix elements Cr, Fe and Ni. In the case of Fe and Ni, matrix separation efficiency is >99.9 %, whilst for Cr it is limited to >90 %. Overall, around 97.5 % of the total matrix could be separated from the target elements for the three high-alloy steels under consideration (T91, 316L, 15-15Ti).

The optimised procedure was validated by analysing (i) steel alloy CRMs, (ii) mock samples and (iii) real high-alloy steels. Experimental results were generally found to be in good agreement with certified values, for all three CRMs, whilst spike recoveries were around 100 % when analysing mock samples. Procedural QLs ($10s$) were determined by analysing procedural blanks, which resulted in optimum values at low $ng\,g^{-1}$ levels for both Re and Hf. Finally, the procedure developed was applied to real steel alloy samples.

The procedure developed in this work was aimed specifically at the analysis of T91, 316L and 15-15Ti high-alloy steels, alloys with a high Cr, Fe and Ni content. Self-evidently, however, the procedure can also be applied to other types of alloys or even other types of samples, such as iron meteorites or high-purity Fe and Ni.

4.5   Appendix

The affinity of B, Al, P, Ti, V, Mn, Fe, Co, Ni, Cu, As, Mo, Zr, Nb, Ta and W, towards the AG 50Wx8 resin, in acidic media, was investigated as described in section 4.3.1. Elution profiles obtained for each of these elements, using a variety of HNO_3, HCl and HF-based eluents, are shown in Figures 4.9 - 4.24, respectively. Varying the concentration of any acid in the eluent, whilst keeping the concentrations of the other two constant, was found to have no discernible or only a limited impact on the elution profiles of B, P, As, Nb or Ta. Each of these elements could be quantitatively recovered from the first 4 to 8 mL of eluate, using any of the eluents under consideration. In addition, varying either the HNO_3 or HCl concentration in the eluent was found to have little impact on the elution profiles of Ti, Zr, Mo or W. However, at higher HF concentrations, these elements were eluted more rapidly (especially Ti and Zr). Conversely, the adsorbability of Al on the AG 50Wx8 resin was found to be higher at low HNO_3, HF and HCl concentrations. However, by increasing any of the acid concentrations in the eluent, Al could be stripped from the cation-exchanger. Furthermore, it was found that the first row transition metals V, Mn, Fe, Co, Ni and Cu could be retained on the resin when the eluent contained only ≤ 0.75 M HNO_3, whilst an eluent containing 4.5 M HNO_3 resulted in rapid elution of these elements. The use of up to 1.2 M HCl in the eluent was not found to impede their retention on the resin, with the exception of V. Moreover, the use of higher HF concentrations in the eluent was found to have little impact on the elution profiles of any of these elements. Lastly, although no reliable elution profiles could be

constructed for Cr, as was already mentioned before, its behaviour was assumed to be similar to the previously mentioned series of first row transition metals.

Examples of elution profiles, for a larger number of elements, obtained by applying the analyte/matrix separation protocol to mock samples prepared from T91, 316L and 15-15Ti steel, are shown in Figures 4.25, 4.26 and 4.27.
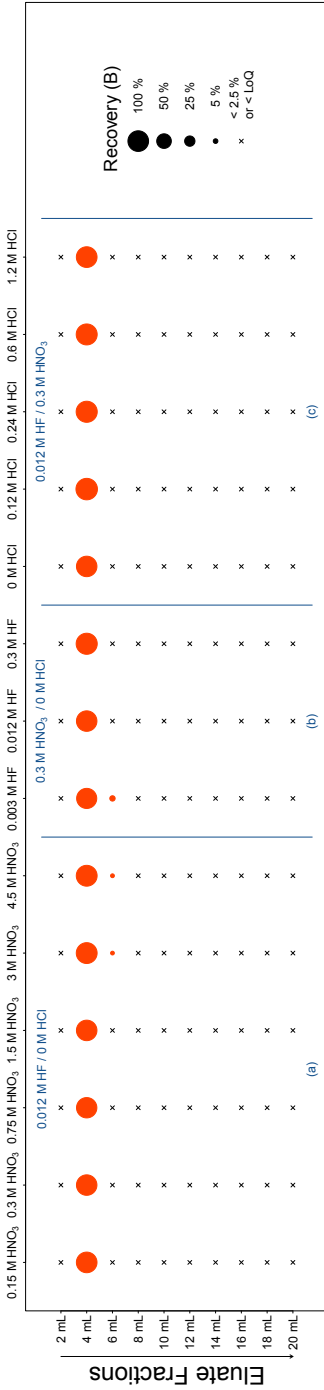
Figure 4.9: Isocratic elution profiles of B obtained upon loading $1\,\text{mL}$ of a synthetic sample, containing $ca.\ 0.2\,\text{mg}\,\text{L}^{-1}$ B, onto a $5\,\text{mL}$ AG 50W×8 column. For each of the different eluents investigated, the elution profile is represented as a series of circles, the areas of which are proportional to the recovery of an element in each respective fraction.

Figure 4.10: Isocratic elution profiles of Al obtained upon loading $1\,\text{mL}$ of a synthetic sample, containing $ca.\ 0.2\,\text{mg}\,\text{L}^{-1}$ Al, onto a $5\,\text{mL}$ AG 50W×8 column. For each of the different eluents investigated, the elution profile is represented as a series of circles, the areas of which are proportional to the recovery of an element in each respective fraction.

Figure 4.11: Isocratic elution profiles of P obtained upon loading $1\,mL$ of a synthetic sample, containing *ca.* $0.2\,mg\,L^{-1}$ P, onto a $5\,mL$ AG 50W×8 column. For each of the different eluents investigated, the elution profile is represented as a series of circles, the areas of which are proportional to the recovery of an element in each respective fraction.

Figure 4.12: Isocratic elution profiles of Ti obtained upon loading $1\,mL$ of a synthetic sample, containing *ca.* $0.2\,mg\,L^{-1}$ Ti, onto a $5\,mL$ AG 50W×8 column. For each of the different eluents investigated, the elution profile is represented as a series of circles, the areas of which are proportional to the recovery of an element in each respective fraction.

Figure 4.13: Isocratic elution profiles of V obtained upon loading 1 mL of a synthetic sample, containing *ca.* $0.2\,\mathrm{mg\,L^{-1}}$ V, onto a $5\,\mathrm{mL}$ AG 50W×8 column. For each of the different eluents investigated, the elution profile is represented as a series of circles, the areas of which are proportional to the recovery of an element in each respective fraction.

Figure 4.14: Isocratic elution profiles of Mn obtained upon loading 1 mL of a synthetic sample, containing *ca.* $0.2\,\mathrm{mg\,L^{-1}}$ Mn, onto a $5\,\mathrm{mL}$ AG 50W×8 column. For each of the different eluents investigated, the elution profile is represented as a series of circles, the areas of which are proportional to the recovery of an element in each respective fraction.
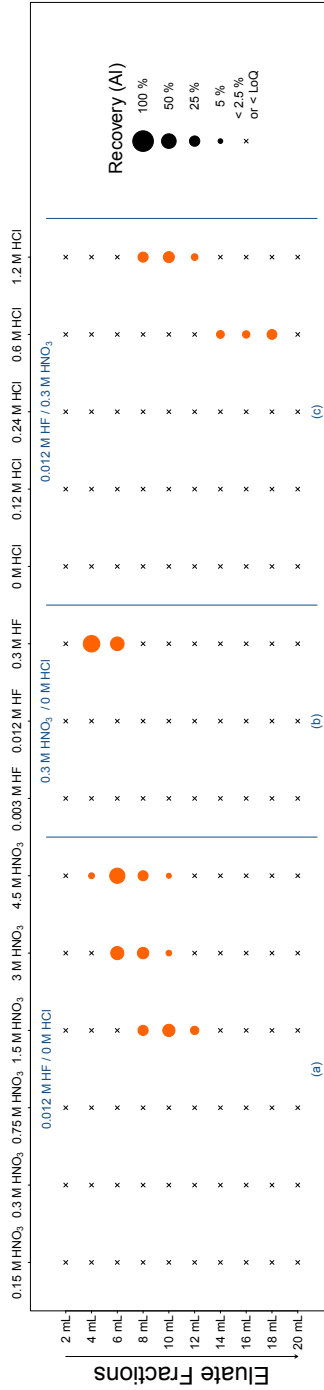
Figure 4.15: Isocratic elution profiles of Fe obtained upon loading 1 mL of a synthetic sample, containing *ca.* 2 mg L^{-1} Fe, onto a 5 mL AG 50W×8 column. For each of the different eluents investigated, the elution profile is represented as a series of circles, the areas of which are proportional to the recovery of an element in each respective fraction.
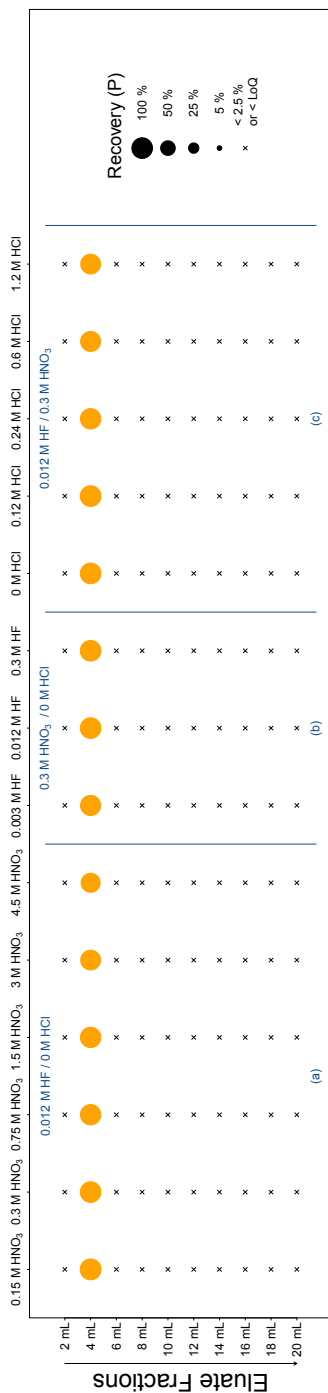

Figure 4.16: Isocratic elution profiles of Co obtained upon loading 1 mL of a synthetic sample, containing *ca.* 0.2 mg L^{-1} Co, onto a 5 mL AG 50W×8 column. For each of the different eluents investigated, the elution profile is represented as a series of circles, the areas of which are proportional to the recovery of an element in each respective fraction.

Figure 4.17: Isocratic elution profiles of Ni obtained upon loading $1\,\mathrm{mL}$ of a synthetic sample, containing $ca.\ 0.2\,\mathrm{mg\,L^{-1}}$ Ni, onto a $5\,\mathrm{mL}$ AG 50W×8 column. For each of the different eluents investigated, the elution profile is represented as a series of circles, the areas of which are proportional to the recovery of an element in each respective fraction.
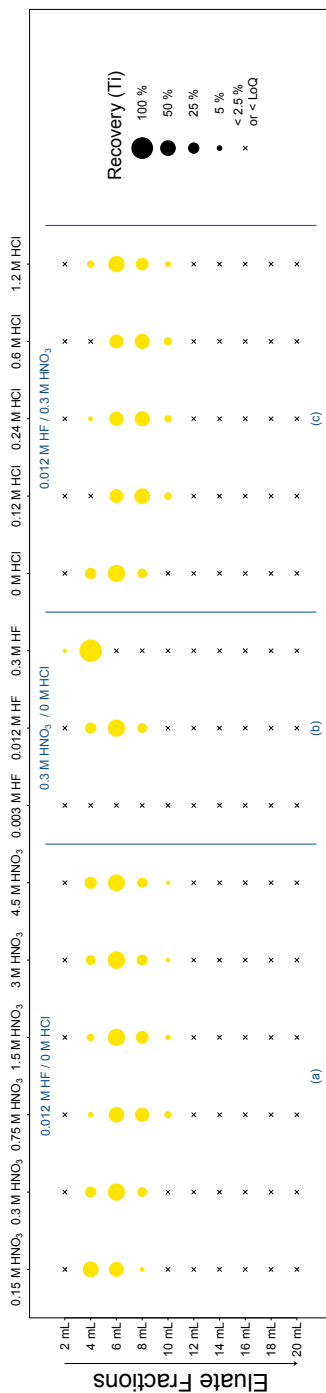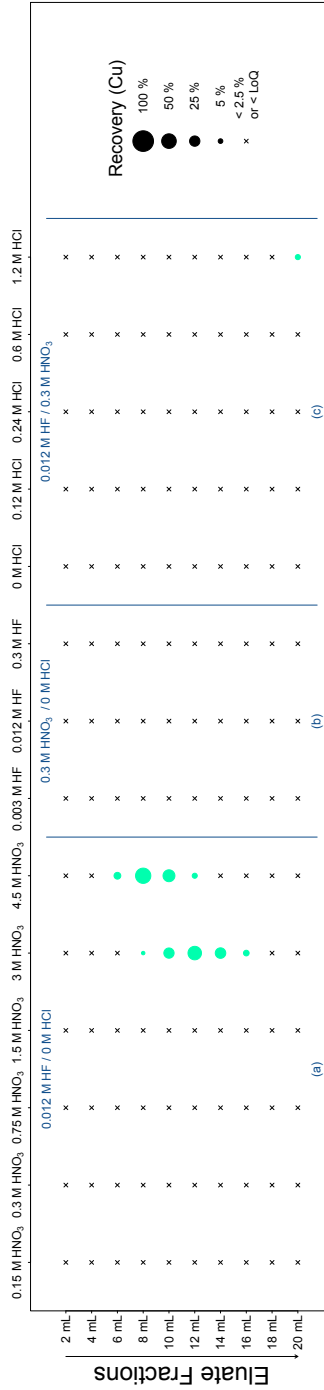

Figure 4.18: Isocratic elution profiles of Cu obtained upon loading $1\,\mathrm{mL}$ of a synthetic sample, containing $ca.\ 0.2\,\mathrm{mg\,L^{-1}}$ Cu, onto a $5\,\mathrm{mL}$ AG 50W×8 column. For each of the different eluents investigated, the elution profile is represented as a series of circles, the areas of which are proportional to the recovery of an element in each respective fraction.
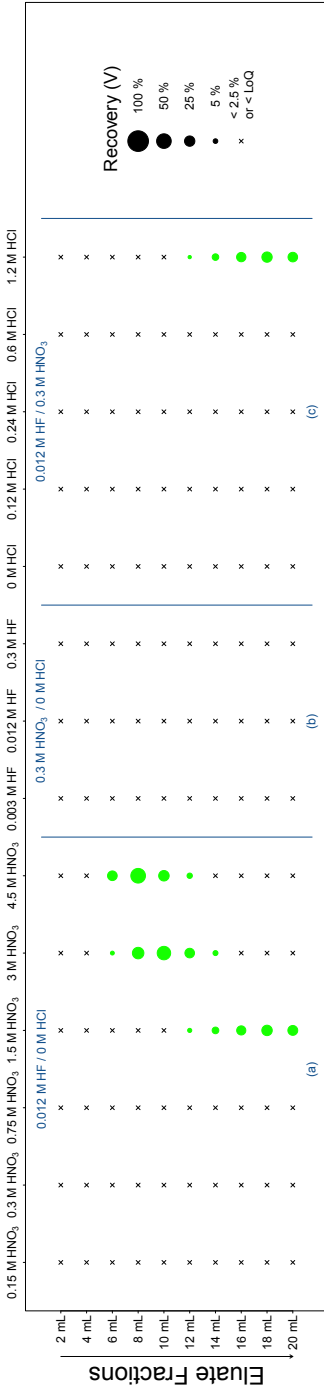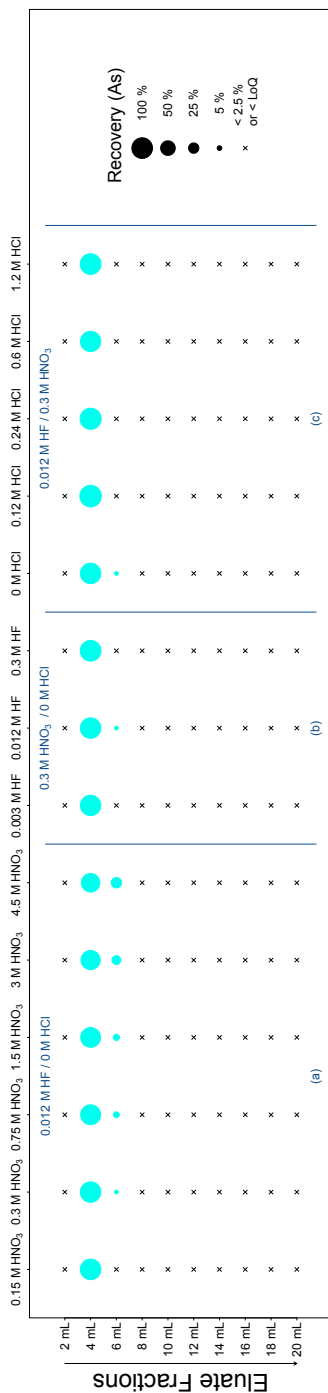
Figure 4.19: Isocratic elution profiles of As obtained upon loading $1\,mL$ of a synthetic sample, containing *ca.* $0.2\,mg\,L^{-1}$ As, onto a $5\,mL$ AG 50W×8 column. For each of the different eluents investigated, the elution profile is represented as a series of circles, the areas of which are proportional to the recovery of an element in each respective fraction.
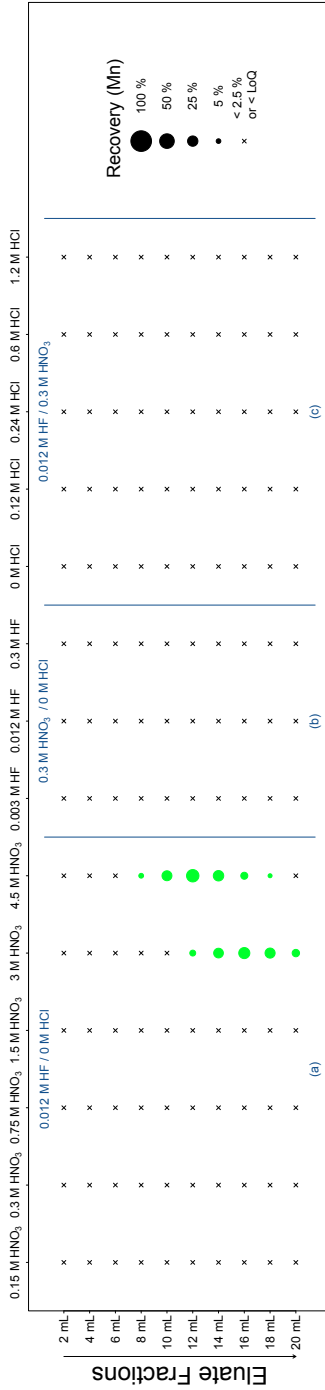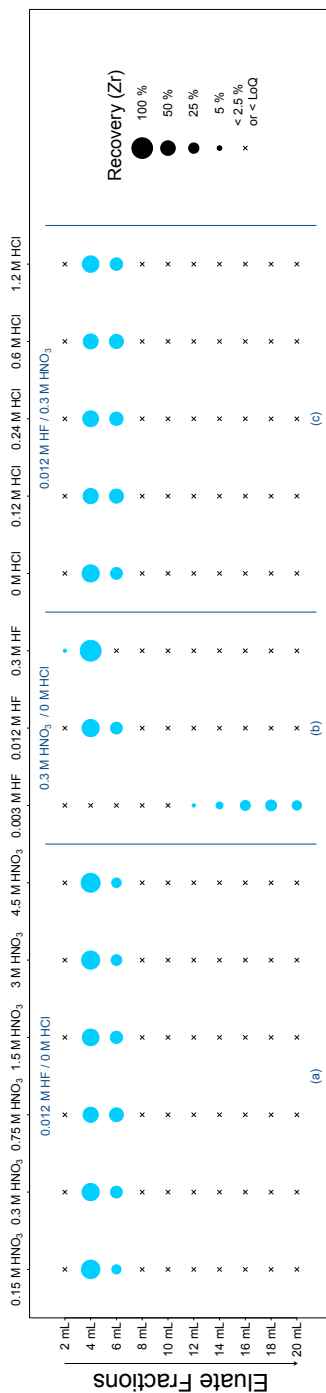

Figure 4.20: Isocratic elution profiles of Zr obtained upon loading $1\,mL$ of a synthetic sample, containing *ca.* $0.2\,mg\,L^{-1}$ Zr, onto a $5\,mL$ AG 50W×8 column. For each of the different eluents investigated, the elution profile is represented as a series of circles, the areas of which are proportional to the recovery of an element in each respective fraction.
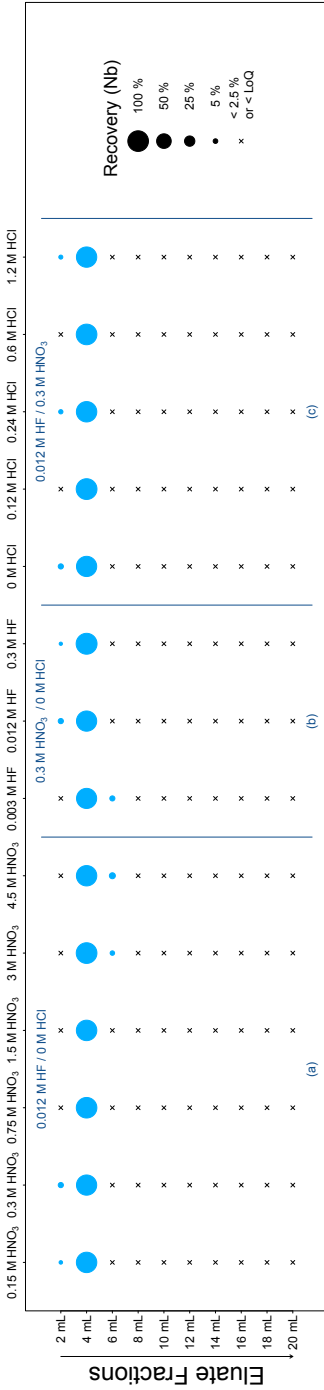
Figure 4.21: Isocratic elution profiles of Nb obtained upon loading 1 mL of a synthetic sample, containing *ca.* $0.2\,\mathrm{mg\,L^{-1}}$ Nb, onto a $5\,\mathrm{mL}$ AG 50W×8 column. For each of the different eluents investigated, the elution profile is represented as a series of circles, the areas of which are proportional to the recovery of an element in each respective fraction.
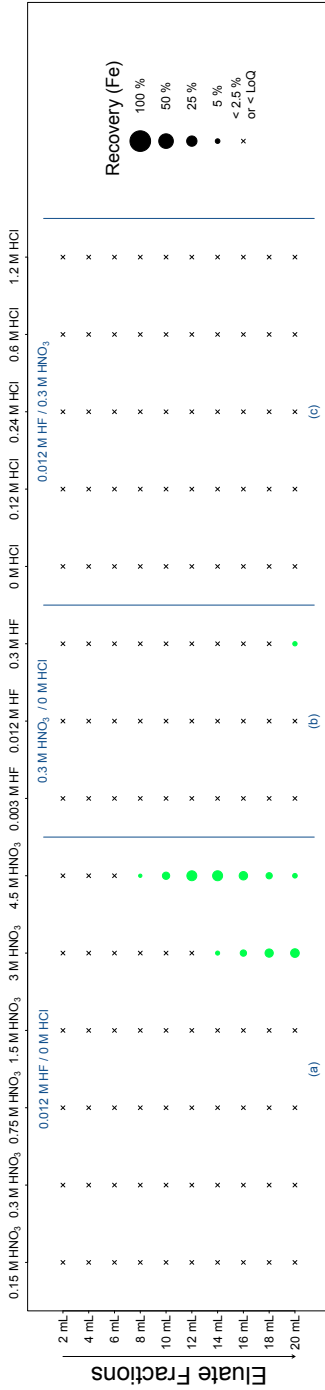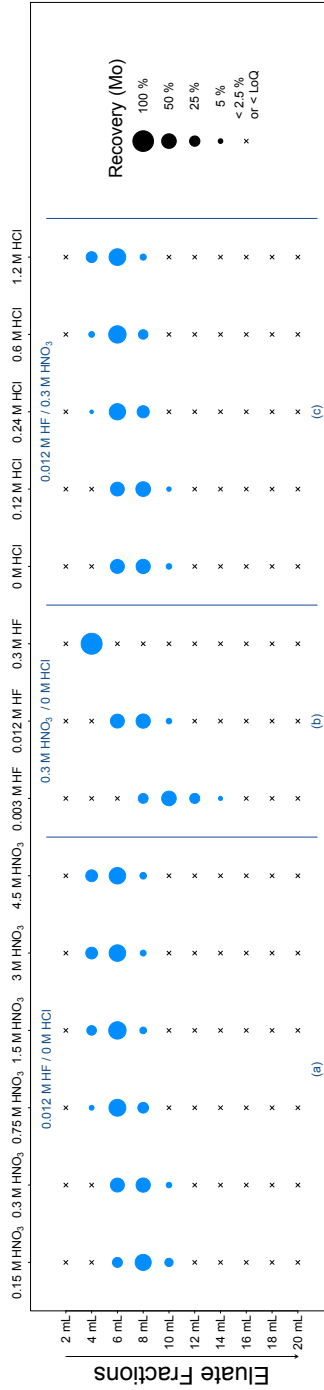

Figure 4.22: Isocratic elution profiles of Mo obtained upon loading 1 mL of a synthetic sample, containing *ca.* $0.2\,\mathrm{mg\,L^{-1}}$ Mo, onto a $5\,\mathrm{mL}$ AG 50W×8 column. For each of the different eluents investigated, the elution profile is represented as a series of circles, the areas of which are proportional to the recovery of an element in each respective fraction.
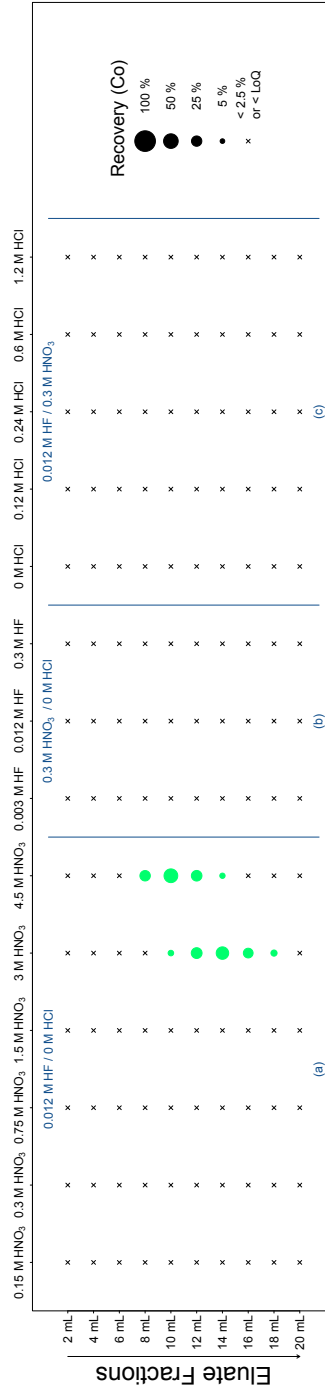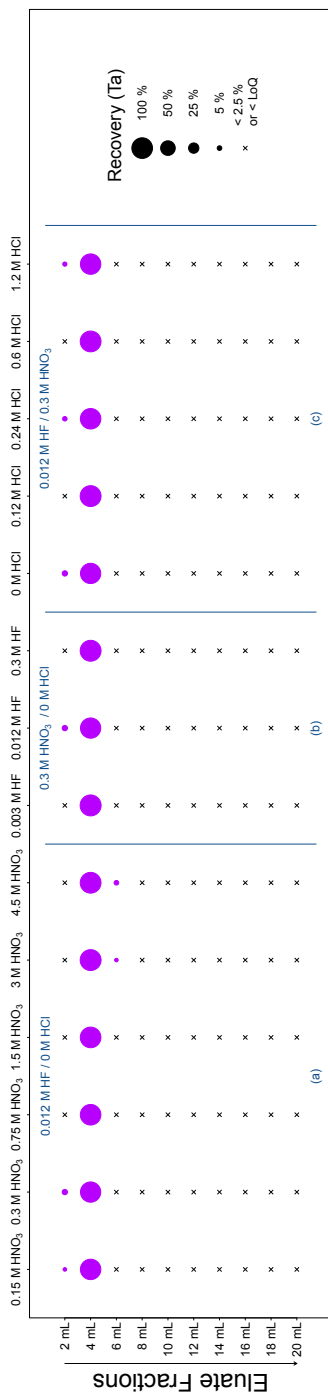
Figure 4.23: Isocratic elution profiles of Ta obtained upon loading 1 mL of a synthetic sample, containing *ca.* $0.2\,\mathrm{mg\,L^{-1}}$ Ta, onto a $5\,\mathrm{mL}$ AG 50W×8 column. For each of the different eluents investigated, the elution profile is represented as a series of circles, the areas of which are proportional to the recovery of an element in each respective fraction.
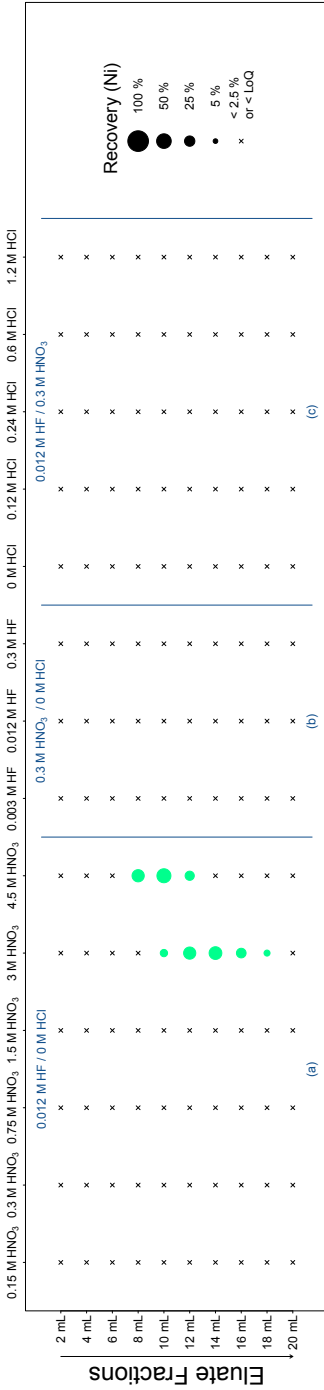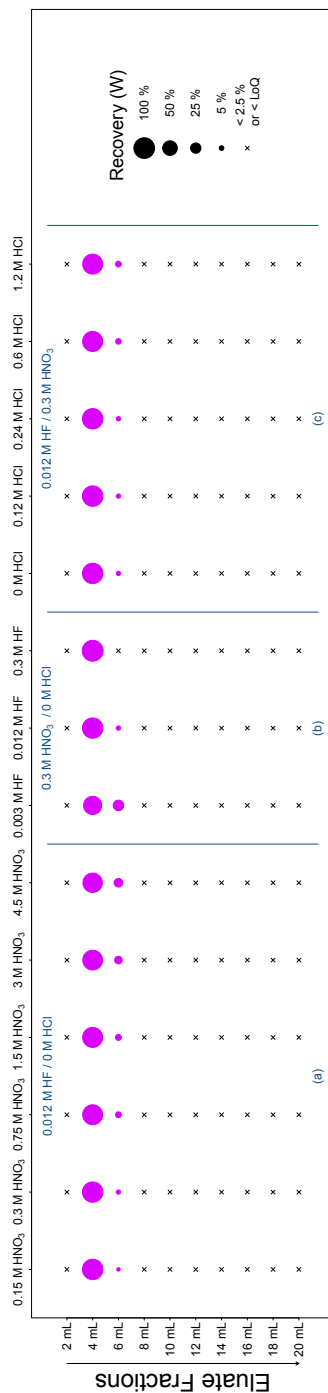

Figure 4.24: Isocratic elution profiles of W obtained upon loading 1 mL of a synthetic sample, containing *ca.* $0.2\,\mathrm{mg\,L^{-1}}$ W, onto a $5\,\mathrm{mL}$ AG 50W×8 column. For each of the different eluents investigated, the elution profile is represented as a series of circles, the areas of which are proportional to the recovery of an element in each respective fraction.

Figure 4.25: Gradient elution profiles for all elements of interest, obtained by applying the procedure developed to a mock sample prepared from T91 high-alloy steel. This mock sample was prepared such that it contained 10 000 - 20 000 mg L^{-1} Fe and acid concentratiosn of, at most, 1.5 M HNO$_3$, 1.2 M HCl and 0.3 M HF. For each element, the elution profile is represented as a series of circles, the areas of which are proportional to the recovery in each respective fraction. The eluent used corresponds to the fractions collected as follows: [2 mL] 1 mL Sample + 1 mL 0.15 M HNO$_3$ / 0.3 M HF; [4 mL - 10 mL] 4 × 2 mL 0.15 M HNO$_3$ / 0.3 M HF; [20 mL - 40 mL] 3 × 10 mL 7.5 M HNO$_3$ / 0.3 M HF.
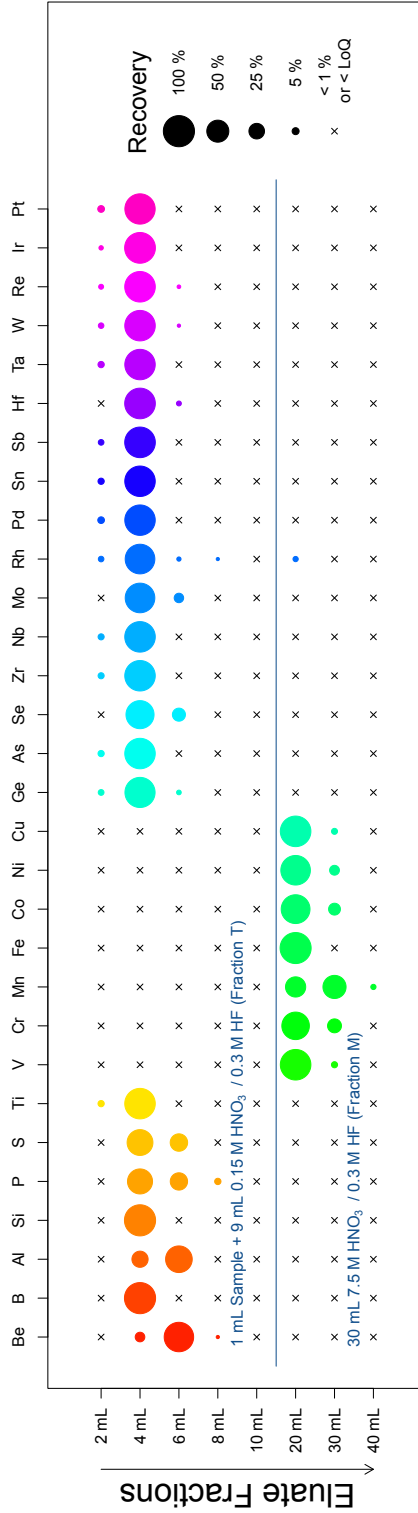
Figure 4.26: Gradient elution profiles for all elements of interest, obtained by applying the procedure developed to a mock sample prepared from 316L high-alloy steel. This mock sample was prepared such that it contained $10\,000 - 20\,000\,\mathrm{mg\,L^{-1}}$ Fe and acid concentratiosn of, at most, $1.5\,\mathrm{M\,HNO_3}$, $1.2\,\mathrm{M\,HCl}$ and $0.3\,\mathrm{M\,HF}$. For each element, the elution profile is represented as a series of circles, the areas of which are proportional to the recovery in each respective fraction. The eluent used corresponds to the fractions collected as follows: $[2\,\mathrm{mL}]$ $1\,\mathrm{mL}$ Sample $+ 1\,\mathrm{mL}$ $0.15\,\mathrm{M\,HNO_3}$ / $0.3\,\mathrm{M\,HF}$; $[4\,\mathrm{mL} - 10\,\mathrm{mL}]$ $4 \times 2\,\mathrm{mL}$ $0.15\,\mathrm{M\,HNO_3}$ / $0.3\,\mathrm{M\,HF}$; $[20\,\mathrm{mL} - 40\,\mathrm{mL}]$ $3 \times 10\,\mathrm{mL}$ $7.5\,\mathrm{M\,HNO_3}$ / $0.3\,\mathrm{M\,HF}$.
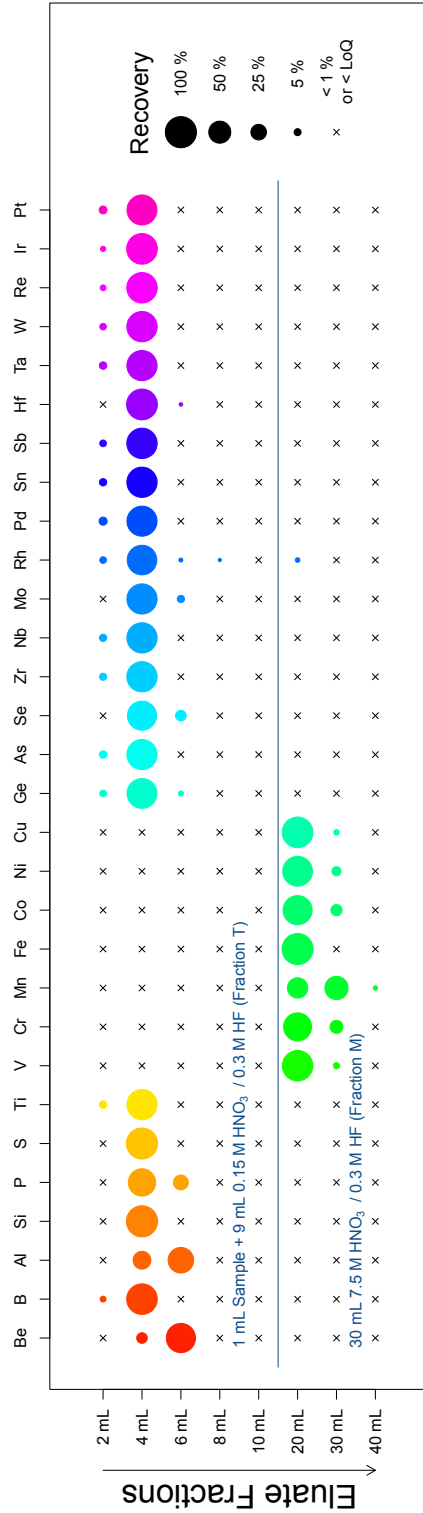
Figure 4.27: Gradient elution profiles for all elements of interest, obtained by applying the procedure developed to a mock sample prepared from 15-15Ti high-alloy steel. This mock sample was prepared such that it contained 10 000 - 20 000 mg L^{-1} Fe and acid concentratiosn of, at most, 1.5 M HNO$_3$, 1.2 M HCl and 0.3 M HF. For each element, the elution profile is represented as a series of circles, the areas of which are proportional to the recovery in each respective fraction. The eluent us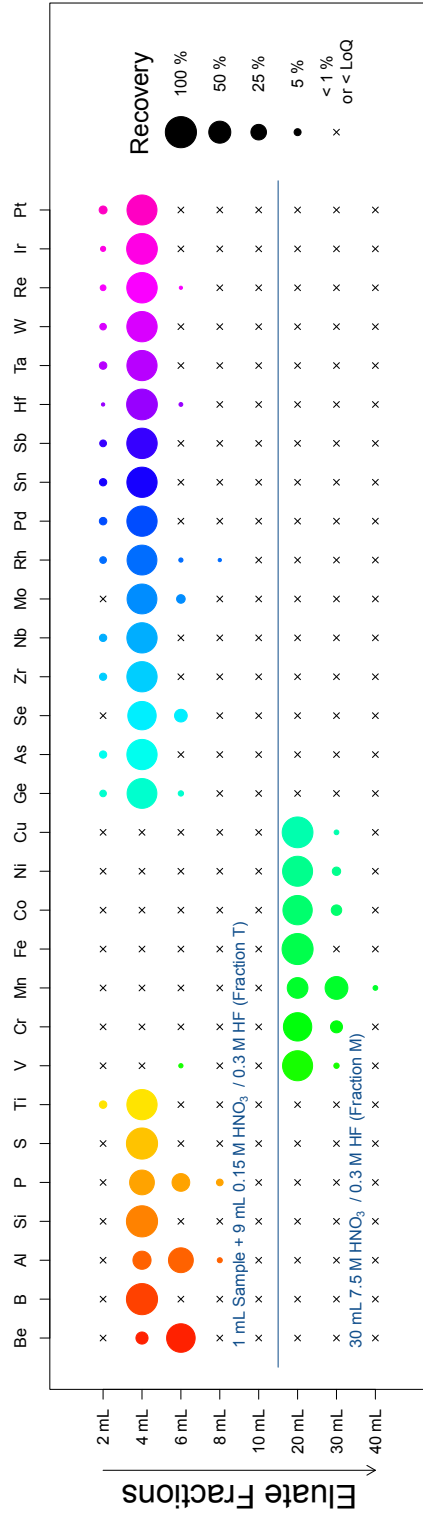ed corresponds to the fractions collected as follows: [2 mL] 1 mL Sample + 1 mL 0.15 M HNO$_3$ / 0.3 M HF; [4 mL - 10 mL] 4 × 2 mL 0.15 M HNO$_3$ / 0.3 M HF; [20 mL - 40 mL] 3 × 10 mL 7.5 M HNO$_3$ / 0.3 M HF.

5

Multi-elemental trace analysis of lead-bismuth eutectic

In this chapter, the development and application of an analytical procedure for the determination of trace elements in *Lead-Bismuth Eutectic* (LBE), by means of ICP-SFMS, is described. Whereas the multi-elemental trace analysis of T91, 316L and 15-15Ti high-alloy steels was the subject of Chapter 4, this chapter deals with the determination of trace elements in the MYRRHA reactor's heavy liquid metal coolant, which is to be in direct physical contact with the steel alloys investigated previously (see Section 1.1.4). Photographs of two solidified LBE samples are shown in Figure 5.1. As was the case for high-alloy steel samples, the accurate and precise analysis of LBE samples by means of ICP-MS is hampered by the occurrence of spectral and non-spectral interferences (see Section 2.9). However, compared to steel alloys, the LBE matrix is a fairly simple one, consisting mainly of Pb (*ca.* 45 wt.%) and Bi (*ca.* 55 wt.%). As a result, the formation of matrix-induced spectral interferents becomes more predictable and therefore, less troublesome. Nonetheless, non-spectral interferences still impede the accurate determination of trace elements in this type of a matrix. As already stated, the occurrence and manifestation of these matrix effects may be particularly difficult to predict *a priori*. On one occasion, when analysing a solution containing *ca.* 40 mg L^{-1} of both Pb and Bi, a signal suppression of *ca.* 20 % was encountered, whilst a signal enhancement of equal magnitude was observed on a different occasion (albeit using a different sample introduction system). Therefore, it was deemed desirable also to perform an analyte/matrix separation prior to analysing digested LBE samples by means of ICP-SFMS. Firstly, however, a list of potentially relevant target elements had to be compiled.

(a) LBE ingot.   (b) LBE rods.

Figure 5.1: Lead-bismuth eutectic samples.

The first row transition elements V, Cr, Mn, Fe, Ni, as well as Nb and Mo, are common alloying elements in high-alloy steels such as T91, 316L and 15-15Ti (see Chapter 4). Corrosion products taken up by the LBE are therefore likely to consist of a number of these elements. In addition, the elements Ti, Cu, Ag, Cd and Tl are common impurities found inherently in LBE. Any of the elements above could give rise to unwanted radiotoxic nuclides, due to exposure to neutron radiation, or could otherwise hamper reactor operation. Furthermore, the determination of radionuclides of Co, Tc, Te, Po, Th, U and Pu will also be important in the future, in the context of safety and radiation protection. In this study, naturally occurring nuclides of these elements (*e.g.* [59]Co) or chemical analogues (*e.g.* Re, Te, Ce) were considered as proxies for their radionuclidic counterparts (*e.g.* [60]Co, Tc, Po, Pu). Taking all of the above into account, a list of potentially relevant target elements consisting of Ti, V, Cr, Mn, Fe, Co, Ni, Cu, Nb, Mo, Ag, Cd, Te, Ce, Re, Tl, Th and U was arrived at. These elements, expected to be present at $\mu g\,g^{-1}$ or sub-$\mu g\,g^{-1}$ levels in the solid material, had to be determined in the presence of a vast excess of the matrix elements Pb and Bi. A second chromatographic analyte/matrix separation protocol was therefore devised, to separate selectively both Pb and Bi from the target elements listed above. The development, validation and application of this highly selective analyte/matrix separation procedure is discussed below. Portions of this chapter have been published previously in Tindemans *et al.*[1]

5.1   Introduction

A suitable analyte/matrix separation procedure, facilitating the accurate trace analysis of LBE samples by means of ICP-SFMS, ought to be capable of selectively removing macro quantities of both Pb and Bi from a wide variety of target elements including Ti, V, Cr, Mn, Fe, Co, Ni, Cu, Nb, Mo, Ag, Cd, Te, Ce, Re, Tl, Th and U. As in Chapter 4, column chromatography was considered for this purpose, due to its simplicity and relative ease of use. Although only two matrix elements need to be isolated, compared to the case of the high-alloy steels, accomplishing this proved to be somewhat more problematic. To complicate matters further, for reasons already discussed in Section 4.1, the use of HCl had to be avoided. As such, to the best of the author's knowledge, whilst respecting the above requirements, no single chromatographic resin was believed capable of selectively removing macro quantities of both Pb and Bi from such a wide variety of target elements. Consequently, two separate chromatographic resins had to be selected, each capable of retaining either Pb or Bi in an HNO_3/HF-based medium, whilst having only a limited affinity towards most of the target elements.

AG 1x4 is a strongly basic anion-exchange resin with quaternary ammonium functional groups attached to a 4 % cross-linked styrene-divinylbenzene copolymer lattice (see Figure 5.2a), which ought to retain Bi selectively in dilute HNO_3 media. Nelson *et al.* first studied the adsorbability of both Bi and Pb on a similar resin (Dowex 1), in HNO_3 as well as in HCl media. They demonstrated that, in

HNO$_3$ media, the anion-exchange resin exhibits only a limited affinity towards Pb, but a more pronounced affinity towards Bi. Their results suggested that at least one type of negatively charged Bi-nitrate complex is present in nitric acid media, probably one with four nitrate ligands. Conversely, retention of Pb in dilute HNO$_3$ media was so limited that, in that study, only the essentially unretained elements or the very strongly retained elements could be separated from Pb. In dilute HCl media, in contrast, the maximum adsorbability of Pb and Bi was shown to be considerably higher than in HNO$_3$ media. A decade later, Faris *et al.* reported distribution coefficients, for a large number of elements, for a strongly basic anion-exchange resin (Dowex 1x10) over a wide range of HNO$_3$ concentrations. Their data suggest that, apart from the matrix element Bi, out of all the target elements, only Mo, Ce, Re, Tl, Th and U would show any appreciable retention on a similar anion-exchange resin in HNO$_3$-based media. [133–135]

The Pb Spec extraction chromatographic resin was first developed by Horwitz *et al.*, for the isolation of Pb from geological samples. The active component of this resin is a crown ether, *i.e.* di-(tert-butylcyclohexano)-18-crown-6 (see Figure 5.2b), in an isodecanol solution sorbed onto an inert polymeric support. Previously, Horwitz *et al.* had also described the Sr Spec resin, which contained the same crown ether at a higher concentration, but which utilised octanol instead of isodecanol as a diluent. At the time, this resin was shown to exhibit a remarkably high affinity towards Sr and Pb in HNO$_3$ media, so high that it was very difficult to strip Pb from the resin. By using a higher molecular weight alcohol diluent, such as isodecanol, instead of octanol, Pb could be stripped more easily from the resin, while the resin's affinity towards Pb still remained relatively high. Still, in order to be able to efficiently strip away macro quantities of Pb from a Pb Spec column, the authors had to use a 0.1 M ammonium citrate eluent. Thus far, the Pb Spec resin has been applied mainly to the highly selective preconcentration of trace amounts of Pb isotopes from a variety of matrices, although Yourd *et al.* successfully developed an online analyte/matrix separation procedure for the determination of trace elements in Pb bullets for forensic purposes. [136–142]
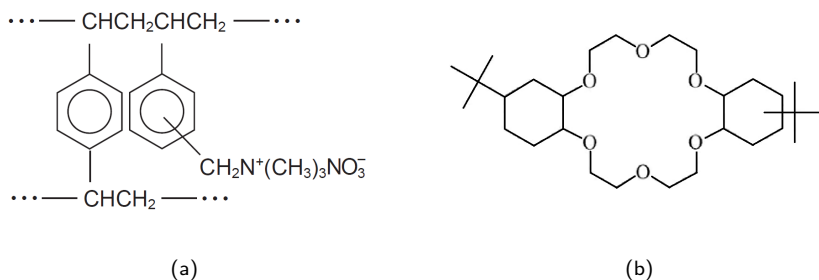
Figure 5.2: (a) A styrene-divinylbenzene copolymer lattice with quaternary ammonium functional groups, such as the AG 1x4 anion-exchange resin, in the nitrate form. (b) The active component of Pb Spec and Sr Spec extraction chromatographic resins (di-(tert-butylcyclohexano)-18-crown-6). [126]

5.2   Experimental

The reagents and labware employed in the preparation of blanks, standards, samples and eluents have been described previously in Chapter 3. That chapter also included an overview of typical instrumental parameters of the Element2 and XSeries2 ICP-MS units. For the specific purposes of these experiments, the sample introduction system of the Element2 ICP-SFMS included a water-cooled glass double-pass Scott-type spray chamber or, on one occasion, a glass cyclonic spray chamber. In addition, a T-piece, positioned just before the nebuliser, was used to mix online the flows of the sample line and the internal standard line, both pumped, in a 1:1 ratio. Unless stated otherwise, all quantitative measurements were performed using this Element2 unit. The ICP-SFMS instrument's relevant data acquisition parameters are discussed below, followed by a detailed description of the relevant sample pretreatment procedures.

5.2.1   Data acquisition parameters

The elements Sc, Y, Rh, Lu, Ir and Th were monitored as internal standards, in at least one resolution mode, because these cover the greater part of the mass range (see Section 2.9.2.2). The nuclides of Ni, Cu, Nb, Mo, Ag, Cd, Te, Ce, Re, Tl, Pb, Bi, Th, U and those of Ti, V, Cr, Mn, Fe, Co were measured in the low and medium resolution mode, respectively. In the case of the target elements, two of the most abundant nuclides, free from isobaric interference, were monitored whenever possible. Generally speaking, the most abundant nuclide was used for quantitative purposes. Typical data acquisition parameters are summarised in Table 5.1. Calibration standards and dilutions were prepared such that the instrument's detector was always able to operate in the pulse counting mode for quantitative analysis.

Table 5.1: Typical data acquisition parameters for the Element2 ICP-SFMS

Setting/parameter	Value/Description	
Resolution ($m/\Delta m$)	300	4000
Runs	6	5-6
Passes	12-20	10-12
Dwell time	10 ms	20 ms
Mass window	5-60 %	90-100 %
Integration window	5-10 %	40-60 %
Samples per peak	100-25	25-20
Element Nuclides	^{60}Ni, ^{62}Ni, ^{63}Cu, ^{65}Cu, ^{93}Nb, ^{95}Mo, ^{98}Mo, ^{107}Ag, ^{109}Ag, ^{110}Cd, ^{111}Cd, ^{125}Te, ^{126}Te, ^{140}Ce, ^{142}Ce, ^{185}Re, ^{187}Re, ^{203}Tl, ^{205}Tl, ^{206}Pb, ^{207}Pb, ^{208}Pb, ^{209}Bi, ^{232}Th, ^{238}U	^{47}Ti, ^{49}Ti, ^{51}V, ^{52}Cr, ^{53}Cr, ^{55}Mn, ^{56}Fe, ^{57}Fe, ^{59}Co
Internal standard nuclides	^{45}Sc, ^{89}Y, ^{103}Rh, ^{175}Lu, ^{193}Ir, ^{232}Th	^{45}Sc, ^{89}Y

5.2.2 Sample preparation procedures

Simple "Synthetic" samples, used in exploratory experiments, were prepared by volumetric serial dilution of multi-element and single-element (in the case of Cr, Fe, Ni, Cu) stock solutions, in such a way that the final sample solution contained *ca.* $2\,mg\,L^{-1}$ of Cr, Fe, Ni, Cu and $0.2\,mg\,L^{-1}$ of each other element.

"Mock" samples were prepared by digesting high-purity Pb and Bi powders, in the same ratio as in LBE, and spiking the resulting solution with small amounts of the target elements. For digestion, *ca.* 0.45 g of Pb powder and *ca.* 0.55 g of Bi powder were weighed accurately in a sealable PTFE digestion vessel. UP water and an aliquot of a solution containing the target elements were then pipetted into this vessel (totaling 2.25 mL), followed by 0.25 mL of 0.25 M HF and 2.5 mL of concentrated HNO_3. This generally initiated an almost instantaneous reaction, the sample solution then being left to stand for at least 1 h. On the few occasions where there was no spontaneous reaction, the solution was heated gently on a hotplate at *ca.* 50 to 75 °C for at least 1 h. Once all apparent reaction had ceased, another 5 mL of UP water was added. If still opaque at that point, the solution would then become clear, revealing a silvery-grey residue. The closed digestion vessel was then placed on a hotplate at *ca.* 125 to 150 °C, for at least 2 h, until the remaining residue was found to be completely dissolved upon visual inspection. The solution was then left to cool and a further 15 mL of UP water was added before reweighing the vessel. The resulting solution contained *ca.* $20\,000\,mg\,L^{-1}$ of Pb and of Bi and *ca.* 0.02 to $0.2\,mg\,L^{-1}$ of the target elements, depending on the amount of spike added, in a dilute acidic matrix consisting of, at most, $1.5\,M\,HNO_3$ and 2.5 mM HF. The amount of spike added was equivalent to *ca.* 0.5 to $5\,\mu g\,g^{-1}$ of each of the target elements in a solid LBE sample.

"Real" LBE samples were prepared in the same way as mock samples, except that chunks of LBE (1 g) were digested and that no target element spike was added. Pb-matrix certified reference materials were also dissolved in a similar fashion, although in this case only *ca.* 0.5 g of material was placed in the sealable PTFE digestion vessel. This ensured that the final Pb concentration in solution was approximately $20\,000\,mg\,L^{-1}$, as it would have been for a real sample. Finally, procedural blanks were also prepared in the same way, except that no actual solid material was transferred into the digestion vessel.

5.3 Results and discussion

The Pb Spec extraction chromatographic resin and the AG 1x4 anion-exchange resin were selected for the development of a highly-selective analyte/matrix chromatographic separation procedure, which would facilitate the multi-elemental trace analysis of LBE samples by means of ICP-SFMS. However, it had already become apparent that neither resin, on its own, could be used for the removal of both Pb and Bi in HNO_3 media. As a result, the use of a tandem-column setup had to be considered, whereby one column loaded with Pb Spec resin was

suspended above a second column, loaded with AG 1x4 resin, for the sequential removal of Pb and Bi. Although a literature review indicated that few of the target elements should exhibit any significant affinity towards either resin in HNO_3 media, these assumptions were first corroborated through a series of simple experiments, for each resin individually. In these tests, the result of adding small amounts of HF to the HNO_3-based eluent was also investigated, since its use was deemed essential to keep Nb stable in solution. In addition, whereas it could be assumed that Pb would be very strongly sorbed on Pb Spec Resin, the AG 1x4 resin's affinity towards Bi was less clear cut and evaluating its applicability and effectiveness required further investigation. The results of these experiments were then used to develop the analyte/matrix separation protocol, which is based on a combination of extraction chromatography and anion-exchange chromatography. The procedure was then optimised in terms of (i) the mineral acid concentrations in the eluents, (ii) the chromatographic column sizes and (iii) the timing of the uncoupling of the tandem-column setup (after which both columns can be eluted further individually). Finally, the procedure was validated for a number of elements and then applied to real samples.

5.3.1   Development of an analyte/matrix separation procedure

The adsorbability of the matrix elements Pb, Bi and the target elements Ti, V, Cr, Mn, Fe, Co, Ni, Cu, Nb, Mo, Ag, Cd, Te, Ce, Re, Tl, Th, U onto the Pb Spec and the AG 1x4 resins was investigated in dilute HNO_3/HF media. Their elution behaviour was studied by loading a 1 mL aliquot of a synthetic sample onto either a Pb Spec or AG 1x4 column. The synthetic samples were then eluted using a range of eluents with different HNO_3 (0.15 M, 0.3 M, 0.75 M, 1.5 M, 3 M, 4.5 M) and HF (0.003 M, 0.03 M, 0.3 M) concentrations, such that either the HF concentration was held constant whilst the HNO_3 concentration was varied, or vice versa. Whilst only a few selected elution profiles are shown below, serving to illustrate the results obtained, the reader is referred to Appendix 5.5.2 for elution profiles of all the elements under consideration. The most crucial results obtained for the Pb Spec and AG 1x4 resins are discussed separately below.

As expected, Pb was retained quantitatively on the Pb Spec resin at all HNO_3 and HF eluent concentrations studied. In contrast, Bi and most of the target elements were found to elute very rapidly. To illustrate this, Figure 5.3 depicts elution profiles of Bi for a range of HNO_3 and HF concentrations. This figure shows that the elution profiles of Bi are not significantly affected by modifying the composition of the eluent. The only target elements to exhibit any appreciable affinity towards the Pb Spec resin were Ag, Re and Tl. As examples of their behaviour, Figures 5.4 and 5.5 depict elution profiles for Re and Ag, respectively. As can be seen in these figures, the retention of Re is so limited that, in practice, it cannot be separated from the virtually unretained Bi (or the rapidly eluting target elements). In contrast, the adsorbability of Ag (and that of Tl) is strong enough such that a separation can be achieved, but only at HNO_3 concentrations ≤ 1.5 M.
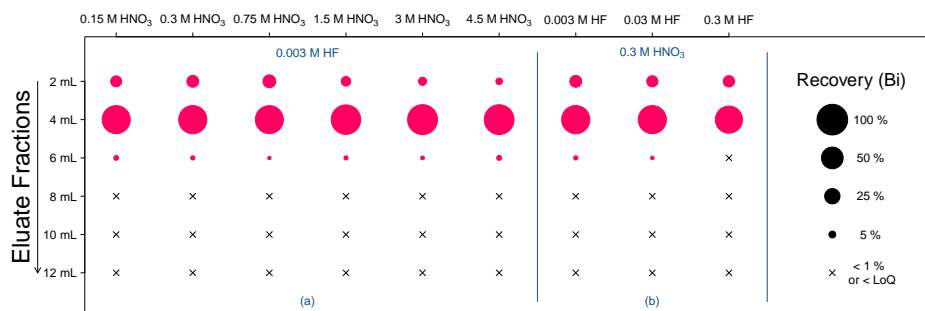
Figure 5.3: Isocratic elution profiles of Bi obtained upon loading $1\,\mathrm{mL}$ of a synthetic sample, containing *ca.* $0.2\,\mathrm{mg\,L^{-1}}$ Bi, on a $2\,\mathrm{mL}$ Pb Spec column. For each of the different eluents investigated, the elution profile is represented as a series of circles, the areas of which are proportional to the recovery of an element in each respective fraction.

Figure 5.4: Isocratic elution profiles of Re obtained upon loading $1\,\mathrm{mL}$ of a synthetic sample, containing *ca.* $0.2\,\mathrm{mg\,L^{-1}}$ Re, on a $2\,\mathrm{mL}$ Pb Spec column. For each of the different eluents investigated, the elution profile is represented as a series of circles, the areas of which are proportional to the recovery of an element in each respective fraction.

Figure 5.5: Isocratic elution profiles of Ag obtained upon loading $1\,\mathrm{mL}$ of a synthetic sample, containing *ca.* $0.2\,\mathrm{mg\,L^{-1}}$ Ag, on a $2\,\mathrm{mL}$ Pb Spec column. For each of the different eluents investigated, the elution profile is represented as a series of circles, the areas of which are proportional to the recovery of an element in each respective fraction.

As was the case for the Pb Spec resin, only a few target elements exhibited any appreciable affinity towards the AG 1x4 anion-exchange resin, in dilute HNO_3 and HF media. The matrix element Bi, as anticipated, was retained significantly at HNO_3 concentrations $\geq 1.5\,M$. In addition, varying the HF concentration was found to have little impact on its affinity towards the resin (see Figure 5.6). The single most strongly retained element, however, was the target element Re, which was assumed to be present as the anionic ReO_4^- in dilute HNO_3 media. This particular element was found to elute only at HNO_3 concentrations $\geq 3\,M$ (see Figure 5.7). The elution behaviour of the other, more typical, target elements is exemplified by the elution profiles of Ag (see Figure 5.8). This figure indicates that modifying either the HNO_3 or the HF molarities has no discernible effect on the adsorbability of this group of elements, *i.e.* they each elute very rapidly at all mineral acid concentrations studied. The few exceptions to this rule, apart from Re already discussed above, are described below. The matrix element Pb and the target elements Ce, Th and U behaved similarly to Bi, with the affinity towards the resin increasing with the HNO_3 concentration. However, at all HNO_3 molarities studied, retention of these elements was so limited that they still co-eluted, at least partially, with the non-retained target elements. In the specific case of Ce and Th, the HF concentration in the eluent was also found to have a significant impact on the affinities of these elements towards the resin. At an HF concentration of $0.3\,M$, both Ce and Th were retained completely on the column. Moreover, the elution profiles of three other target elements, Ti, Nb and Mo, were also affected strongly by modifying the molarity of HF in the eluent. This particular behaviour is illustrated by the elution profiles obtained for Nb (see Figure 5.9). As shown in this figure, Nb is retained completely on the column at HF concentrations $\geq 0.03\,M$. Conversely, an increase in the HNO_3 molarity appears to reduce the adsorbability of Nb onto the anion-exchanger. This can possibly be explained by the fact that HF is a weak acid, whereas HNO_3 is a strong acid. As the HNO_3 concentration is increased, HF dissociates to a lesser extent, whereby the availability of free F^- ligands decreases. This, in turn, may limit the formation of anionic fluoride (*e.g.* NbF_7^{2-}) and oxy-fluoride (*e.g.* $NbOF_5^{2-}$) complexes, which ought to bind strongly to an anion-exchange resin.[143,144]

These findings confirmed that neither resin alone was capable of removing both Pb and Bi from the target elements in dilute HNO_3/HF media. Consequently, a tandem-column setup was considered, in which a Pb Spec column was suspended above an AG 1x4 column. For this purpose, a single eluent had to be selected such that Pb and Bi would be retained strongly on the Pb Spec and AG 1x4 resins, respectively. Since Pb, fortunately, was retained at all HNO_3/HF molarities studied, only the removal of Bi by the AG 1x4 resin had to be taken into consideration. An eluent containing $1.5\,M$ HNO_3 / $2.5\,mM$ HF was eventually selected, even though Bi is more strongly retained at even higher HNO_3 molarities. At higher concentrations, however, the adsorbabilities of the strongly retained Re and rapidly eluting U decrease and increase, respectively, resulting in their co-elution with Bi. The HF concentration of the eluent, on the other hand, was selected such that Nb
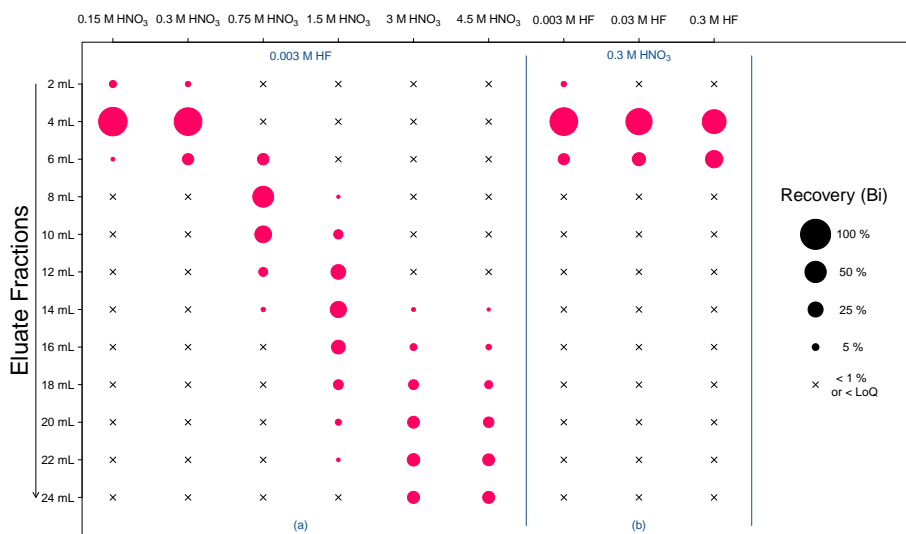
Figure 5.6: Isocratic elution profiles of Bi obtained upon loading $1\,\mathrm{mL}$ of a synthetic sample, containing *ca.* $0.2\,\mathrm{mg\,L^{-1}}$ Bi, on a $2\,\mathrm{mL}$ AG 1x4 column. For each of the different eluents investigated, the elution profile is represented as a series of circles, the areas of which are proportional to the recovery of an element in each respective fraction.
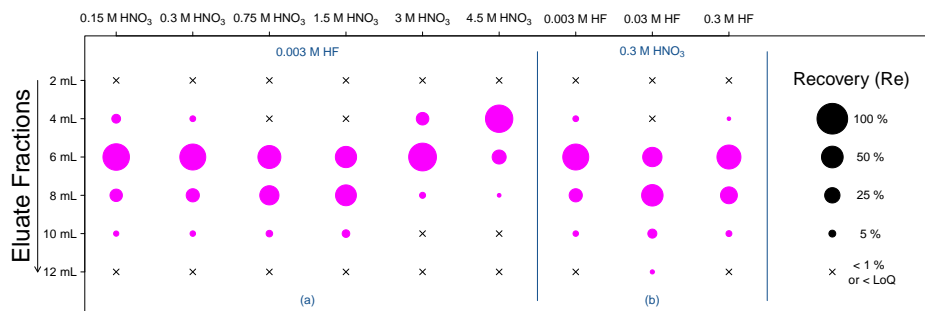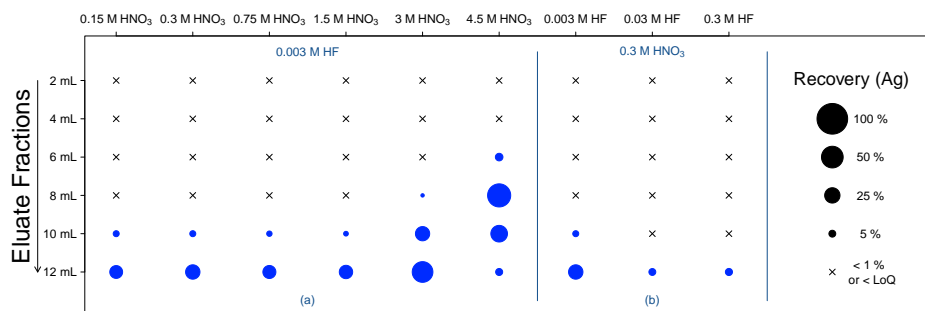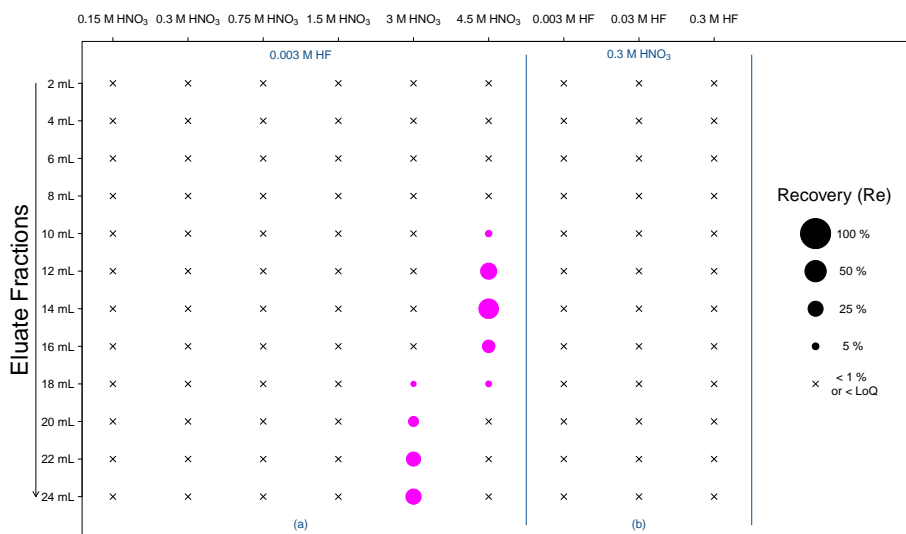

Figure 5.7: Isocratic elution profiles of Re obtained upon loading $1\,\mathrm{mL}$ of a synthetic sample, containing *ca.* $0.2\,\mathrm{mg\,L^{-1}}$ Re, on a $2\,\mathrm{mL}$ AG 1x4 column. For each of the different eluents investigated, the elution profile is represented as a series of circles, the areas of which are proportional to the recovery of an element in each respective fraction.
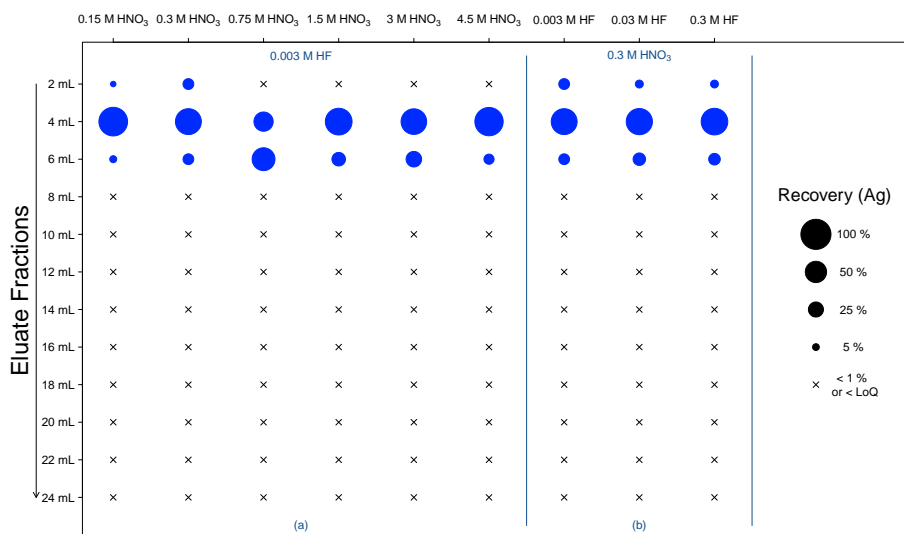
Figure 5.8: Isocratic elution profiles of Ag obtained upon loading $1\,\mathrm{mL}$ of a synthetic sample, containing *ca.* $0.2\,\mathrm{mg\,L^{-1}}$ Ag, on a $2\,\mathrm{mL}$ AG 1x4 column. For each of the different eluents investigated, the elution profile is represented as a series of circles, the areas of which are proportional to the recovery of an element in each respective fraction.

Figure 5.9: Isocratic elution profiles of Nb obtained upon loading $1\,\mathrm{mL}$ of a synthetic sample, containing *ca.* $0.2\,\mathrm{mg\,L^{-1}}$ Nb, on a $2\,\mathrm{mL}$ AG 1x4 column. For each of the different eluents investigated, the elution profile is represented as a series of circles, the areas of which are proportional to the recovery of an element in each respective fraction.
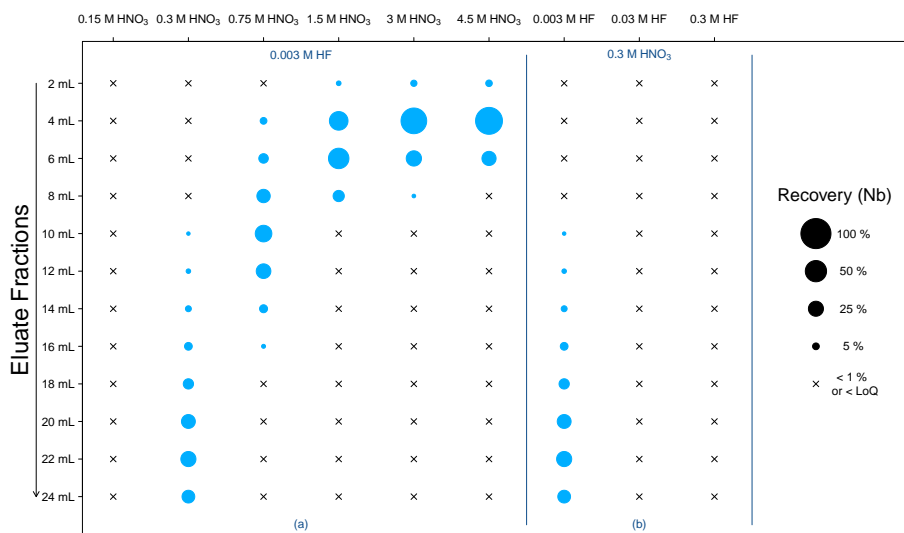
remained stable in solution, yet still eluted rapidly, whereby co-elution with Bi was minimal. To improve the separation further, the AG 1x4 resin was loaded into 5 mL polypropylene columns, instead of into 2 mL ones, in all subsequent work. The last major hurdle remaining when using a tandem-column setup, was the fact that the delayed arrival of Ag and Tl on the AG 1x4 resin, as a result of their affinity towards the Pb Spec resin, resulted in their co-elution with Bi from the lower column. The solution to this problem was to uncouple the tandem-column setup after Bi and most of the other target elements had eluted completely from the Pb Spec column but just before Ag and Tl had had a chance to. An unfortunate side-effect of this approach was that Re had to be recovered from two separate fractions. The finalised procedure is described in greater detail in the section below.

5.3.2 Description of the optimised separation procedure

The optimised analyte/matrix separation procedure is based on the use of a tandem-column setup, in which a 2 mL column loaded with Pb Spec resin is initially suspended above a 5 mL column loaded with AG 1x4 resin. This tandem-column setup is then uncoupled part way through the procedure, after which both columns are further eluted individually. Such a setup permits both the matrix elements, Pb and Bi, to be removed, successively, from a sample, in an HNO_3/HF medium. Examples of elution profiles, obtained by applying the optimised chromatographic separation procedure to a mock sample, containing *ca.* $20\,000\,\mathrm{mg\,L^{-1}}$ of the matrix elements and *ca.* $0.02\,\mathrm{mg\,L^{-1}}$ of the target elements in a dilute acidic matrix consisting of, at most, $1.5\,\mathrm{M}$ HNO_3 and $2.5\,\mathrm{mM}$ HF, are shown in Figure 5.10. This figure also provides the reader with a schematic representation of the proposed procedure and an overview of the eluents employed. To construct these elution profiles, eluate was collected in small fractions after which the presence of each element in each fraction was determined by means of ICP-SFMS.

Since the target elements Ti, V, Cr, Mn, Fe, Co, Ni, Cu, Cd, Ce and Th behave nearly identically, their elution profiles have been combined into one single profile ("Oth."). High recoveries (sometimes $> 200\,\%$) were obtained for a number of elements (*e.g.* Cu, Ag, Tl), due to the inherent impurities in the Pb and Bi powders that were used in the preparation of the mock samples. For routine application, the eluate was collected in larger fractions, based on the elution profiles shown in Figure 5.10, as indicated by the curly brackets in this figure. For the experimental data depicted in this figure, more than $99.5\,\%$ of the original LBE matrix was separated from all of the target elements. Figure 5.10 also illustrates that the vast majority of the target elements are eluted from the AG 1x4 column with only $14\,\mathrm{mL}$ of $1.5\,\mathrm{M}$ HNO_3 / $2.5\,\mathrm{mM}$ HF eluent. These $14\,\mathrm{mL}$ can be divided into two separate $7\,\mathrm{mL}$ fractions, T1 and T2. Fraction T2 still contains an appreciable amount of the matrix, in the form of Bi. However, most target elements are found in fraction T1 only. A more detailed description of the optimised separation procedure, for routine application, is given below.

A $1\,\mathrm{mL}$ aliquot of a dissolved LBE sample, containing *ca.* $20\,000\,\mathrm{mg\,L^{-1}}$ of

Figure 5.10: Gradient elution profiles obtained by applying the analyte/matrix separation procedure to a mock sample containing *ca.* 20 000 mg L^{-1} of the matrix elements and *ca.* 0.02 mg L^{-1} of the target elements. (left) Elution from tandem-column setup and individual elution from the AG 1x4 column after uncoupling: [C2 - C6] 1 mL sample + 5 mL 1.5 M HNO$_3$*, [A8 - A16] 10 mL 1.5 M HNO$_3$†, [A18 - A28] 12 mL 0.3 M HNO$_3$*, [A30 - A46] 18 mL 7.5 M HNO$_3$†. (right) Individual elution from the Pb Spec column after uncoupling: [P8 - P46] 40 mL 0.3 M HNO$_3$*, [P56 - P76] 30 mL 0.09 M ammonium citrate. († 2.5 mM HF in all HNO$_3$-based eluents)

the matrix elements in a dilute acidic matrix consisting of, at most, $1.5\,M\ HNO_3$ and $2.5\,mM$ HF, is brought onto a $2\,mL$ Pb Spec column. This $2\,mL$ column is itself suspended above a $5\,mL$ AG 1x4 column, such that the eluent passes through both columns in succession. Following the $1\,mL$ sample, another $5\,mL$ of $1.5\,M\ HNO_3$ / $2.5\,mM$ HF eluent is brought onto the top column. By this time, the majority of the target elements have already passed though the Pb Spec column onto the AG 1x4 column. However, a few elements (Pb, Tl, Ag and part of the Re) are still to be found on the Pb Spec column. The tandem-column setup is then uncoupled and both columns are further eluted individually.

An additional $10\,mL$ of $1.5\,M\ HNO_3$ / $2.5\,mM$ HF eluent is passed through the AG 1x4 column, thereby eluting all target elements that had previously eluted from the Pb Spec column onto this lower column. The one exception is that part of the Re able to reach the AG 1x4 column prior to the uncoupling, which is strongly bound to the anion-exchanger at these relatively low acid concentrations, probably as the perrhenate anion. The eluent is then adjusted and $12\,mL$ of $0.3\,M\ HNO_3$ / $2.5\,mM$ HF eluent is used to elute Bi in a timely fashion. Finally the eluent is adjusted once again and $18\,mL$ of $7.5\,M\ HNO_3$ / $2.5\,mM$ HF eluent is needed to strip the strongly bound Re from the AG 1x4 column.

Meanwhile, Ag, Tl and a part of the total Re are eluted from the Pb Spec resin by flushing the column with $30\,mL$ of $0.3\,M\ HNO_3$ / $2.5\,mM$ HF eluent. Finally, Pb is stripped by passing $30\,mL$ of $0.09\,M$ ammonium citrate through the column. A white precipitate observed in the final fraction, presumably Pb-citrate, can be dissolved readily by the addition of 1 to $2\,mL$ of concentrated HNO_3.
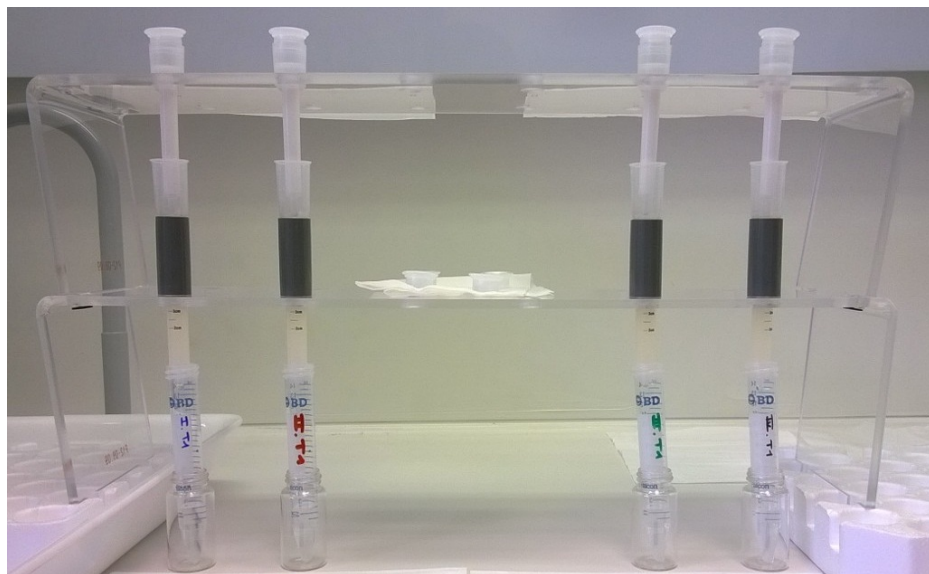
Figure 5.11: Tandem-column setups in which four $2\,mL$ Pb Spec columns are suspended above four $5\,mL$ AG 1x4 columns. The top rack is lifted to uncouple the columns.

5.3.3   Validation and application of the procedure

The procedure was validated by analysing three types of samples. Firstly, the procedure was applied to Pb-matrix certified reference materials (IMN PL33 and PL66) since, to the best of the author's knowledge, no Pb/Bi-alloy CRMs are available. Secondly, in an effort to evaluate the procedure for elements whose concentration in the CRMs was not certified, it was also applied to mock samples, which were prepared from high-purity Pb and Bi powders and multi-element spiking solutions. Thirdly, the procedure was applied to five samples from a real batch of LBE, the results of which could be compared to those obtained via *Neutron Activation Analysis* (NAA). Procedural *Quantification Limits* (QL, $10s$) for all eighteen target elements were estimated by analysing three independent procedural blank samples. In order to express the procedural QLs in terms relevant to solid samples, a nominal mass of 1 g of hypothetically dissolved LBE was used in all calculations. The values obtained ranged from low $ng\,g^{-1}$ levels for Th to sub-$µg\,g^{-1}$ levels for the contamination-prone Fe, as can be seen in Table 5.2. The analyses that were performed in the context of method validation, were each carried out in triplicate ($n = 3$), quadruplicate ($n = 4$) or quintuplicate ($n = 5$), most often under reproducibility conditions, unless explicitly stated otherwise.

Certified values as well as experimentally determined concentrations, for both CRMs, are presented in Table 5.3. In these experiments, Bi was treated as a target element, since it is present at very low levels in the CRMs. For those elements of which the contents in CRM IMN PL33 are certified, experimentally determined concentrations showed good agreement with certified values. As such, the experimentally determined concentrations lay within a range of $-5\,\%$ to $+2\,\%$ of certified values for Ni, Cu, Ag, Cd, Te, Tl and Bi. In contrast, the results for CRM IMN PL66 were not quite as clear-cut, although experimentally determined concentrations were still in fairly good agreement with certified values, with experimentally determined concentrations laying in a range of $-9\,\%$ to $+21\,\%$ of certified values for Ni, Cu, Ag, Cd, Tl and Bi. The only real exception with regard to the accuracy of the procedure was Te, for which the experimentally determined concentration deviated greatly from the certified value, resulting in a bias of *ca.* $-70\,\%$. No explanation for this observation is available at this time, although the separation procedure itself is likely not to blame. None of the earlier experiments with synthetic samples, mock samples or the other CRM had ever indicated a problem for this particular element, so the cause is therefore more likely to be found in the digestion procedure.

The performance of the procedure was further evaluated by applying it to mock samples, prepared from high-purity Pb and Bi powders and multi-element spike solutions, because the Pb-matrix CRMs were certified for only a limited number of target elements. Each of these mock samples contained Pb and Bi at concentrations of *ca.* $20\,000\,mg\,L^{-1}$, whilst the target elements were expected to be present at a far lower level of *ca.* $0.2\,mg\,L^{-1}$. However, it was found that the so-called high-purity Pb and Bi powders themselves contained considerable

Table 5.2: Procedural quantification limits (QL, $10s$) for all the target elements.

QL ($\mu g\ g^{-1}$)	Ti 0.02	V 0.005	Cr 0.05	Mn 0.009	Fe 0.5	Co 0.004	Ni 0.1	Cu 0.09	Nb 0.003
	Mo 0.04	Ag 0.07	Cd 0.003	Te 0.005	Ce 0.008	Re 0.06	Tl 0.04	Th 0.002	U 0.01

Table 5.3: Experimental results and certified values for all target elements of which the concentration in CRMs IMN PL33 and PL66 are certified. The uncertainties on the experimentally determined concentrations have been rounded to two significant figures, whilst the associated average values have been rounded to be in accordance.

PL33 ($\mu g\ g^{-1}$)	Ni	Cu	Ag	Cd	Te	Tl	Bi[†]
Experimental (n=4, u=2×SE)	39.48 ± 0.43	102.5 ± 2.1	17.0 ± 1.2	15.9 ± 2.3	240.6 ± 6.1	26.41 ± 0.83	96.4 ± 6.3
Certified (k=2)	39.7 ± 1.1	104 ± 1.8	17 ± 1.2	15.7 ± 0.6	235 ± 5.7	26.4 ± 1	101 ± 3.4

PL66 ($\mu g\ g^{-1}$)	Ni	Cu	Ag	Cd	Te	Tl	Bi
Experimental (n=3, u=2×SE)	5.08 ± 0.21	5.80 ± 0.54	66.47 ± 0.22	620 ± 23	3.07 ± 0.12	464.9 ± 7.2	44.2 ± 4.1
Certified (k=2)	5.5 ± 0.3	4.8 ± 0.3	65.2 ± 2.9	624 ± 25.6	10 ± 3.3	491 ± 8.4	48.8 ± 1.1

[†] $n=3$ due to an extreme outlier

amounts of the target elements Ti, Mn, Fe, Cu, Ag, Cd, Te and Tl. As a result, powder mixes were digested again, but without the addition of any spike solution, and analysed, so that a blank correction could be applied when analysing the mock samples. The corrected recoveries obtained for each of the target elements are presented in Table 5.4. These ranged from 96 % to 107 % for the vast majority of the elements, with the exception of Fe for which a recovery of only 74 % was obtained. The concentration of Fe in the high-purity powders was found to be somewhat variable and especially high when compared to the other impurities that were encountered, resulting in a recovery of *ca.* 200 % if not corrected for. As a result, the applied blank correction is most likely not very accurate.

Lastly, five samples taken from one batch of LBE (referred to as JVB S1) were subjected to the analytical procedure described in this chapter. In contrast to the analyses described in the previous paragraphs, these analyses were carried out under repeatability conditions, instead of under reproducibility conditions, *i.e.* ICP-SFMS measurements for the five samples were performed in a single sequence. This same batch of LBE had previously been analysed by means of NAA at SCK•CEN, also in quintuplicate. The results of these NAA analyses were kindly made available to the author, whereby both techniques could be directly compared. The averages of the experimentally determined concentrations, as well as their associated uncertainties, are presented in Table 5.5, for both techniques. The target elements Ni, Cu, Ag, Cd, Te and Tl could be determined quantitatively by means of ICP-SFMS, whereas all others were found to be present at levels below the reported QL. Of these elements, only Cu, Ag and Cd could also be determined quantitatively by means of NAA. In addition to these three target elements, NAA analyses indicated that Cr was present at considerable levels (*ca.* $0.5\,\mu g\,g^{-1}$), in four out of the five replicate measurements. ICP-SFMS results, on the other hand, suggested that the Cr concentration could be at least an order of magnitude lower ($< 0.05\,\mu g\,g^{-1}$). It is, however, worth noting that the samples, which were analysed by means of ICP-SFMS, were not physically identical to those analysed by means of NAA, although each of them did originate from the same batch of LBE. Therefore, local heterogeneities or contaminations might account for the discrepancy observed. The fact that, for one of the five replicate analyses carried out by means of NAA, a concentration of $< 0.03\,\mu g\,g^{-1}$ was reported, may suggest that Cr was not uniformly distributed throughout the entire LBE batch. The average concentrations of Cu, Ag and Cd, as determined by ICP-SFMS and NAA, were in good agreement with one another. The target elements Ni, Cd and Tl were found to be homogeneously distributed within the LBE batch (RSD < 5 %), whereas the replicate measurements suggested that Cu, Ag and Te were distributed more heterogeneously (RSD ≈ 10 %). In addition, a positive correlation was found between the concentration of Ag and Cu ($\rho = 0.98$), both by means of ICP-SFMS and by NAA. Hence, a relationship appeared to exist between the distributions of Cu and Ag in the batch of LBE under consideration. In the course of this work, several other batches of LBE were also analysed by means of the procedure described in this chapter. The samples under consideration included

Table 5.4: Recoveries for target elements, obtained by applying the analyte/matrix separation procedure developed to mock samples prepared from high-purity Pb and Bi powders. The recoveries of the target elements are expressed as percentages of the amount of spike, added via multi-element stock solution, that was recovered.

Recovery (%)	Ti	V	Cr	Mn	Fe	Co	Ni	Cu	Nb	Mo	Ag	Cd	Te	Ce	Re	Tl	Th	U
Mock LBE ($n=3$, $u=2\times$SE)	101.5 ± 1.6	100.9 ± 2.0	100.8 ± 1.9	101.3 ± 3.2	73 ± 16	100.5 ± 2.5	101.3 ± 1.6	106 ± 12	99.9 ± 3.1	99.6 ± 2.3	96.8 ± 4.7	107.4 ± 6.0	96.0 ± 5.5	99.2 ± 3.3	98.3 ± 4.4	96.7 ± 4.1	99.7 ± 3.6	100.2 ± 4.0
Fraction	T1	T1	T1	T1	T1	T1	T1	T1	T1+T2	T1+T2	AgReTl	T1	T1+T2	T1	AgReTl +Re	AgReTl	T1	T1+T2

Table 5.5: Experimentally determined concentrations of trace elements in a batch of LBE (JVB S1), as obtained by means of ICP-SFMS and NAA.

Conc. (µg g^{-1}) ($n=5$, $u=2\times$SE)	Ti	V	Cr[†]	Mn[‡]	Fe	Co	Ni	Cu	Nb
ICP-SFMS	< 0.02	< 0.005	< 0.05	< 0.009	< 0.5	< 0.004	2.220 ± 0.053	7.28 ± 0.70	< 0.003
NAA	< 2	< 0.001	0.570 ± 0.047	0.0082 ± 0.0055	< 4	< 0.007	< 10	6.98 ± 0.40	< 3

Conc. (µg g^{-1}) ($n=5$, $u=2\times$SE)	Mo	Ag	Cd	Te	Ce	Re	Tl	Th	U
ICP-SFMS	< 0.04	18.5 ± 1.9	0.588 ± 0.026	0.0431 ± 0.0037	< 0.008	< 0.06	5.036 ± 0.060	< 0.002	< 0.01
NAA	< 0.2	17.6 ± 1.6	0.453 ± 0.044	< 0.3	< 0.2	< 0.008	-	< 0.01	< 0.06

[†] $n=4$ for the result obtained by NAA, 5th replicate reported as $< 0.03\,\mu g\,g^{-1}$
[‡] $n=3$ for the result obtained by NAA, 4th and 5th replicate reported as $< 0.007\,\mu g\,g^{-1}$

both pre- and post-experimental LBE, *i.e.* relatively pure LBE as well as samples in which increased levels of corrosion products were expected. The results of these analyses, along with results obtained by means of other techniques (*i.e.* NAA and ICP-QMS), are presented in Appendix 5.5.1 at the end of this chapter.

5.4   Conclusions and outlook

An analyte/matrix separation procedure, based on a combination of extraction and anion-exchange chromatography, has been applied successfully for the determination of trace levels of Ti, V, Cr, Mn, Fe, Co, Ni, Cu, Nb, Mo, Ag, Cd, Te, Ce, Re, Tl, Th and U in LBE samples by means of ICP-SFMS. In the procedure, a tandem-column set-up is used, whereby a 2 mL Pb Spec column is suspended above a 5 mL AG 1x4 column. The matrix element Pb is retained on the Pb Spec column whilst Bi shows an appreciable affinity towards the AG 1x4 column, whereas the vast majority of the target elements exhibit no affinity towards either resin. As a result, over 99 % of the LBE matrix could be separated from the rapidly eluting target elements. The element Re, which serves as a chemical analogue for Tc, shows an affinity towards both resins and ends up in two separate fractions. Re could nonetheless be separated successfully from the matrix. In addition, although also Ag and Tl exhibit an affinity for the Pb Spec resin, they could still be separated from the LBE matrix.

The optimised procedure was validated by applying it to (i) Pb-matrix CRMs, (ii) mock samples and (iii) real LBE samples. Procedural QLs ($10s$), ranging from low $ng\,g^{-1}$ levels for Th to sub-$\mu g\,g^{-1}$ levels for the contamination-prone Fe, were estimated by analysing procedural blanks. Experimentally determined concentrations, of elements for which the concentrations in the IMN PL33 and PL66 Pb-matrix CRMs were certified (*i.e.* Ni, Cu, Ag, Cd, Te, Tl and Bi), were generally found to be in good agreement with their respective certified values. The only truly problematic element was Te, but only when considering CRM IMN PL66, for which a bias of *ca.* -70 % was observed. The author believes that the cause may possibly be attributed to the digestion procedure, but not to the actual separation procedure itself, as no such issues were encountered for mock samples or for the other CRM. However, further research would be required to identify the problem. Analysis of mock samples demonstrated excellent recoveries for most target elements, but the result for Fe was of some concern. However, the poor recovery of Fe may be attributed to the fact that the high-purity Pb and Bi powders, used to prepare the mock samples, contained relatively high levels of Fe which also appeared to be heterogeneously distributed. In addition, the QL for the contamination-prone Fe was poor when compared to those obtained for the other target elements. Comparing results obtained by means of the optimised procedure with those obtained by means of NAA, for five replicate analyses of a batch of LBE, showed good agreement between the two sets of data, with the exception of Cr. Certain elements were found to be more homogeneously distributed in these LBE samples (*i.e.* Ni, Cd and Tl) than other (*i.e.* Cu, Ag and Te). In

addition, a correlation ($\rho = 0.98$) was found between the distributions of Cu and Ag in the LBE samples, based on the analysis of the five replicate samples.

Several other batches of LBE, procured at SCK•CEN, originating from experiments involving the study of LBE corrosion, were also analysed by means of the analytical procedure described in this chapter. These comprised both pre- and post-experimental LBE samples, *i.e.* relatively pure LBE as well as samples in which increased levels of corrosion products were expected. A number of these specimens were also analysed by means of ICP-QMS, by the author, or by means of NAA, elsewhere at SCK•CEN. For a more detailed overview of the results obtained for these samples, the reader is referred to Appendix 5.5.1 at the end of this chapter. It is important to note, however, that when ICP-QMS was employed, simple dilutions were considered for mitigating matrix effects and memory effects, rather than applying the analyte/matrix separation protocol developed in the course of the work. As a result of the increased need for sample dilution with this approach, as well as the poorer sensitivity and instrumental background typically associated with quadrupole instruments, ICP-SFMS yielded superior QLs across the board. To illustrate, *e.g.* for V and Co, *i.e.* elements less prone to contaminations, the QL reported for ICP-SFMS was as much as two orders of magnitude better than the one reported for ICP-QMS. In addition, memory effects for Pb and Bi are of some concern when simple dilution is considered, which may result in a need for more frequent instrument maintenance. When the target element concentration was high enough, however, there was good agreement between the results obtained with both techniques, in nearly all cases. Therefore, depending on the requirements posed for the analysis of a particular sample, either ICP-SFMS, preceded by an analyte/matrix separation, or ICP-QMS, preceded by simple dilution, may both be found to be fit-for-purpose. In contrast, when the results for NAA were compared to those of ICP-SFMS, the difference in QLs was less clear cut, although those obtained for ICP-SFMS were most often at least on par with those reported for NAA. In a select few cases, however, *e.g.* when Nb was considered, the QL obtained for ICP-SFMS was as much as two or three orders order of magnitude better than that for NAA. In other cases still, the QL obtained with NAA was slightly superior. Typically, when the concentration of the target elements was high enough, such that quantitative analysis with both techniques was possible, results obtained with both techniques showed good agreement. The one exception, once again, being Cr, as had been the case or the samples taken from LBE batch JVB S1. Both techniques may be viewed as complementary, with their preferred use depending on the analytes of interest. In the case of NAA, however, irradiation facilities, which are becoming increasingly rare, need to be available, although this issue is naturally of lesser concern at nuclear research institutes such as SCK•CEN. The main benefit of ICP-SFMS over NAA has to do with sample throughput, which is expected to be considerably poorer for NAA when compared to ICP-SFMS (for about a dozen samples, > 4 weeks rather than < 2 weeks), in part as a result of the required cooling time after sample irradiation.

At this point, it is important to remind the reader of the fact that a few

of the target elements actually served as proxies for important radionuclides, whose true behaviour is still left to be determined. Literature data for the AG 1x10 anion-exchange and Sr Spec resins, the latter being similar to Pb Spec resin, suggests that Re might indeed correctly serve as a chemical analogue for Tc throughout the proposed separation procedure. However, based on the same literature data, it appears unlikely that this is also the case for Te and Po or for Ce and Pu. Therefore, it will be necessary to apply the procedure to irradiated LBE samples, mainly to confirm the behaviour of Po. [135,136]

Lastly, it should also be noted that the procedure described in this work was aimed specifically at the quantitative analysis of LBE samples originating from research projects related to the development of the MYRRHA reactor at SCK•CEN. Certain reactor designs, however, may involve the use of other liquid metal coolants. One Gen IV nuclear reactor design proposed for commercial power generation, *i.e.* the lead-cooled fast reactor, would rely on the use of pure Pb as a primary coolant (see Section 1.1.2). The accurate multi-elemental trace analysis of Pb samples, by means of ICP-SFMS, would also be hampered by non-spectral interferences, although the observed matrix effects would be induced by only a single matrix element instead of two. As a result, a much simplified analyte/matrix separation procedure could be employed, based on the use of the Pb Spec extraction chromatographic resin only. An analyte/matrix separation procedure using only Pb Spec resin would be more straightforward and quicker because it avoids the complications of using multiple eluents and a tandem-column setup.

5.5 Appendix

The first part of this appendix contains an overview of ICP-SFMS analyses that were performed on real LBE samples, which were procured at SCK•CEN, as was already mentioned in Section 5.3.3. In addition, in the second part of this appendix, a more complete overview of elution profiles is provided, whereas only a limited number of these were presented in the main text, to illustrate the elution behaviour of selected matrix elements and target elements from Pb Spec and AG 1x4 columns.

5.5.1 Analysis of real lead-bismuth eutectic samples

In each case, the ICP-SFMS analyses that are reported were preceded by the analyte/matrix separation procedure, as described in the main text of this chapter, in an effort to attenuate non-spectral interferences. A number of these samples were also analysed by means of NAA or by means of ICP-QMS. In the latter case, simple dilutions were applied for overcoming matrix effects, rather than performing an analyte/matrix separation. In contrast to the analysis of LBE batch JVB S1, reported upon in Section 5.3.3, which was performed in quintuplicate, only single ICP-MS replicate measurements were performed on these particular samples. As a result, rather than reporting the uncertainty as a standard error on a number of replicate measurements, the expanded uncertainty u_c ($k = 2$) on the experimental result c was estimated by the equation below,

which, based on previous experience at SCK•CEN, was considered to be a realistic yet conservative approach to estimating the measurement uncertainty.[145]

$$u_c = \sqrt{\left(\frac{1}{10} \cdot c\right)^2 + \left(\frac{2}{3} \cdot QL\right)^2} \tag{5.1}$$

Firstly, a series of relatively pure LBE samples, referred to as JVB S6, JVB S7, JVB S8, JVB S9 and JVB S10, were analysed. The batches of LBE, from which these samples originated, were also analysed by means of NAA at SCK•CEN, the results of which were kindly made available to the author. Secondly, a number of additional LBE samples, originating from experiments involving the study of LBE corrosion, were also analysed. These samples, which were expected to contain a number of corrosion products, are referred to as BC S1, BC S2, BC S3, BC S4 and BC S5 in this text. These same five samples were also analysed by means of ICP-QMS by the author, after preparing appropriate dilutions from the respective digest solutions. The final series of LBE samples to be analysed also originated from an experiment designed to investigate LBE corrosion. The LBE used in these experiments originally came from the same batch of LBE as sample JVB S6, whilst the post-experiment samples are referred to as KR S1, KR S2, KR S3 and KR S4. As such, the uptake of corrosion products could be monitored by comparing the trace element composition of sample JVB S6 with those of KR S1 - S4. This last series of samples was also to be analysed by means of NAA at SCK•CEN but, at the time of writing, these results were not yet available to the author.

For samples JVB S6 - S10, the results obtained by means of ICP-SFMS were found to be in good agreement with those obtained by means of NAA. The one real exception, once again, was Cr, just as was the case for the five replicate analyses of LBE batch JVB S1 (see Section 5.3.3). For four out of the five samples, a Cr concentration of *ca.* $0.5\,\mu g\,g^{-1}$ was reported by NAA, whereas ICP-SFMS analyses indicated that the Cr concentration ought to be at least an order of magnitude lower ($< 0.05\,\mu g\,g^{-1}$). An overview of the results obtained by both techniques is given in Table 5.6, showing that the most prevalent impurities in these particular batches of LBE were Ni (*ca.* 0.2 to $0.4\,\mu g\,g^{-1}$), Cu (*ca.* 4 to $7\,\mu g\,g^{-1}$), Ag (*ca.* 10 to $15\,\mu g\,g^{-1}$), Cd (*ca.* 0.5 to $3.5\,\mu g\,g^{-1}$), Te (*ca.* 0.01 to $0.05\,\mu g\,g^{-1}$) and Tl (*ca.* 8 to $12\,\mu g\,g^{-1}$), whilst traces of Ti (up to *ca.* $0.07\,\mu g\,g^{-1}$) and Fe (up to *ca.* $0.6\,\mu g\,g^{-1}$) were also observed in some samples. However, for these last two elements, the values obtained via ICP-SFMS lay near the procedural QL.

In the case of samples BC S1 - S5, it was expected that a number of corrosion products would be present, in addition to a number of the inherent impurities that had already been identified in samples JVB S6 - S10. Whereas samples BC S1 - S2 represented the bulk of this particular batch of LBE, BC S3 - S5 originated from the LBE's surface layer and the walls or the bottom of its containment vessel. Small bits of metallic debris were clearly discernible in these last three solid samples, suggesting that especially high minor and trace element concentrations could be expected for these particular samples. In addition to subjecting these

samples to the analytical procedure described in this chapter, each sample digest was also analysed by means of ICP-QMS. The results of these analyses are shown in Table 5.7. As a result of the poorer sensitivity typically associated with ICP-QMS and the need for increased sample dilution for attenuating matrix and memory effects, the ICP-SFMS measurements generally yielded superior QLs. In nearly all cases, however, there was good agreement between the results obtained with both techniques, except for sample BC S2, for which the Ni and Cu concentrations differed considerably. The most prevalent trace or minor elements in these five samples were found to be Ni ($ca.$ 4 to $20\,\mu g\,g^{-1}$), Cu ($ca.$ 7 to $25\,\mu g\,g^{-1}$), Ag ($ca.$ 22 to $25\,\mu g\,g^{-1}$), Cd ($ca.$ 0.02 to $50\,\mu g\,g^{-1}$), Te ($ca.$ 0.1 to $1\,\mu g\,g^{-1}$) and Tl ($ca.$ 8 to $9\,\mu g\,g^{-1}$), whilst Ti (up to $ca.$ $2\,\mu g\,g^{-1}$), V (up to $ca.$ $3\,\mu g\,g^{-1}$), Cr (up to $ca.$ $500\,\mu g\,g^{-1}$), Mn (up to $ca.$ $100\,\mu g\,g^{-1}$), Fe (up to $ca.$ $30\,000\,\mu g\,g^{-1}$), Co (up to $ca.$ $3\,\mu g\,g^{-1}$), Nb (up to $ca.$ $0.02\,\mu g\,g^{-1}$) and Mo (up to $ca.$ $1\,\mu g\,g^{-1}$) were also found to be present in significant quantities in a number of samples.

Samples KR S1 - S4 were also suspected of containing a number of corrosion products, with samples KR S1 - S2 representing the bulk of the LBE and samples KR S3 - S4 having been taken from its surface layer. Each of these samples was measured in triplicate, in case of heterogeneity, with each replicate measurement being denoted as either A, B, or C. The result of each ICP-SFMS analysis is given in Table 5.8, along with the trace element composition of sample JVB S6 ($i.e.$ representing the pre-experiment LBE composition). The results obtained for sample KR S2C are not taken into account, however, as the reported trace element concentrations may, at least in part, originate from a contamination. A relatively high W concentration was found in that particular sample's digest solution, equivalent to ca. $50\,\mu g\,g^{-1}$ W in solid LBE material. This suggests that the solid tungsten carbide drill bit, that was used in the sampling process, may have contaminated the sample. Most important, however, was that none of the other samples were found to contain W at similar levels (all being $< 0.1\,\mu g\,g^{-1}$ W). Samples KR S3 - S4, fortunately, were collected from a larger piece of LBE by using a set of cutting shears instead of a drill bit, whereby the risk of contamination was comparatively minimal. The remaining samples were found to contain Ni ($ca.$ 5 to $6\,\mu g\,g^{-1}$), Cu ($ca.$ 5 to $6\,\mu g\,g^{-1}$), Ag ($ca.$ 13 to $16\,\mu g\,g^{-1}$), Cd ($ca.$ 0.02 to $0.03\,\mu g\,g^{-1}$), Te ($ca.$ 0.01 to $0.02\,\mu g\,g^{-1}$) and Tl ($ca.$ 10 to $12\,\mu g\,g^{-1}$), whilst traces of V (up to $ca.$ $0.01\,\mu g\,g^{-1}$), Cr (up to $ca.$ $0.4\,\mu g\,g^{-1}$), Mn (up to $ca.$ $0.04\,\mu g\,g^{-1}$), Fe (up to $ca.$ $2\,\mu g\,g^{-1}$), Co (up to $ca.$ $0.01\,\mu g\,g^{-1}$) and Mo (up to $ca.$ $0.07\,\mu g\,g^{-1}$) were also thought to be present in at least one of the samples. When compared to the initial composition of sample JVB S6, there was no discernible change in the concentrations of the Cu, Ag and Tl impurities. In contrast, a relatively large increase in the Ni concentration was observed across the board. This observation fits with the selective dissolution of Ni, that has been reported for high-alloy steels such as 316L in direct contact with liquid LBE.[146] In addition, a marked decrease in the Cd concentration was observed, for which no apparent mechanism could be proposed. At the time of writing, no NAA analysis data was available to corroborate this result.

5.5.2   Adsorbability of the elements on selected resins

The affinity of Ti, V, Cr, Mn, Fe, Co, Ni, Cu, Nb, Mo, Ag, Cd, Te, Ce, Re, Tl, Pb, Bi, Th and U, towards the AG 1x4 and Pb Spec resins, in dilute acidic media, was investigated as described in Section 5.3.1. The elution behaviour of each of these elements, from columns loaded with AG 1x4 resin, using a variety of HNO_3 and HF-based eluents, is presented in Figures 5.12 - 5.31. In addition, comparable elution profiles, but obtained for the Pb Spec resin, are presented in Figures 5.32 -5.51. The most important conclusions to be drawn from these elution profiles, for the purposes of this thesis, have already been discussed in Section 5.3.1.

Table 5.6: Determination of trace elements in relatively pure LBE samples by means of ICP-SFMS and NAA.

Conc. (μg g^{-1}) ($k = 2$)	JVB S6		JVB S7		JVB S8		JVB S9		JVB S10	
	ICP-SFMS	NAA	ICP-SFMS	NAA	ICP-SFMS	NAA	ICP-SFMS	NAA	ICP-SFMS	NAA
Ti	< 0.02	< 2	< 0.02	< 2	< 0.02	< 2	0.070 ± 0.015	< 2	0.022 ± 0.014	< 2
V	< 0.005	< 0.001	< 0.005	< 0.001	< 0.005	< 0.001	< 0.005	< 0.001	< 0.005	0.0009 ± 0.0004
Cr	< 0.05	< 0.1	< 0.05	0.55 ± 0.21	< 0.05	0.57 ± 0.21	< 0.05	0.41 ± 0.16	< 0.05	0.54 ± 0.15
Mn	< 0.009	< 0.007	< 0.009	< 0.0007	< 0.009	0.0084 ± 0.0032	< 0.009	< 0.006	< 0.009	< 0.005
Fe	< 0.5	< 4	< 0.5	< 4	< 0.5	< 4	< 0.5	< 2	0.56 ± 0.34	< 2
Co	< 0.004	< 0.007	< 0.004	< 0.005	< 0.004	< 0.002	< 0.004	< 0.003	< 0.004	< 0.004
Ni	0.255 ± 0.071	< 10	0.295 ± 0.073	< 2	0.414 ± 0.078	< 10	0.241 ± 0.071	< 10	0.312 ± 0.074	< 10
Cu	5.09 ± 0.51	4.82 ± 0.24	7.10 ± 0.71	7.0 ± 0.5	4.84 ± 0.49	6.0 ± 0.5	4.17 ± 0.42	4.03 ± 0.33	7.16 ± 0.72	7.01 ± 0.37

↓ Continued from previous page

Nb	< 0.003	< 3	< 0.003	< 3	< 0.003	< 3	< 0.003	< 2	< 0.003	< 2
Mo	< 0.04	< 0.3	< 0.04	< 0.3	< 0.04	< 0.3	< 0.04	< 0.3	< 0.04	< 0.2
Ag	14.8 ± 1.5	13.5 ± 0.6	14.5 ± 1.5	13.2 ± 0.6	10.6 ± 1.1	12.8 ± 0.6	9.74 ± 0.98	9.9 ± 0.5	14.2 ± 1.4	13.9 ± 0.7
Cd	0.851 ± 0.085	0.63 ± 0.06	1.47 ± 0.15	1.24 ± 0.08	3.39 ± 0.34	3.52 ± 0.18	0.74 ± 0.074	0.62 ± 0.05	1.49 ± 0.15	1.36 ± 0.08
Te	0.0122 ± 0.0035	< 0.3	0.0355 ± 0.0049	< 0.2	0.0237 ± 0.0041	< 0.3	0.0100 ± 0.0035	< 0.2	0.0352 ± 0.0049	< 0.2
Ce	< 0.008	< 0.2	< 0.008	< 0.3	< 0.008	< 0.3	< 0.008	< 0.2	< 0.008	< 0.3
Re	< 0.06	< 0.007	< 0.06	< 0.01	< 0.06	< 0.02	< 0.06	< 0.01	< 0.06	< 0.01
Tl	11.5 ± 1.2	-	8.51 ± 0.85	-	11.9 ± 1.2	-	11.2 ± 1.1	-	8.47 ± 0.85	-
Th	< 0.002	< 0.01	< 0.002	< 0.01	< 0.002	< 0.01	< 0.002	< 0.006	< 0.002	< 0.008
U	< 0.01	< 0.05	< 0.01	< 0.06	< 0.01	< 0.06	< 0.01	< 0.06	< 0.01	< 0.05

Table 5.7: Determination of trace elements in LBE samples, originating from LBE corrosion experiments, by means of ICP-SFMS and ICP-QMS.

Conc. (μg g^{-1}) ($k = 2$)	BC S1		BC S2		BC S3		BC S4		BC S5	
	ICP-SFMS	ICP-QMS	ICP-SFMS	ICP-QMS	ICP-SFMS	ICP-QMS	ICP-SFMS	ICP-QMS	ICP-SFMS	ICP-QMS
Ti	< 0.02	< 3	< 0.02	< 3	0.85 ± 0.34	< 3	< 0.5	< 3	2.17 ± 0.40	3.7 ± 2.0
V	< 0.005	< 0.8	< 0.005	< 0.8	0.171 ± 0.069	< 0.8	< 0.1	< 0.8	2.64 ± 0.27	2.65 ± 0.58
Cr	< 0.05	< 1	< 0.05	< 1	33.7 ± 3.4	33.0 ± 3.5	13.6 ± 1.5	13.7 ± 1.7	517 ± 52	511 ± 71
Mn	0.0095 ± 0.0061	< 2	< 0.009	< 2	22.1 ± 2.2	21.7 ± 2.4	13.7 ± 1.4	13.7 ± 1.7	113 ± 11	109 ± 11
Fe	< 0.5	< 2	0.68 ± 0.34	< 2	2920 ± 290	2610 ± 270	1050 ± 110	960 ± 110	35 100 ± 3500	31 700 ± 4100
Co	< 0.004	< 0.1	< 0.003	< 0.1	0.445 ± 0.069	0.48 ± 0.10	0.144 ± 0.049	0.221 ± 0.088	3.35 ± 0.34	3.36 ± 0.35
Ni	8.49 ± 0.85	9.2 ± 1.3	3.76 ± 0.38	6.8 ± 1.1	15.4 ± 1.5	16.0 ± 1.9	6.96 ± 0.70	6.3 ± 1.1	19.2 ± 1.9	20.6 ± 2.3
Cu	7.14 ± 0.72	7.6 ± 1.5	7.48 ± 0.75	22.9 ± 2.6	24.3 ± 2.4	23.9 ± 2.7	10.0 ± 1.0	9.9 ± 1.6	20.0 ± 2.0	20.3 ± 2.4

↓ Continued from previous page

Nb	< 0.003	< 0.2	< 0.002	< 0.2	0.0072 ± 0.0021	< 0.2	< 0.0030	< 0.2	0.0219 ± 0.003	< 0.2
Mo	< 0.04	< 0.9	< 0.04	< 0.9	0.543 ± 0.060	< 0.9	0.188 ± 0.033	< 0.9	1.31 ± 0.13	1.48 ± 0.61
Ag	24.7 ± 2.5	24.6 ± 2.5	22.8 ± 2.3	22.5 ± 2.3	23.1 ± 2.3	22.4 ± 2.3	22.6 ± 2.3	22.1 ± 2.2	22.2 ± 2.2	21.8 ± 2.2
Cd	0.0174 ± 0.0027	0.147 ± 0.068	0.0364 ± 0.0042	0.111 ± 0.066	50.7 ± 5.1	50.8 ± 5.1	0.538 ± 0.054	0.573 ± 0.087	0.0632 ± 0.0066	0.183 ± 0.067
Te	0.175 ± 0.018	< 0.4	0.183 ± 0.019	< 0.4	0.911 ± 0.091	0.92 ± 0.29	0.323 ± 0.033	< 0.4	0.185 ± 0.019	< 0.4
Ce	0.0100 ± 0.0054	< 0.06	< 0.007	< 0.06	0.0213 ± 0.0057	< 0.06	< 0.008	< 0.06	< 0.008	< 0.06
Re	< 0.06	< 0.08	< 0.06	< 0.08	< 0.07	< 0.08	< 0.06	< 0.08	< 0.06	< 0.08
Tl	8.29 ± 0.83	8.27 ± 0.84	8.37 ± 0.84	8.27 ± 0.84	8.54 ± 0.85	8.63 ± 0.88	8.57 ± 0.86	8.51 ± 0.86	8.09 ± 0.81	7.88 ± 0.80
Th	< 0.002	< 1	< 0.002	< 1	0.0161 ± 0.0021	< 1	< 0.002	< 1	< 0.002	< 1
U	< 0.01	< 0.07	< 0.01	< 0.06	< 0.01	< 0.07	< 0.01	< 0.06	< 0.01	< 0.06

Table 5.8: Determination of trace elements in LBE samples, originating from LBE corrosion experiments, by means of ICP-SFMS. The batch of LBE that was used in these experiments was the same as that of sample JVB S6, the trace element composition of which was already given in Table 5.6.

Conc. (µg g^{-1}) ($k = 2$)	JVB S6	KR S1A	KR S1B	KR S1C	KR S2A	KR S2B	KR S2C†	KR S3A	KR S3B	KR S3C	KR S4A	KR S4B	KR S4C
Ti	< 0.02	< 0.02	< 0.02	< 0.02	< 0.02	< 0.02	0.155 ± 0.020	< 0.02	< 0.02	< 0.02	< 0.02	< 0.02	< 0.02
V	< 0.005	< 0.005	< 0.005	< 0.005	< 0.005	< 0.005	0.571 ± 0.057	0.0140 ± 0.0036	< 0.005	< 0.005	< 0.005	< 0.005	< 0.005
Cr	< 0.05	< 0.05	< 0.05	< 0.05	< 0.05	< 0.05	3.48 ± 0.35	0.414 ± 0.053	< 0.05	< 0.05	0.126 ± 0.036	< 0.05	< 0.05
Mn	< 0.009	< 0.009	< 0.009	< 0.009	< 0.009	< 0.009	0.0585 ± 0.0084	0.0398 ± 0.0072	< 0.009	< 0.009	0.0170 ± 0.0062	< 0.009	< 0.009
Fe	< 0.5	< 0.5	< 0.5	< 0.5	< 0.5	< 0.5	4.45 ± 0.56	1.89 ± 0.38	< 0.5	< 0.5	0.54 ± 0.34	< 0.5	< 0.5
Co	< 0.004	0.0050 ± 0.0027	< 0.004	< 0.004	< 0.004	< 0.004	106 ± 11	0.0088 ± 0.0028	< 0.004	< 0.004	0.0052 ± 0.0027	< 0.004	0.0054 ± 0.0027
Ni	0.255 ± 0.071	6.06 ± 0.61	5.89 ± 0.59	5.98 ± 0.60	5.86 ± 0.59	6.00 ± 0.60	6.90 ± 0.69	6.08 ± 0.61	5.71 ± 0.57	5.82 ± 0.59	5.97 ± 0.60	5.90 ± 0.59	5.82 ± 0.59
Cu	5.09 ± 0.51	5.32 ± 0.53	5.25 ± 0.53	5.27 ± 0.53	5.23 ± 0.53	5.24 ± 0.53	5.26 ± 0.53	5.26 ± 0.53	5.10 ± 0.51	5.13 ± 0.52	5.26 ± 0.53	5.25 ± 0.53	5.07 ± 0.51

↓ Continued from previous page

Nb	< 0.003	< 0.003	< 0.003	< 0.003	< 0.003	< 0.003	0.0188 ± 0.0027	< 0.003	< 0.003	< 0.003	< 0.003	< 0.003	< 0.003
Mo	< 0.04	< 0.04	< 0.04	< 0.04	< 0.04	< 0.04	< 0.04	0.068 ± 0.028	< 0.04	< 0.04	< 0.04	< 0.04	< 0.04
Ag	14.8 ± 1.5	15.3 ± 1.5	14.9 ± 1.5	15.8 ± 1.6	15.3 ± 1.5	14.7 ± 1.5	15.2 ± 1.5	14.3 ± 1.4	14.5 ± 1.4	14.2 ± 1.4	14.3 ± 1.4	14.5 ± 1.5	13.7 ± 1.4
Cd	0.851 ± 0.085	0.0284 ± 0.0035	0.0294 ± 0.0036	0.0279 ± 0.0034	0.0274 ± 0.0034	0.0269 ± 0.0034	0.0278 ± 0.0034	0.0280 ± 0.0034	0.0259 ± 0.0033	0.0271 ± 0.0034	0.0269 ± 0.0034	0.0280 ± 0.0034	0.0253 ± 0.0032
Te	0.0122 ± 0.0035	0.0200 ± 0.0039	0.0207 ± 0.0039	0.0204 ± 0.0039	0.0200 ± 0.0039	0.0187 ± 0.0038	0.0184 ± 0.0038	0.0208 ± 0.0039	0.0205 ± 0.0039	0.0183 ± 0.0038	0.0193 ± 0.0039	0.0195 ± 0.0039	0.0179 ± 0.0038
Ce	< 0.008	< 0.008	< 0.008	< 0.008	< 0.008	< 0.008	< 0.008	< 0.008	< 0.008	< 0.008	< 0.008	< 0.008	< 0.008
Re	< 0.06	< 0.06	< 0.06	< 0.06	< 0.06	< 0.06	< 0.06	< 0.06	< 0.06	< 0.06	< 0.06	< 0.06	< 0.06
Tl	11.5 ± 1.2	10.9 ± 1.1	10.7 ± 1.1	10.9 ± 1.1	11.1 ± 1.1	11.0 ± 1.1	11.0 ± 1.1	11.1 ± 1.1	11.2 ± 1.1	11.2 ± 1.1	11.2 ± 1.1	11.3 ± 1.1	11.1 ± 1.1
Th	< 0.002	< 0.002	< 0.002	< 0.002	< 0.002	< 0.002	< 0.002	< 0.002	< 0.002	< 0.002	< 0.002	< 0.002	< 0.002
U	< 0.01	< 0.01	< 0.01	< 0.01	< 0.01	< 0.01	< 0.01	< 0.01	< 0.01	< 0.01	< 0.01	< 0.01	< 0.01

† A high concentration of W was found in the sample digest, which would have been equivalent to a concentration of *ca.* 50 µg g^{-1} W in the solid LBE material. As a result, the reported target element concentration may be the result of a severe contamination, originating from the solid tungsten carbide drill bit that was used in the sampling process.
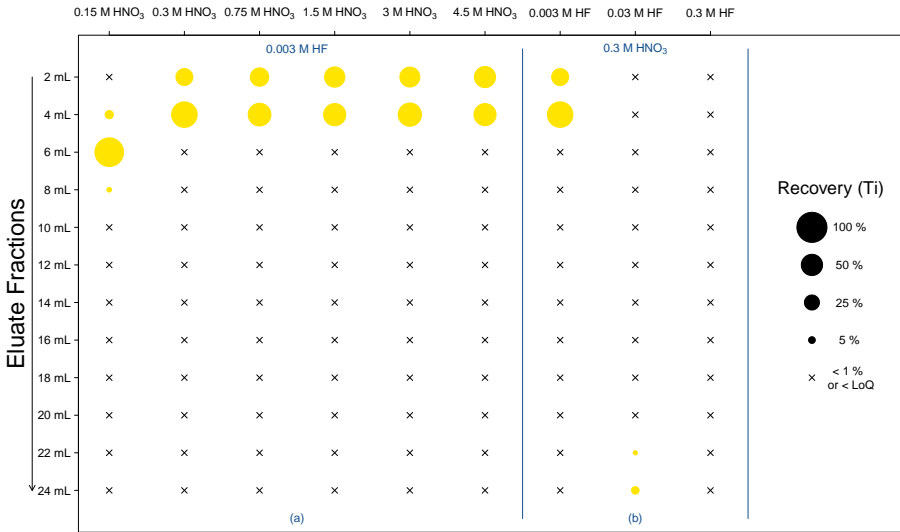
Figure 5.12: Isocratic elution profiles of Ti obtained upon loading $1\,\mathrm{mL}$ of a synthetic sample, containing *ca.* $0.2\,\mathrm{mg\,L^{-1}}$ Ti, on a $2\,\mathrm{mL}$ AG 1x4 column. For each of the different eluents investigated, the elution profile is represented as a series of circles, the areas of which are proportional to the recovery of an element in each respective fraction.

Figure 5.13: Isocratic elution profiles of V obtained upon loading $1\,\mathrm{mL}$ of a synthetic sample, containing *ca.* $0.2\,\mathrm{mg\,L^{-1}}$ V, on a $2\,\mathrm{mL}$ AG 1x4 column. For each of the different eluents investigated, the elution profile is represented as a series of circles, the areas of which are proportional to the recovery of an element in each respective fraction.

Figure 5.14: Isocratic elution profiles of Cr obtained upon loading $1\,\mathrm{mL}$ of a synthetic sample, containing *ca.* $2\,\mathrm{mg\,L^{-1}}$ Cr, on a $2\,\mathrm{mL}$ AG 1x4 column. For each of the different eluents investigated, the elution profile is represented as a series of circles, the areas of which are proportional to the recovery of an element in each respective fraction.

Figure 5.15: Isocratic elution profiles of Mn obtained upon loading $1\,\mathrm{mL}$ of a synthetic sample, containing *ca.* $0.2\,\mathrm{mg\,L^{-1}}$ Mn, on a $2\,\mathrm{mL}$ AG 1x4 column. For each of the different eluents investigated, the elution profile is represented as a series of circles, the areas of which are proportional to the recovery of an element in each respective fraction.
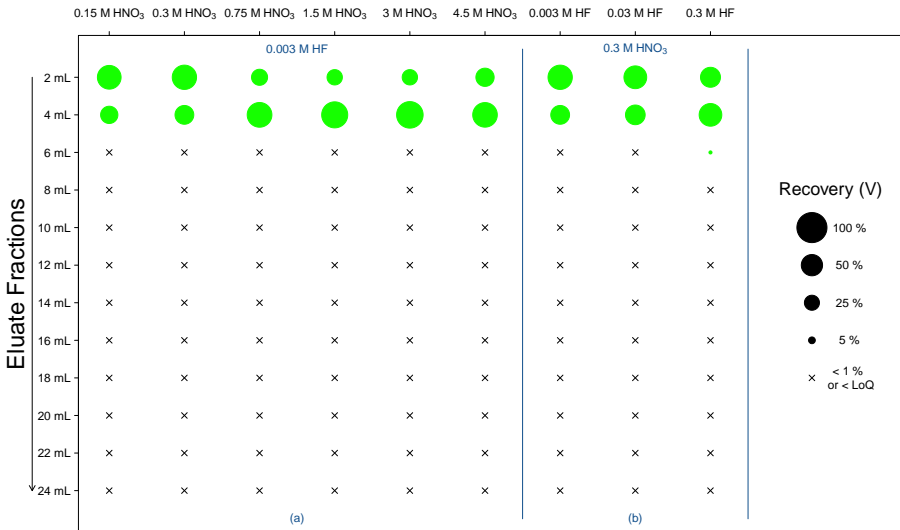
Figure 5.16: Isocratic elution profiles of Fe obtained upon loading $1\,\mathrm{mL}$ of a synthetic sample, containing *ca.* $2\,\mathrm{mg\,L^{-1}}$ Fe, on a $2\,\mathrm{mL}$ AG 1x4 column. For each of the different eluents investigated, the elution profile is represented as a series of circles, the areas of which are proportional to the recovery of an element in each respective fraction.

Figure 5.17: Isocratic elution profiles of Co obtained upon loading $1\,\mathrm{mL}$ of a synthetic sample, containing *ca.* $0.2\,\mathrm{mg\,L^{-1}}$ Co, on a $2\,\mathrm{mL}$ AG 1x4 column. For each of the different eluents investigated, the elution profile is represented as a series of circles, the areas of which are proportional to the recovery of an element in each respective fraction.
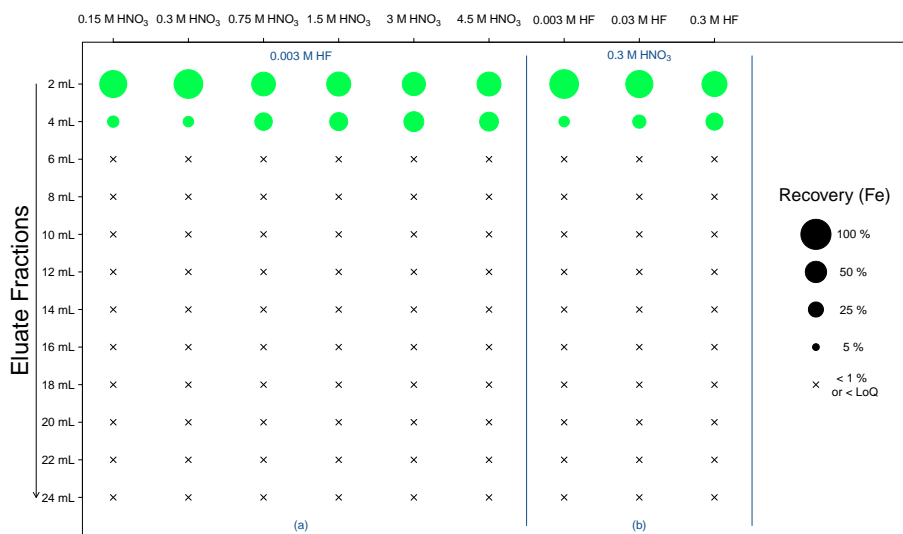
Figure 5.18: Isocratic elution profiles of Ni obtained upon loading $1\,\mathrm{mL}$ of a synthetic sample, containing *ca.* $2\,\mathrm{mg\,L^{-1}}$ Ni, on a $2\,\mathrm{mL}$ AG 1x4 column. For each of the different eluents investigated, the elution profile is represented as a series of circles, the areas of which are proportional to the recovery of an element in each respective fraction.
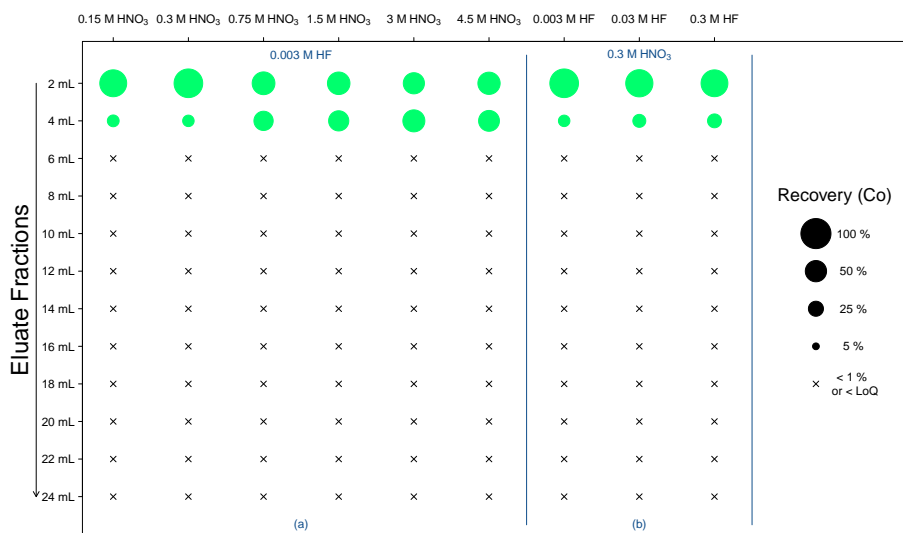

Figure 5.19: Isocratic elution profiles of Cu obtained upon loading $1\,\mathrm{mL}$ of a synthetic sample, containing *ca.* $2\,\mathrm{mg\,L^{-1}}$ Cu, on a $2\,\mathrm{mL}$ AG 1x4 column. For each of the different eluents investigated, the elution profile is represented as a series of circles, the areas of which are proportional to the recovery of an element in each respective fraction.
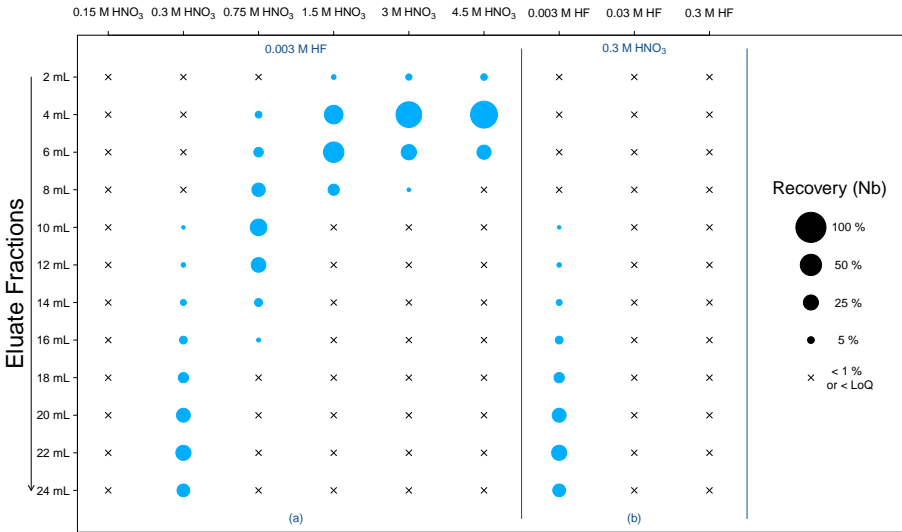
Figure 5.20: Isocratic elution profiles of Nb obtained upon loading $1\,\mathrm{mL}$ of a synthetic sample, containing *ca.* $0.2\,\mathrm{mg\,L^{-1}}$ Nb, on a $2\,\mathrm{mL}$ AG 1x4 column. For each of the different eluents investigated, the elution profile is represented as a series of circles, the areas of which are proportional to the recovery of an element in each respective fraction.

Figure 5.21: Isocratic elution profiles of Mo obtained upon loading $1\,\mathrm{mL}$ of a synthetic sample, containing *ca.* $0.2\,\mathrm{mg\,L^{-1}}$ Mo, on a $2\,\mathrm{mL}$ AG 1x4 column. For each of the different eluents investigated, the elution profile is represented as a series of circles, the areas of which are proportional to the recovery of an element in each respective fraction.
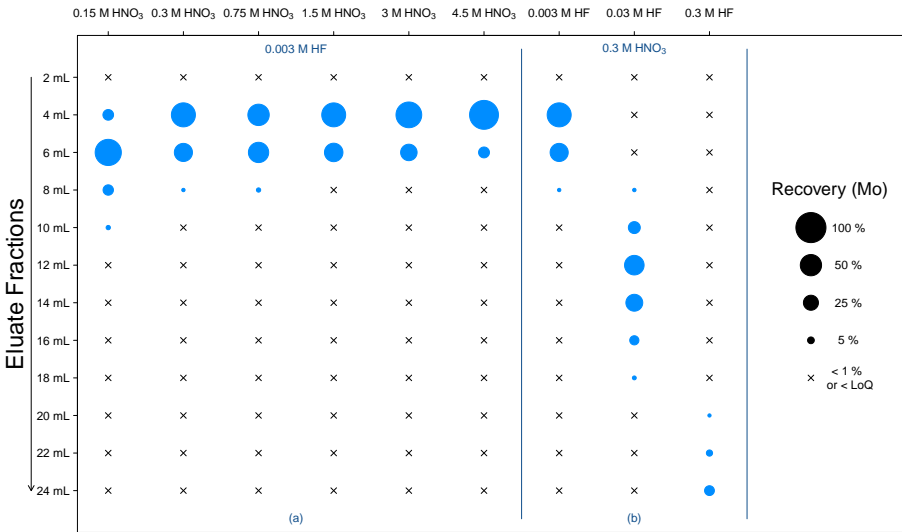
Figure 5.22: Isocratic elution profiles of Ag obtained upon loading $1\,\mathrm{mL}$ of a synthetic sample, containing *ca.* $0.2\,\mathrm{mg\,L^{-1}}$ Ag, on a $2\,\mathrm{mL}$ AG 1x4 column. For each of the different eluents investigated, the elution profile is represented as a series of circles, the areas of which are proportional to the recovery of an element in each respective fraction.
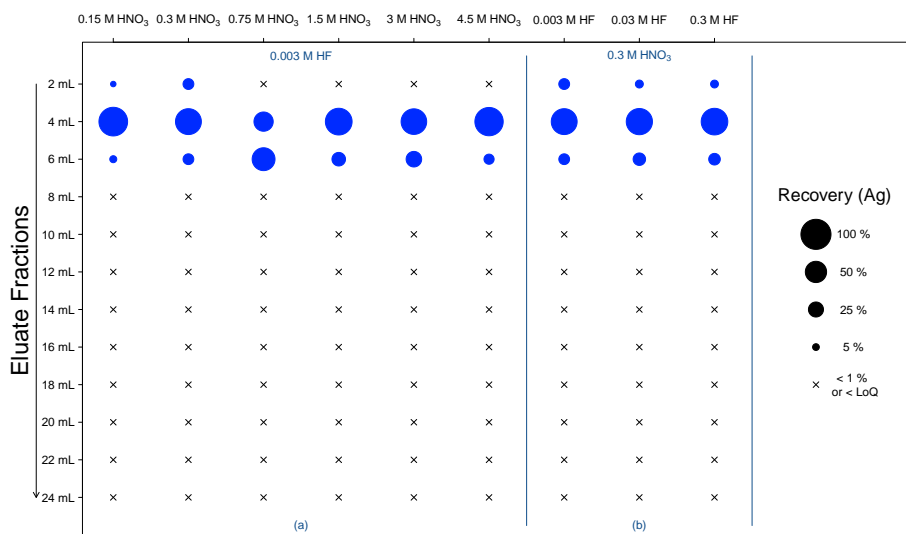

Figure 5.23: Isocratic elution profiles of Cd obtained upon loading $1\,\mathrm{mL}$ of a synthetic sample, containing *ca.* $0.2\,\mathrm{mg\,L^{-1}}$ Cd, on a $2\,\mathrm{mL}$ AG 1x4 column. For each of the different eluents investigated, the elution profile is represented as a series of circles, the areas of which are proportional to the recovery of an element in each respective fraction.
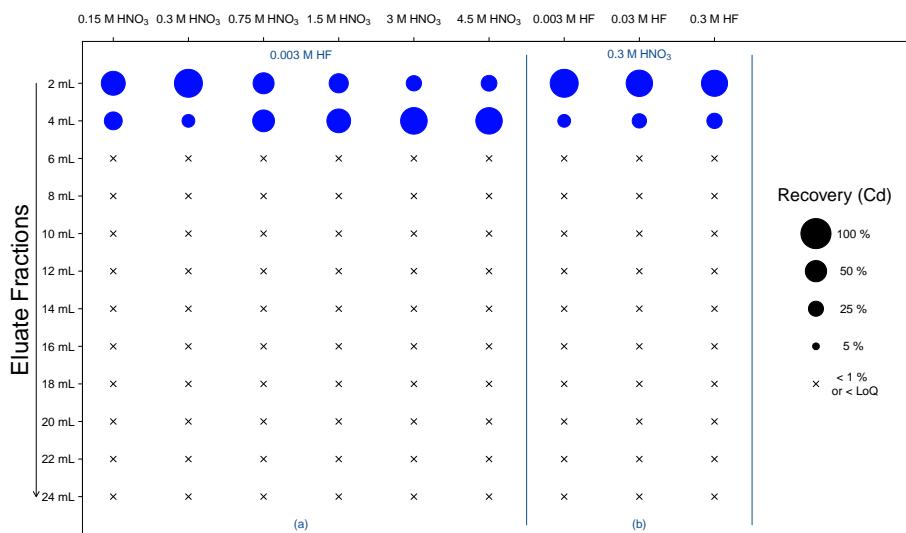
Figure 5.24: Isocratic elution profiles of Te obtained upon loading $1\,\mathrm{mL}$ of a synthetic sample, containing *ca.* $0.2\,\mathrm{mg\,L^{-1}}$ Te, on a $2\,\mathrm{mL}$ AG 1x4 column. For each of the different eluents investigated, the elution profile is represented as a series of circles, the areas of which are proportional to the recovery of an element in each respective fraction.

Figure 5.25: Isocratic elution profiles of Ce obtained upon loading $1\,\mathrm{mL}$ of a synthetic sample, containing *ca.* $0.2\,\mathrm{mg\,L^{-1}}$ Ce, on a $2\,\mathrm{mL}$ AG 1x4 column. For each of the different eluents investigated, the elution profile is represented as a series of circles, the areas of which are proportional to the recovery of an element in each respective fraction.
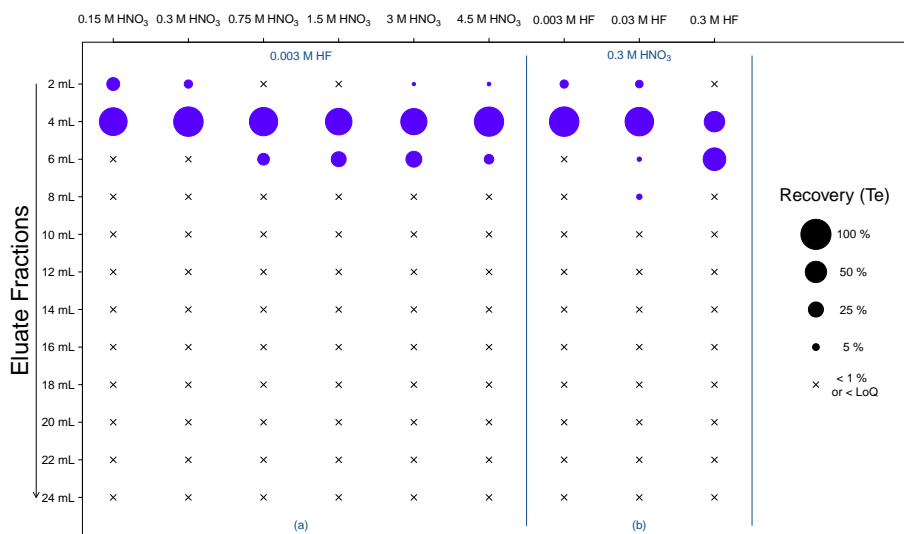
Figure 5.26: Isocratic elution profiles of Re obtained upon loading $1\,\mathrm{mL}$ of a synthetic sample, containing *ca.* $0.2\,\mathrm{mg\,L^{-1}}$ Re, on a $2\,\mathrm{mL}$ AG 1x4 column. For each of the different eluents investigated, the elution profile is represented as a series of circles, the areas of which are proportional to the recovery of an element in each respective fraction.
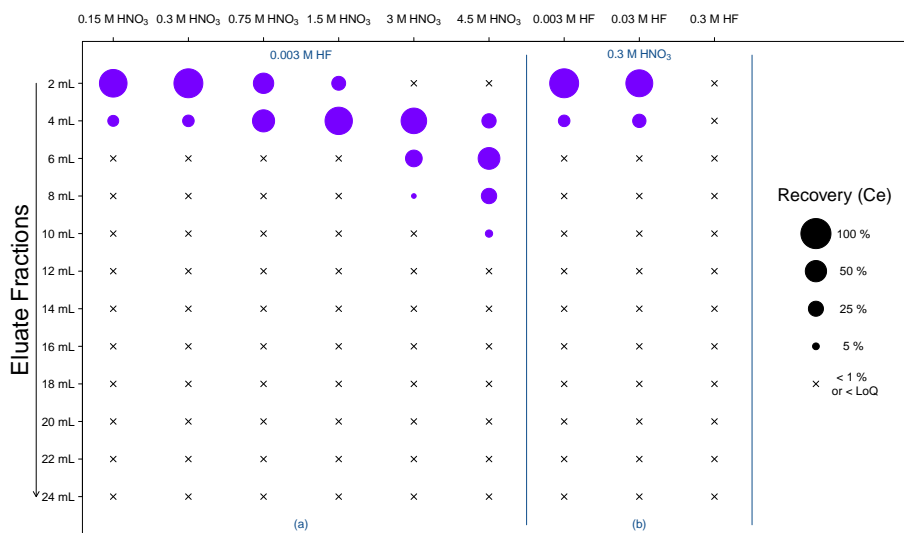

Figure 5.27: Isocratic elution profiles of Tl obtained upon loading $1\,\mathrm{mL}$ of a synthetic sample, containing *ca.* $0.2\,\mathrm{mg\,L^{-1}}$ Tl, on a $2\,\mathrm{mL}$ AG 1x4 column. For each of the different eluents investigated, the elution profile is represented as a series of circles, the areas of which are proportional to the recovery of an element in each respective fraction.
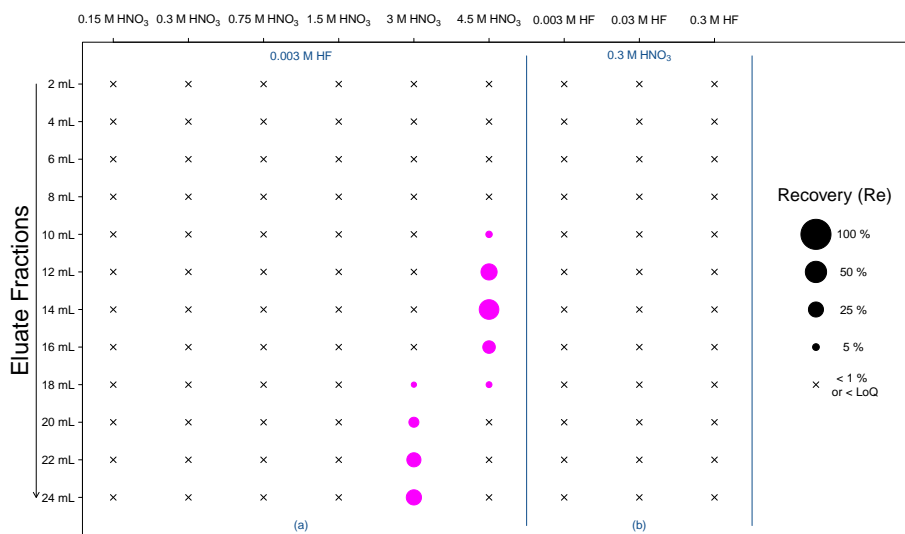
Figure 5.28: Isocratic elution profiles of Pb obtained upon loading $1\,\mathrm{mL}$ of a synthetic sample, containing *ca.* $0.2\,\mathrm{mg}\,\mathrm{L}^{-1}$ Pb, on a $2\,\mathrm{mL}$ AG 1x4 column. For each of the different eluents investigated, the elution profile is represented as a series of circles, the areas of which are proportional to the recovery of an element in each respective fraction.
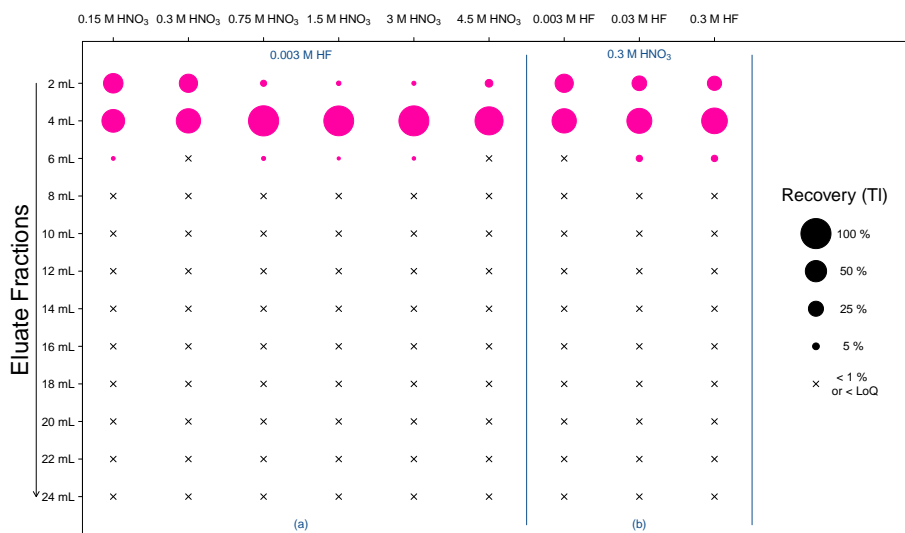

Figure 5.29: Isocratic elution profiles of Bi obtained upon loading $1\,\mathrm{mL}$ of a synthetic sample, containing *ca.* $0.2\,\mathrm{mg}\,\mathrm{L}^{-1}$ Bi, on a $2\,\mathrm{mL}$ AG 1x4 column. For each of the different eluents investigated, the elution profile is represented as a series of circles, the areas of which are proportional to the recovery of an element in each respective fraction.

Figure 5.30: Isocratic elution profiles of Th obtained upon loading $1\,\mathrm{mL}$ of a synthetic sample, containing *ca.* $0.2\,\mathrm{mg\,L^{-1}}$ Th, on a $2\,\mathrm{mL}$ AG 1x4 column. For each of the different eluents investigated, the elution profile is represented as a series of circles, the areas of which are proportional to the recovery of an element in each respective fraction.
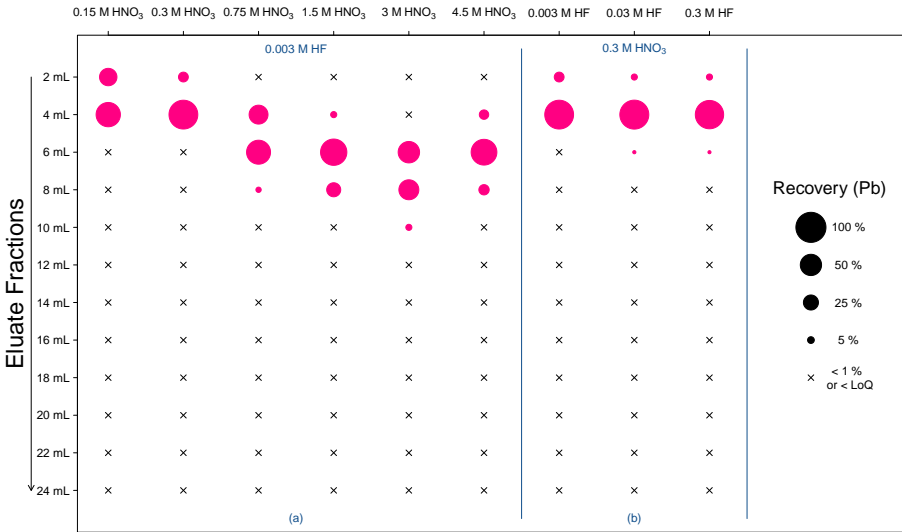

Figure 5.31: Isocratic elution profiles of U obtained upon loading $1\,\mathrm{mL}$ of a synthetic sample, containing *ca.* $0.2\,\mathrm{mg\,L^{-1}}$ U, on a $2\,\mathrm{mL}$ AG 1x4 column. For each of the different eluents investigated, the elution profile is represented as a series of circles, the areas of which are proportional to the recovery of an element in each respective fraction.
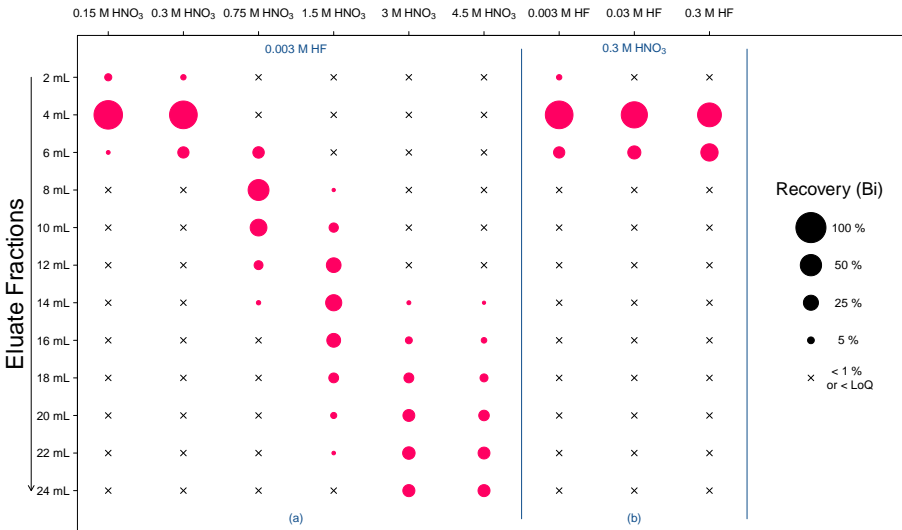
Figure 5.32: Isocratic elution profiles of Ti obtained upon loading $1\,\mathrm{mL}$ of a synthetic sample, containing *ca.* $0.2\,\mathrm{mg\,L^{-1}}$ Ti, on a $2\,\mathrm{mL}$ Pb Spec column. For each of the different eluents investigated, the elution profile is represented as a series of circles, the areas of which are proportional to the recovery of an element in each respective fraction.
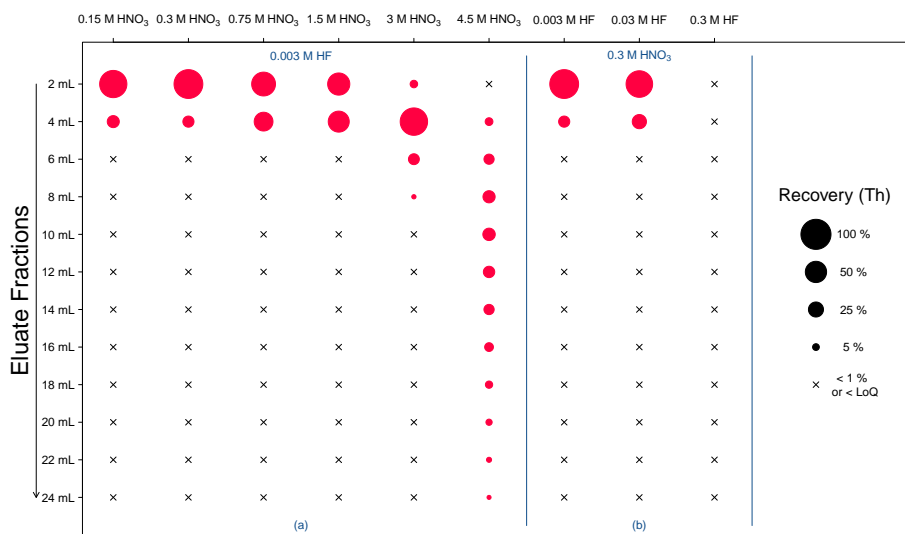

Figure 5.33: Isocratic elution profiles of V obtained upon loading $1\,\mathrm{mL}$ of a synthetic sample, containing *ca.* $0.2\,\mathrm{mg\,L^{-1}}$ V, on a $2\,\mathrm{mL}$ Pb Spec column. For each of the different eluents investigated, the elution profile is represented as a series of circles, the areas of which are proportional to the recovery of an element in each respective fraction.

Figure 5.34: Isocratic elution profiles of Cr obtained upon loading $1\,\mathrm{mL}$ of a synthetic sample, containing *ca.* $2\,\mathrm{mg\,L^{-1}}$ Cr, on a $2\,\mathrm{mL}$ Pb Spec column. For each of the different eluents investigated, the elution profile is represented as a series of circles, the areas of which are proportional to the recovery of an element in each respective fraction.
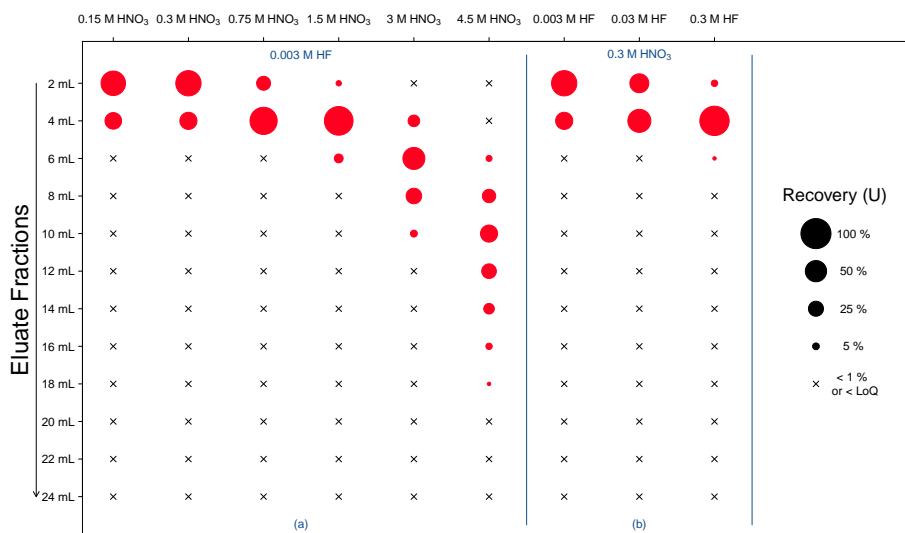
Figure 5.35: Isocratic elution profiles of Mn obtained upon loading $1\,\mathrm{mL}$ of a synthetic sample, containing *ca.* $0.2\,\mathrm{mg\,L^{-1}}$ Mn, on a $2\,\mathrm{mL}$ Pb Spec column. For each of the different eluents investigated, the elution profile is represented as a series of circles, the areas of which are proportional to the recovery of an element in each respective fraction.
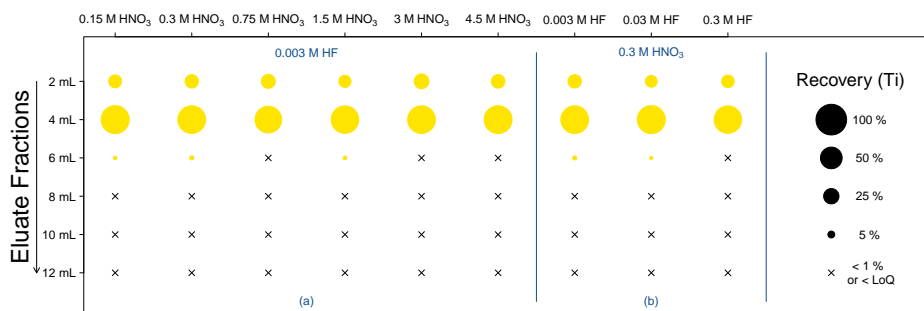

Figure 5.36: Isocratic elution profiles of Fe obtained upon loading $1\,\mathrm{mL}$ of a synthetic sample, containing *ca.* $2\,\mathrm{mg\,L^{-1}}$ Fe, on a $2\,\mathrm{mL}$ Pb Spec column. For each of the different eluents investigated, the elution profile is represented as a series of circles, the areas of which are proportional to the recovery of an element in each respective fraction.
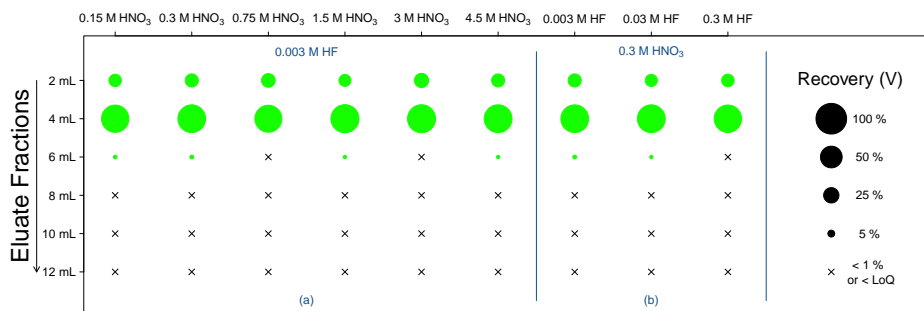

Figure 5.37: Isocratic elution profiles of Co obtained upon loading $1\,\mathrm{mL}$ of a synthetic sample, containing *ca.* $0.2\,\mathrm{mg\,L^{-1}}$ Co, on a $2\,\mathrm{mL}$ Pb Spec column. For each of the different eluents investigated, the elution profile is represented as a series of circles, the areas of which are proportional to the recovery of an element in each respective fraction.

Figure 5.38: Isocratic elution profiles of Ni obtained upon loading $1\,\mathrm{mL}$ of a synthetic sample, containing *ca.* $2\,\mathrm{mg\,L^{-1}}$ Ni, on a $2\,\mathrm{mL}$ Pb Spec column. For each of the different eluents investigated, the elution profile is represented as a series of circles, the areas of which are proportional to the recovery of an element in each respective fraction.
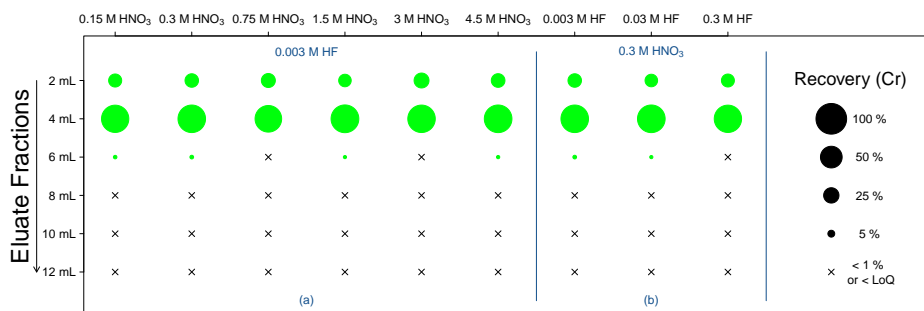

Figure 5.39: Isocratic elution profiles of Cu obtained upon loading $1\,\mathrm{mL}$ of a synthetic sample, containing *ca.* $2\,\mathrm{mg\,L^{-1}}$ Cu, on a $2\,\mathrm{mL}$ Pb Spec column. For each of the different eluents investigated, the elution profile is represented as a series of circles, the areas of which are proportional to the recovery of an element in each respective fraction.
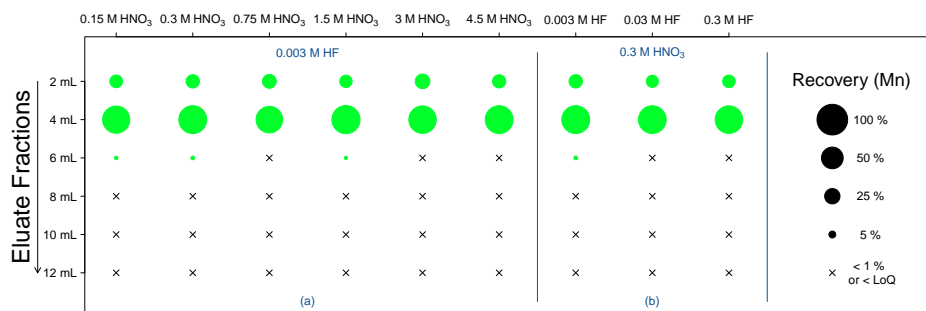

Figure 5.40: Isocratic elution profiles of Nb obtained upon loading $1\,\mathrm{mL}$ of a synthetic sample, containing *ca.* $0.2\,\mathrm{mg\,L^{-1}}$ Nb, on a $2\,\mathrm{mL}$ Pb Spec column. For each of the different eluents investigated, the elution profile is represented as a series of circles, the areas of which are proportional to the recovery of an element in each respective fraction.
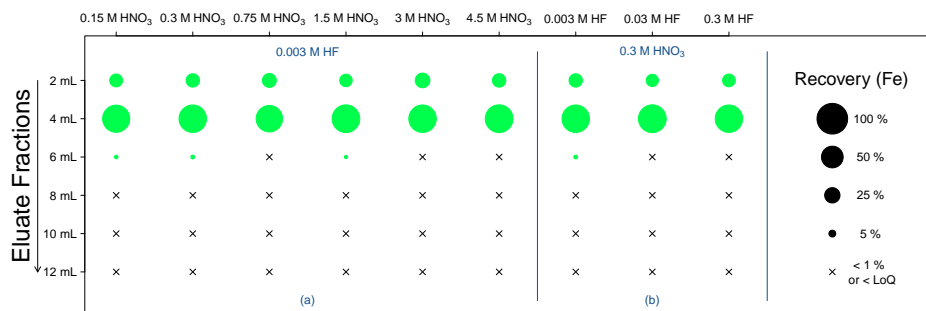
Figure 5.41: Isocratic elution profiles of Mo obtained upon loading $1\,\mathrm{mL}$ of a synthetic sample, containing *ca.* $0.2\,\mathrm{mg\,L^{-1}}$ Mo, on a $2\,\mathrm{mL}$ Pb Spec column. For each of the different eluents investigated, the elution profile is represented as a series of circles, the areas of which are proportional to the recovery of an element in each respective fraction.
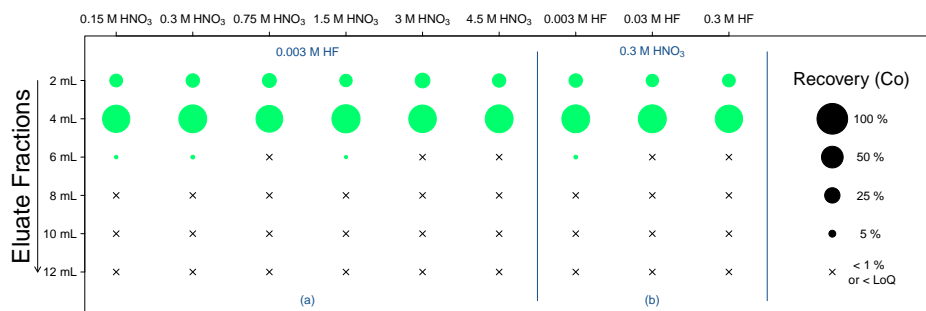

Figure 5.42: Isocratic elution profiles of Ag obtained upon loading $1\,\mathrm{mL}$ of a synthetic sample, containing *ca.* $0.2\,\mathrm{mg\,L^{-1}}$ Ag, on a $2\,\mathrm{mL}$ Pb Spec column. For each of the different eluents investigated, the elution profile is represented as a series of circles, the areas of which are proportional to the recovery of an element in each respective fraction.

Figure 5.43: Isocratic elution profiles of Cd obtained upon loading $1\,\mathrm{mL}$ of a synthetic sample, containing *ca.* $0.2\,\mathrm{mg\,L^{-1}}$ Cd, on a $2\,\mathrm{mL}$ Pb Spec column. For each of the different eluents investigated, the elution profile is represented as a series of circles, the areas of which are proportional to the recovery of an element in each respective fraction.
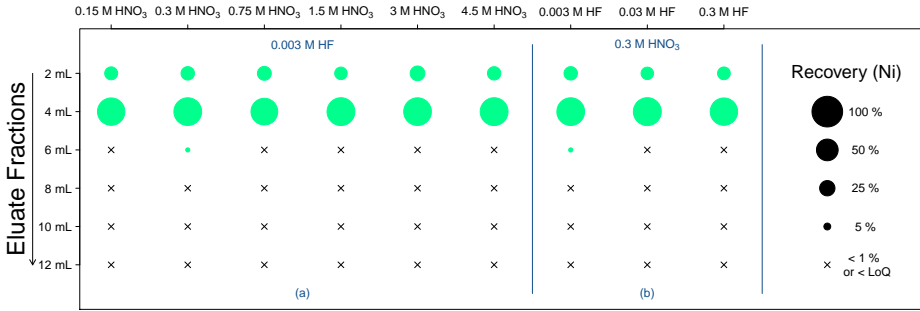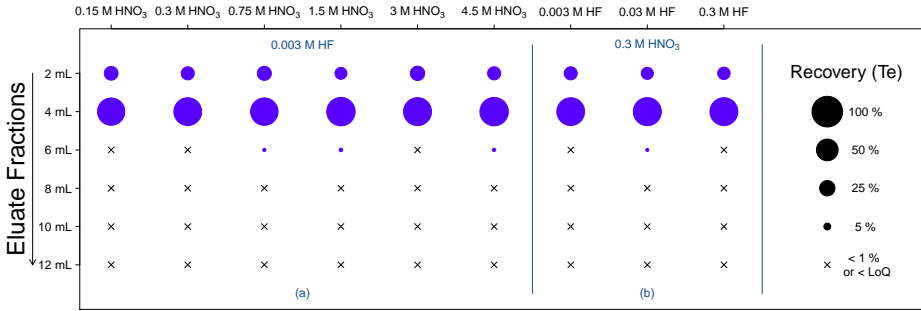
Figure 5.44: Isocratic elution profiles of Te obtained upon loading $1\,\text{mL}$ of a synthetic sample, containing *ca.* $0.2\,\text{mg}\,\text{L}^{-1}$ Te, on a $2\,\text{mL}$ Pb Spec column. For each of the different eluents investigated, the elution profile is represented as a series of circles, the areas of which are proportional to the recovery of an element in each respective fraction.
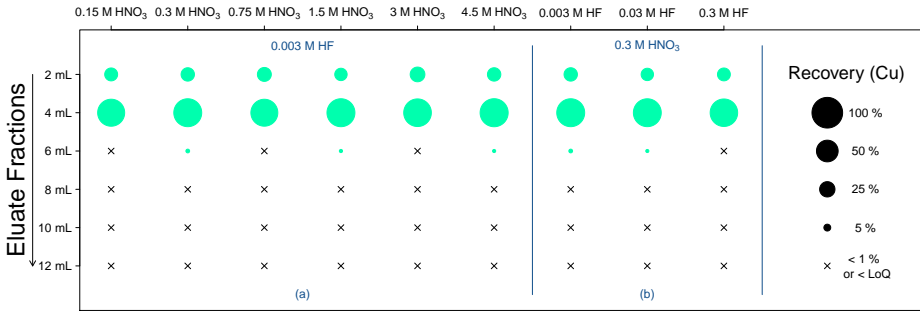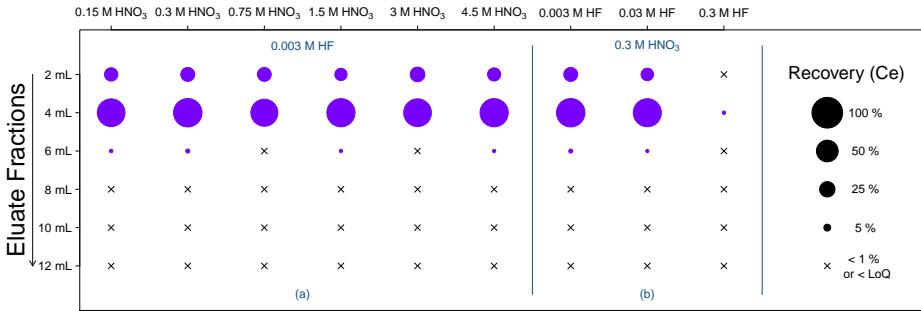

Figure 5.45: Isocratic elution profiles of Ce obtained upon loading $1\,\text{mL}$ of a synthetic sample, containing *ca.* $0.2\,\text{mg}\,\text{L}^{-1}$ Ce, on a $2\,\text{mL}$ Pb Spec column. For each of the different eluents investigated, the elution profile is represented as a series of circles, the areas of which are proportional to the recovery of an element in each respective fraction.
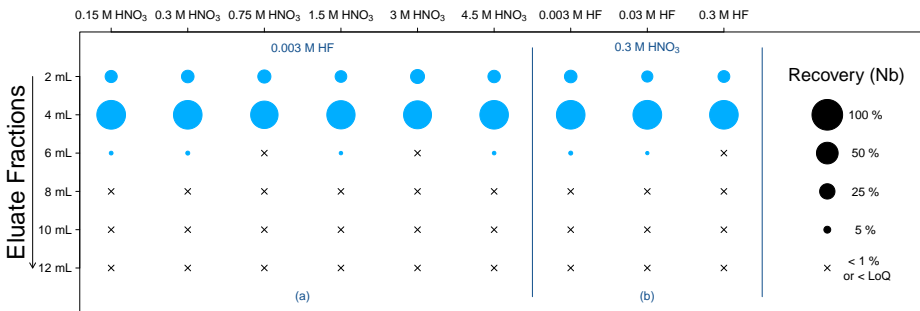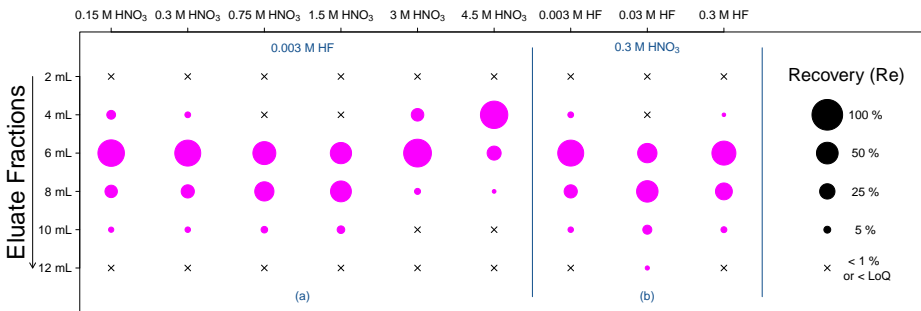

Figure 5.46: Isocratic elution profiles of Re obtained upon loading $1\,\text{mL}$ of a synthetic sample, containing *ca.* $0.2\,\text{mg}\,\text{L}^{-1}$ Re, on a $2\,\text{mL}$ Pb Spec column. For each of the different eluents investigated, the elution profile is represented as a series of circles, the areas of which are proportional to the recovery of an element in each respective fraction.
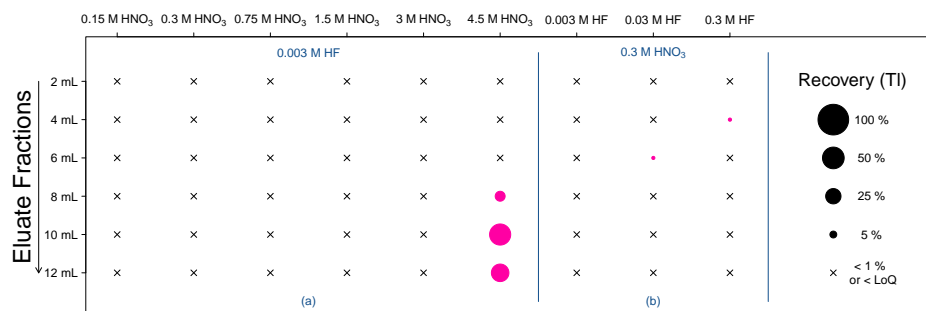
Figure 5.47: Isocratic elution profiles of Tl obtained upon loading $1\,\mathrm{mL}$ of a synthetic sample, containing *ca.* $0.2\,\mathrm{mg\,L^{-1}}$ Tl, on a $2\,\mathrm{mL}$ Pb Spec column. For each of the different eluents investigated, the elution profile is represented as a series of circles, the areas of which are proportional to the recovery of an element in each respective fraction.
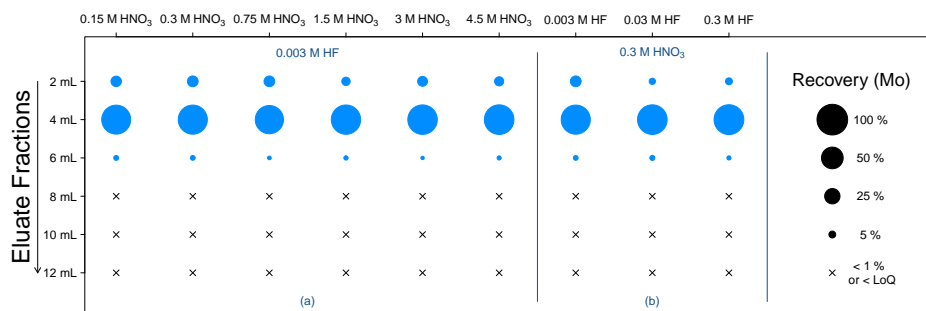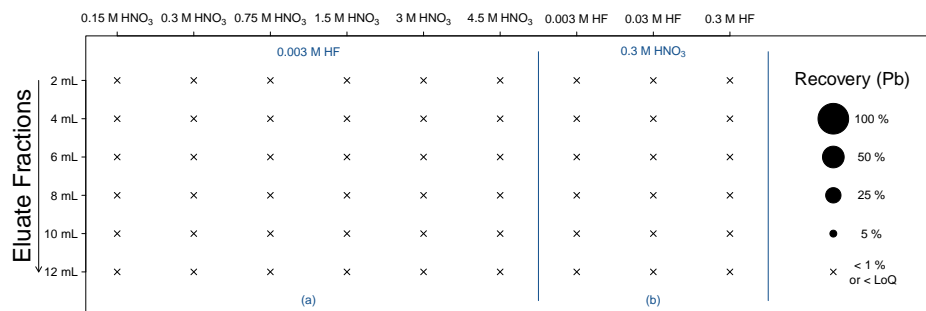

Figure 5.48: Isocratic elution profiles of Pb obtained upon loading $1\,\mathrm{mL}$ of a synthetic sample, containing *ca.* $0.2\,\mathrm{mg\,L^{-1}}$ Pb, on a $2\,\mathrm{mL}$ Pb Spec column. For each of the different eluents investigated, the elution profile is represented as a series of circles, the areas of which are proportional to the recovery of an element in each respective fraction.
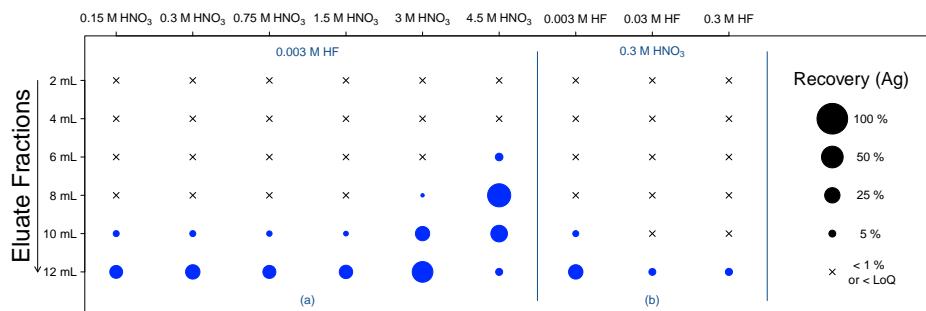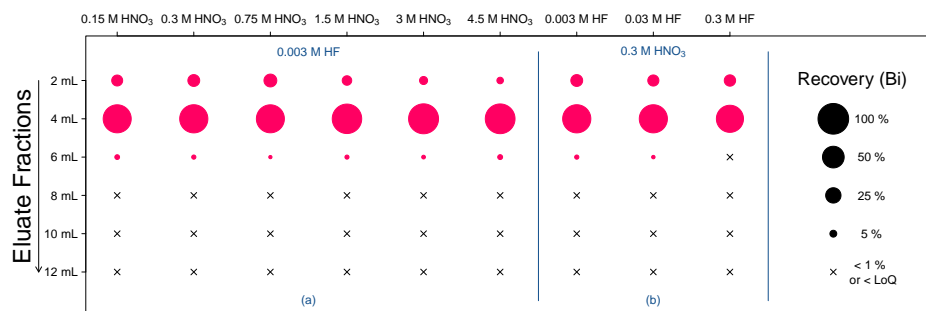

Figure 5.49: Isocratic elution profiles of Bi obtained upon loading $1\,\mathrm{mL}$ of a synthetic sample, containing *ca.* $0.2\,\mathrm{mg\,L^{-1}}$ Bi, on a $2\,\mathrm{mL}$ Pb Spec column. For each of the different eluents investigated, the elution profile is represented as a series of circles, the areas of which are proportional to the recovery of an element in each respective fraction.
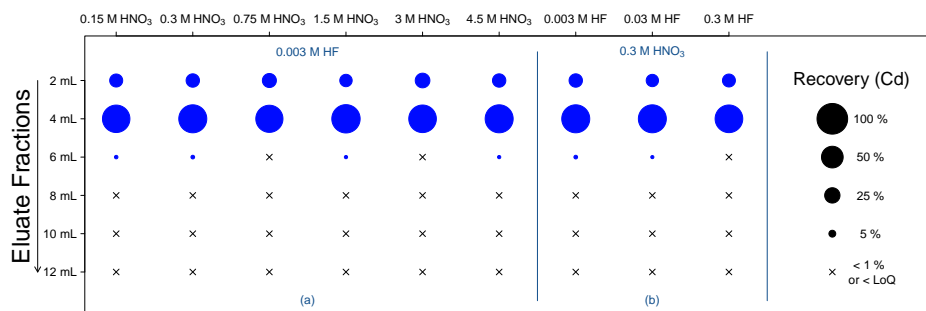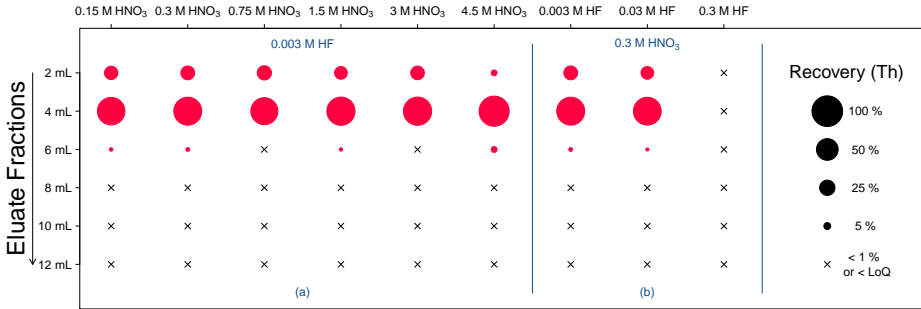
Figure 5.50: Isocratic elution profiles of Th obtained upon loading $1\,\mathrm{mL}$ of a synthetic sample, containing *ca.* $0.2\,\mathrm{mg\,L^{-1}}$ Th, on a $2\,\mathrm{mL}$ Pb Spec column. For each of the different eluents investigated, the elution profile is represented as a series of circles, the areas of which are proportional to the recovery of an element in each respective fraction.
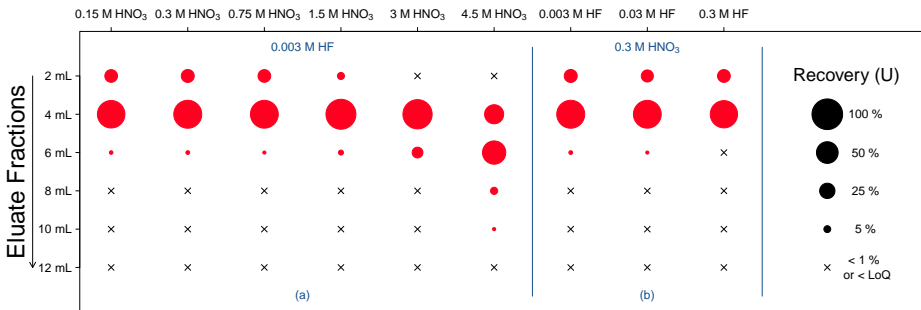
Figure 5.51: Isocratic elution profiles of U obtained upon loading $1\,\mathrm{mL}$ of a synthetic sample, containing *ca.* $0.2\,\mathrm{mg\,L^{-1}}$ U, on a $2\,\mathrm{mL}$ Pb Spec column. For each of the different eluents investigated, the elution profile is represented as a series of circles, the areas of which are proportional to the recovery of an element in each respective fraction.

<div style="display:inline-block">6</div>

Determination of isotope ratios by means of ICP-SFMS

This sixth chapter reports on an evaluation of the capabilities of a nuclearised Element2 ICP-SFMS instrument for the determination of isotope ratios. As previously discussed in Chapter 1, the isotopic analysis of experimental or commercial nuclear fuels, in the context of fuel qualification or spent fuel burnup programs, is already carried out routinely at SCK•CEN, *e.g.* by means of an ageing VG Sector 54 MC-TIMS instrument. For the analytical assays in question, the isotopic analysis of selected lanthanides is of particular importance, which is why mainly the elements Nd, Sm, Eu, Gd and Dy are considered in this chapter. For this particular group of elements, the performance of the ICP-SFMS instrument was compared directly to that of the MC-TIMS instrument, mainly in terms of the attainable isotope ratio precision. Even though an MC-TIMS instrument ought to provide a superior precision, the ICP-SFMS instrument may still be found to be fit-for-purpose in select cases, *i.e.* due to its superior sensitivity or the reduced need for time-consuming sample preparation procedures.

6.1 Introduction

An isotope-number ratio is defined as the ratio of the number of atoms of one isotope to the number of atoms of another isotope, of the same chemical element, in the same system.[147] Thus, when the number of atoms of an isotope ^xE in a substance P is denoted by $N\left(^xE\right)_P$, then isotope-number ratios are given by

$$R\left(^iE/^nE\right)_P = \frac{N\left(^iE\right)_P}{N\left(^nE\right)_P} \tag{6.1}$$

When the substance P contains n distinct isotopes ^iE of the chemical element E, then $n-1$ independent isotope-number ratios may be defined. If the nth isotope represents the reference isotope used in each of the $n-1$ ratios, then the isotopic abundance $x\left(^iE\right)_P$ of each of the isotopes may be calculated via

$$x\left(^iE\right)_P = \frac{R\left(^iE/^nE\right)_P}{\sum\limits_{i=1}^{n} R\left(^iE/^nE\right)_P} \tag{6.2}$$

As such, accurate and precise measurements of isotope-number ratios are a prerequisite to the precise and accurate determination of the isotopic abundances of an element's istopes in samples such as spent nuclear fuels. In this text, for the sake of brevity, the shorthand term "isotope ratio" and symbol R_{true} are employed to refer to an isotope-number ratio as defined above. Fortunately, when using a mass spectrometric system such as an ICP-MS instrument, this isotope ratio

may be determined in a fairly straightforward manner, *i.e.* by monitoring the ion
currents corresponding to the singly charged ions of the two isotopes of interest,
and ratioing the resulting signal intensities against one another. However, the
measured isotope ratio R_{meas} may differ quite substantially from the true isotope
ratio R_{true} as a result of the occurrence of dead time-induced count rate losses or
mass discrimination effects, important issues that need to be addressed and which
are discussed and investigated in greater detail below (see Sections 6.3.1 and 6.3.2).
In addition, it is important for the reader to know that, for the purposes of this
text, the isotope ratio precision is defined as a simple standard deviation of a
number of replicate measurements performed on a single sample (rather than *e.g.*
a standard error on the mean). Whereas MC-TIMS is capable of providing isotope
ratio precisions of $\leq 0.01\,\%$ RSD on a routine basis, more modest isotope ratio
precisions of just $\leq 0.05\,\%$ RSD have been reported for single-collector ICP-SFMS
instruments in the literature. [42] Such values were obtained only under the most
favourable of ICP-SFMS measurement conditions, *i.e.* whilst operating the instru-
ment in the lowest resolution mode and when considering an isotope ratio of *ca.* 1:1
for an element that was present at sufficiently high concentration. When a single-
collector ICP-SFMS instrument is operated at higher mass resolution, to eliminate
spectral interferences, its characteristic flat-top peaks are sacrificed in favor of
more or less triangular peaks. As a result, the attainable isotope ratio precision
deteriorates (see Section 2.7.2) to values of $\geq 0.1\,\%$ RSD, as has been reported
in the literature previously. [148] However, Trešl *et al.* reported that the attainable
isotope ratio precision at higher mass resolution was initially poorer than expected,
due to a significant mass scale shift, whereby offline data treatment was deemed
essential to overcome this problem. [149] Therefore, only the lowest resolution mode
was considered in this work, even though many of the oxide-based polyatomic
interferences that often hamper the determination of the heavier lanthanides under
consideration ought to be resolvable in the Element2's highest resolution mode.
In contrast, MC-TIMS measurements typically suffer less from spectral interfer-
ences, in part due to the application of extensive sample pretreatment procedures
designed to selectively isolate the analytes. However, its superior precision not
withstanding, TIMS also has a number of important limitations which should
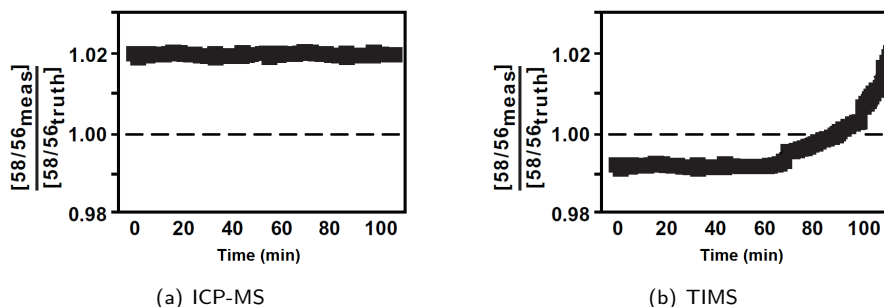

(a) ICP-MS   (b) TIMS

Figure 6.1: Schematic representation of the mass discrimination and mass fractionation effects that are
observed during isotope ratio measurements by means of ICP-MS and TIMS, respectively. [90]

be taken into account. Firstly, generating positive ions by thermal ionisation is only efficient for non-volatile target elements with ionisation energies below 7.5 eV, although these issues can be attenuated by employing ionisation activators or by generating negative ions instead of positive ones. In addition, the target elements should be selectively isolated from their concomitant matrix, before loading them onto a filament, to allow for their efficient ionisation. Such filaments are then placed in the TIMS instrument's sample introduction compartment, prior to this chamber being evacuated by means of a vacuum pump over the course of several hours. All things considered, sample pretreatment is relatively complicated, laborious and time-consuming. In contrast, target elements with an ionisation energy of ≥ 7.5 eV can be efficiently ionised in an ICP source, irrespective of the concomitant matrix (although a significant signal suppression or enhancement may still be observed). As a result, for less demanding applications, there may be a reduced need for labour-intensive sample pretreatment procedures than with TIMS. In addition, ICP-SFMS measurements are typically less time-consuming than TIMS measurements; minutes versus hours, and, when the instrument is coupled to a solid-sampling technique such as laser ablation, the need for extensive and drawn out sample pretreatment may disappear. However, in contrast to a thermal surface ionisation source, an ICP is a relatively noisy source of ions, as a result of short term fluctuations in the sample introduction, ionisation and extraction efficiencies. In MC-ICP-SFMS instruments, the observed fluctuations do not deteriorate the isotope ratio precision greatly, because the nuclides of interest are all monitored simultaneously whereby these fluctuations cancel each other out to a certain extent. As a result, optimum isotope ratio precisions of as low as *ca.* 0.002 % RSD have been reported for MC-ICP-SFMS, rivaling those attainable by means of MC-TIMS.[150] Conversely, on a single-collector ICP-SFMS instrument, the observed signal flicker can be counteracted to some extent by employing high scanning speeds. In this context, the so-called peak-hopping mode is employed, whereby the mass analyser setting is changed discontinuously, such that the mass spectrometer "jumps" quickly from nuclide to nuclide, in an effort to cancel out at least part of the observed signal flicker, although the isotope ratio precision does inevitably suffer when only a single collector is used. Another issue that hampers ICP-SFMS analyses is that of mass discrimination, *i.e.* a higher transport efficiency for heavier nuclides versus lighter ones, which results in a significant, but relatively constant mass bias (see Figure 6.1a). Several approaches have been proposed to correct for the mass discrimination effects observed in ICP-SFMS, although this phenomenon is not yet as well understood as the mass fractionation effects that are observed for TIMS measurements, *i.e.* a time-dependent variation of the ion beam composition as a result of the initial preferential thermal ionisation of lighter nuclides (see Figure 6.1b). Furthermore, whereas MC-TIMS and MC-ICP-SFMS instruments often employ an array of highly stable Faraday cups as detectors, the Element2 ICP-SFMS is equipped with a single discrete-dynode *Secondary Electron Multiplier* (SEM) only. When an SEM is operated in the analog mode rather than in the pulse counting mode, the observed mass bias is typically more

pronounced, because the secondary electron yield from the conversion dynode is also mass-dependent.[90] Therefore, this type of detector is usually operated in the pulse counting mode, in which the number of pulses is recorded rather than an analog current, in order to reduce the mass-dependence of the signal output. However, the use of the pulse counting mode does result in dead time-induced count rate losses, as has already been discussed in Section 2.8.1. If this phenomenon is not corrected for, it leads to a non-linear detector response, an issue that becomes increasingly important when determining extreme isotope ratios where the count rate of one nuclide is affected much more severely than the other. In this work, the abovementioned considerations regarding the determination of isotope ratios by means of single-collector ICP-SFMS were examined. Most importantly, the performance of SCK•CEN's nuclearised Element2 ICP-SFMS instrument was evaluated in terms of the attainable isotope ratio precision.[37,42,43,49,90,148–158]

6.2   Experimental

The reagents and labware used in the preparation of samples, blanks and rinse solutions have been discussed in Chapter 3. That chapter also included an overview of the typical instrumental parameters of SCK•CEN's nuclearised Element2. For the determination of isotope ratios, the instrument's sample introduction system usually consisted of a low-flow self-aspirating PFA concentric nebuliser and a quartz dual cyclonic/double-pass Scott-type spray chamber. Initially, a glass cyclonic spray chamber was also considered, but the resulting experimental data indicated that the isotope ratio precision would probably be poorer by a factor of *ca.* 2. In terms of isotope ratio precision, those same exploratory experiments revealed no discernible difference between pumped or self-aspirating modes, in terms of isotope ratio precision. Nonetheless, a self-aspirating nebuliser was selected on the recommendation of the spray chamber's manufacturer. This nebuliser had a very low sample uptake rate (*ca.* 60 µL min^{-1}), which reduced the risk of liquid buildup in the dual spray chamber's second compartment (which is not evacuated by means of a drain). The use of an additional Ar gas flow, introduced into the second compartment of the dual spray chamber, was also briefly considered. However, since no marked improvement was observed in terms of sensitivity or isotope ratio precision, its use was not investigated further. The most commonly used data acquisition parameters are presented below, along with a limited discussion of the sample preparation techniques employed.

6.2.1   Data acquisition parameters

For the purposes of these experiments, the instrument's detector was forcibly operated in the pulse counting mode, instead of in the dual pulse counting/analog mode. To accommodate the detector's reduced linear range ($\leq 4\,000\,000$ counts s^{-1}), each sample had to be prepared accordingly. Nuclides were monitored only in the low resolution mode, with the selected mass windows corresponding to a section of the trapezoidal flat-top peaks' plateaus. Typical data acquisition parameters are

Table 6.1: Typical data acquisition parameters of the Element2 ICP-SFMS for isotopic analysis.

Setting/parameter	Value/Description
Resolution ($m/\Delta m$)	300
Detector mode	Pulse counting
Scan optimisation	Speed
Number of prescans	10
Dead time	$12\,\text{ns}^{\dagger}$
Runs	5
Passes	600
Dwell time	10 ms (2 nuclides)
	6.6 ms (3 nuclides)
Mass window	2 %
Integration window	2 %
Samples per peak	250
Settling time	1 ms
Total data acquisition time	$5 \times 60\,\text{s}$

† *Dead time correction performed offline*

summarised in Table 6.1. The time spent monitoring a single nuclide is determined by several different settings, provided in this table, including the observed mass window and the number of samples per peak, which together determine the number of data points for each nuclide. When the mass window is set to 2 %, and the number of samples per peak is set to 250, a total of 5 data points are obtained for each peak for every single mass scan (or "pass"). The dwell time, in turn, represents the measurement time for each data point acquired as part of such a mass scan. Thus, when 5 data points are acquired separately for two nuclides, whilst the dwell times for both isotopes are set to 10 ms, then a single pass lasts 100 ms (not taking into account the settling times that are required when jumping from data point to data point). Finally, if a measurement (or "run") consists of 600 sequential passes, then the total data acquisition time amounts to 60 s. Most often, and unless stated otherwise, the dwell times were balanced, with each nuclide being monitored for the same amount of time during a measurement. In general, when either 2 or 3 individual isotopes were monitored sequentially, the dwell times were 10 ms and 6.6 ms, respectively. Initially, shorter dwell times were also considered (down to 1 ms), accompanied by an increase in the number of passes (up to 6000), such that the total data acquisition time was kept constant (60 s for each run). However, the isotope ratio precision was not noticeably affected and the duty cycle had therefore been unnecessarily reduced.

6.2.2   Sample preparation procedures

Synthetic samples were prepared by volumetric serial dilution of $1000\,\text{mg}\,\text{L}^{-1}$ single-element stock solutions, to concentrations of *ca.* 0.2 to $8\,\mu\text{g}\,\text{L}^{-1}$ in a 1 M HNO_3 matrix. Elemental concentrations were selected in advance such that the maximum signal intensity for any of the nuclides under consideration never exceeded $3\,200\,000\,\text{counts}\,\text{s}^{-1}$. The natural isotopic abundances for each

Table 6.2: Representative terrestrial isotopic composition of selected rare-earth elements, expressed via relative abundances of naturally occurring isotopes. [159] The nuclides that were chosen as reference isotopes in the context of this work are highlighted in red. In addition, for each of these elements, an indication is given of the approximate concentration that was typically required for generating a signal intensity of *ca.* $1\,000\,000\,\mathrm{counts\,s^{-1}}$ on the reference isotope with the ICP-SFMS instrument used.

Nuclide	Ba	Nd	Sm	Eu	Gd	Dy	Lu
130	0.001 06						
131							
132	0.001 01						
133							
134	0.024 17						
135	0.065 92						
136	0.078 54						
137	0.112 32						
138	0.716 98						
⋮							
142		0.271 52					
143		0.121 74†					
144		0.237 98	0.0307				
145		0.082 93					
146		0.171 89					
147			0.1499				
148		0.057 56	0.1124				
149			0.1382				
150		0.056 38	0.0738				
151				0.4781			
152			0.2675		0.0020		
153				0.5219			
154			0.2275		0.0218		
155					0.1480		
156					0.2047	0.000 56	
157					0.1565		
158					0.2484	0.000 95	
159							
160					0.2186	0.023 29	
161						0.188 89	
162						0.254 75	
163						0.248 96	
164						0.282 60	
⋮							
175							0.974 01
176							0.025 99
Conc. $(\mathrm{ng\,L^{-1}})$	1.2	5.0	3.2	1.6	4.2	2.6	0.8

† *Radiogenic nuclide*

of the elements considered in this chapter are given in Table 6.2. In this table, the reference nuclide, *i.e.* the denominator in an isotope ratio, for each of the elements under consideration is highlighted in red. In addition, for each element, the approximate concentration that ought to result in a signal intensity of *ca.* $1\,000\,000\,\mathrm{counts\,s^{-1}}$ on the reference nuclide is indicated.

6.3   Results and discussion

A number of the most important aspects related to the determination of iso-
tope ratios by means of ICP-SFMS, as already discussed briefly in the intro-
duction, are examined below. The selected topics include (i) the correction for
dead time-induced count rate losses, (ii) the correction for mass discrimination
effects and (iii) an evaluation of the internal precision attainable.

6.3.1   Dead time correction

The mechanism behind the dead time-induced count rate losses that are typically
encountered in pulse counting systems was described previously in Section 2.8.1.
That section also provided a correction equation applicable to non-paralysable
systems, which is shown again below, with τ representing the dead time.

$$I_\tau = \frac{I_{meas}}{1 - I_{meas} \cdot \tau}$$ (6.3)

In this equation, the measured and dead time-corrected signal intensities are
denoted by I_{meas} and I_τ, respectively. As a result of the fact that the deter-
mination of the dead time is crucial for accurate isotopic analysis, a number
of authors have seen fit to describe their own approaches for characterising τ
in ICP-MS systems, including van Heuzen *et al.*, Vanhaecke *et al.*, Held and
Taylor, Appelblad and Baxter and Ramebäck *et al.*[160–164] Each proposed proce-
dure relies either on performing isotope ratio measurements on standards with
various elemental concentrations or on performing measurements on the detection
system's electrical circuitry. When comparing a selection of these procedures,
Nelms *et al.* and Moser *et al.* found that each resulted in similar dead times.[165,166]
In this work, only the approach described by Appelblad and Baxter was used.
Applying this procedure yields an unambiguous value for τ, along with an es-
timate of its associated uncertainty, whilst mass discrimination is taken into
account without requiring knowledge of an element's true isotopic composition.

In the approach of Appelblad and Baxter, the dead time correction is first
disabled in the instrument's software, after which a series of isotope ratio mea-
surements are performed on standards with various elemental concentrations.
A suitable element ought to possess at least one isotope pair with a ratio
significantly different from 1:1, such as ^{137}Ba/^{138}Ba or ^{176}Lu/^{175}Lu (see Ta-
ble 6.2). As the elemental concentration in the standards is increased, the
measured isotope ratio R_{meas} is also subject to change, because the signal inten-
sity corresponding to the major isotope (*e.g.* ^{138}Ba) is increasingly susceptible
to dead time-induced count rate losses, when compared to that of the minor
isotope (*e.g.* ^{137}Ba). Although isotope ratios are usually defined as the ratio
of the signal intensity of the minor isotope versus that of the major isotope,
a dead time-corrected isotope ratio R_τ can also be expressed inversely as

$$R_\tau = \frac{I_{\tau,M}}{I_{\tau,m}}$$ (6.4)

where $I_{\tau,m}$ and $I_{\tau,M}$ represent the dead time-corrected count rates of the minor and major isotopes, respectively. However, due to the mass discrimination effects that were described previously, a significant bias is usually observed between the dead time-corrected isotope ratio R_{τ} and the true isotope ratio R_{true}, *i.e.* the measured ratio deviates from the true ratio. The mass bias can itself be corrected for by means of a so-called K-factor (see Section 6.3.2).

$$R_{true} = K_{bias} \cdot R_{\tau} \tag{6.5}$$

Substitution of Equations 6.3 and 6.5 into Equation 6.4 results in

$$\frac{R_{true}}{K_{bias}} = \frac{I_{meas,m}^{-1} - \tau}{I_{meas,M}^{-1} - \tau} \tag{6.6}$$

which can then be rearranged to yield a linear relationship between the measured isotope ratio and the measured signal intensity of the major isotope

$$\frac{I_{meas,M}}{I_{meas,m}} = \tau \cdot \left(1 - \frac{R_{true}}{K_{bias}}\right) \cdot I_{meas,M} + \frac{R_{true}}{K_{bias}} \tag{6.7}$$

$$= a \cdot I_{meas,M} + b' \tag{6.8}$$

As a result, if a first degree polynomial is fitted to data points corresponding to isotope ratio measurements performed on several standards with different elemental concentrations, via linear least squares regression, then the dead time can be calculated from the slope a and intercept b' of the curve (see Figure 6.2).

$$\tau = \frac{a}{1 - b'} \tag{6.9}$$

The uncertainties associated with the regression coefficients can be estimated by linear least squares theory, although only if the assumptions underlying

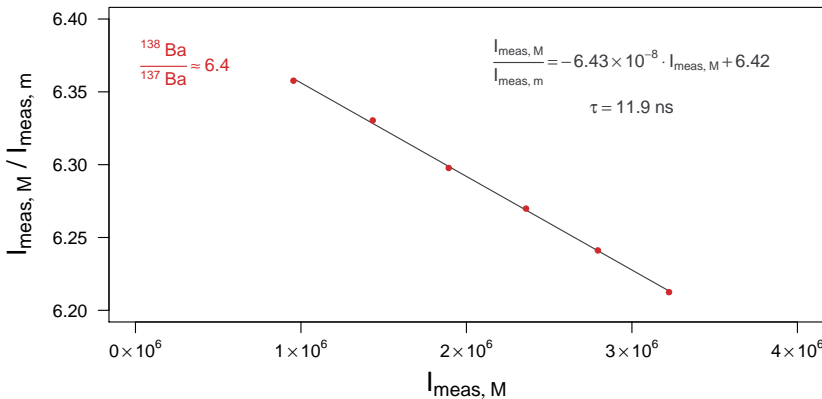**Figure 6.2:** Illustration of the procedure described by Appelblad and Baxter, for determining the dead time in ICP-MS systems. In this case, the measured $^{138}Ba/^{137}Ba$ ratio was monitored and plotted against the measured signal intensity for ^{138}Ba, whereafter a linear least squares model was fitted to the data. The dead time could then be calculated from the regression coefficients via Equation 6.9.

this linear model are valid, after which the uncertainty on the dead time itself can be estimated by error propagation. Although Appelblad and Baxter suggested that the predictor variable may first be centred, in order to reduce the covariance between the coefficients to zero, they instead assumed it to be negligible and did not provide the required calculations. The necessary equations are therefore described briefly below, starting by first modifying Equation 6.8 and expressing it in terms of a centred predictor variable.

$$\frac{I_{meas,M}}{I_{meas,m}} = a \cdot I_{meas,M} - a \cdot \overline{I_{meas,M}} + a \cdot \overline{I_{meas,M}} + b' \tag{6.10}$$

$$= a \cdot \left(I_{meas,M} - \overline{I_{meas,M}} \right) + b \tag{6.11}$$

Where $\overline{I_{meas,M}}$ is the average of the predictor variable. Centering the predictor variable only affects the intercept, such that the slope and intercept equate to

$$a = \tau \cdot \left(1 - \frac{R_{true}}{K_{bias}} \right) \tag{6.12}$$

$$b = a \cdot \overline{I_{meas,M}} + \frac{R_{true}}{K_{bias}} \tag{6.13}$$

Eliminating the mass bias correction factor from these two equations, and rearranging the resulting statement results in an expression of the dead time

$$\tau = \frac{a}{1 + a \cdot \overline{I_{meas,M}} - b} \tag{6.14}$$

An estimate of the combined uncertainty u_c $(k = 1)$, which is associated with the dead time's value, can be found through error propagation, which results in

$$u_c \left(\tau \right) = \sqrt{u_1 \left(\tau \right) + u_2 \left(\tau \right)} \tag{6.15}$$

$$u_1 \left(\tau \right) = \frac{\left(u \left(a \right) \right)^2}{\left(1 + a \cdot \overline{I_{meas,M}} - b \right)^2} \tag{6.16}$$

$$u_2 \left(\tau \right) = \frac{a^2}{\left(1 + a \cdot \overline{I_{meas,M}} - b \right)^4} \times \left[\left(\overline{I_{meas,M}} \cdot u \left(a \right) \right)^2 + \left(u \left(b \right) \right)^2 \right] \tag{6.17}$$

The regression coefficients a and b and their associated uncertainties $u \left(a \right)$ and $u \left(b \right)$, required in Equations 6.14 and 6.15, can be obtained in a straightforward manner by performing a linear least squares regression in commonly used spreadsheet software such as *MS Excel* or statistical software packages such as *R*.[167]

Whilst some authors have reported that the dead time is subject to change as an instrument's detector ages, other have claimed that its value may also be dependent on an analyte's mass number, at least for some types of detectors.[161,168] In this work, the dead time was therefore determined multiple times, at random intervals over a period of more than ten weeks, at more than one SEM voltage setting. Moreover, two separate elements were used for this purpose, one slightly lower in
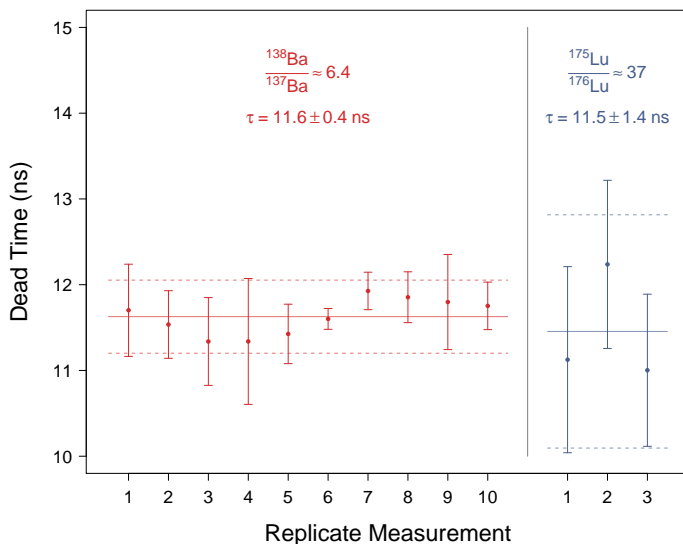
Figure 6.3: The dead time of the Element2's detector, as determined by means of the procedure described by Appelblad and Baxter. Results are shown for a number of replicate analyses, performed over a period of several weeks, for two different elements. The error bars on each individual data point represent the estimated expanded uncertainty ($k = 2$), which was calculated by means of Equation 6.15. The dashed lines correspond to $\tau \pm 2 \cdot s(\tau)$, for each of the two elements under consideration.

mass than the lanthanides of interest (*i.e.* Ba) and one with a mass that was slightly higher (*i.e.* Lu). The result of these replicate analyses are presented in Figure 6.3. As can be seen in that figure, the detector's dead time was found to remain constant, within the estimated expanded uncertainty ($k = 2$), over this period of time. In addition, there was good agreement between the dead times obtained by using both Ba and Lu, indicating that the dead time is mass-independent over the mass range of interest. It should be noted that the instrument's manufacturer recommends using an extreme isotope pair, such as that observed in Lu, because a larger difference in dead time-induced count rate losses between both isotopes is considered favourable. Nonetheless, the dead time as determined by means of Ba was used in all subsequent work, because a less extreme isotope ratio, but still significantly different from 1:1, could be determined with a superior internal precision. In the end, that resulted in an improvement of the uncertainty associated with the dead time. Aside from the detector dead time issue, some authors have also reported the occurrence of "sag", which manifests itself as a count rate reduction, more so than would be expected from the abovementioned dead time-induced losses.[169] At higher count rates, the detector's gain diminishes such that the magnitude of the pulses generated by incident ions is reduced. However, as a result, some pulses can no longer be registered by the detection system, if the magnitude of these pulses falls below a certain threshold value. Fortunately though, no such effect was observed at count rates of up to $3\,200\,000\,\text{counts}\,\text{s}^{-1}$.[44]

6.3.2 Mass bias correction

The mass discrimination effects observed in ICP-MS typically manifest themselves as a higher sensitivity for ions with a higher mass, resulting from the mass-dependencies of the ion extraction, transmission and detection efficiencies. The magnitude of the bias thus created (mass bias) is typically denoted by means of a K-factor, as was illustrated in the previous section, where it was defined as

$$K_{bias} = \frac{R_{true}}{R_{\tau}} \tag{6.18}$$

Although the mechanisms behind the occurrence of mass discrimination in ICP-MS are not yet fully understood, a number of potentially contributing factors have been identified. As the plasma is sampled via the interface and positive ions are transported through the extraction lens behind the skimmer cone, they move at the same speed, *i.e.* that of the bulk plasma gas. As a result, the positive ions' kinetic energies are mass-dependent rather than uniform, affecting their respective transport efficiencies. As was already mentioned in Chapter 2, the positive ions in the ion beam repel one another, due to the occurrence of so-called space-charge effects. As a result of this phenomenon, ions with a lower kinetic energy, *i.e.* lighter ones, have a higher probability of being expelled from the ion beam than those with a higher kinetic energy, *i.e.* heavier ones. In addition, processes that take place during the supersonic expansion of the plasma gas, which emerges from behind the sampler cone, are also believed to play a role. Moreover, the detector's response may also be mass-dependent (see Section 6.3.1), although the Element2's SEM has been designed such that the resulting mass bias should be minimal (see Section 3.1.1). However, specifically in the case of ICP-SFMS instruments such as the Element2, an additional important aspect may affect the observed mass discrimination. When a mass spectrum is acquired through a so-called E-scan at a fixed magnetic field strength, it is necessary to reduce the accelerator voltage for monitoring ions of increasing mass-to-charge ratios (see Section 2.7.2). Reducing the accelerator voltage has the side effect of reducing the ion transport efficiency, whereby the sensitivity for heavier ions is reduced as one moves further away from the magnetic sector's rest mass. It should be noted that this "negative" mass bias counteracts the abovementioned "positive" mass bias effects to some extent. Moreover, the concentration of an analyte, or more likely its concomitant matrix, may also exert an important influence with regard to the magnitude of the observed mass bias. In whichever way they may manifest themselves, several approaches have been considered for coping with the mass discrimination effects observed in ICP-MS with the purpose of performing more accurate isotopic analysis, a number of which are highlighted below. These approaches are typically subdivided into two separate groups, those based on the simultaneous analysis of a calibrator and the measurand (internal correction) and those based on their sequential analysis in a standard-sample-standard bracketing approach (external correction).[39,44,90]

There are two widely employed internal correction procedures, used for the purpose of mass bias correction in isotopic analysis by means of ICP-MS, which

are based either on an inter- or on an intra-element correction. Firstly, an internal standard element (*e.g.* Tl) of known isotopic composition, and of similar mass with respect to the analyte (*e.g.* Pb), may be added to each sample. In this way, the measurement of an independent, but well characterised, isotope ratio (*e.g.* ^{203}Tl/^{205}Tl) may be used to perform a mass bias correction on the measurement of an analyte's isotope ratio (*e.g.* ^{207}Pb/^{208}Pb). However, for a single-collector instrument, where each nuclide has to be measured sequentially, but in rapid succession to cope with the fact that the ICP is a noisy ion source, monitoring additional masses inevitably leads to a deterioration of the isotope ratio precision attainable. Secondly, an analyte element (*e.g.* Sr) with a radiogenic isotope (*e.g.* ^{87}Sr) may posses an additional isotope pair of which the relative composition is almost invariant in nature (*e.g.* ^{86}Sr, ^{88}Sr). Simultaneously measuring an invariant isotope ratio (*e.g.* ^{86}Sr/^{88}Sr) allows one to correct for the mass bias that affects the measurement of the isotope ratio of interest (*e.g.* ^{87}Sr/^{88}Sr). However, this second approach is certainly not applicable to samples with aberrant isotopic compositions, such as those encountered in spent nuclear fuels. With both approaches described above, correction equations have to be applied to account for the fact that the magnitude of the mass bias is dependent on how far the two isotopes are spaced apart in the mass spectrum, requiring the mass bias to be expressed on a per mass unit basis. Three commonly employed empirical equations are presented below, which assume that the mass discrimination factor varies as a linear, power-law or exponential function with the difference in mass between the two isotopes, respectively.

$$K_{bias} = \frac{R_{true}}{R_\tau} = (1 + \epsilon_{lin} \cdot \Delta m) \tag{6.19}$$

$$K_{bias} = \frac{R_{true}}{R_\tau} = (1 + \epsilon_{pow})^{\Delta m} \tag{6.20}$$

$$K_{bias} = \frac{R_{true}}{R_\tau} = e^{\epsilon_{exp} \cdot \Delta m} \tag{6.21}$$

The linear equation is the simplest of these models and may be sufficient perhaps to correct for mass bias when using a single-collector instrument. Conversely, the more complicated power-law and exponential models have both been considered for high-precision isotopic analysis, when using multi-collector instruments, although these equations are closely related to one another and have been shown to give similar results.[90] However, whereas the above equations only take into account differences in mass, Russell's exponential equation goes one step further and also considers the isotopes' actual masses, which is more congruent with empirical results (*i.e.* that mass bias is more pronounced for lighter isotope pairs).[170] Russell's exponential model, which is, somewhat confusingly, sometimes also referred to simply as the exponential model, is presented below.

$$K_{bias} = \frac{R_{true}}{R_\tau} = \left(\frac{m_2}{m_1}\right)^{\beta_{exp}} \tag{6.22}$$

Moreover, the use of a number of additional, increasingly complex, equations

has also been described in the literature to correct for mass bias in high-precision isotope ratio measurements, but these are not considered in this text. However, whereas the abovementioned internal correction procedures, and the accompanying correction equations, are used routinely for isotopic analyses by means of ICP-QMS and MC-ICP-SFMS, they may not be applicable in all cases where a single-collector ICP-SFMS instrument is employed. Indeed, when the observed mass bias was expressed on a per mass unit basis via Russell's equation (β_{exp}), Quétel *et al.* found a significant difference in mass discrimination when considering three separate U isotope ratios on an ICP-SFMS.[171] In contrast, the same authors observed no such discrepancy for two ICP-QMS instruments and a single MC-ICP-SFMS instrument. As a result, this aberrant behaviour was attributed to the fact that the accelerator voltage is reduced in order to perform a mass scan, which, as a side effect, also reduces the transmission efficiency for heavier ions. Therefore, it was deemed necessary to first corroborate this observation for SCK•CEN's nuclearised Element2, in this case for three separate but simultaneously determined Dy isotope ratios. Of the lanthanides under consideration, Dy was selected because its natural isotopic composition has been relatively well characterised and because it possesses four isotopes of similar abundance (see Table 6.2), while the element's isotopic composition is not particularly highly variable in nature. The mass biases per mass unit, as given by the linear equation and by Russell's exponential model, for thirty replicate measurements of the three Dy isotope ratios under consideration, are presented in Figure 6.4. Ideally speaking, no discernible difference ought to be visible between the three isotope ratios. Unfortunately, as expected based on Quétel's reported observations, this turned out to not be the case, for either model. As a result, using an internal correction procedure will inevitably lead to erroneous

(a) Linear model

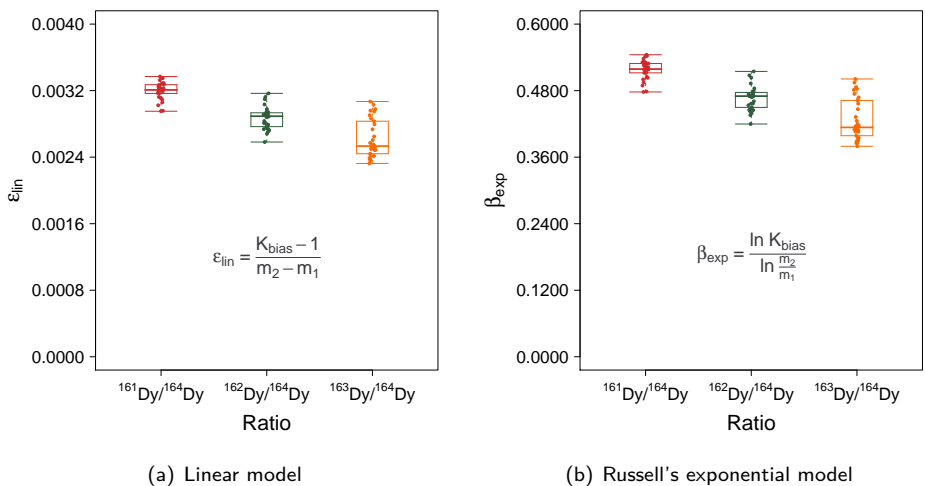(b) Russell's exponential model

Figure 6.4: Mass bias on a per mass unit basis for three separate Dy isotope ratios that were determined within a single analysis ($n = 30$). The linear and the exponential model yield similar results, neither being capable of compensating for mass bias when an internal correction procedure is employed.

results, because the mass bias correction factor expressed on a per mass unit basis for a given pair of isotopes cannot be well characterised by means of a different isotope pair, when using either of the models under consideration.[37,39,44,90,158,170–172]

Consequently, an external mass bias correction procedure was deemed necessary, rather than applying any of the internal correction procedures described above, to permit the most accurate isotopic characterisation of samples by means of an Element2 ICP-SFMS. In this approach, the isotopic analysis of samples and standards is performed sequentially, with standards bracketing the sample(s), *i.e.* an isotope ratio is measured in a single or a small number of samples, each time preceded and followed by the measurement of the same isotope ratio in a well defined isotopic standard. In this way, the mass bias correction factors K_{bias} for the samples can be calculated on the basis of the mass biases that are observed for the standard solutions, through *e.g.* averaging or interpolation. Most important, is the fact that none of the mass bias correction equations described above need be considered, if and when the exact same isotope pair is considered in the samples as in the standards. However, in this approach, is it especially critical that the mass bias correction factor K_{bias} remains relatively constant in time during a measurement sequence, in addition to the fact that analytes should be isolated or that samples and standards ought to be at least matrix-matched, to cope with matrix-induced mass discrimination effects. Therefore, the short- and long-term stability of the mass bias correction factor was first investigated (see Figure 6.5). For that purpose, thirty replicate isotope ratio measurements were performed, over a period of $3\,h$, on five separate days, using a $2.5\,\mu g\,L^{-1}$ Dy standard of natural isotopic composition prepared in a $1\,M\,HNO_3$ matrix. As can be seen in Figure 6.5a, typically, no significant drift trend could be

(a) Short-term stability   (b) Long-term stability
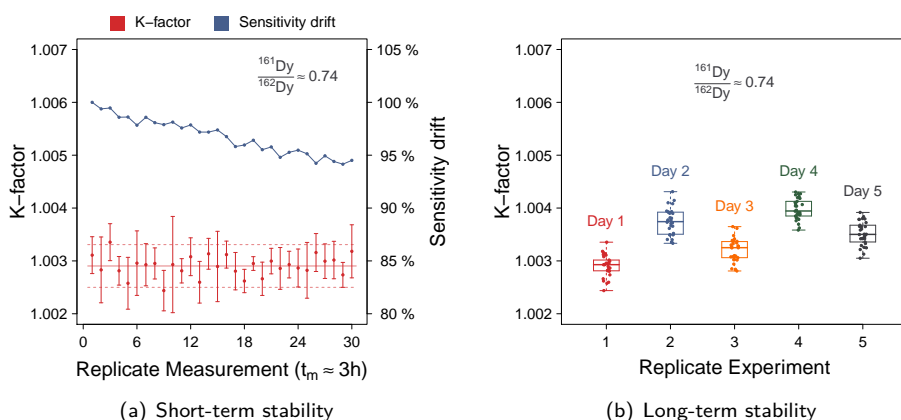
Figure 6.5: (a) Stability of the mass bias correction factor over a single measurement sequence of *ca.* $3\,h$ in duration, as determined for a given Dy ratio in a simple acidic matrix. The error bars represent the internal precision, expressed as a standard deviation on the five runs that define a single data point. The dashed lines represent $K_{bias} \pm 2 \cdot s\,(K_{bias})$ for the thirty replicate measurements in a single sequence. (b) Long-term stability of the K-factor over a number of days with slightly variable operating conditions.

observed throughout a measurement sequence of only a few hours in duration,
even though the instrument's sensitivity was often found to decline by about
5 % over that same period of time. In contrast, the magnitude of the mass bias
was found to be subject to change on a day-to-day basis, as can be seen in
Figure 6.5b, where the label "Day 1" refers to the data that are presented in
Figure 6.5a. As a result, if analytes have been isolated from their concomitant
matrix, or if samples and isotopic standards have been matrix-matched, then
the mass bias correction factor may perhaps be thought of as constant during a
single measurement sequence, although it is of course vital that its magnitude be
determined on a daily basis and verified throughout each sequence. Furthermore,
the constancy of the mass bias correction factor, versus analyte concentration,
was also investigated (see Figure 6.6). For this purpose, two separate Dy isotope
ratios were measured ten-fold in three separate standard solutions, containing Dy
at different concentrations in a $1\,\mathrm{M}\ HNO_3$ matrix. The replicate measurements
of a given isotope ratio were each carried out at alternating Dy concentrations,
in a single measurement sequence. Two separate isotope ratios were considered,
mainly because deviations induced by an inadequate dead time correction would
be more apparent for a ratio deviating from 1:1 (*i.e.* ^{160}Dy/^{162}Dy), whereas other
effects would likely also be observed for a ratio closer to 1:1 (*i.e.* ^{161}Dy/^{162}Dy).
In both cases, whilst taking into account their inherent variability, the mass
bias correction factors were believed to be independent of analyte concentration
over the range studied ($\leq 8\,\mu\mathrm{g\,L}^{-1}$). For the ^{160}Dy/^{162}Dy ratio, however, the
measurements corresponding to the lowest concentration standard are not shown
in Figure 6.6b, because contamination of reagents was of some concern, especially
when a less abundant nuclide such as ^{160}Dy is considered at relatively low Dy
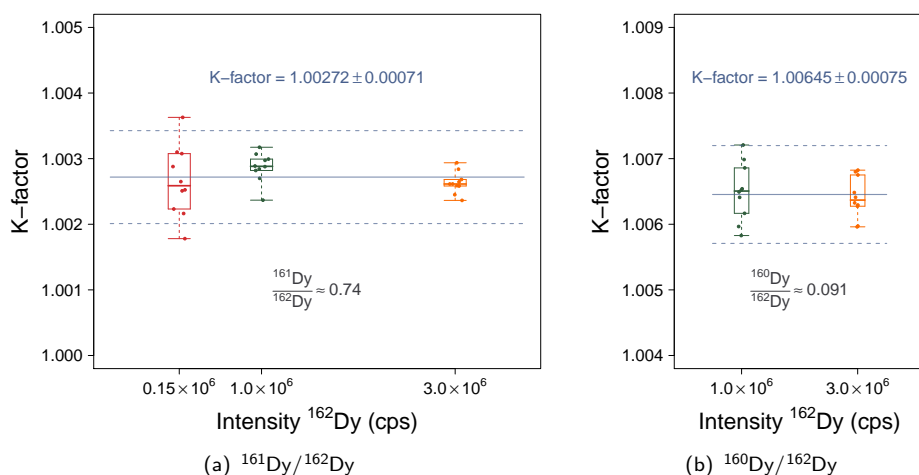

Figure 6.6: Mass bias correction factors as a function of analyte concentration, for two separate Dy
isotope ratios. The dashed lines represent $K_{bias} \pm 2 \cdot s\,(K_{bias})$ for each and every mass bias correction
factor observed for a given isotope pair, regardless of the analyte concentration.

concentrations. In that one case, no reliable mass discrimination factors could be determined, since no blank correction was applied for this experiment, with lanthanide blank signals typically ranging from 50 to 200 counts s^{-1}.[37,39,44,90]

6.3.3   Internal precision

For the purposes of this text, the internal precision was defined as a simple standard deviation of a number of replicate measurements performed on a single sample (referred to as "runs" in the Element2's software suite). Although the precision may be improved in various ways, *e.g.* through proper selection of the sample introduction system, a lower limit is eventually inevitably reached that cannot be surpassed. This fundamental limitation arises from the fact that arrival of ions at the detector is considered to be a random process governed by Poisson counting statistics. As a result, the arrival and detection of positive ions by means of an SEM is subject to white noise, which can never be fully eliminated. If the assumption holds that the number of incident ions is a random variable following a Poisson distribution, then the probability $P(c)$ of counting c ions is given by

$$P\left(c\right) = \frac{N^c \cdot e^{-N}}{c!} \tag{6.23}$$

for which it can be shown that the parameter N represents the expected number of events as well as its corresponding variance. As such, the standard deviation on a detector signal corresponding to N counts is theoretically given by

$$s\left(N\right) = \sqrt{N} \tag{6.24}$$

Let us then consider an isotope ratio R for a pair of nuclides, in which two count rates I_1 and I_2 are ratioed against each other, each corresponding to total numbers of counts N_1 and N_2, respectively. The count rates and total numbers of counts relate to one another via measurement times t_1 and t_2, spent monitoring each respective nuclide during a single run. Thus, the isotope ratio is given by

$$R = \frac{I_1}{I_2} \tag{6.25}$$

$$= \frac{N_1}{N_2} \cdot \frac{t_2}{t_1} \tag{6.26}$$

The relative standard deviation on this isotope ratio can then be determined, in a relatively straightforward manner, via the laws of error propagation. Assuming that the measurements times t_1 and t_2 are constants and furthermore that the total number of counts are independently Poisson-distributed, it can be shown that the relative standard deviation of the isotope ratio equates to

$$\frac{s\left(R\right)}{R} = \sqrt{\left(\frac{s\left(N_1\right)}{N_1}\right)^2 + \left(\frac{s\left(N_2\right)}{N_2}\right)^2} \tag{6.27}$$

$$= \sqrt{\frac{1}{N_1} + \frac{1}{N_2}} \tag{6.28}$$

Even if the contribution of most sources of noise was eliminated, the attainable isotope ratio precision would still always be limited by Equation 6.28.[90,158]

As a result of Equation 6.28, it is clear that the attainable isotope ratio precision can only be improved further by increasing the number of pulses that is collected by the detector. This may be achieved in three ways, either by increasing the analyte concentration, the instrument sensitivity or the total measurement time. However, when the detector is operated in the pulse counting mode, the signal intensities corresponding to higher analyte concentrations are subject to increased dead time-induced pulse count losses. In addition, due to issues with the long term precision of ICP-MS instrumentation, measurement times cannot be prolonged indefinitely to further improve the precision. Therefore, signal intensities and measurement times are typically limited to reasonable values of *e.g.* $1\,000\,000$ counts s^{-1} and 1 min, respectively. To illustrate what kinds of isotope ratio precisions ought to be theoretically attainable, Equation 6.28 is first rewritten in terms of the Element2's data acquisition parameters.[90]

$$\frac{s(R)}{R} = \sqrt{\frac{1}{\frac{w_{i,1}}{100\,\%} \cdot n_{s,1} \cdot t_{d,1} \cdot n_{p,1} \cdot I_1} + \frac{1}{\frac{w_{i,2}}{100\,\%} \cdot n_{s,2} \cdot t_{d,2} \cdot n_{p,2} \cdot I_2}} \qquad (6.29)$$

In Equation 6.29, I represents the observed signal intensity, w_i represents the integration window, n_s represents the number of samples per peak, t_d represents the dwell time and n_p represents the number of passes in a single run. As a result, when using the data acquisition parameters that are presented and described in Table 6.1 and the main text of Section 6.2.1, the optimum isotope ratio precision theoretically amounts to *ca.* 0.026 % RSD, if signal intensities of $1\,000\,000$ counts s^{-1} are
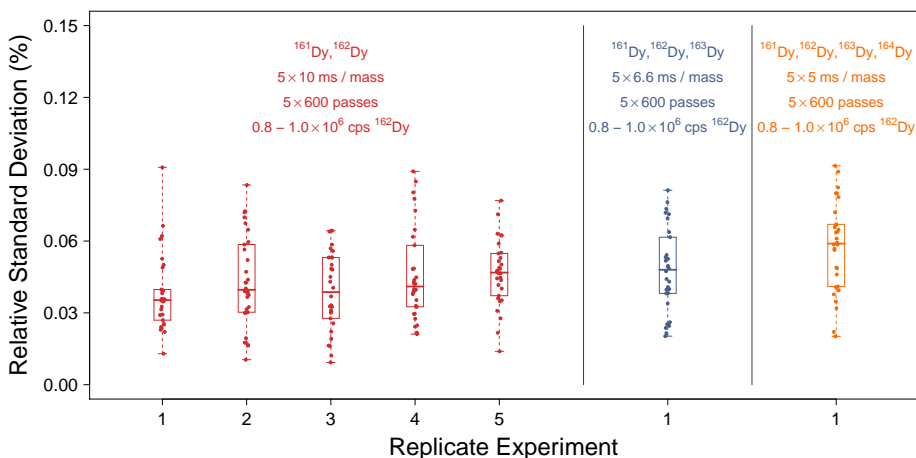
Figure 6.7: (left) Isotope ratio precision for thirty ^{161}Dy/^{162}Dy ratios, determined under optimum conditions in a single measurement sequence, on five separate days. (middle and right) isotope ratio precision for thirty ^{161}Dy/^{162}Dy ratios, with additional masses included in the mass scan, whilst keeping the total data acquisition time constant ($R_{true} \approx 0.74$, results for additional ratios not included).

assumed for two isotopes of similar abundance (*i.e.* for a 1:1 ratio). The actual experimentally attainable isotope ratio precision, under optimum conditions, was determined by performing thirty ^{161}Dy/^{162}Dy isotope ratio measurements, at similar signal intensities when compared to those described above, on five separate days (see Figure 6.7). In $\geq 75\%$ of cases, the isotope ratio precision, calculated on the basis of five consecutive runs, was $\leq 0.06\%$ RSD with an average of about 0.04 % RSD, which is comparable to values that have previously been reported in the literature (see Section 6.1). In addition, the monitoring of additional nuclides was also investigated, for the determination of multiple isotope ratios within a single analysis. This leads not only to a deterioration in counting statistics, if the total measurement time is kept constant, but also reduces the ability of a single-collector instrument for coping with short term fluctuations in the ion beam. However, when three isotopes were monitored instead of two, the isotope ratio precision was not found to be severely affected. When four isotopes were monitored in sequence, instead of two, the isotope ratio precision deteriorated by *ca.* 0.02 %, about half of which was accounted for by the poorer counting statistics. However, whereas an optimum isotope ratio precision of *ca.* 0.04 % had been observed, under optimal conditions with an isotope ratio of about 1:1 for an element that was present at sufficiently high concentration, such favourable prerequisites will most often not be met in practice. Therefore, the attainable isotope ratio precision was further investigated, as a function of signal intensity and of isotope ratio.

The extent to which the attainable isotope ratio precision is affected by analyte concentration is presented in Figure 6.8, for two different Dy isotope ratios. For each ratio, three different standards were considered, each analysed ten-fold, alternatingly, in a single measurement sequence. The experimentally determined isotope ratio precisions were comparable to those predicted theoretically by Poisson counting statistics, whereby the isotope ratio precision was found to improve with increasing analyte concentration, according to a trend similar to that established by Equation 6.29. As is apparent from this figure, the isotope ratio precision predicted and observed for the ^{160}Dy/^{162}Dy is worse across the board, when compared to the ^{161}Dy/^{162}Dy ratio, due to the poorer counting statistics for the lower abundant minor isotope. The effect that an extreme ratio has on the isotope ratio precision is illustrated in Figure 6.9a, where the results for three significantly different Dy ratios are considered. While the signal intensity of the major isotopes remains constant, the isotope ratio precision deteriorates due to the increasingly poor counting statistics on the minor isotopes. As before, the observed precision follows a trend similar to that described theoretically by Poisson counting statistics. However, for a ratio differing significantly from 1:1, the isotope ratio precision may be improved, without increasing either the analyte concentration or adjusting the measurement time, by shifting the total data acquisition time's centre of gravity towards the minor isotope. This is illustrated in Figure 6.9b, where the isotope ratio precision is depicted as a function of the dwell time on the minor isotope. Once again, experimental observations were comparable with predictions based upon Poisson counting statistics. At this point, it is worth noting that the optimum allocation
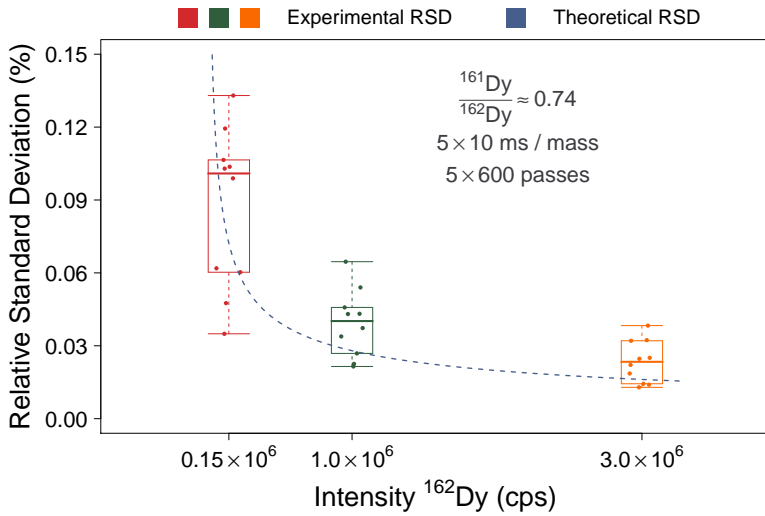
(a) ^{161}Dy/^{162}Dy
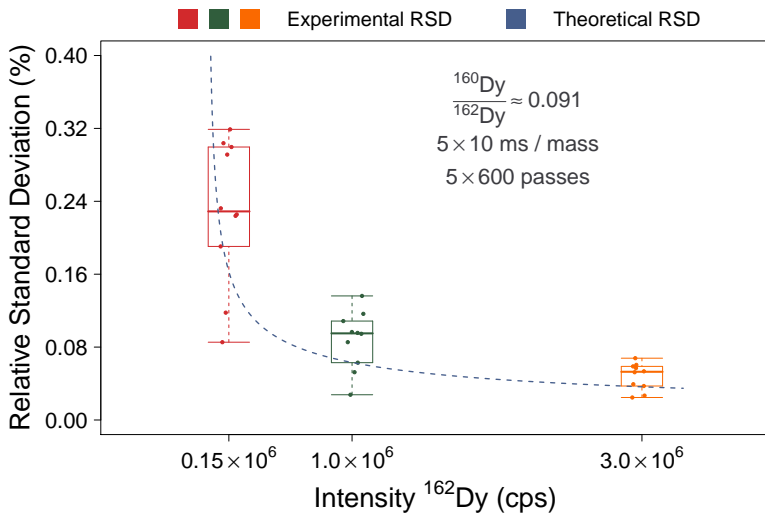
(b) ^{160}Dy/^{162}Dy

Figure 6.8: isotope ratio precision for two separate Dy ratios, as a function of the signal intensity observed for the major isotope ^{162}Dy. For each ratio, each standard was analysed ten-fold, alternatingly, in a single measurement sequence such that the isotope ratios could be directly compared. The experimental RSDs were calculated on the basis of five sequential runs, comprising a single analysis, whilst the theoretical isotope ratio precision was calculated on the basis of Equation 6.29.

(a) Isotope ratio

(b) Dwell time
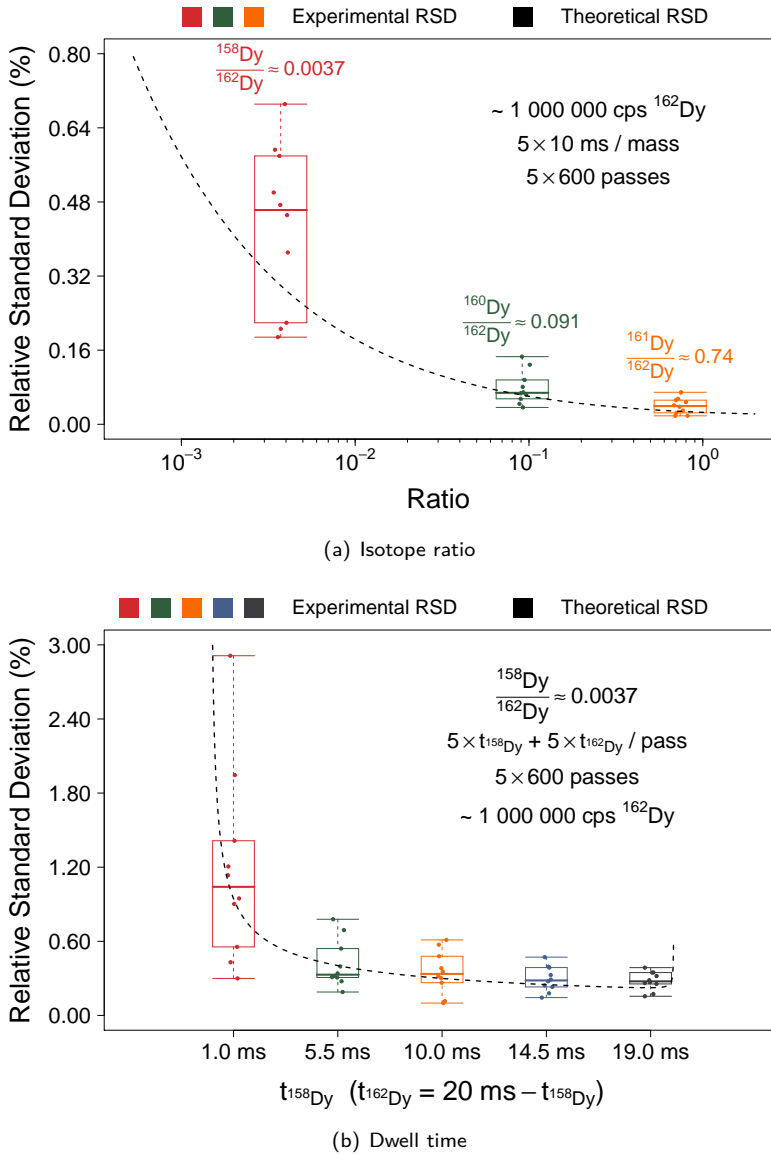
Figure 6.9: (a) isotope ratio precision as a function of the magnitude of the isotope ratio itself. A single standard was considered, wherein each of the three isotope ratios under consideration was measured ten-fold, alternatingly, in a single measurement sequence. (b) isotope ratio precision as a function of dwell time on the minor isotope, for the ^{158}Dy/^{162}Dy ratio. A single standard was considered, wherein the isotope ratio under consideration was determined using any of five different dwell times. Each isotope ratio measurement, for a given dwell time, was carried out ten-fold, alternatingly, in a single measurement sequence. In each case, the dwell time on the major isotope was also adjusted, such that the data acquisition time remained constant at $100\,\mathrm{ms}$ per pass. The experimental RSDs were calculated on the basis of five sequential runs, comprising a single measurement, whilst the theoretical isotope ratio precision was calculated on the basis of Equation 6.29, under the assumption that the signal intensity on the major isotope ^{162}Dy amounted to $1\,000\,000\,\mathrm{counts\,s^{-1}}$.

of data acquisition time between two isotopes showing a relatively extreme ratio, can also be determined beforehand, if the attainable isotope ratio precision is assumed to be governed only by Poisson counting statistics. The derivation of a relatively simple equation that can be employed to this end is derived below.

First consider Equation 6.28 once again, which states that the theoretical optimum isotope ratio precision is limited by the total numbers of counts that are collected. Similarly to Equation 6.29, but in a more general case, this equation can be rewritten in terms of signal intensities I and acquisition times t.

$$\frac{s\left(R\right)}{R} = \sqrt{\frac{1}{I_1 \cdot t_1} + \frac{1}{I_2 \cdot t_2}} \tag{6.30}$$

If the total data acquisition time is given by t, which is the sum of the times allocated to each isotopes, then a parameter f can be defined as

$$f = \frac{t_1}{t} \tag{6.31}$$

$$1 - f = \frac{t_2}{t} \tag{6.32}$$

Furthermore, if the mass bias can be considered to be negligible and if an estimate of the isotope ratio is also available, then that ratio R can be written as

$$R = \frac{I_1}{I_2} \tag{6.33}$$

Substituting Equations 6.31, 6.32 and 6.33 into Equation 6.30 yields

$$\frac{s\left(R\right)}{R} = \sqrt{\frac{1}{I_1 \cdot t \cdot f} + \frac{R}{I_1 \cdot t \cdot (1 - f)}} \tag{6.34}$$

Thus, varying f, which is a measure for the allocation of data acquisition time between both isotopes, expressed as a fraction in the range $]0, 1[$, clearly has an important influence on the lower limit of the isotope ratio precision attainable. Finding the specific value of f that corresponds to the theoretical optimum isotope ratio precision is a straightforward matter. In this simple minimisation problem, the radicand under the root in Equation 6.34 is first derived with respect to f

$$\frac{\partial}{\partial f}\left(\frac{1}{I_1 \cdot t \cdot f} + \frac{R}{I_1 \cdot t \cdot (1 - f)}\right) = 0 \tag{6.35}$$

$$f^2 \cdot (R - 1) + f \cdot 2 - 1 = 0 \tag{6.36}$$

When solved for f, Equation 6.36 yields two solutions, one of which is meaningful in this context. As such, for an isotope ratio R, the theoretical optimum

isotope ratio precision can be attained when using the parameter f given by

$$f_{opt} = \frac{-2 + \sqrt{4 - 4 \cdot (R - 1) \cdot (-1)}}{2 \cdot (R - 1)} \tag{6.37}$$

$$= \frac{\sqrt{R} - 1}{R - 1} \tag{6.38}$$

$$= \frac{1}{\sqrt{R} + 1} \tag{6.39}$$

As expected, when governed by Poisson counting statistics, the optimum value of f is only dependent on the isotope ratio under consideration. Logically, for a ratio near unity, its optimum value is 0.5, such that the total data acquisition time ought to be distributed evenly between both isotopes. However, a relation that is more easily interpretable can be obtained by defining an additional quantity q, as the ratio of the data acquisition times for both isotopes

$$q_{opt} = \frac{t_{opt,1}}{t_{opt,2}} \tag{6.40}$$

$$= \frac{f_{opt} \cdot t}{(1 - f_{opt}) \cdot t} \tag{6.41}$$

$$= \frac{1}{\sqrt{R}} \tag{6.42}$$

Consequently, to obtain a theoretically optimum isotope ratio precision, the ratio of the data acquisition times ought to equate to the inverse of the square root of the ratio of the approximate isotopic abundances, *e.g.* the minor isotope should be monitored 100 times longer than the major isotope for an isotope ratio near 10^{-4}. However, it should be noted this relation assumes that isotope ratio precision is
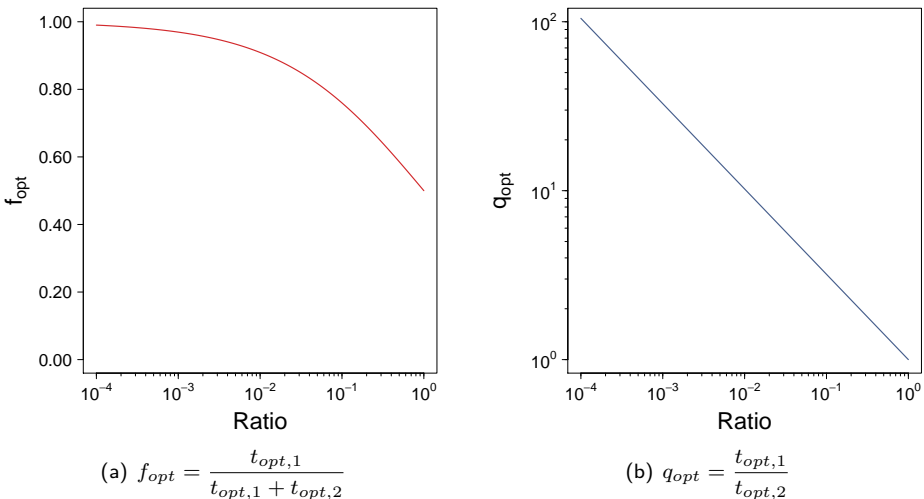

(a) $f_{opt} = \dfrac{t_{opt,1}}{t_{opt,1} + t_{opt,2}}$ (b) $q_{opt} = \dfrac{t_{opt,1}}{t_{opt,2}}$

Figure 6.10: Optimum allocation of data acquisition time between the minor and the major isotope.

governed only by Poisson counting statistics, which may not hold true if other significant sources of noise are present (*e.g.* the scan rate may also need to be considered to cope with ion beam instabilities). Plots of the optimum fractions f_{opt} and ratios q_{opt}, as defined in Equations 6.31 and 6.40, respectively, versus the values of the corresponding isotope ratios, are presented in Figure 6.10.

Up to this point, results of only a limited number of Dy isotope ratio measurements have been reported upon. To allow for a comparison to be made between the isotope ratio precision characteristic of the Element2 ICP-SFMS and that which is typically observed for SCK•CEN's Sector 54 MC-TIMS instrument, supplemental data was collected, for a wider ranger of lanthanides. To that end, isotope ratio measurements were performed, in pairs of two, on Nd, Sm, Eu, Gd and Dy standard solutions. As such, three nuclides were monitored sequentially during each measurement. For each element, a standard solution was prepared such that the signal intensity on the selected reference isotope, as indicated in Table 6.2, was *ca.* $1\,000\,000$ counts s^{-1}. For data acquisition, dwell times of 6.6 ms were employed for each of the isotopes under consideration, even though this resulted in sub-optimum conditions for the more extreme isotope ratios. As a result, the total measurement time, of the three nuclides combined, amounted to *ca.* 60 s for a single run. The results of these measurements are shown in Figure 6.11. As can be seen in this figure, $> 50\,\%$ of the experimentally determined isotope ratio precisions lie in-between one and two times those that were predicted theoretically by Poisson counting
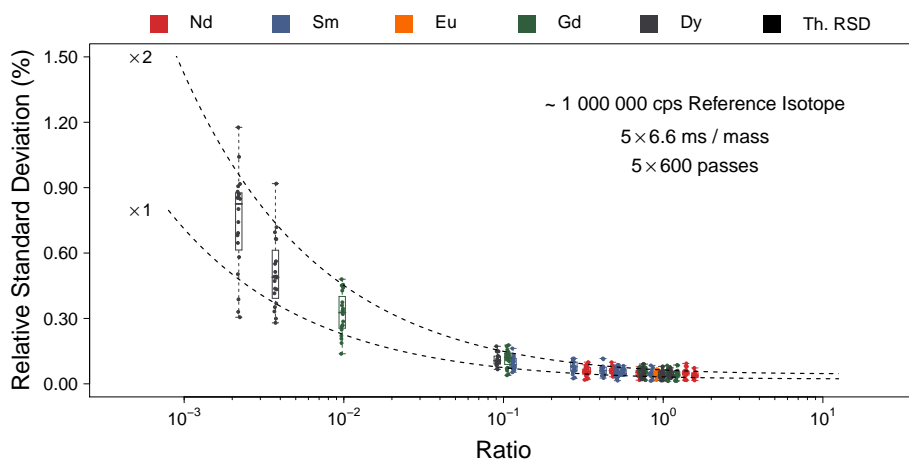
Figure 6.11: isotope ratio precision depicted as a function of the value of the isotope ratio under investigation. For each of the lanthanides under consideration, single but separate standard solutions were prepared such that the signal intensity on the reference isotope would amount to ca· $1\,000\,000$ counts s^{-1}. isotope ratio measurements on these samples were performed in pairs of two, whereby three isotopes were monitored sequentially (except when considering Eu). The experimental RSDs were calculated on the basis of five sequential runs, comprising a single measurement. For each of the isotope ratios, such measurements were performed twenty-fold in a single sequence over a period of *ca.* 2 h. The theoretical isotope ratio precision was calculated on the basis of Equation 6.29, under the assumption that the signal intensity for the reference isotope amounted to $1\,000\,000$ counts s^{-1}. Two dotted lines are shown, corresponding to one and two times the theoretical isotope ratio precision.

statistics. However, it is difficult to compare these specific isotope ratio precisions with those that have previously been obtained and reported upon at SCK•CEN, for isotopic analysis of lanthanides by means of MC-TIMS, in a routine setting, because the isotopic abundances of the lanthanides native to spent nuclear fuel are so different from those encountered in nature (*e.g.* the naturally occurring ^{142}Nd isotope is not present at significant levels in spent nuclear fuel samples). As a result, for the nuclearised Element2 ICP-SFMS instrument, two times the theoretically predicted value was considered to be a conservative, yet realistic, estimate of the attainable isotope ratio precision by the author, which could then be compared to those values that have historically been obtained with SCK•CEN's Sector 54 MC-TIMS instrument and which have kindly been made available to the author.

At SCK•CEN, Nd isotope ratio measurements, performed with the abovementioned Sector 54 MC-TIMS instrument, are typically carried out in the static multiple Faraday collector mode. For that particular element, experimental data for three different samples were made available to the author, in which a number of isotope ratios with values ranging from *ca.* 0.2 to 3 were determined. For these samples, the observed internal precisions for each of the isotope ratios ranged from *ca.* 0.005 to 0.03 % RSD, with an average value of about 0.01 %. The isotope ratio precisions that would be attainable with the Element2 ICP-SFMS, on the other hand, were estimated as two times that predicted by Poisson counting statistics, using Equations 6.34 and 6.42, under the assumptions that the signal intensity on the reference isotope would amount to $1\,000\,000\,\text{counts}\,\text{s}^{-1}$ and that the total measurement time was 60 s. In this way, for isotope ratios ranging from 0.2 to 3, estimated internal precisions of *ca.* 0.041 to 0.084 % RSD were calculated. Thus, for Nd, the isotope ratio precisions attainable with the ICP-SFMS unit were found to be inferior to those previously obtained with the MC-TIMS instrument. Moreover, the need to correct for mass bias, which is not only more pronounced for ICP-MS instruments than for TIMS instruments, but which is also more prone to variation, was not yet taken into account. When the mass bias correction factor is determined by means of an isotopically well characterised external calibration standard, then its uncertainty is governed mainly by the associated isotope ratio measurement. Consequently, if a an isotope ratio of similar magnitude was considered in the standard as in the sample, then the precision on the mass bias corrected isotope ratio would be deteriorated further by at least a factor $\sqrt{2}$, according to the rules of error propagation.

Whereas Nd isotope ratio measurements were typically carried out in the TIMS instrument's multi-collector mode, Sm and Gd isotope ratios were determined using a single Daly detector in the peak hopping mode. As a result, the isotope ratio precisions associated with these measurements were markedly poorer. For 25 isotope ratios with values ranging from 0.3 to 3, the observed internal precisions ranged from *ca.* 0.03 to 3 % RSD, with an average value of about 0.24 %. Secondly, for 17 isotope ratios with values ranging from 0.03 to 0.3, the observed internal precisions lay in between 0.01 and 6 % RSD, with an average value of about 0.26 %. Lastly, for 13 isotope ratios in the range 0.003 to 0.03, internal

precisions of *ca.* 0.04 to 10 % RSD were observed, with an average value of about 0.85 %. The estimated isotope ratio precision attainable with the ICP-SFMS instrument, on the other hand, when calculated as described above, amounted to *ca.* 0.50, 0.18, 0.073 and 0.041 % RSD for isotope ratios of 0.003, 0.03, 0.3 and 3, respectively. Consequently, these values were found to be competitive with those previously obtained with the Sector 54 instrument, even when a deterioration of the precision with a factor $\sqrt{2}$ is taken into account, resulting from the need for mass bias correction via an external calibration standard.

6.4 Conclusions and outlook

A number of the most important aspects related to the determination of isotope ratios by means of a single-collector ICP-SFMS were investigated, including (i) the correction for dead time-induced count rate losses, (ii) the correction for mass discrimination effects and (iii) the attainable internal precision.

The detector's dead time was determined via a slightly modified version of the procedure described by Appelblad and Baxter, which yields an unambiguous value of τ along with an estimate of its associated combined uncertainty $u_c(\tau)$. At the same time, mass bias is taken into account, whilst the true isotope ratio does not need to be known for determining τ. Some authors have reported that the dead time is subject to change as a detector ages, although, in this case, no significant change in τ could be discerned over a period of about ten weeks, at more than one SEM voltage setting. It has also been reported that, for some types of detectors, the dead time may be mass-dependent. However, no such differences could be observed for the Element2's detector when Ba and Lu were considered, although the elements in question clearly do not differ immensely with respect to mass. As a result, a single dead time of 12 ns was used in all subsequent work. This value was determined via isotope ratio measurements of the ^{137}Ba/^{138}Ba pair, a ratio which differs significantly from unity, although not so extreme that it cannot be determined with a relatively decent internal precision. Lastly, whereas some authors have reported the occurrence of sag, in addition to dead time-induced pulse pile-up, this phenomenon was not observed at count rates of up to $3\,200\,000$ counts s^{-1}.

Conversely, the correction for mass bias effects, when using single-collector ICP-SFMS instruments such as the Element2, is somewhat more complicated than for *e.g.* ICP-QMS instruments. As such, it was found that internal correction procedures cannot be applied, because the mass bias correction factor cannot be well characterised by means of the most commonly used correction equations. Quétel *et al.* attributed this aberrant behaviour to the fact that the Element2's accelerator voltage has to be adjusted to enable rapid mass scans, whilst the magnetic sector's rest mass remains constant. As a result, for this type of instrument, external correction procedures have to be considered, whereby isotopic standards and samples are measured sequentially in a bracketing approach. If the same isotope pair is considered in the standards as in the samples, then none of the correction equations referred to above need be employed. However,

in this case, sample pretreatment is more critical to attenuate matrix-induced mass discrimination effects. In addition, isotopic reference materials have to be available for each of the elements under consideration. Moreover, the mass bias correction factor needs to either remain relatively constant or vary along a well-established trend. Fortunately, at least for simple standard solutions, it was found that the mass bias correction factor can be thought of as constant during a single measurement sequence. In addition, in the range studied, the mass bias correction factor was found to be independent of analyte concentration.

The optimum internal precision, defined as a simple relative standard deviation of a number of runs, comprising a single analysis, was, on average, about 0.04 % RSD. Such values were obtained for an isotope ratio of *ca.* 0.74, with a signal intensity of *ca.* $1\,000\,000$ counts s^{-1} for the reference isotope and data acquisition times of about 30 s for both nuclides. If the total numbers of counts for both isotopes are assumed to be independently Poisson-distributed, then it can be shown that, under the abovementioned conditions, the lower limit of the attainable precision falls just below 0.03 % RSD. As a result, Poisson counting statistics were found to be the predominant source of noise, a specific source of noise which can never be fully eliminated. In addition, it was demonstrated that the isotope ratio precision follows along a similar trend predicted by Poisson counting statistics, for varying isotope ratios, dwell times and signal intensities. Moreover, two times the theoretical isotope ratio precision was considered to be a conservative, yet realistic, estimate of the experimentally attainable isotope ratio precision, when simultaneously determining two ratios of Nd, Sm, Gd or Dy (*i.e.* when monitoring three nuclides sequentially). Compared to the isotope ratio precisions that have previously been reported upon at SCK•CEN, for an ageing Sector 54 MC-TIMS instrument, those attainable with the Element2 were found to be competitive in a few cases. However, as anticipated, the optimum isotope ratio precision of *ca.* 0.005 % RSD, obtained with the Sector 54 instrument operating in its multi-collector mode, could not be matched. In contrast, for elements for which the MC-TIMS instrument is typically operated with a single Daly detector only, the Element2 might even be found to surpass the Sector 54 unit in terms of isotope ratio precision. However, whereas the current study encompassed a number of simple exploratory experiments only, further research will be required to evaluate the use of the Element2 ICP-SFMS for isotope ratio measurements in a routine setting at SCK•CEN.

7 Summary

The development, evaluation and application of a number of element- and isotope-selective analytical methods was described in this text. More specifically, this work aims to make a small contribution to the efforts of the *Belgian Nuclear Research Centre* (SCK•CEN) towards the development of novel nuclear technologies. Despite its controversial reputation, especially in the wake of the recent Fukushima Dai-ichi accident, nuclear power currently still provides for more than 25 % of Europe's electricity demands and it will most likely continue to play a pivotal role in the foreseeable future. However, to ensure the sustainability and continued social acceptance of nuclear power, the development of novel nuclear systems is essential. To that end, the fourth generation of nuclear fission reactors is currently being developed throughout the world, although these novel systems, such as the proposed *Lead-cooled Fast Reactor* (LFR) design, will most likely not come to fruition before 2030. One of the most important applications that is envisioned for these types of technologies, aside from commercial power generation, is the management of new and existing nuclear waste. Combined with partitioning, transmutation of minor actinides into stable or shorter-lived nuclides with a fast reactor system could reduce the storage time required for high-level nuclear waste by potentially several orders of magnitude to as little as 1000 a. Important in the context of this work is the fact that the efforts of SCK•CEN towards the development of such innovative systems have been consolidated in the MYRRHA project.

Once operational, this *Multi-purpose hYbrid Research Reactor for High-tech Applications* (MYRRHA) will serve as a source of protons and neutrons for a variety of R&D applications, including research into structural materials and fuels for advanced nuclear systems. Although the MYRRHA research reactor will not itself be a Gen IV reactor, it will be based on the use of heavy liquid metal-cooled fast reactor technology, which will enable it to contribute significantly to the development of the LFR concept and other Gen IV designs. However, the innovative nature of the MYRRHA concept does pose some important design challenges with regard to structural materials performance. The envisaged primary coolant is a liquid *Lead-Bismuth Eutectic* alloy (LBE), which consists of *ca.* 45 wt.% Pb and *ca.* 55 wt.% Bi. Despite its favourable thermophysical and neutronic properties, this heavy liquid metal alloy is highly corrosive towards high-alloy steels, which results in stringent requirements with regard to the selection of structural materials. To that end, three different high-alloy steels were selected as candidate materials for various reactor components (T91, 316L and 15-15Ti), each of which is expected to exhibit some resistance towards the corrosive nature of the LBE. In this context, the multi-elemental trace analysis of LBE and high-alloy steels is of importance, *e.g.* for the determination of trace elements that may affect

a steels mechanical characteristics or to monitor the corrosion product uptake rate of the coolant. In both cases, however, the elements of interest are only expected to be present at $\mu g\,g^{-1}$ levels or below, whereby the use of a highly sensitive technique is of paramount importance. Moreover, in the context of nuclear fuel research and transmutation studies to be carried out at the MYRRHA facility, isotope-selective analytical methods will also be called for in the future, *e.g.* for the development and validation of computer models that are used to determine the extent to which fissile materials have been burnt. For a more in-depth discussion of the context and objectives of this work, the reader is referred to Chapter 1.

Double-focusing Sector-Field Inductively Coupled Plasma-Mass Spectrometry (ICP-SFMS) is a highly-sensitive element-selective analytical technique, which combines the multi-elemental capabilities of *Inductively Coupled Plasma-Optical Emission Spectrometry* (ICP-OES) with detection limits that surpass even those associated with *Graphite Furnace Atomic Absorption Spectrometry* (GFAAS). Therefore, this technique is an ideal candidate for the multi-elemental trace analysis of a wide variety of samples, including LBE samples and high-alloy steels. Furthermore, in addition to mere elemental concentrations, the easily interpretable atomic mass spectra also provide an isotopic fingerprint. The latter allows for the isotopic analysis of several types of samples, including spent nuclear fuels or transmutation targets. Compared to the more widely adopted *Quadrupole Inductively Coupled Plasma-Mass Spectrometers* (ICP-QMS), ICP-SFMS instruments are typically characterised by a superior sensitivity, a lower background and the potential to operate at higher resolution modes in order to eliminate many of the frequently occurring spectral interferences. As a result, detection limits in the $ng\,L^{-1}$ range and below have been reported in the literature for the majority of elements, levels which are most often limited by the blank levels attainable rather than by instrument performance. However, whilst spectral interferences can often be resolved in a straightforward manner when using an ICP-SFMS instrument, attenuating matrix effects is typically more troublesome. One straightforward and elegant approach to deal with these non-spectral interferences is to apply highly selective analyte/matrix separation procedures, prior to analysis by means of ICP-SFMS. For that purpose, column chromatography is often considered, owing to its simplicity and ease of use, whereby one or a few target elements are retained on a specifically chosen highly selective resin, whilst the same resin exhibits little or no affinity for the concomitant matrix elements (or vice versa). In addition to being highly suited for ultra-trace elemental analysis, the use of ICP-SFMS for isotopic analysis is justified as a result of its superior isotope ratio precision, *e.g.* when compared to traditional ICP-QMS instruments, with optimum values of *ca.* 0.05 % RSD having been reported in the literature, a fact which has been attributed to the technique's characteristic flat-top peaks. Even though such values are of course more modest than the ≤ 0.01 % RSD values that are routinely reported for *Multi-Collector Thermal Ionisation Mass Spectrometers* (MC-TIMS), the use of single-collector ICP-SFMS may still be found to be fit-for-purpose in select cases, *e.g.* due to a reduced need for labourious and time-consuming

sample preparation procedures. For an overview of the strengths, weaknesses and operating principles of ICP-SFMS, the reader is referred to Chapter 2.

The single-collector ICP-SFMS instrument used throughout this work is a nuclearised Element2 (Thermo Scientific, Germany). This instrument has been coupled to a stainless steel nuclear glovebox, which houses all components up to and including the interface region. The glovebox is kept at a slight underpressure and permits the analysis of radioactive samples, if desired. A small number of samples was also analysed by means of a more commonly used XSeries2 (Thermo Scientific, Germany) ICP-QMS instrument, such that the performance of both instruments could be compared. For both ICP-MS instruments, typical instrumental and data acquisition parameters are described in detail in Chapter 3. Moreover, that chapter contains an overview of the reagents and labware that were used throughout in the preparation of blanks, samples and standards.

The development and application of an analytical procedure for the multi-elemental trace analysis of T91, 316L and 15-15Ti high-alloy steels was the subject of Chapter 4. The main matrix elements in these alloys were identified as being Cr, Fe and Ni in addition to lower amounts of Si, V, Mn, Co, Cu and Mo. In addition, a list of potentially interesting target elements comprising B, Al, P, S, Ti, As, Zr, Nb, Ta and W, was also compiled. These elements needed to be determined at trace levels in a vast excess of the matrix elements. In order to attenuate spectral and non-spectral interferences, as well as pronounced memory effects, which often hamper ICP-MS analyses of this kind, a highly selective analyte/matrix separation procedure was developed and applied. In the ideal case, the envisaged analyte/matrix separation procedure should have allowed for all target elements to be selectively isolated from all matrix elements. Most important, though, was the fact that at least the three main matrix elements Cr, Fe and Ni were eliminated. For that purpose, a quick and efficient column chromatographic analyte/matrix separation protocol was devised, based on the use of AG 50Wx8 cation-exchange resin. In this procedure, the major matrix elements Cr, Fe and Ni and a few of the minor matrix elements are selectively retained on the cation-exchanger in a dilute HNO_3/HF medium, whilst the target elements themselves exhibit little to no affinity for the resin and elute rapidly under the same conditions. In the case of Fe and Ni, matrix separation efficiency is $> 99.9\%$, whilst for Cr it is $> 90\%$. Overall, about $> 97.5\%$ of the total matrix could be separated from the target elements for the three high-alloy steels under consideration. In addition, this protocol was later found to be applicable not only for the ultra-trace analysis of B, Al, P, S, Ti, As, Zr, Nb, Ta and W in such steel alloys, but also to the determination of a wider range of trace elements including Be, Ge, Se, Rh, Pd, Sn, Sb, Hf, Re, Ir and Pt.

The procedure that was proposed for the analysis of high-alloy steels was validated by analysing (i) steel alloy *Certified Reference Materials* (CRMs), (ii) mock samples and (iii) real high-alloy steels. Experimental results were generally found to be in good agreement with certified values for all three CRMs,

whilst spike recoveries were around 100% when analysing mock samples. Proce-
dural *Quantification Limits* (QL, $10s$) were determined by analysing independent
procedural blanks, with optimum values at low $ng\,g^{-1}$ levels for Re and Hf.
Finally, the procedure was applied to real steel alloy samples obtained from
SCK•CEN, whereby the presence of most of the target elements was detected
in at least one of the samples, with the exception of Be, S, Se, Hf and Ir. The
procedure described above was specifically aimed at the analysis of T91, 316L
and 15-15Ti high-alloy steels, alloys with a high Cr, Fe and Ni content. Self-
evidently, however, the procedure can also be applied to other types of alloys or
even other types of samples, such as iron meteorites or high-purity Fe and Ni.

Whereas the multi-elemental trace analysis of T91, 316L and 15-15Ti high-alloy
steels was the subject of Chapter 4, Chapter 5 instead dealt with the determination
of trace elements in LBE, the MYRRHA research reactor's primary heavy liquid
metal coolant, which is to be in direct physical contact with the abovementioned
steel alloys. For these types of samples, a separate list of potentially interesting
target elements comprising Ti, V, Cr, Mn, Fe, Co, Ni, Cu, Nb, Mo, Ag, Cd,
Te, Ce, Re, Tl, Th and U was compiled (consisting *e.g.* of expected corrosion
products). As was the case for high-alloy steel samples, the accurate and precise
analysis of LBE samples by means of ICP-SFMS is hampered by the occurrence
of spectral and non-spectral interferences. However, compared to steel alloys,
the LBE matrix is a fairly simple one, consisting mainly of Pb and Bi. As a
result, the formation of matrix-induced spectral interferents is more predictable
and therefore less troublesome. Nonetheless, non-spectral interferences would
still impede the accurate determination of trace elements in this type of a ma-
trix. Therefore, prior to subjecting a digested sample to ICP-SFMS analysis,
the application of a highly selective analyte/matrix separation procedure was
deemed essential. However, although only two matrix elements needed to be
considered in this case, no single resin capable of selectively retaining both Pb
and Bi in an HNO_3/HF medium could be identified. As a result, two separate
chromatographic resins had to be selected, each capable of retaining either Pb
or Bi, whilst having only a limited affinity towards most of the target elements.
In the optimised analyte/matrix separation protocol, a tandem-column set-up is
used, whereby a $2\,mL$ column loaded with extraction chromatographic Pb Spec
resin is suspended above a $5\,mL$ column loaded with AG 1x4 anion-exchange resin.
The matrix element Pb is retained on the Pb Spec column whereas its counterpart
Bi shows an appreciable affinity for the AG 1x4 column. The vast majority of
the target elements, on the other hand, exhibit no affinity for either resin. As
a result, over 99% of the LBE matrix can separated from the rapidly eluting
target elements. The target element Re shows an affinity for both resins and
ends up in two separate fractions, this element could nonetheless be successfully
separated from the matrix. In addition, although Ag and Tl also exhibit an affinity
for the Pb Spec resin, they could still be separated from the LBE matrix.

The optimised procedure for the analysis of LBE samples was validated by
applying it to (i) Pb-matrix CRMs, (ii) mock samples and (iii) real LBE samples.

Procedural QLs (10*s*), ranging from low ng g^{-1} levels for Th to sub-µg g^{-1} levels for the contamination-prone Fe, were established by analysing procedural blanks. Experimentally determined concentrations of elements for which the concentrations in the Pb-matrix CRMs IMN PL33 and IMN PL66 was certified (*i.e.* Ni, Cu, Ag, Cd, Te, Tl and Bi), were generally found to be in good agreement with their respective certified values. The only truly problematic element was Te, but only when considering CRM IMN PL66, for which a bias of *ca.* −70 % was observed. The author believes that the cause may be attributed to the digestion procedure, but not to the actual separation procedure itself, as no such issues were encountered for mock samples or for the other CRM. Analysis of mock samples revealed excellent recoveries for most target elements, but the result for Fe was of some concern. However, the poor recovery of Fe may be attributed to the fact that the high-purity Pb and Bi powders, used to prepare the mock samples, contained relatively high levels of Fe that also appeared to be heterogeneously distributed. In addition, the QL (10*s*) for the contamination-prone Fe was poor when compared to those obtained for the other target elements. Comparison of results that were obtained by means of the optimised procedure with results that were obtained by means of *Neutron Activation Analysis* (NAA) at SCK•CEN for five replicate analysis of a batch of LBE showed good agreement between one another, with the exception of Cr. Certain elements were found to be more homogeneously distributed in these LBE samples (*i.e.* Ni, Cd and Tl) than others (*i.e.* Cu, Ag and Te). Moreover, a correlation ($\rho = 0.98$) was found between the distributions of Cu and Ag in the LBE samples, by analysis of the five replicate samples. A few of the target elements served as chemical analogues for radionuclides that were in actuality of interest, but to what extent their respective behaviours will be similar remains to be seen. Literature data for the AG 1x10 anion-exchange and Sr Spec resins, the latter being similar to Pb Spec resin, suggest that Re might indeed correctly serve as a chemical analogue for Tc throughout the proposed separation procedure. However, based on the same literature data, it appears unlikely that this is also the case for Te and Po or for Ce and Pu. Therefore, it will be necessary to apply the procedure to irradiated LBE samples, mainly to confirm the behaviour of ^{210}Po (which is formed due to neutron capture of ^{209}Bi). The procedure described in this work was aimed specifically at the quantitative analysis of LBE samples originating from research projects related to the development of the MYRRHA research reactor at SCK•CEN. Certain reactor designs, however, may involve the use of other liquid metal coolants. One proposed Gen IV nuclear reactor design for commercial power generation (*i.e.* the lead-cooled fast reactor) would rely on the use of pure Pb as a primary coolant. The accurate multi-elemental trace analysis of Pb samples, by means of ICP-SFMS, would also be hampered by non-spectral interferences, although the observed matrix effects would be induced by only a single matrix element instead of two. As a result, a much simplified analyte/matrix separation procedure could be employed, based on the use of the Pb Spec extraction chromatographic resin only. An analyte/matrix separation procedure using only Pb Spec resin would be more straightforward and quicker because

it avoids the complications of using multiple eluents and a tandem-column setup.

When the abovementioned procedure was applied to actual LBE samples, originating from experimental setups used at SCK•CEN in the context of structural material performance studies, a number of impurities and corrosion products could be identified. For further details, the reader is referred to Appendix 5.5.1. A number of these samples were also analysed by means of ICP-QMS, in combination with simple dilution rather than analyte/matrix separation for attenuating non-spectral interferences and memory effects, the results of which were generally found to be in good agreement with those obtained using ICP-SFMS. Self evidently, however, QLs obtained via ICP-QMS were poorer across the board. Furthermore, a number of additional samples were also analysed by means of NAA at SCK•CEN, the results of which were once again made available to the author. Although the difference in QLs was less obvious, those obtained with ICP-SFMS were most often at least on par with those reported for NAA, whilst quantifiable results were generally found to be in good agreement with one another (with the exception of Cr). When comparing the trace element content of a batch of LBE, before and after prolonged contact with 316L high-alloy steel, a stark increase in the Ni concentration was most apparent, which fits with the widely reported selective dissolution of Ni from such alloys into the LBE. In addition, there appeared to be a significant decrease in the Cd concentration, for which no apparent mechanism could be identified. Even though these samples were also to be analysed by means of NAA at SCK•CEN, those results were not yet available at the time of writing. As a result, this observation could not be independently verified.

Lastly, in Chapter 6, the capabilities of SCK•CEN's nuclearised Element2 ICP-SFMS instrument for the determination of isotope ratios was investigated. The isotopic analysis of experimental or commercial nuclear fuels, in the context of fuel qualification or spent fuel burnup programs, is already carried out routinely at SCK•CEN, *e.g.* by means of an ageing Sector 54 MC-TIMS instrument. For the analytical assays in question, the isotopic characterisation of select lanthanides is of particular importance, which is why it is mainly these elements that were considered in that chapter (*i.e.* Nd, Sm, Eu, Gd, Dy). Even though MC-TIMS instruments are capable of providing superior isotope ratio precisions of $\leq 0.01\,\%$ RSD on a routine basis, compared to more modest optimum values of $\leq 0.05\,\%$ RSD that have been reported for single-collector ICP-SFMS instruments, the Element2 may still be found to be fit-for-purpose in select cases, *i.e.* due to its superior sensitivity or the reduced need for labour-intensive and time-consuming sample preparation procedures. In this context, a few of the relevant considerations with regard to the determination of isotope ratios by means of single-collector ICP-SFMS had to be investigated.

The most important aspects that were investigated included (i) the correction for dead time-induced count rate losses, (ii) the correction for mass discrimination effects and (iii) the attainable internal precision. The detector's dead time was determined via a slightly modified version of the procedure described by Appelblad and Baxter, which yields an unambiguous value of τ along with an estimate of its

associated combined uncertainty $u_c(\tau)$. At the same time, mass bias is taken into account, whilst the true isotope ratio does not need to be known for determining τ. Some authors have reported that the dead time is subject to change as a detector ages, although, in this case, no significant change in τ could be discerned over a period of about ten weeks, at more than one SEM voltage setting. It has also been reported that, for some types of detectors, the dead time may be mass-dependent. However, no such differences could be observed for the Element2's detector when Ba and Lu were considered, although the elements in question clearly do not differ immensely with respect to mass. As a result, a single dead time of 12 ns was used in all subsequent work. This value was determined via isotope ratio measurements of the $^{137}Ba/^{138}Ba$ pair, making up an isotope ratio that differs significantly from unity, although it is not too extreme, such that it can still be determined with a relatively decent internal precision. Lastly, whereas some authors have reported the occurrence of sag, in addition to dead time-induced pulse pile-up, this phenomenon was not observed at count rates of up to $3\,200\,000\,\text{counts}\,\text{s}^{-1}$. The correction for mass bias effects, when using single-collector ICP-SFMS instruments such as the Element2, is somewhat more complicated than for *e.g.* ICP-QMS instruments. As such, it was found that internal correction procedures cannot be applied, because the mass bias correction factor cannot be well characterised by means of the most commonly used correction equations. Quétel *et al.* attributed this aberrant behaviour to the fact that the Element2's accelerator voltage has to be adjusted to enable rapid mass scans, whilst the magnetic sector's rest mass remains constant. As a result, for this type of instrument, external correction procedures have to be used, whereby isotopic standards and samples are measured sequentially in a bracketing approach. If the same isotope pair is considered in the standards as in the samples, then none of the correction equations referred to above need be employed. However, in this case, sample pretreatment is more critical to attenuate matrix-induced mass discrimination effects. In addition, isotopic reference materials have to be available for each of the elements under consideration. Moreover, the mass bias correction factor needs to either remain relatively constant or vary along a well established trend within a single bracket. For simple standard solutions, it was found that the mass bias correction factor can be thought of as constant during a single measurement sequence. In addition, in the range studied, the mass bias correction factor was found to be independent of analyte concentration. The optimum internal precision, defined as a simple relative standard deviation on a number of runs, comprising a single analysis, was, on average, about 0.04 % RSD. Such values were obtained for an isotope ratio of *ca.* 0.74, with a signal intensity of *ca.* $1\,000\,000\,\text{counts}\,\text{s}^{-1}$ for the reference isotope and data acquisition times of about 30 s for each of both nuclides. If the total number of counts for both isotopes are assumed to be independently Poisson-distributed, then it can be shown that, under the abovementioned conditions, the lower limit of the attainable precision falls just below 0.03 % RSD. As a result, Poisson counting statistics were found to be the predominant source of noise, a specific source of noise which can never be fully eliminated. In addition, it was demonstrated that

the isotope ratio precision follows a trend similar to that predicted by Poisson counting statistics, for varying isotope ratios, dwell times and signal intensities. Moreover, two times the theoretical isotope ratio precision was considered to be a conservative, yet realistic, estimate of the experimentally attainable isotope ratio precision, when simultaneously determining two ratios of Nd, Sm, Gd or Dy (*i.e.* when monitoring three nuclides sequentially). Compared to the optimum isotope ratio precisions of *ca.* 0.005 % RSD that have previously been reported upon at SCK•CEN, for an ageing Sector 54 MC-TIMS instrument operating in the multiple Faraday collector mode, those obtained with the Element2 ICP-SFMS were about an order of magnitude worse. In contrast, of elements for which the MC-TIMS instrument is typically operated in the single-collector mode, by using a single Daly detector only, in the peak-hopping mode, the Element2 might even be found to surpass the Sector 54 unit in terms of isotope ratio precision. However, whereas the current study encompassed a number of simple exploratory experiments only, further research will be required to evaluate the use of the Element2 ICP-SFMS for isotope ratio measurements in a routine setting at SCK•CEN.

8   Samenvatting

In de loop van deze tekst werd de ontwikkeling, evaluatie en toepassing van een aantal element- en isotoop-selectieve analytische methoden beschreven. In het bijzonder probeert dit werk een kleine bijdrage te leveren tot de inspanningen die het *studiecentrum voor kernenergie* SCK•CEN levert ten behoeve van de ontwikkeling van nieuwe nucleaire technologieën. Ondanks zijn bijzonder omstreden reputatie, zeker in de nasleep van de kernramp bij Fukushima, voorziet nucleaire energie momenteel nog in meer dan 25 % van de elektriciteitsbehoefte van de EU. Zodoende is het zeer waarschijnlijk dat nucleaire energie een belangrijke rol zal blijven spelen in de nabije toekomst. Desalniettemin is het essentieel dat er innovatieve nucleaire technologieën ontwikkeld worden, die de duurzaamheid van nucleaire energie in de toekomst moeten verbeteren om zo de blijvende steun vanuit de publieke opinie te verzekeren. Ondanks de wereldwijde inspanningen die geleverd worden op dit vlak, zullen nucleaire systemen van de vierde generatie (Gen IV), zoals de *lood-gekoelde snelle reactor* (LFR), waarschijnlijk niet voor 2030 operationeel zijn. Één van de belangrijkste beoogde toepassingen voor deze types reactoren, naast de opwekking van elektriciteit, heeft betrekking tot het beheer van bestaand en toekomstig nucleair afval. De partitie en transmutatie van langlevende actiniden, in een snelle reactor, zou de benodigde opslagtijd voor hoog-radioactief afval drastisch kunnen verminderen tot minder dan 1000 a. Belangrijk in de context van dit werk is het feit dat de inspanningen die het SCK•CEN levert met betrekking tot de ontwikkeling van zulke innovatieve systemen geconsolideerd zijn in het MYRRHA project.

Van zodra hij operationeel is, zal deze *multifunctionele hybride-onderzoeksreactor voor innovatieve toepassingen* (MYRRHA) dienst doen als bron van protonen en neutronen voor verscheidene toepassingen, waarbij hij onder meer zal aangewend worden bij het onderzoek naar brandstoffen en structurele materialen voor geavanceerde nucleaire systemen. Hoewel de MYRRHA reactor zelf nog geen Gen IV kernreactor zal zijn, is hij wel gebaseerd op zware metalen-gekoelde snelle reactor technologie, waardoor deze onderzoeksreactor zeker zal kunnen bijdragen tot de ontwikkeling van de LFR en andere Gen IV systemen. Het innovatieve karakter van de MYRRHA onderzoeksreactor zorgt er wel voor dat er nog een aantal belangrijke uitdagingen bestaan die dienen overwonnen te worden, onder andere met betrekking tot de performantie van structurele materialen. Het beoogde primaire koelmiddel is *eutectisch lood-bismut* (LBE), dat uit *ca.* 45 wt.% Pb en *ca.* 55 wt.% Bi bestaat. Ondanks zijn gunstige thermofysische en neutronische eigenschappen is dit koelmiddel uiterst corrosief ten opzichte van hooggelegeerde stalen, waardoor er strenge eisen gesteld worden aan de structurele materialen die zouden aangewend worden. Zodoende werden er drie hooggelegeerde stalen geselecteerd waarvan verwacht wordt dat ze enigszins zullen bestand zijn tegen

de corrosieve werking van het LBE (T91, 316L en 15-15Ti). In deze context is de multi-element sporenanalyse van LBE en hooggelegeerde stalen van belang, bijvoorbeeld voor de bepaling van spoorelementen die bepalend zijn voor de mechanische eigenschappen van staallegeringen of om de opname van corrosieproducten door het koelmiddel te monitoren. In beide gevallen zullen de spoorelementen in kwestie echter slechts op $\mu g \, g^{-1}$ niveau, of lager, aanwezig zijn, waardoor het gebruik van een uiterst gevoelige analytische techniek essentieel is. Daarbovenop zal er in de toekomst ook nood zijn aan isotoop-selectieve analytische methoden, in het kader van het onderzoek dat uitgevoerd zal worden in de MYRRHA reactor, onder andere naar nieuwe nucleaire brandstoffen en naar de transmutatie van actiniden in nucleair afval. Voor een diepgaander overzicht van de bredere context en de objectieven van dit werk wordt de lezer verwezen naar Hoofdstuk 1.

Dubbel-focusserende sector-veld inductief gekoppeld plasma-massaspectrometrie (ICP-SFMS) is een uiterst gevoelige element-selectieve analytische techniek, die de multi-element mogelijkheden van *inductief gekoppeld plasma-optische emissiespectrometrie* (ICP-OES) combineert met bepalingsgrenzen die zelfs nog lager zijn dan de reeds uitstekende waarden die geassocieerd worden met *grafietoven atomaire absorptiespectrometrie* (GFAAS). Daarom is het de techniek bij uitstek voor de multi-element analyse van een grote verscheidenheid aan monsters, zoals LBE en hooggelegeerde stalen. Bovenop elementaire concentraties leveren zijn relatief simpele massaspectra ook een isotopische vingerafdruk, wat de isotopische analyse van monsters zoals nucleaire brandstoffen toelaat. In vergelijking met de wijdverspreide *quadrupool inductief gekoppeld plasma-massaspectrometers* (ICP-QMS) beschikken ICP-SFMS instrumenten typisch over een hogere gevoeligheid, een lagere achtergrond en de mogelijkheid om te opereren bij hogere massaresoluties, zodat vele spectrale interferenties kunnen geresolveerd worden. Bijgevolg zijn detectielimieten tot onder het $ng \, L^{-1}$ niveau haalbaar voor vele elementen, waarbij contaminaties meestal de beperkende factor blijken te zijn. Hoewel vele van de vaakst voorkomende spectrale interferenties op eenvoudige wijze kunnen geresolveerd worden wanneer een ICP-SFMS instrument aangewend wordt, blijven niet-spectrale interferenties vaak problematisch. De meest eenvoudige en elegante manier om deze matrixeffecten te elimineren bestaat uit het selectief afscheiden van de matrix, alvorens de spoorelementen te bepalen aan de hand van ICP-SFMS. Om dit te bewerkstelligen wordt vaak gebruik gemaakt van kolomchromatografie, omwille van zijn eenvoud en gebruiksgemak, waarbij meestal één of een klein aantal spoorelementen weerhouden worden op een zeer selectief hars terwijl ditzelfde hars geen enkele affiniteit vertoont voor de matrixelementen (of vice versa). Buiten het feit dat ICP-SFMS instrumenten uiterst geschikt zijn voor multi-element analyses, wordt het gebruik van deze techniek voor isotopische analyses gerechtvaardigd door zijn uitstekende isotopen ratio precisie, in vergelijking met wanneer bijvoorbeeld traditionele ICP-QMS instrumenten aangewend worden. In het verleden werden voor enkele-collector ICP-SFMS instrumenten optimale isotopen ratio precisies van 0.05 % RSD gerapporteerd in de literatuur, wat werd toegeschreven aan de karakteristieke trapeziumvormige

pieken, met een vlakke top, die typisch verkregen worden bij de laagste massa-resolutie. Zulke waarden zijn natuurlijk vrij bescheiden in vergelijking met de $\leq 0.01\,\%$ RSD die op routinematige basis gerapporteerd wordt voor *multipele-collector thermische ionisatie massaspectrometrie* (MC-TIMS), maar ICP-SFMS kan in bepaalde gevallen nog steeds geschikt gevonden worden, bijvoorbeeld door een verminderde nood aan tijdrovende en arbeidsintensieve monstervoor-bereidingsprocedures. Voor een gedetailleerd overzicht van de sterktes, zwaktes en basisprincipes van ICP-SFMS wordt de lezer verwezen naar Hoofdstuk 2.

Het enkele-collector ICP-SFMS instrument dat gebruikt werd doorheen dit werk is een genucleariseerde Element2 (Thermo Scientific, Duitsland). Bij een genucleariseerde ICP-MS wordt het instrument gekoppeld aan een handschoenkast, waarin alle componenten tot en met de interface ondergebracht worden, en waarin een lichte onderdruk heerst, wat de analyse van radioactieve monsters toelaat. Een beperkt aantal monsters werd ook geanalyseerd met behulp van een XSeries2 (Thermo Scientific, Duitsland) ICP-QMS instrument, zodat de prestaties van deze instrumenten vergeleken konden worden. Voor beide toestellen worden de typische instrumentele en data acquisitie parameters beschreven in Hoofdstuk 3. Datzelfde hoofdstuk bevat ook een overzicht van het labomateriaal en de reagentia die doorheen dit werk aangewend werden bij de gebruikte monstervoorbereidings-procedures alsook bij de bereiding van blanco's, standaarden en eluenten.

De ontwikkeling en toepassing van een analytische methode die de multi-element analyse van hooggelegeerde stalen zoals T91, 3165L en 15-15Ti toelaat werd beschreven in Hoofdstuk 4. De voornaamste matrixelementen die in deze stalen verwacht werden waren Cr, Fe en Ni naast kleinere hoeveelheden Si, V, Mn, Co, Cu and Mo. De lijst van potentieel interessante spoorelementen die daaropvolgend werd samengesteld omvatte op zijn beurt B, Al, P, S, Ti, As, Zr, Nb, Ta en W. Deze elementen dienden bepaald te worden op sporen- of ultra-sporenniveau in de aanwezigheid van een grote overmaat van de matrixele-menten. Om niet enkel spectrale en niet-spectrale interferenties, die vaak gepaard gaan met ICP-MS analyses, te elimineren, maar ook om uitgesproken geheugen-effecten te vermijden, werd een zeer selectieve scheidingsprocedure ontwikkeld en toegepast. In het ideale geval had deze procedure moeten toelaten om de te bepalen spoorelementen te isoleren van al de matrixelementen, maar op zijn minst had het mogelijk moeten zijn om de drie voornaamste matrixelementen Cr, Fe en Ni af te scheiden. Hiertoe werd een snelle en efficiënte kolomchro-matografische scheidingsprocedure bedacht, gebaseerd op het gebruik van AG 50Wx8 kationenuitwisselingshars. In dit protocol worden niet enkel Cr, Fe en Ni, maar ook een aantal van de minder belangrijke matrixelementen, selectief weerhouden op de kationenwisselaar, vanuit een verdund HNO_3/HF medium, terwijl de spoorelementen slechts een beperkte affiniteit voor het hars vertonen en snel elueren. In het geval van Fe en Ni is de afscheidingsefficiëntie $> 99.9\,\%$, terwijl ze voor Cr beperkt is tot $> 90\,\%$. In het algemeen, voor de drie hooggelegeerde stalen in kwestie, bleek het meestal mogelijk om $> 97.5\,\%$ van de gehele matrix

af te scheiden van de spoorelementen. In een later stadium bleek dat deze methode niet enkel toegepast kon worden voor de bepaling van B, Al, P, S, Ti, As, Zr, Nb, Ta and W in hooggelegeerde stalen, maar dat ze ook de sporenanalyse van Be, Ge, Se, Rh, Pd, Sn, Sb, Hf, Re, Ir in Pt in zulke stalen toeliet.

De procedure die ontwikkeld werd voor de bepaling van spoorelementen in hooggelegeerde stalen werd gevalideerd aan de hand van de analyse van (i) *gecertificeerde referentie materialen* (CRM), (ii) gespikete imitatiemonsters en (iii) echte stalen. Bij de analyse van drie verschillende CRM's was er over het algemeen een goede overeenstemming tussen de experimenteel bepaalde concentraties en de overeenkomstige gecertificeerde waarden, terwijl de terugvinding meestal ongeveer $100\,\%$ bedroeg bij de analyse van gespikete imitatiemonsters. De procedurele bepalingsgrenzen (QL, $10s$) werden bepaald door de analyse van verschillende onafhankelijk procedurele blanco's, waarbij optimale waarden tot in het lage $\mathrm{ng\,g^{-1}}$ niveau verkregen werden voor onder meer Re en Hf. Uiteindelijk werd de procedure ook toegepast op monsters van echte hooggelegeerde stalen, die verkregen werden vanuit het SCK•CEN, waarbij de aanwezigheid van de meeste spoorelementen kon aangetoond worden in ten minste één van de beschikbare monsters, met uitzondering van Be, S, Se, Hf en Ir. Het protocol dat hierboven beschreven werd, werd specifiek ontwikkeld voor de multi-element sporenanalyse van T91, 316L en 15-15Ti legeringen, hooggelegeerde stalen die voornamelijk samengesteld zijn uit Cr, Fe en Ni. Het is echter voor de hand liggend dat dit protocol breder toepasbaar zou kunnen zijn, bijvoorbeeld voor de analyse van andere legeringen of ijzermeteorieten.

Terwijl in Hoofdstuk 4 een analytische methode werd beschreven voor de multi-element sporenanalyse van hooggelegeerde stalen zoals T91, 316L en 15-15Ti, werd een soortgelijke methode voor de multi-element sporenanalyse van LBE besproken in Hoofdstuk 5. Dit LBE is het beoogde koelmiddel voor de MYRRHA onderzoeksreactor, dat in direct fysiek contact zal komen met bovengenoemde hooggelegeerde stalen. Voor dit type monster werd een aparte lijst van mogelijk interessante spoorelementen samengesteld, bestaande uit Ti, V, Cr, Mn, Fe, Co, Ni, Cu, Nb, Mo, Ag, Cd, Te, Ce, Re, Tl, Th en U, waarin onder meer een aantal te verwachten corrosieproducten omvat zitten. Net zoals bij hooggelegeerde stalen wordt de analyse van LBE monster gehinderd door het voorkomen van spectrale en niet-spectrale interferenties. Echter, in vergelijking met staallegeringen, bezit LBE een vrij eenvoudige matrix, die voornamelijk uit Pb en Bi bestaat. Derhalve is het voorkomen van matrix-geïnduceerde spectrale interferenties voorspelbaarder en daarom ook minder problematisch. Desondanks zou de accurate bepaling van spoorelementen nog steeds gehinderd kunnen worden door niet-spectrale interferenties. Zodoende werd het nodig geacht om opgeloste LBE monsters te onderwerpen aan een scheidingsprocedure, om de problematische matrix te elimineren alvorens de spoorelementen te bepalen aan de hand van ICP-SFMS. Hoewel in dit geval slechts twee matrix elementen dienden geïsoleerd te worden bleek dit in eerste instantie minder eenvoudig dan bij de hooggelegeerde stalen, aangezien geen enkel hars geïdentificeerd kon worden dat zowel Pb als Bi selectief had kunnen afscheiden, van de spoorelementen, in een verdund $\mathrm{HNO_3/HF}$ medium. Daarom werden

twee verschillende harsen geselecteerd, die elk op zich in staat waren om ofwel Pb ofwel Bi te weerhouden, terwijl ze slechts een beperkte affiniteit vertoonden voor de spoorelementen. In de geoptimaliseerde kolomchromatografische scheidingsprocedure worden twee kolommen in tandem gebruikt, waarbij één kolom van 2 mL, die beladen is met extractiechromatografisch Pb Spec hars, geplaatst wordt boven een tweede kolom van 5 mL, die op zijn beurt beladen is met AG 1x4 anionenuitwisselingshars. Het matrixelement Pb wordt weerhouden op het Pb Spec hars terwijl het andere matrix element Bi een grote affiniteit vertoont voor het AG 1x4 hars. De meeste spoorelementen, op hun beurt, vertonen slechts een beperkte affiniteit voor beide harsen en elueren snel. Bijgevolg kan meer dan 99 % van de LBE matrix afgescheiden worden van de te bepalen spoorelementen. Het spoorelement Re vertoont een affiniteit voor beide harsen en belandt mede daarom in twee verschillende fracties, maar kan desalniettemin geïsoleerd worden van de matrix. Daarbovenop vertonen ook Ag en Tl een affiniteit voor het Pb Spec hars, maar deze elementen konden eveneens afgescheiden worden van de LBE matrix.

Het geoptimaliseerde protocol voor de multi-element sporenanalyse van LBE monsters werd gevalideerd aan de hand van de analyse van (i) Pb-matrix CRM's, (ii) gespikete imitatiemonsters en (iii) echte LBE monsters. Procedurele bepalingsgrenzen (QL, 10s), gaande van lage ng g^{-1} niveaus voor Th tot sub-µg g^{-1} niveaus voor Fe, werden bepaald aan de hand van de analyse van verschillende onafhankelijk procedurele blanco's. Voor de elementen waarvan de concentratie in de twee Pb-matrix CRM's gecertificeerd was, werd over het algemeen een goede overeenstemming vastgesteld met de overeenkomstige experimenteel bepaalde waarden (meer bepaald voor Ni, Cu, Ag, Cd, Te, Tl en Bi). Het enige echt problematische spoorelement was Te, waarvoor de experimenteel bepaalde concentratie ongeveer −70 % afweek van de gecertificeerde waarde. De auteur gaat ervan uit dat het probleem mogelijk terug te traceren valt tot bij de oplosprocedure, maar dat het tegelijk onwaarschijnlijk is dat de kolomchromatografische scheidingsprocedure aan de bron van deze afwijking ligt, omdat dit probleem niet waargenomen werd bij de analyse van gespikete imitatiemonsters. Voor de meeste elementen was de terugvinding bij de analyse van gespikete imitatiemonsters ongeveer 100 %, hoewel er een significante afwijking vastgesteld werd in het geval van Fe. Dit afwijkende resultaat kan echter verklaard worden door het feit dat de "zuivere" Pb en Bi poeders, die gebruikt werden om de imitatiemonsters te bereiden, relatief grote hoeveelheden Fe bleken te bevatten, dat bovendien heterogeen verdeeld leek te zijn. Daarbovenop was de procedurele bepalingsgrens voor Fe relatief hoog in vergelijking met die van de andere spoorelementen, omdat dit element bijzonder vatbaar is voor contaminaties. De analytische methode werd vervolgens toegepast op vijf monsters van eenzelfde batch LBE, een batch waarvan elders op het SCK•CEN ook een aantal monsters geanalyseerd werden met behulp van *neutronen activeringsanalyse* (NAA). Voor de meeste elementen was er een goede overeenstemming tussen de concentraties die bepaald werden met beide technieken, behalve voor Cr. Sommige van de spoorelementen (Ni, Cd en Tl) leken homogener verdeeld te zijn over de batch LBE dan andere (Cu, Ag end Te). Bovendien werd

een correlatie teruggevonden tussen de concentraties van Cu en Ag, in de monsters die werden genomen van deze batch LBE. Een aantal van de geselecteerde spoorelementen fungeerden eigenlijk als chemische analogen voor mogelijk interessante radionucliden, maar het valt nog af te wachten in hoeverre hun gedrag in de realiteit gelijklopend zal zijn. In de literatuur zijn gegevens beschikbaar voor AG 1x10 anionenuitwisselingshars en Sr Spec extractiechromatografisch hars, de laatstgenoemde lijkend op Pb Spec hars, dewelke suggereren dat Re inderdaad zou kunnen fungeren als chemisch analoog voor Tc doorheen de scheidingsprocedure. Daartegenover staat dat dit waarschijnlijk niet het geval zal zijn voor Te en Po of Ce en Pu, waardoor het noodzakelijk zal zijn om bestraalde LBE monsters te onderwerpen aan de ontwikkelde analytische methode, voornamelijk om het gedrag van ^{210}Po doorheen de scheiding te verifiëren (wat gevormd wordt als gevolg van neutronenvangst door ^{209}Bi). De procedure die beschreven werd in Hoofdstuk 5 werd in het bijzonder ontwikkeld voor de analyse van LBE monsters afkomstig van onderzoeksprojecten die verband houden met de ontwikkeling van de MYRRHA onderzoeksreactor bij SCK•CEN. Sommige andere geavanceerde nucleaire systemen zullen mogelijk gebruik maken van andere vloeibare zware metalen als primair koelmiddel, zoals de LFR waarbij het gebruik van zuiver Pb wordt beoogd. De multi-element sporenanalyse van Pb stalen afkomstig van zo'n reactor, aan de hand van ICP-SFMS, zal eveneens gehinderd worden door het voorkomen van niet-spectrale interferenties, hoewel er in dat geval slechts één in plaats van twee matrix elementen zou aanwezig zijn. Bijgevolg zou het protocol dat hierboven beschreven werd sterk vereenvoudigd kunnen worden, omdat enkel het Pb Spec extractiechromatografisch hars dan nog van belang zou zijn, waardoor er noch nood is aan het gebruik van verschillende eluenten, noch aan de tweede kolom, die in het bestaande protocol beladen wordt met AG 1x4 anionenuitwisselingshars.

De hierboven beschreven procedure werd tenslotte toegepast op een aantal echte LBE stalen, afkomstig van experimenten die uitgevoerd werden op het SCK•CEN in het kader van het onderzoek naar de corrosieve aard van LBE ten opzichte van hooggelegeerde stalen in geavanceerde nucleaire systemen zoals de MYRRHA reactor. In deze monsters konden een aantal inherente onzuiverheden en corrosieproducten geïdentificeerd worden, waarvoor de lezer verwezen wordt naar de bespreking in Appendix 5.5.1. Een aantal van deze stalen werd ook geanalyseerd aan de hand van ICP-QMS, waarbij verdunningen aangewend werden om de invloed van niet-spectrale interferenties te verminderen, in plaats van een kolomchromatografische scheiding toe te passen. Over het algemeen was er een goede overeenstemming tussen de resultaten die verkregen werden met beide technieken, hoewel de bepalingsgrenzen die haalbaar waren met het ICP-QMS instrument vanzelfsprekend slechter waren. Een aantal andere monsters werd ook geanalyseerd aan de hand van NAA op het SCK•CEN, waarvan de resultaten beschikbaar werden gemaakt aan de auteur. In dit geval was het verschil in bepalingsgrenzen duidelijk minder groot, hoewel diegene die haalbaar waren met ICP-SFMS meestal, op zen minst, vergelijkbaar waren met diegene die gerapporteerd werden voor NAA. Over het algemeen was er ook hier goede overeenstemming tussen de resultaten

die behaald werden met beide technieken (wederom met uitzondering van Cr). Bij een monster van een batch LBE die in langdurig contact met 316L hooggelegeerd staal had gestaan, werd een sterke toename van de Ni concentratie vastgesteld, wat in overeenstemming is met de selectieve dissolutie van Ni door LBE die in het verleden reeds gerapporteerd werd. Daarenboven werd ook een daling van de Cd concentratie vastgesteld, maar hier kon geen eenvoudig mechanisme voor geïdentificeerd worden. Hoewel deze monsters ook geanalyseerd zullen worden aan de hand van NAA op het SCK•CEN, waren deze resultaten nog niet beschikbaar ten tijde van dit schrijven, waardoor dit resultaat niet onafhankelijk bevestigd kon worden.

Tenslotte werden in Hoofdstuk 6 de mogelijkheden van SCK•CEN's genucleariseerde Element2 ICP-SFMS met betrekking tot de bepaling van isotopen ratio's onderzocht. De isotopische analyse van experimentele of commerciële kernbrandstoffen vindt al op routinematige basis plaats bij SCK•CEN, in het kader van *burnup* programma's of voor de kwalificatie van nieuwe brandstoffen, bijvoorbeeld aan de hand van een verouderd Sector 54 MC-TIMS instrument. In deze context is de isotopische analyse van bepaalde lanthaniden van bijzonder groot belang, waardoor vooral deze elementen beschouwd werden in dat hoofdstuk (meer bepaald Nd, Sm, Eu, Gd, Dy). Hoewel MC-TIMS instrumenten in staat zijn om op een routinematige basis een superieure isotopen ratio precisie van $\leq 0.01\,\%$ RSD te leveren, in vergelijking met de meer bescheiden isotopen ratio precisies van $\leq 0.05\,\%$ die in het verleden werden gerapporteerd voor ICP-SFMS instrumenten, zou de Element2 nog steeds geschikt kunnen blijken in bepaalde gevallen, bijvoorbeeld als gevolg van zijn hogere gevoeligheid of door een verminderde nood aan arbeidsintensieve en tijdrovende staalvoorbereidingsprocedures. In dit kader werden een aantal van de belangrijkste aandachtspunten met betrekking tot de bepaling van isotopen ratio's aan de hand van ICP-SFMS onderzocht.

De belangrijkste aspecten die werden onderzocht, waren (i) de correctie voor dode tijd-geïnduceerde telverliezen, (ii) de correctie voor massadiscriminatie-effecten en (iii) de haalbare interne precisie. De dode tijd van de detector werd bepaald aan de hand van een licht aangepaste versie van de procedure die beschreven werd door Appelblad en Baxter, dewelke een eenduidige waarde voor τ oplevert samen met een schatting van de bijhorende gecombineerde onzekerheid $u_c(\tau)$. Tegelijkertijd wordt er rekening gehouden met massadiscriminatie, terwijl de waarde van het echte isotopen ratio eigenlijk niet gekend hoeft te zijn om τ te bepalen. Een aantal auteurs hebben gerapporteerd dat de dode tijd kan veranderen doorheen de levensloop van een detector, hoewel er in dit geval geen significante verandering in τ kon vastgesteld worden over een periode van ongeveer tien weken, bij meer dan één verschillende SEM spanning. Andere auteurs maakten dan weer melding van het feit dat de dode tijd massa-afhankelijk is voor sommige types detectoren. Wederom kon dit fenomeen niet waargenomen worden bij de detector van SCK•CEN's Element2, hoewel de twee elementen die beschouwd werden, Ba en Lu, niet sterk van elkaar verschilden op vlak van massa. Bijgevolg werd één enkele dode tijd van $12\,\mathrm{ns}$ gebruikt in alle hierop volgende werk, een waarde die bepaald werd aan de hand van metingen van het $^{137}\mathrm{Ba}/^{138}\mathrm{Ba}$ ratio.

Het beschouwde isotopen ratio is significant verschillend van één, hoewel het niet te extreem is, zodat de isotopen ratio metingen nog steeds gepaard gaan met een goede interne precisie. Tenslotte zijn er ook een aantal auteurs die het voorkomen van "sag" waargenomen hebben, wat bijkomende telverliezen veroorzaakt, maar ook dit fenomeen kon niet geobserveerd worden, bij signaalintensiteiten tot en met $3\,200\,000\,\mathrm{counts\,s^{-1}}$. De correctie voor massadiscriminatie-effecten is helaas moeilijker voor enkele-collector ICP-SFMS instrumenten zoals de Element2 dan voor ICP-QMS of MC-ICP-SFMS instrumenten, omdat de massadiscriminatie correctiefactor niet goed genoeg gekarakteriseerd kan worden aan de hand van de vaakst gebruikte correctievergelijkingen, waardoor interne correctieprocedures niet aangewend kunnen worden. Quétel *et al.* schreven dit afwijkend gedrag toe aan het feit dat de versnellingspotentiaal van de Element2 verlaagd moet worden om een snelle massascan te kunnen uitvoeren, terwijl de rustmassa van de magnetische sector constant blijft. Bijgevolg dienen externe correctieprocedures aangewend te worden, in plaats van interne, waarbij isotopische standaarden en monsters afwisselend gemeten worden. Als hetzelfde isotopen ratio beschouwd wordt in de monsters als in de standaarden, dienen de bovengenoemde correctievergelijkingen niet gebruikt te worden. In dit geval is de staalvoorbereiding echter van groter belang, omdat er matrix-geïnduceerde massadiscriminatie-effecten kunnen optreden. Bovendien moeten er geschikte isotopische referentiematerialen beschikbaar zijn. Daarenboven is het essentieel dat de massadiscriminatie min of meer constant blijft tussen de metingen van de standaarden en de monsters. Voor eenvoudige standaardoplossingen bleek dat de massadiscriminatie relatief constant blijft gedurende reeksen van metingen die gespreid worden over een periode van ongeveer $3\,\mathrm{h}$. Daarbovenop bleek dat de massadiscriminatie onafhankelijk was van de spoorelementconcentratie over het gebied dat bestudeerd werd. De optimale interne precisie, die gedefinieerd werd als een relatieve standaarddeviatie op een aantal herhaalde metingen, die samen één enkele analyse vormen, was gemiddeld ongeveer $0.04\,\%$ RSD. Zulke waarden werden bekomen voor een isotopen ratio van ongeveer 0.74, met een signaalintensiteit van ongeveer $1\,000\,000\,\mathrm{counts\,s^{-1}}$ voor de meest abundante nuclide en een integratie tijd van ongeveer $30\,\mathrm{s}$ voor beide isotopen. Indien aangenomen wordt dat de totale aantal tellen voor beide isotopen onafhankelijk Poisson-verdeeld zijn, kan aangetoond worden dat de ondergrens voor de interne precisie iets minder dan $0.03\,\%$ RSD bedraagt. Bijgevolg bleek Poisson-telstatistiek de grootste bron van onzekerheid te zijn, een bron waarvan de bijdrage nooit volledig geëlimineerd kan worden. Het werd ook aangetoond dat de geobserveerde interne precisie eenzelfde trend vertoont als diegene die theoretisch voorspeld wordt door Poisson-telstatistiek, bij variaties in de waarde van het isotopen ratio, de integratietijden en de signaalintensiteiten. Twee maal de theoretisch voorspelde isotopen ratio precisie kon daarom beschouwd worden als een conservatieve maar realistische schatting van de interne precisie die experimenteel haalbaar is, wanneer twee verschillende isotopen ratio's bepaald werden in dezelfde meting. De optimale interne precisie van ongeveer $0.04\,\%$ RSD, die haalbaar bleek te zijn met de Element2 ICP-SFMS, is echter niet vergelijkbaar

met de optimale isotopen ratio precisie van $0.005\,\%$ RSD die in het verleden verkregen werd met SCK•CEN's Sector 54 MC-TIMS instrument. Om zulke waarde te kunnen bekomen moet het MC-TIMS instrument echter gebruik maken van zijn statische multipele-collector modus, dewelke op het SCK•CEN enkel voor Nd aangewend wordt. Voor elementen waarbij de TIMS metingen uitgevoerd worden in de zogenaamde "peak-hopping mode", met één enkele Daly detector, in plaats van een reeks minder gevoelige Faraday collectoren, is het echter wel mogelijk dat de Element2 in staat zou kunnen zijn om een betere isotopen ratio precisie te leveren. Aangezien dit werk slechts een beperkte verkennende studie omvatte, zal het echter nodig zijn om bijkomende experimenten uit te voeren, om te kunnen aantonen of enkele-collector ICP-SFMS al dan niet geschikt is voor de bepaling van isotopen ratio's in een routine setting bij SCK•CEN.

Bibliography

[1]   T. Tindemans, A. Dobney, D. Wambeke and F. Vanhaecke, On the determination of trace elements in lead-bismuth eutectic by means of sector-field inductively coupled plasma-mass spectrometry, *Journal of Analytical Atomic Spectrometry*, 2013, **28**, 1345–1353.

[2]   T. Tindemans, A. Dobney, D. Wambeke and F. Vanhaecke, Development and application of an analyte/matrix separation procedure for multi-element trace analysis of steel alloys by means of sector-field ICP-mass spectrometry, *Journal of Analytical Atomic Spectrometry*, 2014, **29**, 1073–1081.

[3]   T. F. Stocker, D. Qin, G. K. Plattner, M. Tignor, S. K. Allen, J. Boschung, A. Nauels, Y. Xia, V. Bex and P. M. Midgley, *Climate Change 2013: The Physical Science Basis. Contribution of Working Group I to the Fifth Assessment Report of the Intergovernmental Panel on Climate Change*, Intergovernmental panel on climate change technical report, 2013.

[4]   O. Edenhofer, R. Pichs-Madruga, Y. Sokona, E. Farahani, S. Kadner, K. Seyboth, A. Adler, I. Baum, S. Brunner, P. Eickemeier, B. Kriemann, J. Savolainen, S. Schlomer, C. von Stechown, T. Zwickel and J. C. Minx, *Climate Change 2014: Mitigation of Climate Change. Contribution of Working Group III to the Fifth Assessment Report of the Intergovernmental Panel on Climate Change*, Intergovernmental panel on climate change technical report, 2014.

[5]   European Union, *EU energy trends to 2030*, 2009.

[6]   European Environment Agency, *Annual European Union greenhouse gas inventory 1990-2012 and inventory report 2014*, European commission technical report, 2014.

[7]   European Union, *Energy Markets in the European Union in 2011*, 2012.

[8]   M. M. Abu-Khader, Recent advances in nuclear power: A review, *Progress In Nuclear Energy*, 2009, **51**, 225–235.

[9]   A. Schmidt, A. Ivanova and M. S. Schäfer, Media attention for climate change around the world: A comparative analysis of newspaper coverage in 27 countries, *Global Environmental Change*, 2013, **23**, 1233–1248.

[10]   International Energy Agency, *Energy technology initiatives 2013: Implementation through multilateral co-operation*, 2013.

[11] International Energy Agency, *Redrawing the energy-climate map: World energy outlook special report*, 2013.

[12] The Generation IV International Forum, *A technology roadmap for generation IV nuclear energy systems*, 2002.

[13] The Generation IV International Forum, *R&D outlook for generation IV nuclear energy systems*, 2009.

[14] The Generation IV International Forum, *Technology roadmap update for generation IV nuclear energy systems*, 2014.

[15] J. Magill, V. Berthou, D. Haas, J. Galy, R. Schenkel, H. W. Wiese, G. Heusener, J. Tommasi and G. Youinou, Impact limits of partitioning and transmutation scenarios on the radiotoxicity of actinides in radioactive waste, *Nuclear Energy-journal of the British Nuclear Energy Society*, 2003, **42**, 263–277.

[16] L. Cinotti, C. F. Smith, H. Sekimoto, L. Mansani, M. Reale and J. J. Sienicki, Lead-cooled system design and challenges in the frame of Generation IV International Forum, *Journal of Nuclear Materials*, 2011, **415**, 245–253.

[17] H. Oigawa, K. Tsujimoto, K. Nishihara, T. Sugawara, Y. Kurata, H. Takei, S. Saito, T. Sasa and H. Obayashi, Role of ADS in the back-end of the fuel cycle strategies and associated design activities: The case of Japan, *Journal of Nuclear Materials*, 2011, **415**, 229–236.

[18] E. P. Loewen and A. T. Tokuhiro, Status of research and development of the lead-alloy-cooled fast reactor, *Journal of Nuclear Science and Technology*, 2003, **40**, 614–627.

[19] International Atomic Energy Agency, *Liquid metal coolants for fast reactors cooled by sodium, lead, and lead-bismuth eutectic*, 2012.

[20] H. A. Abderrahim, T. Aoust, E. Malambu, V. Sobolev, K. Van Tichelen, D. De Bruyn, D. Maes, W. Haeck and G. Van den Eynde, MYRRHA, A Pb-Bi experimental ADS: Specific approach to radiation protection aspects, *Radiation Protection Dosimetry*, 2005, **116**, 433–441.

[21] H. A. Abderrahim and P. D'Hondt, MYRRHA: A European experimental ADS for R&D applications - Status at mid-2005 and prospective towards implementation, *Journal of Nuclear Science and Technology*, 2007, **44**, 491–498.

[22] Nuclear Science Committee, *Handbook on lead-bismuth eutectic alloy and lead properties, materials compatibility, thermal-hydraulics and technologies*, Oecd nuclear energy agency technical report, 2007.

[23] OECD Nuclear Energy Agency, *Independent evaluation of the MYRRHA project: Report by an international team of experts*, 2009.

[24] H. A. Abderrahim, P. Baeten, D. De Bruyn, J. Heyse, P. Schuurmans and J. Wagemans, MYRRHA, a Multipurpose hYbrid Research Reactor for High-end Applications, *Nuclear Physics News*, 2010, **20**, 24–28.

[25] D. De Bruyn, H. A. Abderrahim, P. Baeten and R. Fernandez, ICAPP'11 - Performance & flexibility:the power of innovation, 2011, pp. 472–478.

[26] H. A. Abderrahim, P. Baeten, D. De Bruyn and R. Fernandez, MYRRHA - A multi-purpose fast spectrum research reactor, *Energy Conversion and Management*, 2012, **63**, 4–10.

[27] H. Baker, *ASM Handbook, Vol. 3 Alloy Phase Diagrams*, 1992.

[28] J. Van den Bosch, R. W. Bosch, D. Sapundjiev and A. Almazouzi, Liquid metal embrittlement susceptibility of ferritic-martensitic steel in liquid lead alloys, *Journal of Nuclear Materials*, 2008, **376**, 322–329.

[29] J. Van den Bosch, A. Almazouzi, G. Mueller and A. Rusanov, Production and preliminary characterization of ferritic-martensitic steel T91 cladding tubes for LBE or Pb cooled nuclear systems, *Journal of Nuclear Materials*, 2011, **415**, 276–283.

[30] O. Gelineau and S. Gavrilov, *Final report material property requirements for ASTRID and MYRRHA ADS system*, 2012.

[31] J. J. Dufrane, Why do we Need to Measure Trace Elements in Steel?, *Journal De Physique IV*, 1995, **05**, C7–23–C7–31.

[32] J. J. Stephens and R. O. Pohl, Trace elements in reactor steels: implications for decommissioning, *Nuclear Engineering and Design*, 1978, **47**, 125–134.

[33] T. Obara, T. Miura and H. Sekimoto, Fundamental study of polonium contamination by neutron irradiated lead-bismuth eutectic, *Journal of Nuclear Materials*, 2005, **343**, 297–301.

[34] International Atomic Energy Agency, *Implementation of burnup credit in spent fuel management systems*, 1997.

[35] OECD Nuclear Energy Agency, *Spent nuclear fuel assay data for isotopic validation*, 2011.

[36] R. Thomas, *Practical Guide to ICP-MS: A Tutorial for Beginners*, Taylor & Francis, 2003.

[37] S. J. Hill, *Inductively Coupled Plasma Spectrometry and its Applications*, Wiley, 2007.

[38] M. Moldovan, E. M. Krupp, A. E. Holliday and O. F. X. Donard, High resolution sector field ICP-MS and multicollector ICP-MS as tools for trace metal speciation in environmental studies: a review, *Journal of Analytical Atomic Spectrometry*, 2004, **19**, 815–822.

[39] N. Jakubowski, T. Prohaska, L. Rottmann and F. Vanhaecke, Inductively coupled plasma- and glow discharge plasma-sector field mass spectrometry, *Journal of Analytical Atomic Spectrometry*, 2011, **26**, 693–726.

[40] K. L. Linge and K. E. Jarvis, Quadrupole ICP-MS: introduction to instrumentation, measurement techniques and analytical capabilities, *Geostandards and Geoanalytical Research*, 2009, **33**, 445–467.

[41] C. Agatemor and D. Beauchemin, Matrix effects in inductively coupled plasma mass spectrometry: A review, *Analytica Chimica Acta*, 2011, **706**, 66–83.

[42] F. Vanhaecke, L. Moens, R. Dams and P. Taylor, Precise measurement of isotope ratios with a double-focusing magnetic sector ICP mass spectrometer, *Analytical Chemistry*, 1996, **68**, 567–569.

[43] J. S. Becker, *Inorganic Mass Spectrometry: Principles and Applications*, John Wiley & Sons, Ltd, 2007.

[44] F. Vanhaecke, L. Balcaen and D. Malinovsky, Use of single-collector and multi-collector ICP-mass spectrometry for isotopic analysis, *Journal of Analytical Atomic Spectrometry*, 2009, **24**, 863–886.

[45] R. S. Houk, V. A. Fassel, G. D. Flesch, H. J. Svec, A. L. Gray and C. E. Taylor, Inductively coupled argon plasma as an ion-source for mass-spectrometric determination of trace-elements, *Analytical Chemistry*, 1980, **52**, 2283–2289.

[46] D. Potter, A commercial perspective on the growth and development of the quadrupole ICP-MS market, *Journal of Analytical Atomic Spectrometry*, 2008, **23**, 690–693.

[47] G. K. Zoorob, J. W. McKiernan and J. A. Caruso, ICP-MS for elemental speciation studies, *Microchimica Acta*, 1998, **128**, 145–168.

[48] K. L. Sutton and J. A. Caruso, Liquid chromatography–inductively coupled plasma mass spectrometry, *Journal of Chromatography A*, 1999, **856**, 243–258.

[49] C. M. Barshick, D. C. Duckworth and D. H. Smith, *Inorganic mass spectrometry : fundamentals and applications*, Marcel Dekker, Inc., New York :, 2000.

[50] B. Bouyssiere, J. Szpunar and R. Lobinski, Gas chromatography with inductively coupled plasma mass spectrometric detection in speciation analysis, *Spectrochimica Acta Part B: Atomic Spectroscopy*, 2002, **57**, 805–828.

[51] A. Cocherie and M. Robert, Laser ablation coupled with ICP-MS applied to U-Pb zircon geochronology: A review of recent advances, *Gondwana Research*, 2008, **14**, 597–608.

[52] M. Aramendia, M. Resano and F. Vanhaecke, Electrothermal vaporization-inductively coupled plasma-mass spectrometry: A versatile tool for tackling challenging samples A critical review, *Analytica Chimica Acta*, 2009, **648**, 23–44.

[53] D. Profrock and A. Prange, Inductively Coupled Plasma-Mass Spectrometry (ICP-MS) for Quantitative Analysis in Environmental and Life Sciences: A Review of Challenges, Solutions, and Trends, *Applied Spectroscopy*, 2012, **66**, 843–868.

[54] A. Westman-Brinkmalm and G. Brinkmalm, *A Mass Spectrometer's Building Blocks*, John Wiley & Sons, Inc., 2008.

[55] R. Thomas, A beginner's guide to ICP-MS - Part I, *Spectroscopy*, 2001, **16**, 38–42.

[56] R. Thomas, A beginner's guide to ICP-MS - Part II: The sample-introduction system, *Spectroscopy*, 2001, **16**, 56–60.

[57] J. Mora, S. Maestre, V. Hernandis and J. L. Todoli, Liquid-sample introduction in plasma spectrometry, *Trends In Analytical Chemistry*, 2003, **22**, 123–132.

[58] B. L. Sharp, Pneumatic nebulizers and spray chambers for inductively coupled plasma spectrometry - A review .1. Nebulizers, *Journal of Analytical Atomic Spectrometry*, 1988, **3**, 613–652.

[59] H. E. Taylor, *Inductively Coupled Plasma-mass Spectrometry: Practices and Techniques*, ACADEMIC PressINC, 2001.

[60] S. M. Nelms, *Inductively coupled plasma mass spectrometry handbook*, Blackwell Pub., 2005.

[61] B. L. Sharp, Pneumatic nebulizers and spray chambers for inductively coupled plasma spectrometry - A review .2. Spray chambers, *Journal of Analytical Atomic Spectrometry*, 1988, **3**, 939–963.

[62] *Inert double-pass Scott-type spray chamber*, http://www.icpms.com/products/spray.php, Accessed: 2014-06-01.

[63] *Double-pass Scott-type spray chamber*, http://www.precisionglassblowing.com/catalog/thermo-finnigan-element-spray-chamber-scott-pyrex-p-233.html, Accessed: 2014-06-01.

[64] *Cyclonic spray chamber*, http://www.precisionglassblowing.com/catalog/twinnabar-p-1833.html, Accessed: 2014-06-01.

[65] *Dual cyclonic/Scott type spray chamber*, http://www.meinhard.com/index.cfm/category/385/thermo-neptune-spray-chambers.cfm, Accessed: 2014-06-01.

[66] R. Thomas, A beginner's guide to ICP-MS - Part XIII - Sampling accessories, *Spectroscopy*, 2002, **17**, 26–33.

[67] R. Thomas, A Beginner's guide to ICP-MS - Part XIV - Sampling accessories, Part II, *Spectroscopy*, 2003, **18**, 42–54.

[68] P. C. Kruger, L. M. Schell, A. D. Stark and P. J. Parsons, Lanthanide distribution in human placental tissue by membrane desolvation-ICP-MS, *Journal of Analytical Atomic Spectrometry*, 2010, **25**, 1298–1307.

[69] Y. Gao, R. Liu and L. Yang, Application of chemical vapor generation in ICP-MS: A review, *Chinese Science Bulletin*, 2013, **58**, 1980–1991.

[70] R. Thomas, A beginner's guide to ICP-MS - Part III: The plasma source, *Spectroscopy*, 2001, **16**, 26–30.

[71] J. Robinson, E. Frame and G. Frame, *Undergraduate Instrumental Analysis, Sixth Edition*, Taylor & Francis, 2004.

[72] *ICP*, http://www.wcaslab.com/tech/tbicpms.htm, Accessed: 2014-06-01.

[73] *Sampler Cone*, http://www.geicp.com/cgi-bin/site/wrapper.pl?c1=Show-part&partno=TF1006A-Pt/Cu, Accessed: 2014-06-01.

[74] *Skimmer Cone*, http://www.geicp.com/cgi-bin/site/wrapper.pl?c1=Show-part&partno=TF1007-Pt, Accessed: 2014-06-01.

[75] R. Thomas, A beginner's guide to ICP-MS - Part IV: The interface region, *Spectroscopy*, 2001, **16**, 26–34.

[76] D. J. Douglas and J. B. French, An improved interface for inductively coupled plasma-mass spectrometry (ICP-MS), *Spectrochimica Acta Part B: Atomic Spectroscopy*, 1986, **41**, 197–204.

[77] N. S. Nonose, N. Matsuda, N. Fudagawa and M. Kubota, Some characteristics of polyatomic ion spectra in inductively coupled plasma mass spectrometry, *Spectrochimica Acta Part B: Atomic Spectroscopy*, 1994, **49**, 955–974.

[78] R. Thomas, A beginner's guide to ICP-MS - Part V: The ion focusing system, *Spectroscopy*, 2001, **16**, 38–44.

[79] R. Thomas, A beginner's guide to ICP-MS - Part VI - The mass analyzer, *Spectroscopy*, 2001, **16**, 44–48.

[80] C. G. Herbert and R. A. W. Johnstone, *Mass spectrometry basics*, Boca Raton, CRC Press, 2003.

[81] P. E. Miller and M. B. Denton, The quadrupole mass filter: Basic operating concepts, *Journal of Chemical Education*, 1986, **63**, 617–623.

[82] R. Thomas, A beginner's guide to ICP-MS - Part VII: Mass separation devices - Double-focusing magnetic-sector technology, *Spectroscopy*, 2001, **16**, 22–27.

[83] J. Mattauch, A Double-Focusing Mass Spectrograph and the Masses of ^{15}N and ^{18}O, *Physical Review*, 1936, **50**, 617–623.

[84] A. O. Nier and T. R. Roberts, The Determination of Atomic Mass Doublets by Means of a Mass Spectrometer, *Physical Review*, 1951, **81**, 507–510.

[85] E. G. Johnson and A. O. Nier, Angular Aberrations in Sector Shaped Electromagnetic Lenses for Focusing Beams of Charged Particles, *Physical Review*, 1953, **91**, 10–17.

[86] N. Jakubowski, L. Moens and F. Vanhaecke, Sector field mass spectrometers in ICP-MS, *Spectrochimica Acta Part B: Atomic Spectroscopy*, 1998, **53**, 1739–1763.

[87] R. Thomas, A beginner's guide to ICP-MS - Part VIII - Mass analyzers: Time-of-flight technology, *Spectroscopy*, 2002, **17**, 36–41.

[88] M. Balcerzak, An overview of analytical applications of time of flight-mass spectrometric (TOF-MS) analyzers and an inductively coupled plasma-TOF-MS technique, *Analytical Sciences*, 2003, **19**, 979–989.

[89] R. Thomas, A beginner's guide to ICP-MS - Part X - Detectors, *Spectroscopy*, 2002, **17**, 34–39.

[90] F. Vanhaecke and P. Degryse, *Isotopic Analysis: Fundamentals and Applications Using ICP-MS*, Wiley, 2012.

[91] R. Thomas, A beginner's guide to ICP-MS - Part XII - A review of interferences, *Spectroscopy*, 2002, **17**, 24–31.

[92] U. Nygren, H. Ramebäck, D. C. Baxter and C. Nilsson, Lanthanide phosphate interferences in actinide determination using inductively coupled plasma mass spectrometry, *Journal of Analytical Atomic Spectrometry*, 2005, **20**, 529–534.

[93] T. W. May and R. H. Wiedmeyer, A table of polyatomic interferences in ICP-MS, *Atomic Spectroscopy*, 1998, **19**, 150–155.

[94] J. S. Becker and H. J. Dietze, Application of double-focusing sector field ICP mass spectrometry with shielded torch using different nebulizers for ultratrace and precise isotope analysis of long-lived radionuclides - Invited lecture, *Journal of Analytical Atomic Spectrometry*, 1999, **14**, 1493–1500.

[95] J. Vogl, M. Rosner and W. Pritzkow, Development and validation of a single collector SF-ICPMS procedure for the determination of boron isotope ratios in water and food samples, *Journal of Analytical Atomic Spectrometry*, 2011, **26**, 861–869.

[96] A. D. Leslie and D. A. Volmer, Dealing with the masses: A tutorial on accurate masses, mass uncertainties, and mass defects, *Spectroscopy*, 2007, **22**, 32–39.

[97] R. Thomas, A beginner's guide to ICP-MS - Part IX - Mass analyzers: Collision/reaction cell technology, *Spectroscopy*, 2002, **17**, 42–48.

[98] S. D. Tanner and V. I. Baranov, A dynamic reaction cell for inductively coupled plasma mass spectrometry (ICP-DRC-MS). II. Reduction of interferences produced within the cell, *Journal of the American Society For Mass Spectrometry*, 1999, **10**, 1083–1094.

[99] S. D. Tanner and V. I. Baranov, Theory, design, and operation of a dynamic reaction cell for ICP-MS, *Atomic Spectroscopy*, 1999, **20**, 45–52.

[100] S. D. Tanner, V. I. Baranov and D. R. Bandura, Reaction cells and collision cells for ICP-MS: a tutorial review, *Spectrochimica Acta Part B: Atomic Spectroscopy*, 2002, **57**, 1361–1452.

[101] A. Leykin and P. Yakimovich, Systems for the suppression of spectral interferences for inductively coupled plasma mass-spectrometry, *Journal of Analytical Chemistry*, 2012, **67**, 677–686.

[102] M. Colon, M. Hidalgo and M. Iglesias, Correction strategies over spectral interferences for arsenic determination in aqueous samples with complex matrices by quadrupole ICP-MS, *Journal of Analytical Atomic Spectrometry*, 2009, **24**, 518–521.

[103] K. Sakata and K. Kawabata, Reduction of fundamental polyatomic ions in inductively coupled plasma mass spectrometry, *Spectrochimica Acta Part B: Atomic Spectroscopy*, 1994, **49**, 1027–1038.

[104] F. Vanhaecke, C. Vandecasteele, H. Vanhoe and R. Dams, Study of the intensity of M^+, M^{2+} and MO^+ signals in icp-ms as a function of instrumental parameters, *Mikrochimica Acta*, 1992, **108**, 41–51.

[105] B. S. Sheppard and J. A. Caruso, Plasma mass spectrometry: consider the source. Invited lecture, *Journal of Analytical Atomic Spectrometry*, 1994, **9**, 145–149.

[106] S. D. Tanner, Space charge in ICP-MS: calculation and implications, *Spectrochimica Acta Part B: Atomic Spectroscopy*, 1992, **47**, 809–823.

[107] K. Busch, Mass spectrometry forum - Space charge in mass spectrometry, *Spectroscopy*, 2004, **19**, 35–38.

[108] *Eichrom Technologies products catalog*, 2013.

[109] B. Kahn, *Radioanalytical Chemistry*, Springer, 2007.

[110] J. Lehto and X. Hou, *Chemistry and Analysis of Radionuclides: Laboratory Techniques and Methodology*, Wiley, 2011.

[111] C. Vandecasteele, M. Nagels, H. Vanhoe and R. Dams, Suppression of analyte signal in inductively-coupled plasma mass-spectrometry and the use of an internal standard, *Analytica Chimica Acta*, 1988, **211**, 91–98.

[112] F. Vanhaecke, H. Vanhoe, R. Dams and C. Vandecasteele, The use of internal standards in ICP-MS, *Talanta*, 1992, **39**, 737–742.

[113] Thermo Fisher Scientific, *Element options: Glovebox*.

[114] Thermo Fisher Scientific, *Element2 High Resolution ICP-MS*.

[115] Thermo Fisher Scientific, *Multi Element Analysis of Samples using XSeries2*.

[116] Thermo Fisher Scientific, *XSeries2 ICP-MS Technical Description*.

[117] H. M. Kuss and M. Muller, Spectral interference of polyatomic ions of Cr, Fe, Mn, Mo, Ni, and W in steel using inductively coupled plasma mass spectrometry, *Steel Research*, 1995, **66**, 516–519.

[118] C. H. Yang and S. J. Jiang, Determination of B, Si, P and S in steels by inductively coupled plasma quadrupole mass spectrometry with dynamic reaction cell, *Spectrochimica Acta Part B: Atomic Spectroscopy*, 2004, **59**, 1389–1394.

[119] Hazan and J. Korkisch, Anion-exchange separation of iron, cobalt and nickel, *Analytica Chimica Acta*, 1965, **32**, 46–51.

[120] H. F. Aly, S. Elreefy and M. Elgarhy, Extraction of Iron, Cobalt, and Manganese From Hydrochloric-acid With Quaternary Amine, Aliquat-336, *Microchemical Journal*, 1972, **17**, 431–435.

[121] F. W. E. Strelow, Improved separation of iron from copper and other elements by anion-exchange chromatography on a 4-percent cross-linked resin with high-concentrations of hydrochloric-acid, *Talanta*, 1980, **27**, 727–732.

[122] T. Kekesi, K. Mimura and M. Isshiki, Ultra-high purification of iron by anion exchange in hydrochloric acid solutions, *Hydrometallurgy*, 2002, **63**, 1–13.

[123] C. J. Park, Determination of boron in steel by isotope-dilution inductively coupled plasma mass spectrometry after matrix separation, *Bulletin of the Korean Chemical Society*, 2002, **23**, 1541–1544.

[124] Z. Grahek and M. R. Macefat, Extraction chromatographic separation of iron from complex liquid samples and the determination of Fe-55, *Journal of Radioanalytical and Nuclear Chemistry*, 2005, **267**, 131–137.

[125] S. G. John and J. F. Adkins, Analysis of dissolved iron isotopes in seawater, *Marine Chemistry*, 2010, **119**, 65–76.

[126] R. M. Wheaton and L. J. Lefevre, *DOWEX Ion Exchange Resins: Fundamentals of Ion Exchange*, Dow liquid separations technical report, 2000.

[127] E. P. Horwitz, M. L. Dietz, D. M. Nelson, J. J. LaRosa and W. D. Fairman, Concentration and separation of actinides from urine using a supported bifunctional organophosphorus extractant, *Analytica Chimica Acta*, 1990, **238**, 263–271.

[128] E. P. Horwitz, R. Chiarizia, M. L. Dietz and H. Diamond, Separation and pre-concentration of actinides from acidic media by extraction chromatography, *Analytica Chimica Acta*, 1993, **281**, 361–372.

[129] E. A. Huff and D. R. Huff, *TRU-spec and RE-spec chromatography: basic studies and applications*, 34th ornl/doe conference on analytical chemistry in energy technology technical report, 1993.

[130] J. S. Fritz, B. B. Garralda and S. K. Karraker, Cation exchange separation of metal ions by elution with hydrofluoric acid, *Analytical Chemistry*, 1961, **33**, 882–886.

[131] F. Nelson, T. Murase and K. A. Kraus, Ion exchange procedures : I. Cation exchange in concentration HCl and HClO$_4$ solutions, *Journal of Chromatography A*, 1964, **13**, 503–535.

[132] F. W. E. Strelow, R. Rethemeyer and C. J. C. Bothma, Ion exchange selectivity scales for cations in nitric acid and sulfuric acid media with a sulfonated polystyrene resin., *Analytical Chemistry*, 1965, **37**, 106–111.

[133] F. Nelson and K. A. Kraus, Anion-exchange Studies : XI. Lead(II) and Bismuth(III) in Chloride and Nitrate Solutions, *Journal of the American Chemical Society*, 1954, **76**, 5916–5920.

[134] R. P. Oertel and R. A. Plane, Raman and infrared study of nitrate complexes of bismuth(III), *Inorganic Chemistry*, 1968, **7**, 1192–1196.

[135] J. P. Faris and R. F. Buchanan, *Anion exchange characteristics of the elements in nitric acid and nitrate solutions and application in trace element analysis*, Argonne national laboratory technical report, Argonne National Laboratory, 1964.

[136] E. P. Horwitz, R. Chiarizia and M. L. Dietz, A novel strontium-selective extraction chromatographic resin, *Solvent Extraction and Ion Exchange*, 1992, **10**, 313–336.

[137] E. P. Horwitz, M. L. Dietz, S. Rhoads, C. Felinto, N. H. Gale and J. Houghton, A lead-selective extraction chromatographic resin and its application to the

isolation of lead from geological samples, *Analytica Chimica Acta*, 1994, **292**, 263–273.

[138] Y. Bakircioglu, S. R. Segade, E. R. Yourd and J. F. Tyson, Evaluation of Pb-Spec for flow-injection solid-phase extraction preconcentration for the determination of trace lead in water and wine by flame atomic absorption spectrometry, *Analytica Chimica Acta*, 2003, **485**, 9–18.

[139] D. De Muynck, C. Cloquet and F. Vanhaecke, Development of a new method for Pb isotopic analysis of archaeological artefacts using single-collector ICP-dynamic reaction cell-MS, *Journal of Analytical Atomic Spectrometry*, 2008, **23**, 62–71.

[140] N. Vajda, J. LaRosa, R. Zeisler, P. Danesi and G. Kis-Benedek, A novel technique for the simultaneous determination of Pb-210 and Po-210 using a crown ether, *Journal of Environmental Radioactivity*, 1997, **37**, 355–372.

[141] M. L. Dietz and E. P. Horwitz, An improved method for the separation of lead-210 from Ra-DEF for radioactive equilibrium experiments - Microscale liquid-liquid extraction using a polymer-supported crown ether, *Journal of Chemical Education*, 1996, **73**, 182–184.

[142] E. R. Yourd, J. F. Tyson and R. D. Koons, On-line matrix removal of lead for the determination of trace elements in forensic bullet samples by flow injection inductively coupled plasma-mass spectrometry, *Spectrochimica Acta Part B: Atomic Spectroscopy*, 2001, **56**, 1731–1745.

[143] G. W. Leddicotte, *The radiochemistry of rhenium*, National research council. nuclear science series technical report, 1961.

[144] E. P. Steinberg, *The radiochemistry of niobium and tantalum*, National research council. nuclear science series technical report, Los Alamos National Laboratory, S.l., 1961.

[145] Internal SCKCEN QA document, *Detectielimieten en meetonzekerheden geaccrediteerde analysemethoden voor interne klanten*, 2010.

[146] E. Yamaki, K. Ginestar and L. Martinelli, Dissolution mechanism of 316L in lead-bismuth eutectic at 500 °C, *Corrosion Science*, 2011, **53**, 3075–3085.

[147] T. B. Coplen, Guidelines and recommended terms for expression of stable-isotope-ratio and gas-ratio measurement results, *Rapid Communications In Mass Spectrometry*, 2011, **25**, 2538–2560.

[148] F. Vanhaecke, L. Moens, R. Dams, I. Papadakis and P. Taylor, Applicability of high-resolution ICP mass spectrometry for isotope ratio measurements, *Analytical Chemistry*, 1997, **69**, 268–273.

[149] I. Trešl, C. R. Quétel and P. D. P. Taylor, Solution to data integration problems during isotope ratio measurements by magnetic sector inductively coupled plasma mass spectrometer at medium mass resolution: application to the certification of an enriched ^{53}Cr material by isotope dilution, *Spectrochimica Acta Part B: Atomic Spectroscopy*, 2003, **58**, 551–563.

[150] A. J. Walder, I. Platzner and P. A. Freedman, Isotope Ratio Measurement of Lead, Neodymium and Neodymium Samarium Mixtures, Hafnium and Hafnium Lutetium Mixtures With A Double Focusing Multiple Collector Inductively Coupled Plasma Mass-spectrometer, *Journal of Analytical Atomic Spectrometry*, 1993, **8**, 19–23.

[151] A. J. Walder and P. A. Freedman, Isotopic Ratio Measurement Using A Double Focusing Magnetic-sector Mass Analyzer With An Inductively Coupled Plasma As An Ion-source, *Journal of Analytical Atomic Spectrometry*, 1992, **7**, 571–575.

[152] J. S. Becker and H. J. Dietze, Double-focusing sector field inductively coupled plasma mass spectrometry for highly sensitive multi-element and isotopic analysis - Invited lecture, *Journal of Analytical Atomic Spectrometry*, 1997, **12**, 881–889.

[153] K. G. Heumann, S. M. Gallus, G. Radlinger and J. Vogl, Precision and accuracy in isotope ratio measurements by plasma source mass spectrometry, *Journal of Analytical Atomic Spectrometry*, 1998, **13**, 1001–1008.

[154] J. S. Becker and H. J. Dietze, Precise and accurate isotope ratio measurements by ICP-MS, *Fresenius Journal of Analytical Chemistry*, 2000, **368**, 23–30.

[155] J. S. Becker, State-of-the-art and progress in precise and accurate isotope ratio measurements by ICP-MS and LA-ICP-MS - Plenary Lecture, *Journal of Analytical Atomic Spectrometry*, 2002, **17**, 1172–1185.

[156] T. Walczyk, TIMS versus multicollector-ICP-MS: coexistence or struggle for survival?, *Analytical and Bioanalytical Chemistry*, 2004, **378**, 229–231.

[157] F. Vanhaecke and L. Moens, Overcoming spectral overlap in isotopic analysis via single- and multi-collector ICP-mass spectrometry, *Analytical and Bioanalytical Chemistry*, 2004, **378**, 232–240.

[158] D. C. Baxter, I. Rodushkin and E. Engström, Isotope abundance ratio measurements by inductively coupled plasma-sector field mass spectrometry, *Journal of Analytical Atomic Spectrometry*, 2012, **27**, 1355–1381.

[159] M. Berglund and M. E. Wieser, Isotopic compositions of the elements 2009 (IUPAC Technical Report), *Pure and Applied Chemistry*, 2011, **83**, 397–410.

[160] A. A. van Heuzen, T. Hoekstra and B. van Wingerden, Precision and accuracy attainable with isotope dilution analysis applied to inductively coupled plasma mass spectrometry: theory and experiments, *Journal of Analytical Atomic Spectrometry*, 1989, **4**, 483–489.

[161] F. Vanhaecke, G. de Wannemacker, L. Moens, R. Dams, C. Latkoczy, T. Prohaska and G. Stingeder, Dependence of detector dead time on analyte mass number in inductively coupled plasma mass spectrometry, *Journal of Analytical Atomic Spectrometry*, 1998, **13**, 567–571.

[162] A. Held and P. D. P. Taylor, A calculation method based on isotope ratios for the determination of dead time and its uncertainty in ICP-MS and application of the method to investigating some features of a continuous dynode multiplier, *Journal of Analytical Atomic Spectrometry*, 1999, **14**, 1075–1079.

[163] P. K. Appelblad and D. C. Baxter, A model for calculating dead time and mass discrimination correction factors from inductively coupled plasma mass spectrometry calibration curves, *Journal of Analytical Atomic Spectrometry*, 2000, **15**, 557–560.

[164] H. Ramebäck, M. Berglund, D. Vendelbo, R. Wellum and P. D. P. Taylor, On the determination of the true dead-time of a pulse-counting system in isotope ratio mass spectrometry, *Journal of Analytical Atomic Spectrometry*, 2001, **16**, 1271–1274.

[165] S. M. Nelms, C. R. Quétel, T. Prohaska, J. Vogl and P. D. P. Taylor, Evaluation of detector dead time calculation models for ICP-MS, *Journal of Analytical Atomic Spectrometry*, 2001, **16**, 333–338.

[166] J. Moser, W. Wegscheider and T. Meisel, Uncertainty of dead time estimation in ICP-MS, *Journal of Analytical Atomic Spectrometry*, 2003, **18**, 508–511.

[167] *The R Project for Statistical Computing*, http://www.r-project.org/, Accessed: 2014-09-05.

[168] M. P. Seah, Effective dead time in pulse counting systems, *Surface and Interface Analysis*, 1995, **23**, 729–732.

[169] G. P. Russ and J. M. Bazan, Isotopic ratio measurements with an inductively coupled plasma source mass spectrometer, *Spectrochimica Acta Part B: Atomic Spectroscopy*, 1987, **42**, 49–62.

[170] W. A. Russell, D. A. Papanastassiou and T. A. Tombrello, Ca isotope fractionation on the Earth and other solar system materials, *Geochimica et Cosmochimica Acta*, 1978, **42**, 1075–1090.

[171] C. R. Quétel, J. Vogl, T. Prohaska, S. M. Nelms, P. D. P. Taylor and P. De Bievre, Comparative performance study of ICP mass spectrometers

by means of U "isotopic measurements", *Fresenius Journal of Analytical Chemistry*, 2000, **368**, 148–155.

[172] C. R. Quétel, T. Prohaska, M. Hamester, W. Kerl and P. D. P. Taylor, Examination of the performance exhibited by a single detector double focusing magnetic sector ICP-MS instrument for uranium isotope abundance ratio measurements over almost three orders of magnitude and down to pg g^{-1} concentration levels, *Journal of Analytical Atomic Spectrometry*, 2000, **15**, 353–358.